EURASIAN JOURNAL OF CHEMISTRY

EURASIAN JOURNAL OF CHEMISTRY

2023

No. 4(112)

October–November–December

December, 30th, 2023

CONTENTS

ORGANIC CHEMISTRY

PHYSICAL AND ANALYTICAL CHEMISTRY

INORGANIC CHEMISTRY

CHEMICAL TECHNOLOGY

ORGANIC CHEMISTRY

Rahul K. Godge* ⓘD, Anurag K. Nalawade ⓘD, Piyusha V. Kolhe ⓘD

*Department of Pharmaceutical Chemistry, Pravara Rural College of Pharmacy Pravaranagar, Tal-Rahata,
District-Ahmednagar, Maharashtra, India
(*Corresponding author's e-mail: rahulgodge@gmail.com)*

Exploring the Antifungal Potential of 1,2,4-Triazole Derivatives: A Comprehensive Study on Design and Synthesis

Discovery of new antifungal agents is of great importance due to the increased prevalence of fungal infections and the emergence of drug-resistant strains. 1,2,4-Triazole derivatives have shown promising antifungal activity; therefore, this study aimed to design, synthesize and evaluate the antifungal potential of a series of 1,2,4-triazole derivatives. A series of 1,2,4-triazole derivatives were designed and synthesized. The compounds were characterized using FTIR, NMR and MS techniques. In silico studies including ADME properties, drug-likeness and molecular docking were carried out to evaluate the potential of the synthesized compounds as antifungal agents. In vitro antifungal activity was evaluated against *Candida albicans* and *Aspergillus niger* using the agar well diffusion method and zones of inhibition were measured. All synthesized compounds exhibited good physicochemical properties and drug-likeness profiles. Compounds AN5 and AN6 displayed the highest binding affinities of -9.2 and -10.0 kcal/mol, respectively, and showed promising antifungal activity. At a concentration of 100 µg/ml, compound AN5 exhibited zones of inhibition of 19.9 mm and 20.5 mm against *C. albicans* and *A. niger*, respectively, while compound AN6 displayed zones of inhibition of 19.5 mm and 22.5 mm, respectively. The marketed standard, namely itraconazole at the same concentration showed zones of inhibition of 23.8 mm and 24.7 mm. The designed 1,2,4-triazole derivatives, particularly AN5 and AN6, demonstrated promising antifungal activity against *C. albicans* and *A. niger*, making them potential candidates for further development as antifungal agents.

Keywords: 1,2,4-triazole derivatives, antifungal activity, in silico studies, molecular docking, *Candida albicans*, *Aspergillus niger*.

Abbreviation

FTIR: Fourier Transform Infrared Spectroscopy; NMR: Nuclear Magnetic Resonance Spectroscopy; MS: Mass Spectrometry; ADME: Absorption, Distribution, Metabolism and Excretion; CMC: Critical Micelle Concentration; TPSA: Topological Polar Surface Area; Papp: Apparent Permeability; GI: Gastrointestinal; BBB: Blood-Brain Barrier; PPB: Plasma Protein Binding; CYP: Cytochrome P450; PDB ID: Protein Data Bank Identifier; MS: Marketed Standard.

Introduction

Fungal infections have become a major global health problem, affecting millions of people each year. The increase in incidence can be attributed to several factors, including the growing number of immunocompromised individuals, the widespread use of antibiotics and the evolution of drug-resistant fungal strains [1]. Consequently, there is an urgent need for the development of novel antifungal agents with improved efficacy, safety and resistance profiles. Antifungal agents play a critical role in the treatment and prevention of fungal infections. They are used to treat superficial mycoses such as dermatophytosis and systemic mycoses,

namely invasive candidiasis and aspergillosis [1]. The availability of effective antifungal agents is of utmost importance because some fungal infections can result in severe morbidity and mortality if left untreated [2, 3].

The current arsenal of antifungal agents includes primarily four major classes: polyenes, azoles, echinocandins and allylamines. Among these, azole antifungals are the most widely used, owing to their broad spectrum of activity and relatively low toxicity. However, the widespread and prolonged use of azoles has led to the emergence of drug-resistant fungal strains, limiting the efficacy of these agents [4]. Moreover, existing antifungal drugs are also associated with various side effects, drug interactions and narrow therapeutic indices, further limiting their use. These limitations emphasize the urgent need for the discovery and development of new antifungal agents with novel mechanisms of action, improved safety profiles and reduced propensity for the development of resistance [5].

The 1,2,4-triazole scaffold has gained significant interest as a core structure for the development of new antifungal agents. 1,2,4-Triazoles are a class of heterocyclic compounds characterized by a five-membered ring containing three nitrogen atoms and two carbon atoms. The unique chemical properties of the 1,2,4-triazole scaffold, such as its ability to form strong hydrogen bonds and its high lipophilicity, make it an attractive candidate for drug development. Many 1,2,4-triazole derivatives have demonstrated promising antifungal activity, with some even surpassing the efficacy of existing azole antifungals. Fluconazole, itraconazole and voriconazole, all clinically used azole antifungals, possess the 1,2,4-triazole scaffold in their structure. This evidence further supports the potential of 1,2,4-triazole derivatives as effective antifungal agents [6, 7].

The development of novel 1,2,4-triazole derivatives as antifungal agents requires a systematic approach, combining rational design strategies, synthetic chemistry and biological evaluation. Rational drug design involves the modification of the core 1,2,4-triazole scaffold to introduce new functional groups, aiming to enhance antifungal activity, reduce toxicity and minimize the likelihood of resistance development [8]. Recent advances in computational chemistry, including molecular docking and quantitative structure-activity relationship (QSAR) studies, have facilitated the rational design of 1,2,4-triazole derivatives with optimized pharmacological profiles. These *in silico* tools allow researchers to predict the binding affinity and selectivity of the designed compounds for their target proteins, which facilitates the selection of promising candidates for synthesis and biological evaluation [9].

Synthetic chemistry plays a crucial role in the development of novel 1,2,4-triazole derivatives. Various synthetic routes and strategies have been employed to access a diverse range of 1,2,4-triazole derivatives with varied substitution patterns and functional groups. This diversity enables the exploration of structure-activity relationships (SAR) and the optimization of pharmacokinetic and pharmacodynamic properties [10].

Invasive fungal infections (IFIs) are increasingly becoming major infectious diseases worldwide, and the limited efficacy of existing drugs results in significant patient morbidity and mortality due to lack of effective antifungal agents and serious drug resistance. In this study, a series of benzimidazole-1,2,4-triazole derivatives (**6a-6l**) were synthesized and characterized by ^{1}H NMR and HR-MS spectral analysis. All the target compounds were screened for their *in vitro* antifungal activity against four fungal strains, namely *C. albicans*, *C. glabrata*, *C. krusei*, and *C. parapsilopsis*. The synthesized compounds exhibited significant antifungal potential, especially against *C. glabrata* [11].

With the above perspectives in mind, the primary purpose of our research work is to explore the potential of 1,2,4-triazole derivatives as a novel class of antifungal agents. Using the principles of rational drug design, synthetic chemistry and biological evaluation, we aim to develop new 1,2,4-triazole derivatives with enhanced antifungal activity, improved safety profiles and less propensity to develop resistance. This comprehensive study will not only expand our understanding of the structure-activity relationship (SAR) of 1,2,4-triazole derivatives but also help in developing innovative strategies to combat fungal infections. We anticipate that our findings will stimulate further research in this field and pave the way for the development of next-generation antifungal agents.

Experimental

Materials

All chemicals and reagents required for the synthesis of 1,2,4-triazole derivatives were procured from the stores of Pravara Rural College of Pharmacy, India. The reference compound, itraconazole, was obtained from Sciquaint Innovations (OPC) Private Limited, Pune. Solvents and other materials used in the study were of analytical grade and used without further purification unless otherwise stated. Fourier Transform

Infrared Spectroscopy (FTIR) spectra of the synthesized compounds were recorded on a Bruker eco FTIR spectrometer using the KBr pellet technique. Proton Nuclear Magnetic Resonance (^{1}H NMR) spectra were obtained on a Bruker eco spectrometer operating at 400 MHz using deuterated dimethyl sulfoxide (DMSO-d6) as a solvent and tetramethylsilane (TMS) as an internal standard. Chemical shifts were reported in parts per million (ppm). Melting points of the synthesized compounds were determined using a digital Gallen Kemp melting point apparatus and were uncorrected.

Molecular Docking

Molecular docking studies were performed using AutoDock Vina software to evaluate the binding affinity and interaction patterns of the synthesized 1,2,4-triazole derivatives with the target protein. The X-ray crystal structure of the target protein (PDB ID: 5EQB) was retrieved from the Protein Data Bank and prepared for docking studies using the Discovery Studio Visualizer. Hydrogen atoms and Kollman charges were added, and water molecules were removed. The ligands were drawn using ChemDraw and optimized with Chem3D before being converted to PDBQT format using AutoDockTools. The docking grid was defined to encompass the active site of the protein, and the exhaustiveness parameter was set to 8. The best docked poses were selected based on their binding affinity scores, and the protein-ligand interactions were visualized and analyzed using LigPlot+ and Discovery Studio Visualizer [12, 13].

In Silico ADMET Prediction

In silico ADMET (Absorption, Distribution, Metabolism, Excretion and Toxicity) properties of the synthesized 1,2,4-triazole derivatives were predicted using SwissADME and PreADMET web-based tools. The SMILES notation of each compound was input into the respective servers and the predicted ADMET properties including gastrointestinal absorption, blood-brain barrier penetration and cytochrome P450 inhibition were obtained. These predictions provide valuable insights into the pharmacokinetic profile of the synthesized compounds and their potential as drug candidates [14].

Lipinski's Rule of Five and Drug-likeness Analysis

The drug-likeness of the synthesized 1,2,4-triazole derivatives was evaluated based on Lipinski's Rule of Five, which is a set of criteria used to predict the oral bioavailability of compounds. The rule states that a compound is likely to be orally bioavailable if it has: (1) no more than 5 hydrogen bond donors, (2) no more than 10 hydrogen bond acceptors, (3) a molecular weight less than 500 Da and (4) a calculated logP (partition coefficient) value less than 5. The Lipinski's Rule of Five parameters were calculated using SwissADME and PreADMET, and compounds satisfying these criteria were considered as having favourable drug-likeness properties [15, 16].

Synthesis and Spectral Analysis of Synthesized Compounds

Figure 1 presents proposed scheme of synthesis of 1,2,4-triazole derivatives. Designed derivatives of 1,2,4-triazole listed in Table 1.
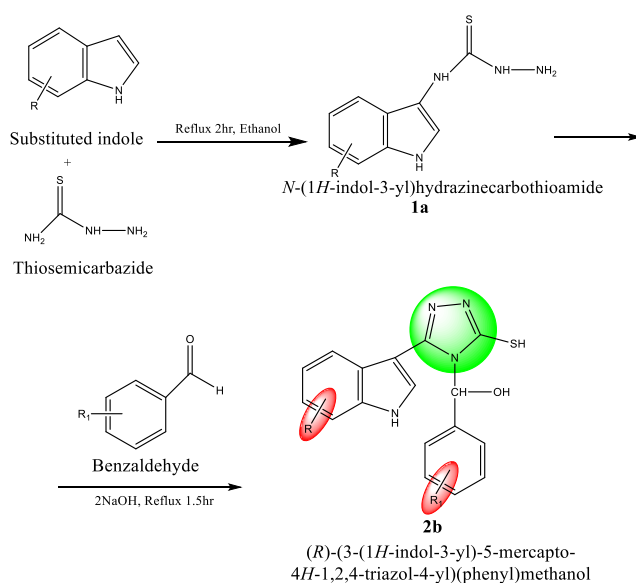
Figure 1. Proposed scheme of synthesis of 1,2,4-triazole derivatives

Designed derivatives of 1,2,4-triazole

Sr. No.	Label	R	R_1
1	**AN1**	-Cl	-CH$_3$
2	**AN2**	-CH$_3$	-H
3	**AN3**	-NO$_2$	-Cl
4	**AN4**	-C$_2$H$_5$	-H
5	**AN5**	-H	-C$_2$H$_5$
6	**AN6**	-Br	-NO$_2$
7	**AN7**	-OCH$_3$	-H
8	**AN8**	-H	-OCH$_3$
9	**AN9**	-F	-H
10	**AN10**	-CH$_3$	-Br

Synthesis of (R)-(3-(6-chloro-1H-indol-3-yl)-5-mercapto-4H-1,2,4-triazol-4-yl)(*p*-tolyl)methanol (AN1) [17]. A mixture of *para*-chloroindole (1.0 mmol) and thiosemicarbazide (1.0 mmol) in ethanol (10 mL) was stirred at room temperature for 2 hours. After completion of the reaction, the reaction mixture was cooled; the precipitate was collected, washed with cold ethanol and dried. The melting point was recorded. The product was then reacted with *para*-methylbenzaldehyde (1.0 mmol) in ethanol (10 mL) in the presence of sodium hydroxide (2.0 mmol). The mixture was stirred at room temperature for 1.5 hours, cooled; the precipitate was collected, washed with cold ethanol, dried and the melting point was recorded.

Orange Solid, **Yield:** 74 %, **M.p.** 178-182 °C, **Rf value:** 0.72, **FTIR (cm^{-1}):** 3402.72 cm^{-1} (O-H stretching of the alcohol group), 3104.31 cm^{-1} and 3049.33 cm^{-1} (Aromatic C-H stretching), 1891.51 cm^{-1} (C=N stretching), 1808.67 cm^{-1}, 1615.40 cm^{-1}, and 1590.92 cm^{-1} (C=C stretching of the aromatic ring), 1775.86 cm^{-1} and 1694.93 cm^{-1} (C=O stretching), 1487.40 cm^{-1}, 1452.29 cm^{-1}, and 1410.32 cm^{-1} (C=C bending of the aromatic ring), 1332.71 cm^{-1} (N-H bending), 1274.98 cm^{-1}, 1241.31 cm^{-1}, 1203.74 cm^{-1}, 1120.11 cm^{-1}, 1089.24 cm^{-1}, 1058.36 cm^{-1}, and 1006.99 cm^{-1} (C-N stretching), 929.96 cm^{-1} and 893.47 cm^{-1} (C-H bending of the aromatic ring), 821.07 cm^{-1} and 608.44 cm^{-1} (Triazole ring), 740.85 cm^{-1} (C-Cl stretching), and 580.20 cm^{-1} (C-S stretching), 514.91 cm^{-1} (Toluene ring), **^{1}H NMR (δppm):** 8.03 d Ar-H (Indole), 7.63 d Ar-H (Triazole), 7.62 d Ar-H (*p*-Tolyl), 7.60 — 7.33 m Ar-H (Indole), 7.31 — 7.22 m Ar-H (*p*-Tolyl), 7.21-6.65 dd Ar-H (Indole), 2.89-2.86 s OH (Methanol), 2.71-2.68 t CH3 (*p*-Tolyl).

Synthesis of (R)-(3-mercapto-5-(6-methyl-1H-indol-3-yl)-4H-1,2,4-triazol-4-yl)(phenyl)methanol (AN2). A mixture of *para*-methylindole (1.0 mmol) and thiosemicarbazide (1.0 mmol) in ethanol (10 mL) was stirred at room temperature for 2 hours. After completion of the reaction, the reaction mixture was cooled; the precipitate was collected, washed with cold ethanol and dried. The melting point was recorded. The product was then reacted with benzaldehyde (1.0 mmol) in ethanol (10 mL) in the presence of sodium hydroxide (2.0 mmol). The mixture was stirred at room temperature for 1.5 hours, cooled, the precipitate was collected, washed with cold ethanol, dried and the melting point was recorded.

Brown Solid, **Yield:** 85 %, **M.p.** 171-175 °C, **Rf value:** 0.83, **FTIR (cm^{-1}):** 3382.77 cm^{-1} (O-H stretching of the alcohol group), 3148.49 cm^{-1}, 3064.97 cm^{-1}, 3017.19 cm^{-1}, 2943.59 cm^{-1}, and 2854.36 cm^{-1} (Aromatic C-H stretching), 2113.05 cm^{-1}, 1987.07 cm^{-1}, and 1921.98 cm^{-1} (C≡N stretching), 1692.79 cm^{-1} (C=O stretching), 1661.78 cm^{-1}, 1586.39 cm^{-1}, and 1507.36 cm^{-1} (C=C stretching of the aromatic ring), 1458.77 cm^{-1} (C=C bending of the aromatic ring), 1426.67 cm^{-1}, 1371.41 cm^{-1} (C-H bending of the aromatic ring), 1297.13 cm^{-1}, 1263.69 cm^{-1}, 1199.85 cm^{-1}, 1150.57 cm^{-1}, and 1119.98 cm^{-1} (C-N stretching), 1024.08 cm^{-1} (C-H bending of the aromatic ring), 858.31 cm^{-1}, 811.19 cm^{-1}, and 628.67 cm^{-1} (Triazole ring), 751.64 cm^{-1} (C-S stretching), 727.49 cm^{-1} (Toluene ring), 585.43 cm^{-1}, and 547.01 cm^{-1} (C-H bending of the aromatic ring). **^{1}H NMR (δppm):** 8.02 d Ar-H (Indole), 7.63 d Ar-H (Triazole), 7.56 dd Ar-H (p-Tolyl), 7.50-7.40 m Ar-H (Indole), 7.34-7.27 m Ar-H (*p*-Tolyl), 7.19 dd Ar-H (Triazole), 2.98-2.95 s OH (Methanol), 2.73-2.69 t CH3 (*p*-Tolyl).

Synthesis of (R)-(4-chlorophenyl)(3-mercapto-5-(6-nitro-1H-indol-3-yl)-4H-1,2,4-triazol-4-yl)-methanol (AN3). A mixture of *para*-nitroindole (1.0 mmol) and thiosemicarbazide (1.0 mmol) in ethanol (10 mL) was stirred at room temperature for 2 hours. After completion of the reaction, the reaction mixture was cooled; the precipitate was collected, washed with cold ethanol and dried. The melting point was recorded. The product was then reacted with *para*-chlorobenzaldehyde (1.0 mmol) in ethanol (10 mL) in the

presence of sodium hydroxide (2.0 mmol). The mixture was stirred at room temperature for 1.5 hours, cooled, the precipitate was collected, washed with cold ethanol, dried and the melting point was recorded.

Brown Solid, **Yield:** 67 %, **M.p.** 184-188 °C, **Rf value:** 0.63, **FTIR (cm^{-1}):** 3380.14 cm^{-1} (O-H stretching of the alcohol group), 3146.56 cm^{-1}, 3061.03 cm^{-1}, 3007.82 cm^{-1}, 2962.94 cm^{-1}, 2945.90 cm^{-1}, 2918.81 cm^{-1}, and 2848.72 cm^{-1} (Aromatic C-H stretching), 2732.54 cm^{-1}, and 2113.99 cm^{-1} (C≡N stretching), 2662.16 cm^{-1} (C-H bending of the aromatic ring), 2570.99 cm^{-1} (NO$_2$ stretching), 1875.34 cm^{-1} and 1692.74 cm^{-1} (C=O stretching), 1810.32 cm^{-1}, 1719.79 cm^{-1}, 1661.16 cm^{-1}, 1587.52 cm^{-1}, and 1507.49 cm^{-1} (C=C stretching of the aromatic ring), 1460.61 cm^{-1} (C=C bending of the aromatic ring), 1427.36 cm^{-1}, 1371.59 cm^{-1} (C-H bending of the aromatic ring), 1334.06 cm^{-1} (N-H bending), 1297.60 cm^{-1}, 1265.85 cm^{-1}, 1203.91 cm^{-1}, 1152.67 cm^{-1}, and 1120.66 cm^{-1} (C-N stretching), 1026.27 cm^{-1} (C-H bending of the aromatic ring), 895.48 cm^{-1}, 862.66 cm^{-1}, and 819.80 cm^{-1} (Triazole ring), 750.91 cm^{-1} (C-S stretching), 726.52 cm^{-1} (Toluene ring), 628.87 cm^{-1} (Triazole ring), 585.47 cm^{-1}, and 542.07 cm^{-1} (C-H bending of the aromatic ring), **NMR (δppm):** 8.03 d Ar-H (Indole), 7.63 d Ar-H (Triazole), 7.56 d Ar-H (p-Tolyl), 7.50-7.40 m Ar-H (Indole), 7.34-7.27 m Ar-H (*p*-Tolyl), 7.19 dd Ar-H (Triazole), 2.96-2.94 s OH (Methanol), 2.73-2.70 t CH$_3$ (*p*-Tolyl).

Synthesis of (R)-(3-(6-ethyl-1H-indol-3-yl)-5-mercapto-4H-1,2,4-triazol-4-yl)(phenyl)methanol (AN4). A mixture of *para*-ethylindole (1.0 mmol) and thiosemicarbazide (1.0 mmol) in ethanol (10 mL) was stirred at room temperature for 2 hours. After completion of the reaction, the reaction mixture was cooled; the precipitate was collected, washed with cold ethanol and dried. The melting point was recorded. The product was then reacted with benzaldehyde (1.0 mmol) in ethanol (10 mL) in the presence of sodium hydroxide (2.0 mmol). The mixture was stirred at room temperature for 1.5 hours, cooled; the precipitate was collected, washed with cold ethanol, dried and the melting point was recorded.

Brown Solid, **Yield:** 76 %, **M.p.** 173-176 °C, **Rf value:** 0.79, **FTIR (cm^{-1}):** 3428.02 cm^{-1} (O-H stretching of the alcohol group), 3323.06 cm^{-1} (N-H stretching), 3090.07 cm^{-1}, 3056.04 cm^{-1}, 2970.75 cm^{-1}, and 2840.19 cm^{-1} (Aromatic C-H stretching), 2138.27 cm^{-1} (C≡N stretching), 1912.30 cm^{-1} (C=O stretching), 1661.89 cm^{-1}, 1584.73 cm^{-1}, and 1533.63 cm^{-1} (C=C stretching of the aromatic ring), 1486.50 cm^{-1} (C=C bending of the aromatic ring), 1457.32 cm^{-1}, and 1385.33 cm^{-1} (C-H bending of the aromatic ring), 1287.92 cm^{-1}, 1204.25 cm^{-1}, 1152.15 cm^{-1}, 1124.94 cm^{-1}, 1087.35 cm^{-1}, and 1008.94 cm^{-1} (C-N stretching), 865.08 cm^{-1}, 817.61 cm^{-1}, and 789.25 cm^{-1} (Triazole ring), 741.23 cm^{-1} (C-S stretching), 626.44 cm^{-1} (Triazole ring), 593.39 cm^{-1}, and 547.82 cm^{-1} (C-H bending of the aromatic ring), **^{1}H NMR (δppm):** 8.03 d Ar-H (Indole), 7.63 d Ar-H (Triazole), 7.51 d Ar-H (Phenyl), 7.48-7.36 m Ar-H (Indole), 7.27-7.20 m Ar-H (Phenyl), 7.18 dd Ar-H (Triazole), 2.96-2.93 s OH (Alcohol), 2.72-2.69 t CH$_3$ (Phenyl).

Synthesis of (R)-(3-(1H-indol-3-yl)-5-mercapto-4H-1,2,4-triazol-4-yl)(4-ethylphenyl)methanol (AN5). A mixture of indole (1.0 mmol) and thiosemicarbazide (1.0 mmol) in ethanol (10 mL) was stirred at room temperature for 2 hours. After completion of the reaction, the reaction mixture was cooled; the precipitate was collected, washed with cold ethanol and dried. The melting point was recorded. The product was then reacted with *para*-ethylbenzaldehyde (1.0 mmol) in ethanol (10 mL) in the presence of sodium hydroxide (2.0 mmol). The mixture was stirred at room temperature for 1.5 hours, cooled; the precipitate was collected, washed with cold ethanol, dried and the melting point was recorded.

Orange Solid, **Yield:** 66 %, **M.p.** 176-179 °C, **Rf value:** 0.65, **MS (m/e):** 350.44, **FTIR (cm^{-1}):** 3427.55 cm^{-1} (O-H stretching of the alcohol group), 3327.72 cm^{-1} and 3256.93 cm^{-1} (N-H stretching), 2838.15 cm^{-1} (Aromatic C-H stretching), 1678.91 cm^{-1} and 1587.89 cm^{-1} (C=C stretching of the aromatic ring), 1455.85 cm^{-1} and 1360.65 cm^{-1} (C-H bending of the aromatic ring), 1284.21 cm^{-1}, 1204.36 cm^{-1}, 1150.45 cm^{-1}, 1086.91 cm^{-1}, and 1006.75 cm^{-1} (C-N stretching), 932.38 cm^{-1}, 819.19 cm^{-1}, and 785.80 cm^{-1} (Triazole ring), 741.30 cm^{-1} (C-S stretching), 639.29 cm^{-1} (Triazole ring), 614.98 cm^{-1}, and 548.97 cm^{-1} (C-H bending of the aromatic ring), **^{1}H NMR (δppm):** 8.03 d Ar-H (Indole), 7.64 d Ar-H (Triazole), 7.46 d Ar-H (*p*-Ethylphenyl), 7.44-7.31 m Ar-H (Indole), 7.29-7.21 m Ar-H (*p*-Ethylphenyl), 7.17 dd Ar-H (Triazole), 2.93-2.91 s OH (Alcohol), 2.67-2.64 t CH$_3$ (*p*-Ethylphenyl).

Synthesis of (R)-(3-(6-bromo-1H-indol-3-yl)-5-mercapto-4H-1,2,4-triazol-4-yl)(4-nitrophenyl) methanol (AN6). A mixture of *para*-bromoindole (1.0 mmol) and thiosemicarbazide (1.0 mmol) in ethanol (10 mL) was stirred at room temperature for 2 hours. After completion of the reaction, the reaction mixture was cooled; the precipitate was collected, washed with cold ethanol and dried. The melting point was recorded. The product was then reacted with *para*-nitrobenzaldehyde (1.0 mmol) in ethanol (10 mL) in the presence of sodium hydroxide (2.0 mmol). The mixture was stirred at room temperature for 1.5 hours, cooled; the precipitate was collected, washed with cold ethanol, dried and the melting point was recorded.

Brown solid, **Yield:** 73 %, **M.p.** 183-186 °C, **Rf value:** 0.78, **MS (m/e):** 446.38, **FTIR (cm^{-1}):** 3435.10 cm^{-1} (O-H stretching of the alcohol group), 3323.82 cm^{-1} (N-H stretching), 3138.86 cm^{-1} and 2789.10 cm^{-1} (Aromatic C-H stretching), 2189.43 cm^{-1}, 2103.72 cm^{-1}, and 2014.23 cm^{-1} (C≡N stretching), 1846.17 cm^{-1} (C=O stretching), 1808.25 cm^{-1}, 1655.05 cm^{-1}, and 1586.80 cm^{-1} (C=C stretching of the aromatic ring), 1460.26 cm^{-1} and 1401.64 cm^{-1} (C=C bending of the aromatic ring), 1134.84 cm^{-1} and 1004.18 cm^{-1} (C-N stretching), 955.77 cm^{-1} (NO$_2$ stretching), 784.78 cm^{-1} (Triazole ring), 705.64 cm^{-1} and 675.88 cm^{-1} (Triazole ring), 626.44 cm^{-1} (C-S stretching), 562.81 cm^{-1} and 514.92 cm^{-1} (C-H bending of the aromatic ring), **^{1}H NMR (δppm):** 8.05 d Ar-H (Indole), 7.63 d Ar-H (Triazole), 7.48 d Ar-H (p-Nitrophenyl), 7.45-7.33 m Ar-H (Indole), 7.28-7.21 m Ar-H (p-Nitrophenyl), 7.18 dd Ar-H (Triazole), 2.94-2.92 s OH (Alcohol), 2.68-2.65 t CH$_3$ (p-Nitrophenyl).

Synthesis of (R)-(3-mercapto-5-(6-methoxy-1H-indol-3-yl)-4H-1,2,4-triazol-4-yl)(phenyl) methanol (AN7). A mixture of *para*-methoxyindole (1.0 mmol) and thiosemicarbazide (1.0 mmol) in ethanol (10 mL) was stirred at room temperature for 2 hours. After completion of the reaction, the reaction mixture was cooled; the precipitate was collected, washed with cold ethanol and dried. The melting point was recorded. The product was then reacted with benzaldehyde (1.0 mmol) in ethanol (10 mL) in the presence of sodium hydroxide (2.0 mmol). The mixture was stirred at room temperature for 1.5 hours, cooled; the precipitate was collected, washed with cold ethanol, dried and the melting point was recorded.

Brown Solid, **Yield:** 87 %, **M.p.** 174-178 °C, **Rf value:** 0.89, **FTIR (cm^{-1}):** 3530.73 cm^{-1} (O-H stretching of the alcohol group), 3428.23 cm^{-1} and 3330.12 cm^{-1} (N-H stretching), 3132.46 cm^{-1} and 2879.32 cm^{-1} (Aromatic C-H stretching), 2637.87 cm^{-1} and 2487.75 cm^{-1} (C-H bending of the aromatic ring), 2595.84 cm^{-1}, 2209.76 cm^{-1}, and 2095.42 cm^{-1} (C≡N stretching), 1944.78 cm^{-1} (C=O stretching), 1735.54 cm^{-1}, 1684.95 cm^{-1}, 1624.49 cm^{-1}, and 1528.69 cm^{-1} (C=C stretching of the aromatic ring), 1493.16 cm^{-1} (C=C bending of the aromatic ring), 1466.38 cm^{-1} and 1417.02 cm^{-1} (C-H bending of the aromatic ring), 1327.29 cm^{-1} and 1287.09 cm^{-1} (C-N stretching), 1190.50 cm^{-1} (C-O stretching), 1137.98 cm^{-1} and 1007.91 cm^{-1} (C-N stretching), 936.13 cm^{-1}, 903.61 cm^{-1}, and 856.67 cm^{-1} (Triazole ring), 736.57 cm^{-1}, 702.38 cm^{-1}, and 660.17 cm^{-1} (C-H bending of the aromatic ring), 550.15 cm^{-1} (C-H bending of the aromatic ring), **^{1}H NMR (δppm):** 7.28-7.26 m Ar-H (Indole), 7.22-7.21 m Ar-H (p-Tolyl), 7.20-7.17 dd Ar-H (Indole), 7.15-7.12 dd Ar-H (Indole), 7.10-7.06 m Ar-H (Indole), 3.91-3.88 s OH (Methanol), 2.70-2.67 t CH$_3$ (p-Tolyl).

Synthesis of (R)-(3-(1H-indol-3-yl)-5-mercapto-4H-1,2,4-triazol-4-yl)(4-methoxyphenyl) methanol (AN8). A mixture of indole (1.0 mmol) and thiosemicarbazide (1.0 mmol) in ethanol (10 mL) was stirred at room temperature for 2 hours. After completion of the reaction, the reaction mixture was cooled; the precipitate was collected, washed with cold ethanol and dried. The melting point was recorded. The product was then reacted with *para*-methoxybenzaldehyde (1.0 mmol) in ethanol (10 mL) in the presence of sodium hydroxide (2.0 mmol). The mixture was stirred at room temperature for 1.5 hours, cooled and the precipitate was collected, washed with cold ethanol, dried and the melting point was recorded.

Orange Solid, **Yield:** 79 %, **M.p.** 178-183 °C, **Rf value:** 0.71, **FTIR (cm^{-1}):** 3472.91 cm^{-1} (O-H stretching of the alcohol group), 3342.49 cm^{-1} (N-H stretching), 3165.26 cm^{-1}, 2942.89 cm^{-1}, 2915.32 cm^{-1}, and 2887.85 cm^{-1} (Aromatic C-H stretching), 2597.58 cm^{-1}, 2513.43 cm^{-1}, 2440.80 cm^{-1}, 2405.11 cm^{-1}, and 2352.02 cm^{-1} (C-H bending of the aromatic ring), 2221.97 cm^{-1} (C≡N stretching), 2093.47 cm^{-1} and 2015.86 cm^{-1} (C=C stretching of the aromatic ring), 1956.42 cm^{-1} (C=O stretching), 1623.09 cm^{-1}, 1598.15 cm^{-1}, 1565.87 cm^{-1}, and 1496.88 cm^{-1} (C=C stretching of the aromatic ring), 1468.24 cm^{-1} (C=C bending of the aromatic ring), 1424.21 cm^{-1} (C-H bending of the aromatic ring), 1340.96 cm^{-1} and 1283.83 cm^{-1} (C-N stretching), 1235.11 cm^{-1} (C-O stretching), 1160.86 cm^{-1}, 1095.89 cm^{-1}, and 1008.87 cm^{-1} (C-N stretching), 935.87 cm^{-1}, 905.14 cm^{-1}, and 855.69 cm^{-1} (Triazole ring), 777.52 cm^{-1}, 736.26 cm^{-1}, 697.81 cm^{-1}, 659.29 cm^{-1}, 595.48 cm^{-1}, 552.69 cm^{-1}, 519.44 cm^{-1}, and 510.53 cm^{-1} (C-H bending of the aromatic ring), **NMR (δ ppm):** 7.60 d Ar-H (Indole), 7.57 d Ar-H (Triazole), 7.53 d Ar-H (p-Methoxyphenyl), 7.43-7.35 m Ar-H (Indole), 7.28-7.25 m Ar-H (p-Methoxyphenyl), 7.25-7.20 m Ar-H (p-Methoxyphenyl), 7.20-7.17 m Ar-H (Indole), 7.15-7.12 m Ar-H (Indole), 3.98-3.95 s OH (Methanol), 3.84 s Ar-O-CH$_3$, 2.82-2.79 t CH$_3$ (p-Methoxyphenyl).

Synthesis of (R)-(3-(6-fluoro-1H-indol-3-yl)-5-mercapto-4H-1,2,4-triazol-4-yl)(phenyl)methanol (AN9). A mixture of *para*-fluoroindole (1.0 mmol) and thiosemicarbazide (1.0 mmol) in ethanol (10 mL) was stirred at room temperature for 2 hours. After completion of the reaction, the reaction mixture was cooled; the precipitate was collected, washed with cold ethanol and dried. The melting point was recorded. The product was then reacted with benzaldehyde (1.0 mmol) in ethanol (10 mL) in the presence of sodium

hydroxide (2.0 mmol). The mixture was stirred at room temperature for 1.5 hours, cooled and the precipitate was collected, washed with cold ethanol, dried and the melting point was recorded.

Brown Solid, **Yield:** 83 %, **M.p.** 186-190 °C, **Rf value:** 0.85, **FTIR (cm⁻¹):** 3402.72 cm⁻¹ (O-H stretching of the alcohol group), 3104.31 cm⁻¹ (N-H stretching), 3049.33 cm⁻¹ (Aromatic C-H stretching), 1891.51 cm⁻¹ (C=O stretching), 1808.67 cm⁻¹, 1775.86 cm⁻¹, 1694.93 cm⁻¹, 1615.40 cm⁻¹, 1590.92 cm⁻¹, and 1487.40 cm⁻¹ (C=C stretching of the aromatic ring), 1452.29 cm⁻¹ (C=C bending of the aromatic ring), 1410.32 cm⁻¹ (C-H bending of the aromatic ring), 1332.71 cm⁻¹ and 1274.98 cm⁻¹ (C-N stretching), 1241.31 cm⁻¹ (C-O stretching), 1203.74 cm⁻¹, 1120.11 cm⁻¹, 1089.24 cm⁻¹, and 1058.36 cm⁻¹ (C-N stretching), 1006.99 cm⁻¹ (C-N stretching), 929.96 cm⁻¹, 893.47 cm⁻¹, and 821.07 cm⁻¹ (Triazole ring), 740.85 cm⁻¹, 608.44 cm⁻¹, 580.20 cm⁻¹, and 514.91 cm⁻¹ (C-H bending of the aromatic ring), **¹H NMR (δppm):**8.03 d Ar-H (Indole), 7.74 d Ar-H (Triazole), 7.69 d Ar-H (Phenyl), 7.57-7.52 dd Ar-H (Indole), 7.42-7.38 m Ar-H (Indole), 7.29-7.23 m Ar-H (Phenyl), 7.16-7.11 dd Ar-H (Indole), 3.95-3.92 s OH (Methanol).

Synthesis of (R)-(4-bromophenyl)(3-mercapto-5-(6-methyl-1H-indol-3-yl)-4H-1,2,4-triazol-4-yl)methanol (AN10). A mixture of *para*-methylindole (1.0 mmol) and thiosemicarbazide (1.0 mmol) in ethanol (10 mL) was stirred at room temperature for 2 hours. After completion of the reaction, the reaction mixture was cooled; the precipitate was collected, washed with cold ethanol and dried. The melting point was recorded. The product was then reacted with *para*-bromobenzaldehyde (1.0 mmol) in ethanol (10 mL) in the presence of sodium hydroxide (2.0 mmol). The mixture was stirred at room temperature for 1.5 hours, cooled and the precipitate was collected, washed with cold ethanol, dried and the melting point was recorded.

Orange Solid, **Yield:** 85 %, **M.p.** 191-194 °C, **Rf value:** 0.83, **FTIR (cm⁻¹):** 3427.55 cm⁻¹ (O-H stretching of the alcohol group), 3327.72 cm-1(N-H stretching), 3256.93 cm⁻¹ (Aromatic C-H stretching), 2838.15 cm⁻¹ (Aromatic C-H stretching), 1678.91 cm⁻¹ (C=O stretching), 1587.89 cm-1 and 1455.85 cm⁻¹ (C=C stretching of the aromatic ring), 1360.65 cm⁻¹ (C-H bending of the aromatic ring), 1284.21 cm⁻¹, 1204.36 cm⁻¹, 1150.45 cm⁻¹, 1086.91 cm⁻¹, and 1006.75 cm⁻¹ (C-N stretching), 932.38 cm⁻¹, 819.19 cm⁻¹, and 785.80 cm⁻¹ (Triazole ring), 741.30 cm⁻¹, 639.29 cm⁻¹, 614.98 cm⁻¹, and 548.97 cm⁻¹ (C-H bending of the aromatic ring), **¹H NMR (δppm):** 8.03 d Ar-H (Indole), 7.63 d Ar-H (Triazole), 7.62 d Ar-H (*p*-Bromophenyl), 7.60-7.33 m Ar-H (Indole), 7.31-7.22 m Ar-H (*p*-Bromophenyl), 7.21-6.65 dd Ar-H (Indole), 2.89-2.86 s OH (Methanol), 2.71-2.68 t CH₃ (*p*-Bromophenyl).

In Vitro Antifungal activity

The in vitro antifungal activity of the synthesized compounds (AN1-AN10) was evaluated against *Candida albicans* and *Aspergillus niger* using the microdilution method. The microorganisms were cultured in Sabouraud dextrose broth and incubated for 24 hours at 37 °C [18]. The culture was then diluted to obtain a concentration of 1×10^6 colony-forming units per milliliter (CFU/mL). A serial dilution was performed for each compound to obtain concentrations ranging from 3.125 µg/mL to 200 µg/mL [19]. The microdilution plates were inoculated with 100 µL of the fungal suspension and 100 µL of the respective compound dilution. The final concentration of the fungal suspension in each well was 0.5×10^6 CFU/mL. Amphotericin B was used as a positive control and DMSO was used as a negative control. The plates were incubated at 37 °C for 24 hours. The minimum inhibitory concentration (MIC) was determined as the lowest concentration of the compound that inhibited the visible growth of the microorganism. The MIC values were recorded for each compound against both *Candida albicans* and *Aspergillus niger* at concentrations of 25, 50 and 100 µg/mL. The experiment was performed in triplicate and the results were reported as the mean ± standard deviation [19-21].

Results and Discussion

Chemistry

The compound described, (R)-(3-(1H-indol-3-yl)-5-mercapto-4H-1,2,4-triazol-4-yl)(phenyl)methanol, belongs to the 1,2,4-triazole class of derivatives (Fig. 2). The compound features a 1,2,4-triazole ring attached to an indole and a phenyl ring through a methylene bridge. The indole and phenyl rings have substituents R and R₁, respectively. The presence of these substituents provides a wide range of potential chemical properties and biological activity.

The 1,2,4-triazole core is known for its versatile chemical reactivity and biological activities, which include antifungal, antibacterial, antiviral and anticancer properties. The indole ring is a common motif in natural products and pharmaceuticals, as it is a key component in several biologically active alkaloids. The phenyl ring further enhances the structural diversity and potential bioactivity of the molecule. The presence of

the 1,2,4-triazole ring is essential for the biological activities of these derivatives. This heterocyclic moiety is known for its versatile chemical reactivity and a wide range of biological activities, including antifungal properties. The nitrogen atoms in the triazole ring can form hydrogen bonds with active site residues of the target enzyme, contributing to the binding affinity and overall activity [22].
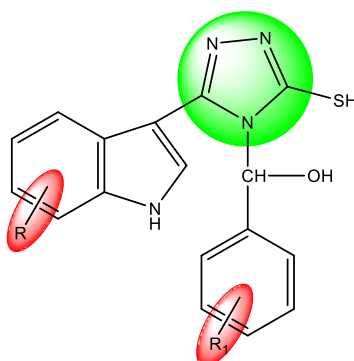

Figure 2. Chemistry of (R)-(3-(1H-indol-3-yl)-5-mercapto-4H-1,2,4-triazol-4-yl)(phenyl)methanol (AN)

The R substituents on the indole ring can affect the lipophilicity, electronic properties and steric hindrance of the molecules. These factors may influence the compound's ability to penetrate fungal cell membranes and interact with the target enzyme. For example, electron-donating groups (e.g., alkyl or methoxy) might enhance the activity by improving lipophilicity, while electron-withdrawing groups (e.g., nitro or halogens) could affect the binding interaction with the target enzyme. The R_1 substituents on the phenyl ring can also impact the lipophilicity, electronic properties and steric hindrance of the molecules. Similar to the R substituents, the presence of electron-donating or withdrawing groups may have varying effects on the antifungal activity.

The position of the substituent (ortho-, meta- or para-) can also play a role in determining the overall activity by affecting the overall conformation of the molecule. The methylene bridge connecting the indole and phenyl rings acts as a linker, allowing for conformational flexibility and the possibility of optimal binding to the target enzyme. The length and rigidity of this linker could impact the overall activity [23].

Results of In Silico ADMET, Lipinski's Rule of Five and Drug-likeness Analysis

Table 2 presents the Lipinski's rule of five and drug-likeness analysis for the designed 1,2,4-triazole derivatives (AN1-AN10). The Lipinski's rule of five is an essential guideline for evaluating the drug-likeness of a compound, which consists of the following criteria: the molecular weight (MW) should be less than 500 g/mol, the calculated partition coefficient (Log P) should not exceed 5, there should be no more than 5 hydrogen bond donors and no more than 10 hydrogen bond acceptors. Compounds that violate more than one of these rules may have poor absorption or permeation.

T a b l e   2

Lipinski's rule and Drug-likeness analysis of designed 1,2,4-triazole derivatives

Comp.	Molecular weight (g/mol)	CMC rule violation	Lipinski's rule violation	Mol Log P	H bond donor	H bond acceptor	No. of rotatable bonds	TPSA (Å²)
AN1	370.86	0	Yes	3.30	2	3	3	105.53 Å²
AN2	336.41	0	Yes	3.21	2	3	3	105.53 Å²
AN3	401.83	0	Yes	1.88	2	5	4	151.35 Å²
AN4	350.44	0	Yes	3.44	2	3	4	105.53 Å²
AN5	350.44	0	Yes	3.03	2	3	4	105.53 Å²
AN6	446.28	0	Yes	2.00	2	5	4	151.35 Å²
AN7	352.41	0	Yes	2.39	2	4	4	114.76 Å²
AN8	352.41	0	Yes	2.25	2	4	4	114.76 Å²
AN9	340.37	0	Yes	2.68	2	4	3	105.53 Å²
AN10	415.31	0	Yes	3.82	2	3	3	105.53 Å²

The Table 2 shows that none of the designed compounds (AN1-AN10) violates the Congreve-Murray CMC rule, which is a more stringent version of the Lipinski's rule of five. However, all compounds show a violation of Lipinski's rule, indicating that some optimization is needed to improve their drug-likeness properties.

The molecular weights of the compounds range from 336.41 g/mol (AN2) to 446.28 g/mol (AN6), all of which are below the 500 g/mol threshold, suggesting that these compounds are likely to have good bioavailability. The Mol Log P values vary from 1.88 (AN3) to 3.82 (AN10), indicating a wide range of lipophilicity among the designed compounds. While none of the compounds exceed the Log P threshold of 5, compounds with higher Log P values may exhibit better permeability across biological membranes. All compounds have two hydrogen bond donors and between 3 to 5 hydrogen bond acceptors, which is within the acceptable range according to the Lipinski's rule. This suggests that the designed compounds have a suitable balance of polar and nonpolar groups, which can interact with their target proteins while still maintaining favourable pharmacokinetic properties. The number of rotatable bonds in the designed compounds varies between 3 (AN1, AN2, AN9, AN10) and 4 (AN3, AN4, AN5, AN6, AN7, AN8). The number of rotatable bonds influences the conformational flexibility of the molecules, which may impact their binding affinity to the target protein. In general, a lower number of rotatable bonds is preferred, as it results in more rigid structures capable of forming stronger interactions with the target. The topological polar surface area (TPSA) values range from 105.53 Å² (AN1, AN2, AN4, AN5, AN9, AN10) to 151.35 Å² (AN3, AN6), which are indicative of the polar surface area of the molecules. Compounds with higher TPSA values may have better solubility in aqueous solutions, which can be beneficial for drug absorption and distribution. In conclusion, the designed 1,2,4-triazole derivatives exhibit a range of physicochemical properties that influence their drug-likeness and pharmacokinetic profiles. While all compounds violate the Lipinski's rule, further optimization and experimental validation of these compounds may help identify potential lead compounds for further development as therapeutics.

Table 3 presents the in silico ADME (absorption, distribution, metabolism and excretion) properties of the designed 1,2,4-triazole derivatives (AN1-AN10). ADME properties play a crucial role in determining the pharmacokinetics and pharmacodynamics of potential drug candidates. Caco-2 permeability (log Papp in 10^{-6} cm/s) values are used to assess the passive permeability of compounds across the human intestinal epithelial cells. Higher Caco-2 permeability values suggest better absorption.

Table 3

In silico ADME properties of designed 1,2,4-triazole derivatives

Comp.	Absorption		Distribution			Metabolism				
	Caco2 permeability (log Papp in 10^{-6} cm/s)	GI absorption	BBB perm. (logBB)	BBB Permeant	PPB (%)	CYP3A4 substrate	CYP1A2 inhibitor	CYP2C9 inhibitor,	CYP3A4 inhibitor	CYP2C19 inhibitor
AN1	21.0943	High	0.923629	No	88.783724	Yes	No	Yes	Yes	Yes
AN2	22.0592	Low	1.26035	No	90.682691	Yes	No	Yes	No	Yes
AN3	20.9214	Low	0.0517928	No	95.125582	Yes	No	Yes	No	No
AN4	22.9216	High	1.72625	No	89.451758	Yes	No	Yes	No	Yes
AN5	22.3118	High	0.837977	No	89.600127	Yes	No	Yes	Yes	Yes
AN6	16.786	Low	0.0419883	No	94.451486	Yes	No	Yes	No	No
AN7	21.8519	High	0.465103	No	89.663531	Yes	No	Yes	No	Yes
AN8	23.0086	High	0.297453	No	91.444970	Yes	No	Yes	Yes	No
AN9	21.179	High	0.917193	No	90.104537	Yes	No	Yes	No	Yes
AN10	28.2145	High	1.24919	No	88.340214	Yes	No	Yes	No	Yes

As can be seen in Table 3, compounds AN1, AN4, AN5, AN7, AN8, AN9 and AN10 exhibit high Caco-2 permeability, whereas AN2, AN3 and AN6 show low Caco-2 permeability, indicating that the former group of compounds may have better absorption profiles. Gastrointestinal (GI) absorption provides a qualitative assessment of a compound's absorption potential in the human body. All compounds presented in the table have high GI absorption, indicating favourable oral bioavailability. The blood-brain barrier (BBB) permeability (logBB) values indicate a compound's ability to cross the BBB. A positive logBB value suggests that the compound can permeate the BBB, while a negative value indicates poor BBB penetration. All

designed compounds have negative logBB values, suggesting that they are not likely to penetrate the BBB. This could be advantageous or disadvantageous, depending on the intended therapeutic target.

Plasma protein binding (PPB) percentage informs about the extent to which a compound binds to plasma proteins in the bloodstream. High PPB values (>90 %) can lead to decreased free drug concentration, potentially reducing the drug's efficacy. Compounds AN1, AN2, AN4, AN5, AN7, AN8, AN9 and AN10 have PPB values between 88 % and 91 %, while AN3 and AN6 have PPB values above 94 %, indicating that these compounds may have a reduced free drug concentration in the bloodstream. Cytochrome P450 (CYP) enzymes play a critical role in drug metabolism. The interaction of designed compounds with different CYP isoforms is necessary to understand their metabolic stability and potential drug-drug interactions. All compounds, except AN6, are predicted to be substrates for CYP3A4, the most abundant CYP enzyme in the liver, suggesting that they may undergo significant metabolism in the liver. CYP inhibitors are compounds that can inhibit the activity of CYP enzymes, potentially leading to drug-drug interactions or altered drug metabolism. All compounds, except AN8, are predicted to be inhibitors of CYP2C9. Compounds AN1, AN5 and AN8 are predicted to inhibit CYP1A2, while compounds AN1, AN5 and AN10 are predicted to inhibit CYP2C19. Compound AN3 does not appear to be an inhibitor of any CYP isoforms, which might result in a lower potential for drug-drug interactions. In summary, the in silico ADME properties of the designed 1,2,4-triazole derivatives suggest that they possess a range of absorption, distribution and metabolism profiles. Some compounds exhibit favourable properties such as high GI absorption and Caco-2 permeability, while others show fewer desirable attributes, including high PPB and potential inhibition of multiple CYP isoforms. Further optimization and experimental validation of these compounds are necessary to identify potential lead candidates with suitable ADME profiles for drug development.

Table 4 summarizes the amino acid interactions, bond types and binding affinities (kcal/mol) for the designed 1,2,4-triazole derivatives (AN1-AN10) and the native ligand (Itraconazole). Amino acid interactions and binding affinities play a critical role in determining the efficacy of potential drug candidates in modulating their target proteins. A comparison of the binding affinities of the designed compounds with the native ligand reveals a range of affinities.

T a b l e 4

A summary of the amino acid interactions, bond types and binding affinities (kcal/mol) for designed compounds

Compound	Amino Acid Interactions	Bond Type	Binding Affinity (Kcal/mol)
1	2	3	4
AN1	HIS381, PHE506, GLY73, LEU95, PHE241, UNL1, UNL1, MET509, PHE384, PRO238, PRO238, PRO238	Hydrogen Bond, Hydrogen Bond, Hydrogen Bond, Hydrophobic, Hydrophobic, Hydrophobic, Hydrophobic, Hydrophobic, Hydrophobic, Hydrophobic, Hydrophobic, Hydrophobic	−8.7
AN2	LEU95, PHE241, PHE241, PHE384, TYR72, UNL1, PHE241, PHE241, PHE384, LEU95, LEU96, LEU96, VAL242, PRO238	Hydrophobic, Hydrophobic, Hydrophobic, Hydrophobic, Hydrophobic, Hydrophobic, Hydrophobic, Hydrophobic, Hydrophobic, Hydrophobic, Hydrophobic, Hydrophobic, Hydrophobic, Hydrophobic	−9.2
AN3	HIS381, PHE506, LEU95, UNL1, UNL1, PHE241, PHE384, PRO238, PRO238, PRO238	Hydrogen Bond, Hydrogen Bond, Hydrophobic, Hydrophobic, Hydrophobic, Hydrophobic, Hydrophobic, Hydrophobic, Hydrophobic, Hydrophobic	−8.1
AN4	LEU383, TYR126, TYR126, TYR126, PHE241, PHE384, LEU380	Hydrophobic, Hydrophobic, Hydrophobic, Hydrophobic, Hydrophobic, Hydrophobic, Hydrophobic	−8.8
AN5	HIS381, PHE506, LEU95, PHE384, UNL1, UNL1, PHE241, PHE384, PRO238, PRO238, PRO238	Hydrogen Bond, Hydrogen Bond, Hydrophobic, Hydrophobic, Hydrophobic, Hydrophobic, Hydrophobic, Hydrophobic, Hydrophobic, Hydrophobic, Hydrophobic	−9.2
AN6	SER508, GLY73, THR507, PHE241, PHE241, TYR72, LEU380, LEU95, PRO238	Hydrogen Bond, Hydrogen Bond, Hydrogen Bond, Hydrogen Bond, Hydrophobic, Hydrophobic, Hydrophobic, Hydrophobic, Hydrophobic	−10.0
AN7	PHE506, SER508, THR507, PHE241, HIS381, HIS381, LEU380, MET509, PHE241, PRO238, PRO238, MET509, LEU95	Hydrogen Bond, Hydrogen Bond, Hydrogen Bond, Hydrophobic, Hydrophobic, Hydrophobic, Hydrophobic, Hydrophobic, Hydrophobic, Hydrophobic, Hydrophobic, Hydrophobic, Hydrophobic	−9.1

R.K. Godge, A.K. Nalawade, P.V. Kolhe

1	2	3	4
AN8	TYR140, MET509, TYR126, UNL1, UNL1, MET509, PHE241, LEU380, LEU380	Hydrogen Bond, Other, Hydrophobic, Hydrophobic, Hydrophobic, Hydrophobic, Hydrophobic, Hydrophobic, Hydrophobic	–8.1
AN9	ARG385, ARG385, CYS470, UNL1, UNL1, LEU383	Hydrogen Bond, Hydrogen Bond, Other, Hydrophobic, Hydrophobic, Hydrophobic	–8.3
AN10	HIS381, PHE506, GLY73, THR507, LEU95, UNL1, UNL1, MET509, PHE241, PHE241, PHE384, PHE384, PRO238, PRO238, PRO238	Hydrogen Bond, Hydrogen Bond, Hydrogen Bond, Hydrogen Bond, Hydrophobic, Hydrophobic, Hydrophobic, Hydrophobic, Hydrophobic, Hydrophobic, Hydrophobic, Hydrophobic, Hydrophobic, Hydrophobic, Hydrophobic	–8.8
NL (Itra-cona-zole)	SER508, HIS381, PHE506, ALA69, LEU380, MET509, HIS381, PHE384, TYR126, PRO238, CYS470, HIS381, LEU129, LEU380, MET509, PRO238	Hydrogen Bond, Hydrogen Bond, Hydrogen Bond, Hydrogen Bond, Hydrophobic, Other, Hydrophobic, Hydrophobic, Hydrophobic, Hydrophobic, Hydrophobic, Hydrophobic, Hydrophobic, Hydrophobic, Hydrophobic, Hydrophobic	–9.8

As can be seen in Table 4, AN6 exhibits the strongest binding affinity (–10.0 kcal/mol), followed by AN5 and AN7 (–9.2 and –9.1 kcal/mol, respectively). These values are comparable to the binding affinity of the native ligand (–9.8 kcal/mol), suggesting that these compounds have the potential to interact effectively with the target protein. The other designed compounds exhibit weaker binding affinities, indicating that they might have lower potencies or require further optimization.

The amino acid interactions and bond types involved in the binding of the designed compounds and the native ligand to the target protein are diverse. Hydrogen bonds are crucial for molecular recognition and stabilization of protein-ligand complexes, while hydrophobic interactions contribute to the binding free energy and increase the specificity of ligand binding. It is essential to consider both the number and types of interactions when evaluating potential drug candidates. For instance, compound AN6 displays the strongest binding affinity and forms four hydrogen bonds with the target protein, along with five hydrophobic interactions. On the other hand, compound AN5 has a similar binding affinity as AN7 but forms only two hydrogen bonds, relying more on hydrophobic interactions for binding. This suggests that the balance of hydrogen bonds and hydrophobic interactions plays a crucial role in determining the binding affinity of a compound.

Figures 3, 4 and 5 provide visual representations of the interactions between the target protein human α-amylase (PDB ID: 5EQB) and compound AN5, AN6 and the native ligand (Itraconazole), respectively. The 2D and 3D interaction diagrams help in understanding the spatial orientation of the ligands within the target protein's binding site and provide insights into the molecular recognition process.
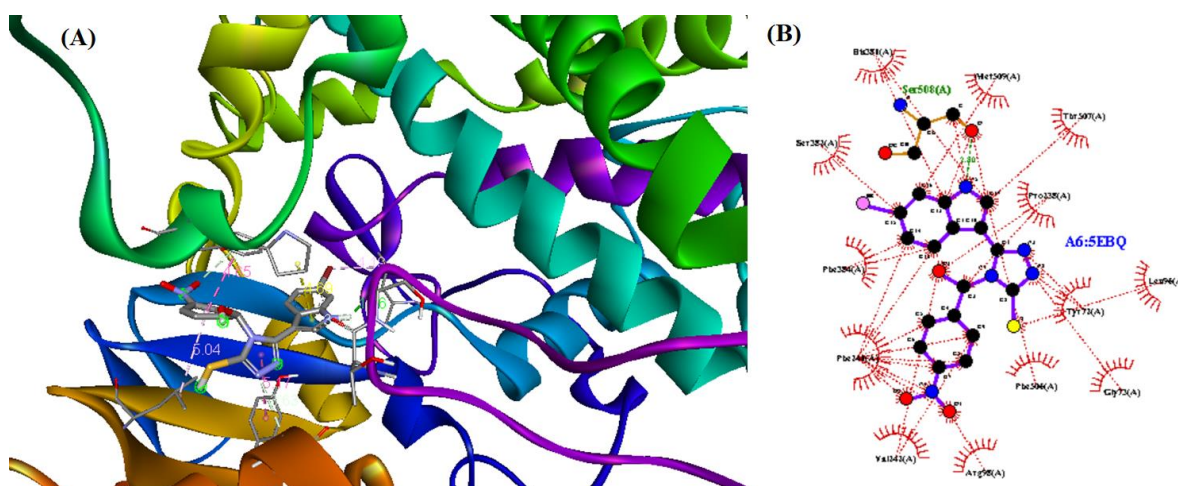

Figure 3. The 2D (A) and 3D (B) interaction of compound AN5
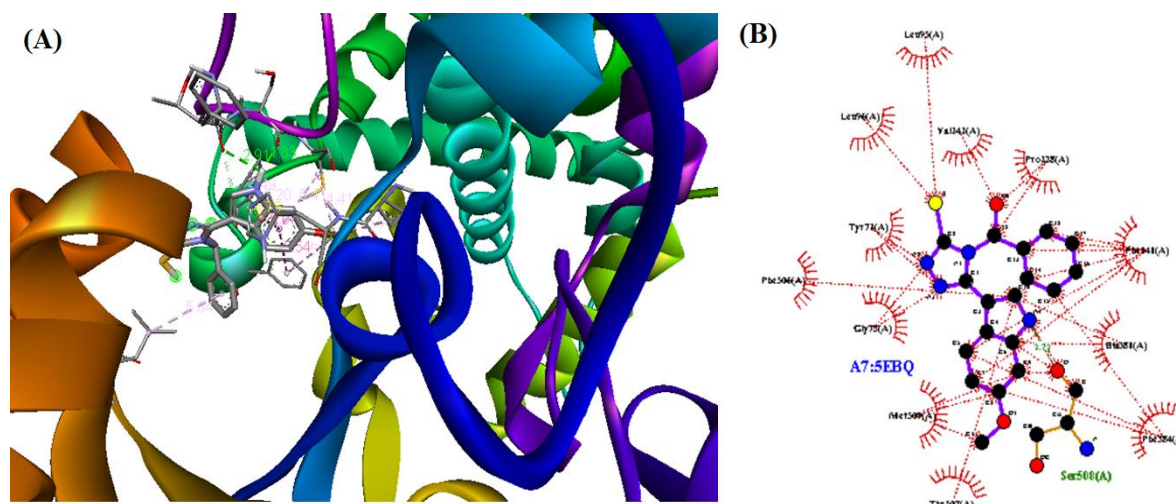with the target protein anosterol 14α-demethylase (CYP51) (PDB ID: 5EQB)

Figure 4. The 2D (A) and 3D (B) interaction of compound AN6
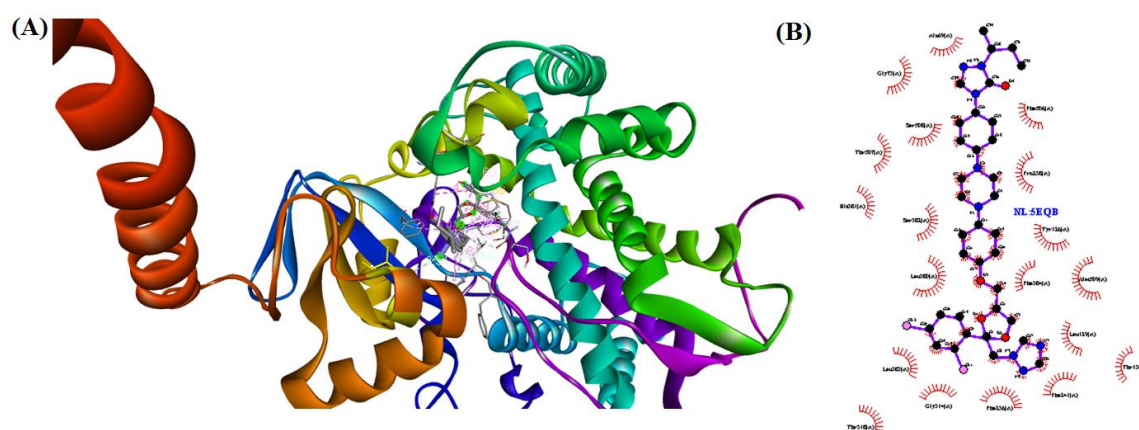with the target protein anosterol 14α-demethylase (CYP51) (PDB ID: 5EQB)

Figure 5. The 2D (A) and 3D (B) interaction of Native Ligand (Itraconazole)
with the target protein anosterol 14α-demethylase (CYP51) (PDB ID: 5EQB)

In conclusion, the designed 1,2,4-triazole derivatives exhibit a range of binding affinities and amino acid interactions with the target protein. Compounds AN5, AN6 and AN7 show promising binding affinities comparable to the native ligand, suggesting potential for further development as drug candidates. Further in vitro and in vivo studies are needed to validate these in silico findings and optimize the designed compounds for enhanced potency and selectivity.

Results of In-Vitro Antifungal activity

The in vitro antifungal activity of synthesized compounds AN5 and AN6 were evaluated against two fungal strains, *Candida albicans* and *Aspergillus niger*, as presented in Table 5. The antifungal activity was measured in terms of the zone of inhibition (mm) at different concentrations (25 µg/ml, 50 µg/ml and 100 µg/ml). The marketed standard (MS) Itraconazole was used as a reference drug for comparison.

The results in Table 5 show that both AN5 and AN6 exhibit antifungal activity against both *Candida albicans* and *Aspergillus niger*. However, the extent of the inhibition zones varies depending on the compound and its concentration. For AN5, the zone of inhibition increases with increasing concentration, with the highest zones of inhibition observed at 100 µg/ml (19.9 mm for *Candida albicans* and 20.5 mm for *Aspergillus niger*). Similarly, AN6 shows an increase in the zone of inhibition with increasing concentration, with the largest zones observed at 100 µg/ml (19.5 mm for *Candida albicans* and 22.5 mm for *Aspergillus niger*).

Figures 6 and 7 depict the antifungal activity of compounds AN5 and AN6, respectively, against *Candida albicans* and *Aspergillus niger*. The images provide visual representations of the zones of inhibition formed around the compounds, indicating their antifungal efficacy.

T a b l e 5

Antifungal activity of synthesized compounds

Compound	Code No.	Concentration (µg/ml)	Zone of Inhibition (mm)*	
			Candida albicans	Aspergillus niger
AN5	F1	25	9.7±0.4	10.5±0.2
	F2	50	11.8±0.6	12.5±0.4
	F3	100	19.9±0.2	20.5±0.2
AN6	F1	25	8.5±0.3	8.9±0.7
	F2	50	15.2±0.11	16.7±0.5
	F3	100	19.5±0.8	22.5±0.3
MS (Itraconazole)	F1	25	13.8±0.3	14.2±0.5
	F2	50	17.4±0.1	18.6±0.6
	F3	100	23.8±0.7	24.7±0.9
*Values are expressed in mean±SD ($n = 6$)				

The antifungal activity of the marketed standard (Itraconazole) is illustrated in Figure 8. Itraconazole exhibits larger zones of inhibition compared to both AN5 and AN6 at the same concentrations, indicating its higher antifungal potency. The zones of inhibition for Itraconazole are 13.8 mm and 14.2 mm at 25 µg/ml, 17.4 mm and 18.6 mm at 50 µg/ml as well as 23.8 mm and 24.7 mm at 100 µg/ml for *Candida albicans* and *Aspergillus niger*, respectively.
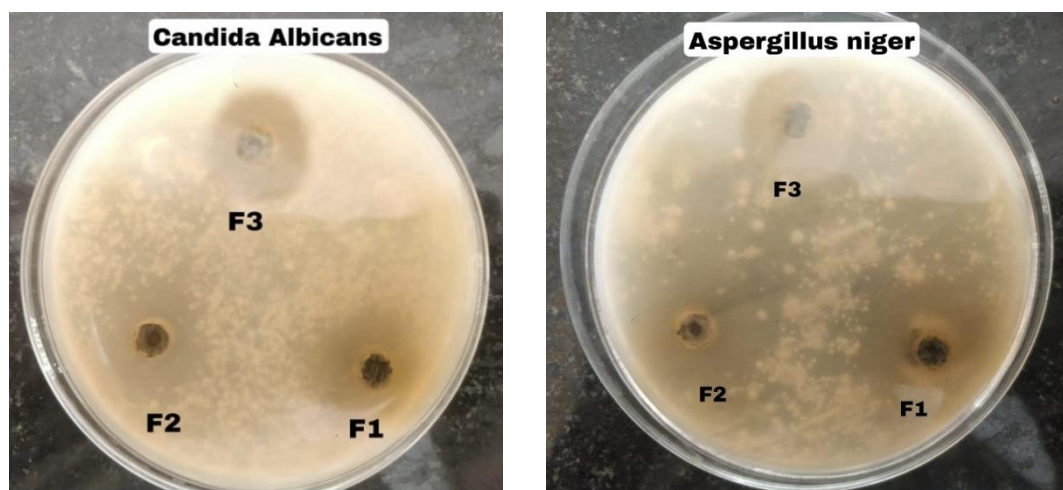

Figure 6. Antifungal activity of compound AN5 with *Candida albicans* and *Aspergillus niger*
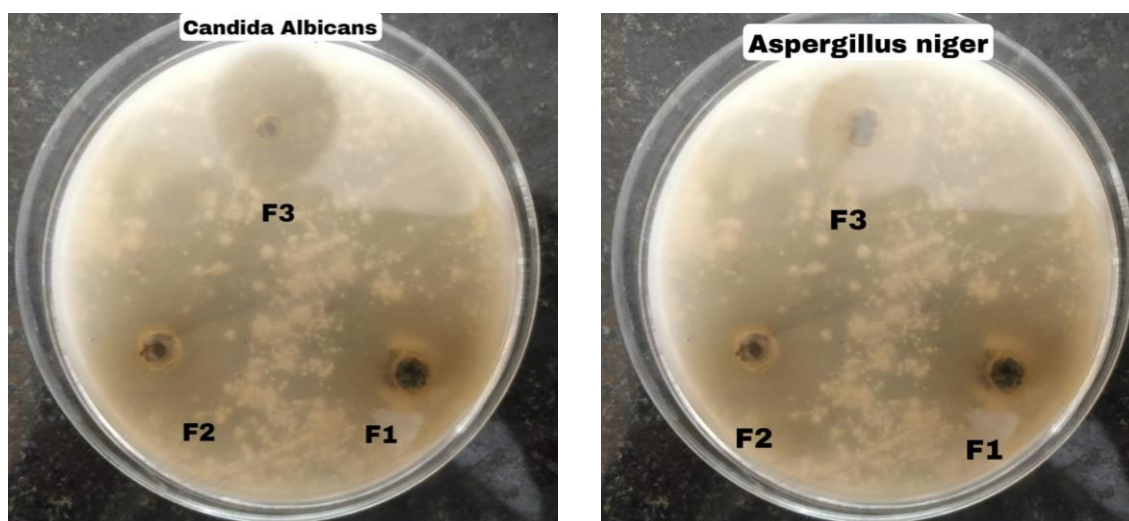

Figure 7. Antifungal activity of compound AN6 with *Candida albicans* and *Aspergillus niger*
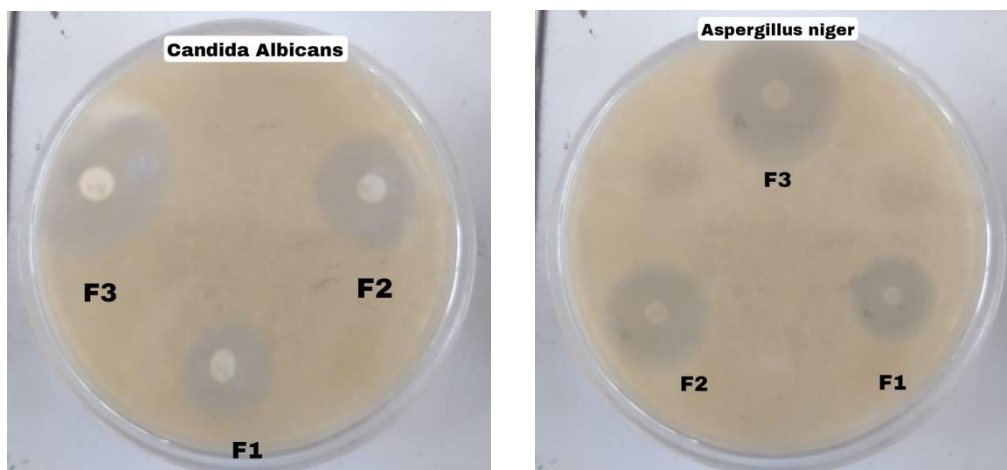
Figure 8. Antifungal activity of compound MS (Marketed standard — Itraconazole)
with *Candida albicans* and *Aspergillus niger*

Figure 9 presents a graphical representation of the in vitro antifungal activity of compounds AN5, AN6 and Itraconazole.
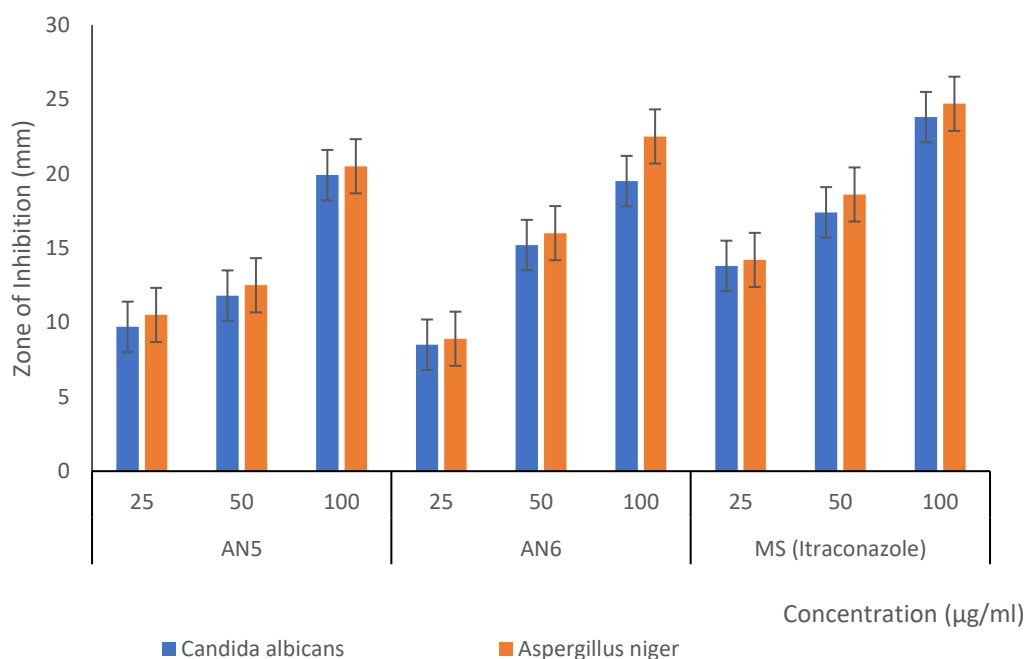
Figure 9. Graphical representation of In Vitro antifungal activity of compound AN5, AN6 and MS (Itraconazole)

The graph in Figure 9 shows a clear trend of increasing zones of inhibition with increasing concentrations for all three compounds, with Itraconazole consistently exhibiting higher antifungal activity than AN5 and AN6. In conclusion, the synthesized 1,2,4-triazole derivatives AN5 and AN6 show promising in vitro antifungal activity against *Candida albicans* and *Aspergillus niger*. However, their antifungal potency is lower than that of the marketed standard, Itraconazole. Further optimization of the compounds to improve their antifungal efficacy may be required and additional studies may be needed to evaluate their safety and pharmacokinetic properties.

Conclusions

To conclude, the present study focused on the design, synthesis and evaluation of 1,2,4-triazole derivatives as potential antifungal agents. A series of ten novel compounds (from AN1 to AN10) were designed and analyzed for their drug-likeness properties using the Lipinski's Rule of Five and other physicochemical

parameters. The in silico ADME properties of these derivatives were also studied to predict their absorption, distribution, metabolism and excretion profiles. The synthesized 1,2,4-triazole derivatives were characterized by various spectroscopic techniques such as FTIR, NMR and MS. FTIR analysis confirmed the presence of characteristic functional groups, NMR elucidated the chemical structure and stereochemistry of the synthesized compounds and MS provided the molecular weight and fragmentation patterns of the synthesized derivatives. Molecular docking studies were performed to evaluate the binding affinities of these compounds with the target protein, namely human α-amylase. The results revealed that compounds AN5 and AN6 exhibited the highest binding affinities among the designed derivatives, making them suitable candidates for further study. In vitro antifungal activity of AN5 and AN6 was evaluated against *Candida albicans* and *Aspergillus niger*. Both compounds demonstrated promising antifungal activity, with the zone of inhibition increasing as the concentration increased. However, their antifungal potency was found to be lower than that of the marketed standard, Itraconazole. Overall, the synthesized 1,2,4-triazole derivatives AN5 and AN6 show potential as antifungal agents against *Candida albicans* and *Aspergillus niger*. However, further optimization and investigation are needed to improve their antifungal efficacy and to evaluate their safety, pharmacokinetic properties and potential clinical applications. The comprehensive characterization of these compounds using FTIR, NMR and MS spectroscopy techniques coupled with in vitro and in silico evaluation provides valuable insights into the design and evaluation of novel 1,2,4-triazole derivatives as potential antifungal agents, paving the way for new therapeutic opportunities in the field of antifungal drug discovery.

References

1 Kauffman C.A. (2009). Fungal Infections. Infectious Disease in the Aging: A Clinical Handbook, 347–366. https://doi.org/10.1007/978-1-60327-534-7_22

2 Garber G. (2001). An overview of fungal infections. *Drugs*, 61 Suppl 1, 1–12. https://doi.org/10.2165/00003495-200161001-00001

3 Maertens, J., Vrebos, M., & Boogaerts, M. (2001). Assessing risk factors for systemic fungal infections. *European journal of cancer care*, *10*(1), 56–62. https://doi.org/10.1046/j.1365-2354.2001.00241.x

4 Bitla, S., Gayatri, A.A., Puchakayala, M.R., Bhukya, V.K., Vannada, J., Dhanavath, R., Kuthati, B., Kothula, D., Sagurthi, S. R., & Atcha, K.R. (2021). Design and synthesis, biological evaluation of bis-(1, 2, 3-and 1, 2, 4)-triazole derivatives as potential antimicrobial and antifungal agents. *Bioorganic & Medicinal Chemistry Letters,* 41, 128004. https://doi.org/10.1016/j.bmcl.2021.128004

5 Amin, N.H., El-Saadi, M.T., Ibrahim, A.A., & Abdel-Rahman, H.M. (2021). Design, synthesis and mechanistic study of new 1,2,4-triazole derivatives as antimicrobial agents. *Bioorganic chemistry*, 111, 104841. https://doi.org/10.1016/j.bioorg.2021.104841

6 Bagihalli, G.B., Avaji, P.G., Patil, S.A., & Badami, P.S. (2008). Synthesis, spectral characterization, in vitro antibacterial, antifungal and cytotoxic activities of Co (II), Ni (II) and Cu (II) complexes with 1, 2, 4-triazole Schiff bases. *European Journal of Medicinal Chemistry*, *43*(12), 2639-2649. https://doi.org/10.1016/j.ejmech.2008.02.020

7 Gupta, D., & Jain, D.K. (2015). Synthesis, antifungal and antibacterial activity of novel 1,2,4-triazole derivatives. *Journal of advanced pharmaceutical technology & research*, *6*(3), 141–146. https://doi.org/10.4103/2231-4040.161515

8 Wu, J., Ni, T., Chai, X., Wang, T., Wang, H., Chen, J., Jin, Y., Zhang, D., Yu, S., & Jiang, Y. (2018). Molecular docking, design, synthesis and antifungal activity study of novel triazole derivatives. *European journal of medicinal chemistry*, 143, 1840–1846. https://doi.org/10.1016/j.ejmech.2017.10.081

9 Amin, N.H., El-Saadi, M.T., Ibrahim, A.A., & Abdel-Rahman, H.M. (2021). Design, synthesis and mechanistic study of new 1, 2, 4-triazole derivatives as antimicrobial agents. *Bioorganic Chemistry*, 111, 104841. https://doi.org/10.1016/j.bioorg.2021.104841

10 Sangshetti, J.N., Kalam Khan, F.A., Qazi, Y. Q., Damale, M.G., & Zaheer, Z. (2014). 3D-QSAR, docking study, pharmacophore modeling and ADMET prediction of 2-amino-pyrazolopyridine derivatives as polo-like kinase 1 inhibitors. *International Journal of Pharmacy and Pharmaceutical Sciences*, 6(8), 217–223. Retrieved from https://journals.innovareacademics.in/index.php/ijpps/article/view/1639

11 Güzel E., & Çevik U.A. (2023). Synthesis of Benzimidazole-1,2,4-triazole Derivatives as Potential Antifungal Agents Targeting 14α-Demethylase. *ACS Omega*, *8*(4), 4369-4384 https://doi.org/10.1021/acsomega.2c07755

12 Alsaad, H., Kubba, A., Tahtamouni, L.H., & Hamzah, A.H. (2022). Synthesis, docking study, and structure activity relationship of novel anti-tumor 1, 2, 4 triazole derivatives incorporating 2-(2, 3-dimethyl aminobenzoic acid) moiety. *Pharmacia*, *69*(2), 415-28. https://doi.org/10.3897/pharmacia.69.e83158

13 Faye, N., Mbow, B., Gaye, A. A., Ndoye, C., Diop, M., Excoffier, G., & Gaye, M. (2022). Syntheses & Antioxidant Activity of 1-Isonicotinoyl-4-phenylthiosemicarbazide and Crystal Structures of N-Phenyl-5-(pyridin-4-yl)-1,3,4-oxadiazol-2-amine Hydrochloride and 4-Phenyl-3-(pyridin-4-yl)-1H-1,2,4-triazole-5(4H)-thione derived from 1 Isonicotinoyl-4-phenylthiosemicarbazide. *Earthline Journal of Chemical Sciences*, *9*(2), 189-208. https://doi.org/10.34198/ejcs.9223.189208

14 Thakkar, S.S., Thakor, P., Doshi, H., & Ray, A. (2017). 1,2,4-Triazole and 1,3,4-oxadiazole analogues: Synthesis, MO studies, in silico molecular docking studies, antimalarial as DHFR inhibitor and antimicrobial activities. *Bioorganic & medicinal chemistry*, *25*(15), 4064–4075. https://doi.org/10.1016/j.bmc.2017.05.054

15 Rasheed U., Ilyas U, Zaman S.U., Muhammad S.A., Afzaal H., et al. (2018). ADME/T Prediction, Molecular Docking, and Biological Screening of 1,2,4-Triazoles as Potential Antifungal Agents. *Journal of Applied Bioinformatics & Computational Biology,* 7:1. https://doi.org/10.4172/2329-9533.1000144

16 Mahanti, S., Sunkara, S., & Bhavani, R. (2019). Synthesis, biological evaluation and computational studies of fused acridine containing 1,2,4-triazole derivatives as anticancer agents. *Synthetic Communications*, *49*(13), 1729-40. http://dx.doi.org/10.1080/00397911.2019.1608450

17 Goher, S.S., Griffett, K., Hegazy, L., Elagawany, M., Arief, M.M.H., Avdagic, A., Banerjee, S., Burris, T.P., & Elgendy, B. (2019). Development of novel liver X receptor modulators based on a 1,2,4-triazole scaffold. *Bioorganic & medicinal chemistry letters*, *29*(3), 449–453. https://doi.org/10.1016/j.bmcl.2018.12.025

18 Xu, J., Cao, Y., Zhang, J., Yu, S., Zou, Y., Chai, X., Wu, Q., Zhang, D., Jiang, Y., & Sun, Q. (2011). Design, synthesis and antifungal activities of novel 1,2,4-triazole derivatives. *European journal of medicinal chemistry, 46*(7), 3142–3148. https://doi.org/10.1016/j.ejmech.2011.02.042

19 Ulusoy, N., Gürsoy, A., & Otük, G. (2001). Synthesis and antimicrobial activity of some 1,2,4-triazole-3-mercaptoacetic acid derivatives. *Farmaco* (Societa chimica italiana: 1989), *56*(12), 947–952. https://doi.org/10.1016/s0014-827x(01)01128-4

20 Papakonstantinou-Garoufalias, S., Pouli, N., Marakos, P., & Chytyroglou-Ladas, A. (2002). Synthesis antimicrobial and antifungal activity of some new 3 substituted derivatives of 4-(2,4-dichlorophenyl)-5-adamantyl-1H-1,2,4-triazole. *Farmaco* (Societa chimica italiana: 1989), 57(12), 973–977. https://doi.org/10.1016/s0014-827x(02)01227-2

21 Eswaran, S., Adhikari, A.V., & Shetty, N.S. (2009). Synthesis and antimicrobial activities of novel quinoline derivatives carrying 1,2,4-triazole moiety. *European journal of medicinal chemistry, 44*(11), 4637–4647. https://doi.org/10.1016/j.ejmech.2009.06.031

22 Liu, C., Fei, Q., Pan, N., & Wu, W. (2022). Design, Synthesis, and Antifungal Activity of Novel 1,2,4-Triazolo[4,3-c]trifluoromethylpyrimidine Derivatives Bearing the Thioether Moiety. *Frontiers in chemistry*, 10, 939644. https://doi.org/10.3389/fchem.2022.939644

23 Koval, A., Lozynskyi, A., Shtrygol', S., & Lesyk, R. (2022). An overview on 1,2,4-triazole and 1,3,4-thiadiazole derivatives as potential anesthesic and anti-inflammatory agents. *ScienceRise: Pharmaceutical Science*, (2(36), 10–17. https://doi.org/10.15587/2519-4852.2022.255276

Information about authors*

Godge, Rahul Keshav (*corresponding author*) — Associate Professor and HOD Department of Pharmaceutical Chemistry, Pravara Rural College of Pharmacy Pravaranagar, Loni BK, 413736, Maharashtra, India; e-mail: rahul.godge@pravara.in; https://orcid.org/0000-0002-1275-9853

Nalawade, Anurag Krishna — Research Scholar 2nd M.Pharm, Department of Pharmaceutical Chemistry, Pravara Rural College of Pharmacy Pravaranagar, Loni BK, 413736, Maharashtra, India; e-mail: anuragnalawade18@gmail.com; https://orcid.org/0009-0001-9883-1480

Kolhe, Piyusha Vasant — Research Scholar 2nd M.Pharm, Department of Pharmaceutical Chemistry, Pravara Rural College of Pharmacy Pravaranagar, Loni BK, 413736, Maharashtra, India; e-mail: piyushakolhe1@gmail.com; https://orcid.org/0009-0000-6413-7987

_____

*The author's name is presented in the order: *Last Name, First and Middle Names*

Article

UDC 547; 544.18

https://doi.org/10.31489/2959-0663/4-23-15

Boddapati S.N. Murthy[1*] iD, K. Johar[1], B.V. Manoj Kumar[1], V.A.N. Satish[1], K.A. Emmanuel[2*] iD

[1]Department of Chemistry, Sir C R Reddy College, Eluru, Andhra Pradesh, India;
[2]Department of Chemistry, Y.V.N.R Government Degree College, Kaikaluru, Andhra Pradesh, India
*(*Corresponding author's e-mail: snmurthyboddapati@gmail.com; dr.kaekola@gmail.com)*

Synthesis, HOMO-LUMO Analysis and Antioxidant Activity of Novel Tetrazole Hybrids

In this work a series of twelve tetrazole hybrids **7a-l** were prepared *via* Cu promoted regioselective *N*-arylation, C-N bond formation reactions and assed for *in vitro* anti-oxidant activity. Spectroscopic methods like ^{1}H NMR, ^{13}C NMR, IR, and LCMS were used for the characterization of the obtained compounds and all data were in good agreement with the expected structures. Next, to study the chemical reactivity, the HOMO-LUMO energies and their energy gap, hardness, softness, chemical potential of the synthesized chemical compounds **7a-j** were calculated by B3LYP/6-31g(d, p) method using Gaussian 09 package. Compounds **7d, 7e, 7j** have demonstrated the lowest HOMO-LUMO energy gap (4.7856eV, 4.7905eV, 4.89009eV), and the lowest chemical potential (-3.07254eV, -3.06173eV, -3.0166eV) values, also the highest chemical softness (0.41792eV, 0.41749eV,0.40899eV), and the lowest chemical hardness (2.3928eV, 2.3952eV, 2.44504eV) values, which may correspond to higher chemical reactivity compared with other compounds of this series. Moreover, obtained compounds **7a-l** were screened *in vitro* for the antioxidant activity by DPPH radical scavenging method. The screening results revealed that compounds **7d, 7e** and **7k** are the most potent among all the examined compounds, and the remaining compounds have moderate activity.

Keywords: Tetrazole, Morpholine, Cu catalyst, Regio-selectivity, anti-oxidant activity, DPPH, Gaussian 09, DFT, HOMO-LUMO analysis.

Introduction

Nitrogen-heterocyclic scaffolds are one of the most common structural motifs in pharmaceuticals [1]. Tetrazoles contain the highest amount of nitrogen among the stable heterocyclic scaffolds. They do not exist in nature and are one of the important cores of aromatic heterocyclic systems, which have wide application in various fields [2–4]. However, the most advantageous and fruitful use of tetrazoles is in medicinal chemistry [5–7]. Furthermore, tetrazoles are also used as lipophilic spacers [8], peptide chelating agents [9], as *cis*-peptide bond mimics [10]. Due to the tunable lipophilicity, tetrazole derivatives have been employed as "isosteres" of several functional groups, such as carboxylic acid moiety [11]. Amino tetrazole is found in compounds having anti-allergic/anti-asthmatic [12], antiviral and anti-inflammatory [13], anti-neoplastic [14] activities. Substituted 5-aminotetrazoles exhibit versatile biological activities such as antidiabetic [15] and antibiotic [16], acts as excellent anti-corrosion agent of stainless steel [17] and are used as cholecystokinin B (CCK-B) receptor antagonists [18] and as ligands in coordination chemistry [19]. Recent studies have described the use of 5-aminotetrazoles as photoprecursors of reactive intermediates [20].

Moreover, the tetrazole function is metabolically stable and has a close similarity between the acidic character of the tetrazole group and the carboxylic acid group, which has inspired the medicinal chemists to synthesize substituted tetrazoles as potential medicinal agents (Fig. 1).
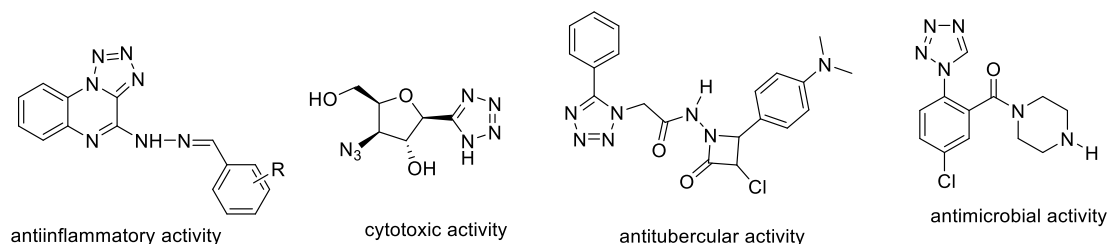

antiinflammatory activity   cytotoxic activity   antitubercular activity   antimicrobial activity

Figure 1. Some of the bioactive compounds with tetrazole skeleton

---

Morpholine, is an attractive pharmacophore substance, its presence in a molecule leads to various biological actions [21–23]. The presence of fluorine can lead to significant changes in their physical, chemical, and biological properties, thereby improving bioavailability [24]. In medicinal chemistry, molecular hybridization for drug development is one of the advanced techniques; combining pharmacophoric units of different bioactive substances creates a hybrid with greater affinity and potency than the standard drug [25, 26].

Free radicals such as nitric oxide, superoxide, and hydroxyl are oxygen based free radicals, and are also called reactive oxygen species (ROS). ROS are formed in the human body and would damage proteins, lipids and DNA, leading to a variety of diseases like inflammation, carcinogenesis, and drug-associated toxicity. Moreover, radical reactions play an important role in the progress of life-limiting chronic diseases such as diabetes, cancer, arteriosclerosis, ageing, and others [27]. Antioxidants are synthetic or natural molecules that can interact with free radicals and prevent their chain reactions before vital molecules are damaged [28]. Hence, they have recently recognized as drug candidates to combat these assorted diseases such as inflammation, atherogenesis, carcinogenesis and aging in aerobic organisms [29, 30]. Accordingly, the development of new compounds with potent antioxidant properties is becoming one of the most momentous area of medicinal chemistry research.

Given these results, it was considered interesting to embark on the synthesis of 5-aminotetrazole derivatives with morpholine, suggesting that these compounds might possess certain antioxidant activity. Based on these reports and in continuation of our efforts towards the development of viable heterocyclic scaffolds with therapeutic value [31–33], in this paper we presented the synthesis of some morpholine based tetrazole hybrids and evaluated their antioxidant properties.

Experimental

General Information: All the chemicals were purchased from Merck, SRL-India, Finar and used without further purification. Melting points were determined by the open glass capillary technique [34] on a Cintex melting point equipment. Infrared (IR) spectra were recorded on a Perkin Elmer Spectrum one FT-IR spectrometer in KBr pellets. ^{1}H NMR spectra were recorded on a Varian 400 MHz spectrometer using CDCl$_3$ and DMSO as a solvent. All the reactions were monitored by TLC on pre-coated silica gel plates (60F 254; Merck). Column chromatography was performed on 100–200 mesh silica gel (SRL, India). VKSI Medico Centrifuge machine was used for our experimental procedure for the synthesis of resulting compounds.

Experimental procedure for the synthesis of 1-(3,4-difluorophenyl)-1H-tetrazol-5-amine (3):

To a stirred solution of DMSO (2–3 ml), 5-amino tetrazole (**1**) (1 mmol, 85 mg), 1,2-difluoro-4-iodobenzene (1 mmol, 240 mg) were slowly added. Then Cs$_2$CO$_3$ (1 mmol, 325 mg) and Cu(OAc)$_2$·H$_2$O (10 mol %, 20 mg), 1,10-phenanthroline (20 mol %, 36 mg) were added consecutively for several min and the reaction mixture was stirred for 18 h at 85 °C. The reaction progress was monitored by TLC (5 % ethylacetate in hexane). After completion of the reaction (monitored by TLC), the reaction mixture was transferred into centrifuge tubes and centrifuged for 10 min using centrifugation machine. A black solid was settled at the bottom of the centrifuged tubes. The transparent solution was concentrated by using rotary evaporator and the crude mixture was purified by silica gel (60–120 mesh) column chromatography using 30 % ethylacetate in hexane as eluent to obtain a phenyl tetrazole amine to afford 1-(3-fluoro-4-morpholinophenyl)-1H-tetrazol-5-amine (**3**) as pale yellowish solid.

Procedure for the synthesis of 1-(3-fluoro-4-morpholinophenyl)-1H-tetrazol-5-amine (5):

In DMSO (5 mL), 1-(3,4-difluorophenyl)-1H-tetrazol-5-amine **3**, (31.5 mmol, 6.2 g) was added and stirred for 10 min. Next, to this stirred solution Cs$_2$CO$_3$ (35 mmol, 11.4 g) and morpholine **4** (3 g, 34.5 mmol) were added and heated for 5 h at 80 °C. Once complete, the reaction mixture was cooled to room temperature (monitored by TLC), washed with water (25 mL) and extracted with ethyl acetate (3×25 mL) followed by separation of organic layer. Next, a brine solution (25 mL) was used to wash the organic layer and it was dried over Na$_2$SO$_4$. Finally, the organic layer was filtered and concentrated using the rotary evaporator to obtain compound (**5**).

General procedure for the synthesis of N-[1-(3-Fluoro-4-morpholinophenyl)-1H-tetrazol-5-yl]-amide derivatives (7a-l):

1-(3-Fluoro-4-morpholinophenyl)-1H-tetrazol-5-amine (**5**) (246 mg, 0.93 mmol) was dissolved in CH$_2$Cl$_2$ (5 mL), cooled to 0 °C and added DIPEA (13 mg, 1 mmol) followed by 1 mmol of acid chlorides (**6a-l**). The reaction mixture was stirred at room temperature for 10 h and extracted with ethyl acetate

(3×10 mL). The combined organic layer was washed with brine solution (10 mL), dried over Na_2SO_4 and concentrated in vacuo to obtain the corresponding tetrazole derivatives **7a-l.**

N-[1-(3-Fluoro-4-morpholinophenyl)-1H-tetrazol-5-yl]benzamide (7a): The compound **7a** was prepared according to general procedure by utilizing benzoyl chloride. Pale pink solid; Yield: 85 %; M.P: 250-252 °C; ^{1}H NMR (400 MHz, DMSO) δ: 11.05 (brs, 1H, NH), 8.09 (d, $J = 7.2$ Hz, 2H, ArH), 7.66 (d, $J = 7.6$ Hz, 1H, ArH), 7.55 (t, $J = 7.6$ Hz, 2H, ArH), 7.39-7.34 (m, 2H, ArH), 6.99 (t, $J = 8.8$ Hz, 1H, ArH), 3.89 (t, $J = 4.8$ Hz, 4H, CH_2), 3.16 (t, $J = 4.8$ Hz, 4H, CH_2); ^{13}C NMR (100 MHz, $CDCl_3$) δ: 166.0, 157.4, 155.4, 145.4, 144.0, 142.9, 132.3; 127.2, 132.3, 127.2, 124.8, 124.1, 123.9, 121.3, 120.4, 54.9, 50.8; IR (KBr, cm^{-1}): 3270, 3081, 2982, 2921, 2839, 1691, 1583, 1546, 1448, 1344, 1265, 1103, 936; m/z (ESI–MS): calculated for $C_{18}H_{18}N_6O_2F$ (M+H)$^+$: 369.36

N-(1-(3-fluoro-4-morpholinophenyl)-1H-tetrazol-5-yl)-3,3-dimethylbutanamide (7e): The compound **7e** was prepared according to general procedure by utilizing 3,3-dimethyl butyryl chloride **6e**. Pale yellow solid; Yield: 79 %; M.P: 138–140 °C; ^{1}H NMR (400 MHz, $CDCl_3$) δ: 11.24 (br s, 1H), 7.61-7.39 (m, 2H, ArH), 7.35 (t, $J = 8.8$, 1H, ArH), 4.24 (d, $J = 4.8$ Hz, 4H, CH_2), 3.52 (t, $J = 4.8$ Hz, 4H, CH_2), 2.87 (s, 2H, CH_2), 1.58 (s, 9H, CH_3); ^{13}C NMR (100 MHz, $CDCl_3$) δ:162.2, 154.8, 135.0, 134.9, 134.0, 133.2, 128.0, 127.5, 125.2, 52.2, 47.4, 46.5, 25.5, 21.5, 18.1; IR (KBr, cm^{-1}): 3433, 3076, 2925, 2852, 1741, 1658, 1607, 1526, 1474, 1351, 1207, 917; m/z (ESI–MS) 363.23 [M + H]$^+$.

N-(1-(3-fluoro-4-morpholinophenyl)-1H-tetrazol-5-yl)-2-nitrobenzamide (7k): The compound **7k** was prepared according to general procedure by utilizing 2-nitrobenzoyl chloride **6k.**Yield: 72 %; M.P: 243–245 °C; ^{1}H NMR (400 MHz, DMSO) δ: 11.09 (brs, 1H), 8.12 (d, $J = 7.7$ Hz, 2H, ArH), 7.66 (t, $J = 7.8$Hz, 1H, ArH), 7.61 (d, $J = 7.8$ Hz, 1H, ArH), 7.39-7.32 (m, 2H, ArH), 6.97 (t, $J = 8.9$ Hz, 1H, ArH), 3.86 (t, $J = 4.9$ Hz, 4H, CH_2), 3.16 (t, $J = 4.9$ Hz, 4H, CH2); ^{13}C NMR (100 MHz, $CDCl_3$) δ: 168.9, 151.8, 142.2, 139.1, 135.8, 130.0, 129.9, 129.6, 129.0, 131.7, 128.7, 124.2, 123.7, 121.2, 120.7, 59.0, 45.8; IR (KBr, cm^{-1}): 3438, 3070, 2923, 2840, 1691, 1543, 1478, 1265, 1132, 945; m/z (ESI–MS) 414.24 [M + H]$^+$.

Procedure for Antioxidant Activity:

Ai Lan Chew *et al.* method [35] was adopted to find out the free radical scavenging activity of the numerous extracts for 2,2-Diphenyl-1-picryl hydrazyl (DPPH). Crude extracts of different concentrations: 25 μg/mL, 50 μg/mL, 100 μg/mL and 200 μg/mL were placed in DMSO. 1 mL of each concentration was mixed with 4 mL of 0.004 % (w/v) DPPH solution prepared in CH_3OH. The reaction mixture was left in the dark for 30 min incubation. CH_3OH was used as control and ascorbic acid was employed as positive control. The absorbance was calculated at 517 nm. The following formula was used to find out the DPPH scavenging activity (%):

$$\text{DPPH scavenging activity (\%)} = [(A_o - A_s) / A_o] \times 100,$$

where, A_o = absorbance of the control, A_s = absorbance of the prepared sample.

Methodology and Programs of Quantum Chemical Calculations:

In this work, we utilized advanced quantum chemical calculations performed using state-of-the-art Gaussian 09 computational software [36, 37]. This software is known for its exceptional accuracy in modeling molecular structures and properties. Our calculations were executed using the [B3LYP/6-31G(d, p)] level of theory, a variant of Density Functional Theory (DFT). This method is highly regarded for its ability to provide accurate insights into molecular behaviour [37, 38]. The chosen level of theory ensures that our simulations capture intricate electronic interactions and structural features, which are critical for understanding the chemistry and properties of the molecules under study. Our study benefits from the robust and well-established combination of Gaussian 09 and the selected DFT method.

The following formulas were used to calculate the Energy Gap, Hardness, Softness, and Chemical Potential:

1. Energy Gap (Eg):

The energy gap, or HOMO-LUMO gap, was calculated as:

$$E_g = \varepsilon_{LUMO} - \varepsilon_{HOMO},$$

where ε_{LUMO} is the energy of the Lowest Unoccupied Molecular Orbital (LUMO); ε_{HOMO} is the energy of the Highest Occupied Molecular Orbital (HOMO).

2. Hardness (η):

The chemical hardness was determined as:

$$\eta = (\varepsilon_{LUMO} - \varepsilon_{HOMO})/2.$$

It measures a molecule's ability to resist changes in electron density.

3. Softness (*S*):
Softness was assessed as the inverse of hardness:
$$S = 1/\eta.$$
It characterizes the ability of a molecule to polarize and interact with other molecules.
4. Chemical Potential (μ):
The chemical potential is related to the electronegativity and was defined as:
$$\mu = (\varepsilon LUMO + \varepsilon HOMO)/2.$$
It provides insights into the reactivity and electron transfer processes within the system.

By following this methodology and using the specified quantum chemistry software, we were able to accurately calculate the energy gap, hardness, softness, and chemical potential, which are fundamental to our study. The chosen calculation method is well-supported by the scientific literature, ensuring the reliability and relevance of our results.

Results and Discussion

Chemistry:
The metal catalyzed arylation of primary amine derivatives of five- and six- membered heterocyclic compounds is of special interest, which have been challenging substrates so far represented [39, 40]. B.D. Glisic et al., [41] showed 5-aminotetrazoles electrostatic potential map, and explained that most of the electron density is located on the tetrazole ring compared to the amino group. This indicates that amino group is electron poor and therefore less nucleophilic. In this paper, we reported the synthesis of novel 1-(3-Fluoro-4-morpholinophenyl)-1H-tetrazol-5-amine derivatives and evaluated their antioxidant properties. The complete synthetic route to produce the target tetrazole motifs **7a-l** is presented in Scheme.
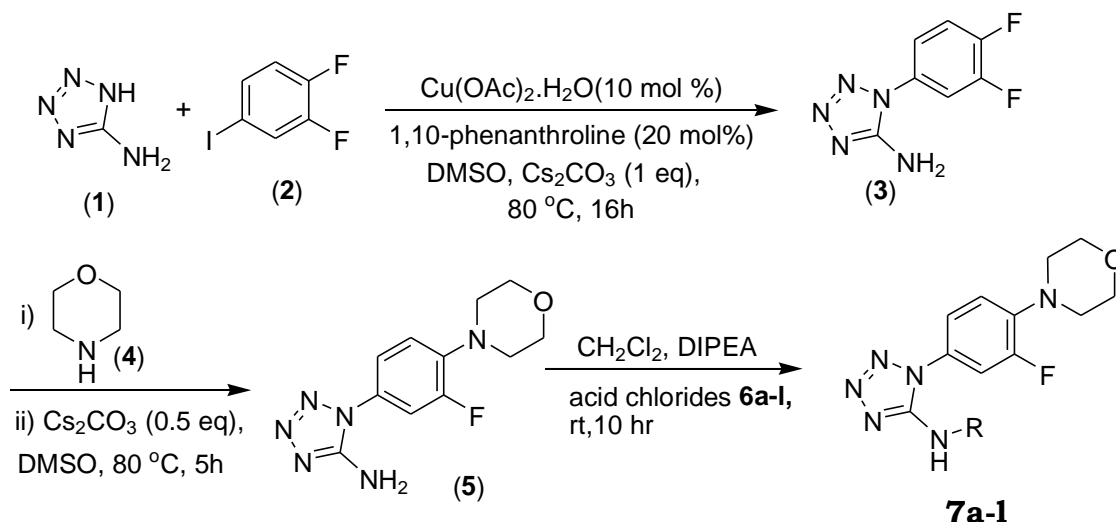
Scheme. Synthesis of novel tetrazole derivatives

Initially, 5-amino tetrazole underwent regioselective *N*-arylation [42] upon reaction with 1,2-difluoro-4-iodobenzene in presence of Cu(OAc)$_2$·H$_2$O as Cu catalyst, Cs$_2$CO$_3$ as base and 1,10-phenanthroline as ligand at 85 °C for 18 h, to obtain the intermediate 1-(3,4-difluorophenyl)-1H-tetrazol-5-amine (**3**). Next the intermediate (**3**) on reaction with morpholine (**4**) in DMSO at 80 °C for 5 h produced the precursor 1-(3-fluoro-4-morpholinophenyl)-1H-tetrazol-5-amine (**5**). Finally, the intermediate (**5**) by the reaction with different acid chlorides **6a-l** in CH$_2$Cl$_2$ and DIPEA at room temperature for about 10 h yielded the target tetrazole motifs **7a-l** in 72-91 % of yields. The total synthetic results are presented in Table 1.

Synthetic results of the targeted tetrazoles 7a-j

Entry	RCOCl, R=	Reaction Time	Product	Yield, %	M.P., °C
1	C_6H_5	7h	**7a**	85	250-252
2	$(CH_3)CH-CH_2$	8h	**7b**	82	180-182
3	$(CH_3)_2CH$	7h	**7c**	84	188-190
4	Cyclopropyl	8h	**7d**	88	210-212
5	$(CH_3)_3C$	9h	**7e**	79	138-140
6	CH_3	6h	**7f**	87	270-272
7	C_2H_5	6h	**7g**	81	258-260
8	$2-F,6-OCH_3C_6H_3$	9h	**7h**	76	260-262
9	$2-OMeC_6H_4$	9h	**7i**	87	234-236
10	$2,6-diFC_6H_4$	9h	**7j**	74	210-212
11	$2-NO_2C_6H_4$	10h	**7k**	72	243-245
12	$2,6-diOMeC_6H_4$	8h	**7l**	91	235-237

The key step of the total protocol is the Cu promoted regioselective *N*-arylation using 1,10-phenanthroline as a ligand (Step 1). In our previous work [42] we used 1,10-phenanthroline as more efficient ligand for Cu catalyzed regio-selective *N*-arylation (C-N coupling). Moreover, efficient *C-N* cross coupling strategies [43-44] were reported using 1,10-phenanthroline as ligand. As it is a hydrophobic and electron-poor heteroaromatic system [45] with a central benzene ring imposing a rigid structure to hold the two nitrogen atoms in juxtaposition [46] and is capable to chelate rings with either a metal or hydrogen to form stable structures [47] it can be used a significant class of chelating ligand to catalyze various reactions. Particularly, 1,10-phenanthroline can be coordinated with Cu to form more active [CuL]. The formed [CuL] mainly catalyzed the key step for the construction of the C–X (X = C, N, O, etc.) bond to promote the whole reaction [48]. However, the tandem reaction is complex and it is difficult to recognize the precise mechanistic role of [CuL], for which the [CuL]-catalyzed transformation may occur at the initial, intermediate or final step. Next, intermediate (**3**) reacts with morpholine (**4**) using Cs_2CO_3 as a base (HF acceptor) to form the key precursor 1-(3-fluoro-4-morpholinophenyl)-1H-tetrazol-5-amine (**5**). It is noteworthy that the tetrazole ring exhibits strong electron-withdrawing inductive effect (–I effect), which is more effective than its weak mesomeric effect (+M effect), behaves as a deactivating group [49-50] and the flow of the electrons is towards the ring. This may be the reason for the selective substitution of florine at the *para* position to form the precursor (**5**). Finally, the intermediate (**5**) reacts with various acid chlorides **6a-j** to form the targeted tetrazole amides **7a-l** in good yields.

The ^{1}H NMR spectrum of the compound (**5**) protons resonating at δ 7.74 ppm (multiplet, 2H) and δ 7.52 ppm (triplet, 1H) corresponds to the 1,2,4-trrisubstituted phenyl ring. The proton signals at δ 5.10 ppm (brs, 2H), δ 4.21 ppm (triplet, 4H) and δ 3.47 ppm (triplet, 4H) represents to the following groups: $-NH_2$, $-O(CH_2)_2$ and $-N(CH_2)_2$ respectively. The IR spectra of the compound (**6**) showed characteristic absorption peaks at 3340, 3154, 2925, 1665 and peaks at 13840-1233 cm^{-1} signifying the presence of distinctive functional groups such as $-NH_2$, =C–H (Ar), –C=N, –C–N, and –C=C(Ar) respectively. On the basis of the above spectral data, the compound (**5**) has been characterized as 1-(3-fluoro-4-morpholinophenyl)-1H-tetrazol-5-amine.

Further, upon characterization of target compound **7e,** the ^{1}H NMR spectrum (Fig. 2) showed proton signals at δ 7.16–7.10 ppm (multiplet, 2H), δ 7.0 ppm (doublet, 1H), phenyl and 1, 2,4-trisubstitute phenyl ring. The proton signals δ 3.85 ppm (triplet, 4H) δ 3.16 ppm (triplet, 4H) represents the $-O(CH_2)_2$ and $-N(CH_2)_2)$ groups respectively, and the signal at δ 2.28 ppm (s, 3H) indicates $-COCH_3$ protons. The IR spectra of the compound **7e** showed characteristic absorption peaks at 3454 cm^{-1} represents N–H stretching, at 1691 cm^{-1} indicates amide –C=O stretching and peaks at 1379-1254 cm^{-1} signifying the presence of distinctive functional groups such as $-NH_2$, –C=N, –C–N aromatic respectively. (M+H)$^+$ peak at 307.14 Da in the ESI mass spectra of the compound **7e** corresponding to molecular formula of $C_{13}H_{15}N_6O_2F$. Finally, the compound **7e** has been characterized as N-(1-(3-fluoro-4-morpholinophenyl)-1H-tetrazol-5-yl)acetamide on the basis of the above spectral data. Similarly the remaining compounds in the series are sufficiently characterized, and are in good relevance with the anticipated structures.

HOMO and LUMO Analysis:

The HOMO-LUMO energies and their Energy gap, Hardness, Softness, Chemical potential of the obtained chemical compounds **7a-l** were calculated by B3LYP/6-31g(d, p) method using Gaussian 09 package [36–38, 51] (Table 2, Fig. 2). Theoretical study showed that compounds 7d, 7e and 7j are more reactive than other obtained tetrazole derivatives. In this study compounds **7d, 7e, 7j** exhibited the HOMO-LUMO gap 4.7856eV, 4.7905eV, 4.89009eV, showed the lowest energy gap values and the lowest chemical potential values (–3.07254eV, –3.06173eV, –3.0166eV) with the highest chemical softness (0.41792eV, 0.41749eV,0.40899eV) values, and the lowest chemical hardness (2.3928eV, 2.3952eV, 2.44504eV), which may contribute to higher chemical reactivity than others (Table 2).
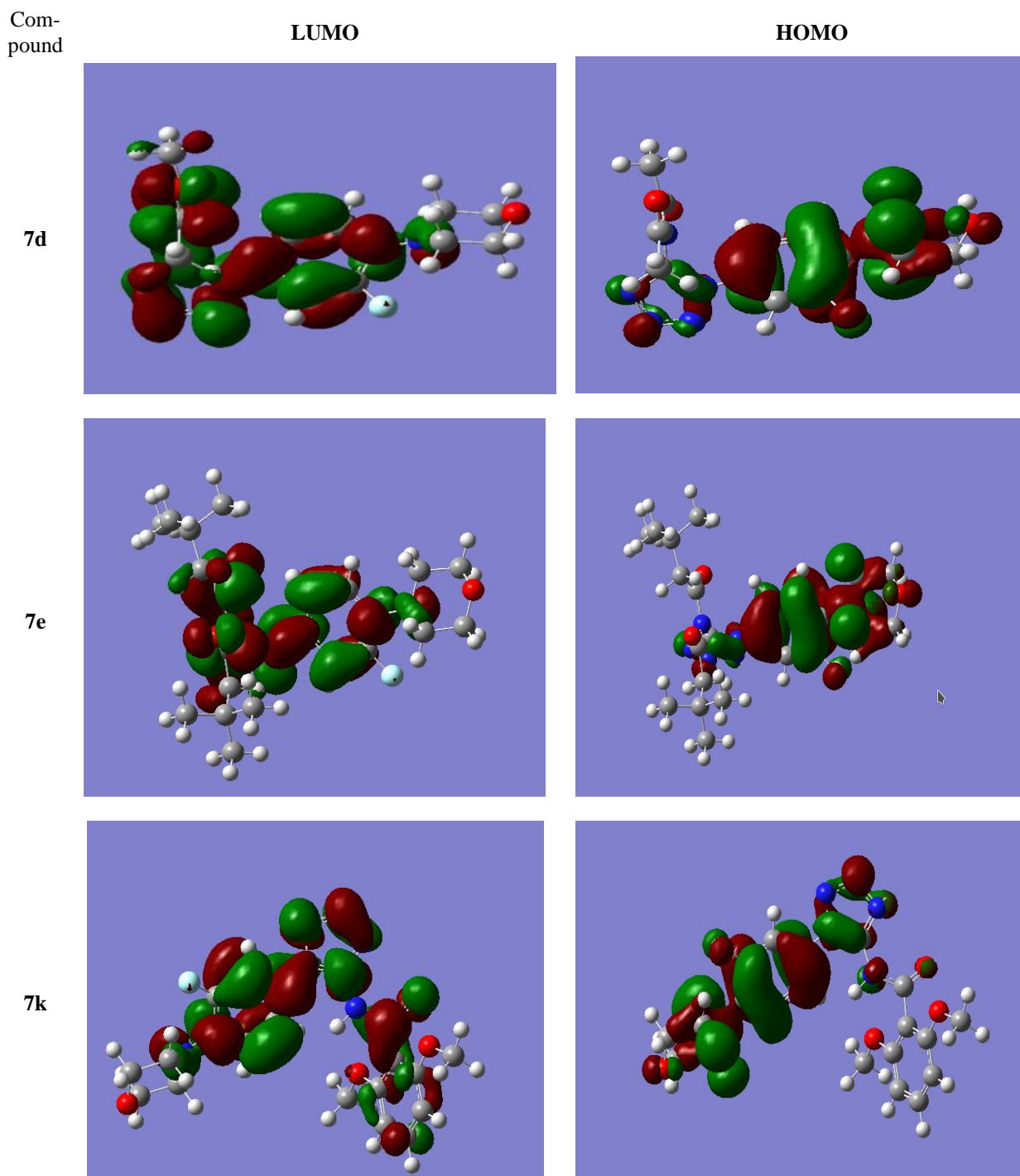
Compound	LUMO	HOMO
7d		
7e		
7k		

Figure 2. Frontier molecular orbital (LUMO-HOMO) of the compounds **7d, 7e** and **7k**

HOMO, LUMO, gap, hardness, and softness of tetrazole hybrids 7d, 7e and 7k

No	Compounds	HOMO	LUMO	Gap	Hardness	Softness	Chemical potential
1	**7d**	–6.0969	–1.3113	4.7856	2.3928	0.41792	–3.07254
2	**7e**	–6.07622	–1.28572	4.7905	2.39525	0.41749	–3.06173
3	**7k**	–5.99268	–1.10259	4.89009	2.44504	0.40899	–3.0166

In general, theoretical study and HOMO-LUMO analysis of the titled compounds showed that compounds **7d**, **7e**, **7k** have the lowest energy gap and the lowest chemical potential values with the highest chemical softness and the lowest chemical hardness values, which may contribute to more high chemical activity than others.

Antioxidant Activity:

The antioxidant activity of the obtained compounds **7a-l** was assessed *in vitro* using a standard literature protocol [35]. For this intention, different extracts were examined for 2,2-diphenyl-1-picrylhydrazyl (DPPH) free radical scavenging activity according to the literature protocol. The crude extracts with different concentrations 25 μg/mL, 50 μg/mL, 100 μg/mL, and 200 μg/mL were tested, using ascorbic acid as a standard positive control. The results of the study are presented in Table 3.

Antioxidant activity of titled compounds 7a-l

Sample	Antioxidant activity (%)			
	25 μg	50 μg	100 μg	200 μg
7a	23.46	25.62	29.82	34.72
7b	18.88	24.67	29.77	36.76
7c	28.87	32.84	38.54	46.45
7d	52.12	56.73	61.13	66.13
7e	54.56	58.45	66.45	72.45
7f	33.49	38.29	42.69	56.29
7g	34.72	40.42	45.98	50.22
7h	29.34	36.34	42.34	48.34
7i	34.65	37.65	39.65	42.65
7j	41.23	45.45	48.78	51.46
7k	56.56	61.45	69.45	71.89
7l	53.23	58.45	63.78	68.46
Ascorbic acid	78.74	86.06	92.81	93.25

The antioxidant activity screening results (Table 3) showed that all the obtained morpholine based tetrazole hybrids exhibited good antioxidant activity. Compounds **7a-l** exhibited a concentration-dependent increase in antioxidant activity, i.e. antioxidant activity was increased with increasing concentration. Compounds **7k** and **7b** displayed maximum and minimum antioxidant activities at the concentrations of 100 μg, 50 μg and 25μg respectively. At 200 μg concentration, the tetrazole hybrids **7e** and **7a** displayed highest and lowest antioxidant activity, respectively. Similarly, compound **7k** showed almost comparable antioxidant activity to compound 7e at the concentration of 200 μg. All the remaining compounds except **7a** and **7b**, exhibited more than 45 % level of antioxidant property at 200 μg concentration. However, all obtained compounds exhibited significantly lower antioxidant activity compared to standard ascorbic acid at all concentrations tested.

Based on the results of antioxidant activity studies, it was assumed that: (i) the electron withdrawing nitro group is responsible for the moderate antioxidant activity of compound **7k**; (ii) Presence of tertiary butyl group in **7e** is accountable for antioxidant drug efficiency; (iii) similarly, the existence of electron releasing methoxy groups at 2nd and 5th positions of phenyl ring is accountable for the good antioxidant activity of compound **7l**.

Conclusions

In summary, the present work describes the synthesis of a sequence of new tetrazole derivatives (**7a-l**) via copper-promoted regioselective *N*-arylation as key step. The obtained compounds were further evaluated for *in vitro* antioxidant activity and the results revealed that compounds **7e**, and **7k** had potent antioxidant activity. Furthermore, the HOMO-LUMO analysis of the title compounds showed that compounds **7d**, **7e**, **7k** have the lowest energy gap and the lowest chemical potential values, with the highest chemical softness, the lowest chemical hardness, which possibly contributes to the higher chemical reactivity than other compounds. All obtained tetrazole analogs were characterized by ^{1}H NMR, mass and IR spectral data. In conclusion, the obtained morpholine tetrazole hybrids represent a promising, gracious surrogate and can be considered as a prime target for medicinal chemists working in the field of antioxidants.

Acknowledgments

References

1   Vitaku, E., Smith D.T., & Njardarson J.T. (2014). Analysis of the structural diversity, substitution patterns, and frequency of nitrogen heterocycles among U.S. FDA approved pharmaceuticals. *Journal of Medicinal Chemistry, 57*, 10257–10274. https://doi.org/10.1021/jm501100b.

2   Herr, R.J. (2002). 5-Substituted-1H-tetrazoles as carboxylic acid isosteres: medicinal chemistry and synthetic methods. *Bioorganic & Medicinal Chemistry, 10*, 3379-3393. https://doi.org/10.1016/S0968-0896(02)00239-0.

3   Tuites, R.C., Whiteley, T.F., & Minsk, L.M. (1971). *US Patent*, 1: 245, 614.

4   Koldobskii, G.I., & Ostrovskii, V.A., (1994). Tetrazoles, *Uspekhi Khimii, 63*, 847. https://doi.org/10.1070/RC1994v063n10ABEH000119

5   Wittenberger, S. (1994). Recent developments in tetrazole chemistry. A review. *Organic Preparations and Procedures International, 26*, 499-532. https://doi.org/10.1080/00304949409458050.

6   Ek, F., Wistrandand, L.G., & Frejd, T. (2003). Synthesis of fused tetrazole- and imidazole derivatives via iodocyclization. *Tetrahedron*, *59*, 6759-6769. https://doi.org/10.1016/S0040-4020(03)00818-4.

7   Rhonnstad, P., & Wensbo, D. (2002). On the relative strength of the 1H-tetrazol-5-yl- and the 2-(triphenylmethyl)-2H-tetrazol-5-yl-group in directed ortho-lithiation. *Tetrahedron Letters*, *43*, 3137-3139. https://doi.org/10.1016/S0040-4039(02)00490-2.

8   Himo, F., Demko, Z.P., Noodleman, L., & Sharpless, K.B. (2003). Why Is Tetrazole Formation by Addition of Azide to Organic Nitriles Catalyzed by Zinc(II) Salts? *Journal of American Chemical Society, 125*, 9983-9987. https://doi.org/10.1021/ja030204q.

9   Lodyga-Chruscinska, E., Sanna, D., Micera, G., Chruscinski, L., Olejnik J., Nachman, R. J., & Zabrocki R. (2006). Chelating ability of proctolin tetrazole analogue. *Journal of Acta Biochimica Polonica, 53*, 65-72.

10   Zabrocki, J., Smith, G.D., Dubar, J.B. Jr., Lijima, H., & Marshal, G.R. (1998). Conformational mimicry. 1. 1,5-Disubstituted tetrazole ring as a surrogate for the cis amide bond. *Journal of American Chemical Society*, 110, 5875-5880. https://doi.org/10.1021/ja00225a045.

11   Hodges, J.C., Hamby, J.M., & Blankley, C.J. (1992). Angiotensin II receptor binding inhibitors. *Drugs Future*, *17*, 575-593.

12   Peet, N.P., Baugh, L.E., Sunder, S. Lewis, J.E., Matthews, E.H., Olberding, E.L., & Shah, D.N. (1986). 3-(1H-Tetrazol-5-yl)-4(3H)-quinazolinone sodium salt (MDL 427): a new antiallergic agent. *Journal of Medicinal Chemistry*, *29*, 2403. https://doi.org/10.1021/jm00161a045.

13   Girijavallabhan, V.M., Pinto, P.A., Genguly, A.K., & Versace R.W. (1988). *European Patent,* EP 274867.

14   Akimoto, H., Ootsuand K., & Itoh F. (1993). *European Patent,* EP530537.

15   Edmont, D., Rocher R., Plisson, C., & Chenault J. (2000). Synthesis and evaluation of quinolone carboxyguanidines as antidiabetic agents. *Bioorganic & Medicinal Chemistry Letters*, *10*, 1831–1834. https://doi.org/10.1016/S0960-894X(00)00354-1.

16   Andrus, A., Partridge, B., Heck, J.V., & Christensen B.G. (1984). The synthesis of N-(tetrazol-5-yl)azetidin-2- ones. *Tetrahedron Letters*, *25*, 911–914. https://doi.org/10.1016/S0040-4039(01)80060-5.

17   Ehsani, A., Mahjani, M.G., Moshre, R., Mostaanzadeh, H., & Shabani Shayeh J. (2014). Electrochemical and DFT study on the inhibition of 316L stainless steel corrosion in acidic medium by 1-(4-nitrophenyl)-5-amino-1H-tetrazole. *RSC Advances 4*, 20031–20037. https://doi.org/10.1039/C4RA01029A.

18   Castro, J.L., Ball, R.G., Broughton, H.B., Russell, M.G.N., Rathbone, D., Watt, A.P., Baker, R., Chapman, K.L., Fletcher, A.E., Patel, S., Smith, A.J., Marshall, G.R., Ryecroft, W., & Matassa, V.G. (1996). Controlled modification of acidity in cholecysto-

kinin B receptor antagonists: N-(1,4-benzodiazepin-3-yl)-N'-[3-(tetrazol-5-ylamino)phenyl]ureas. *Journal of Medicinal Chemistry*, *39*, 842–849. https://doi.org/10.1021/jm9506736.

19 Serebryanskaya, T.V., Yung T.A., Bogdanov, A., Shchebet, A., Johnsen, S.A., Lyakhov, A., Ivashkevich, S.L., Ibrahimava, Z.A., Garbuzenco, T.S., Kolesnikova, T.S., Melnova, N.I., Gaponik P.N., & Ivashkevich, O.A. (2013). Synthesis, characterization, and biological evaluation of new tetrazole-based platinum(II) and palladium(II) chlorido complexes – Potent cisplatin analogues and their trans isomers. *Journal of Inorganic Biochemistry*, *120*, 44–53. https://doi.org/10.1016/j.jinorgbio.2012.12.001.

20 Ismael, A., Fausto, R., & Cristiano, M.L.S. (2016). Photochemistry of 1- and 2-Methyl-5-aminotetrazoles: Structural Effects on Reaction Pathways. *Journal of Organic Chemistry, 81*, 11656–11663. https://doi.org/10.1021/acs.joc.6b02023.

21 Ahmadi, A., Khalili, M., Hajikhani, R., *et al.* (2012). Anti-inflammatory effects of two new methyl and morpholine derivatives of diphenhydramine on rats. *Medicinal Chemistry Research*, *21*(11), 3532–3540. https://doi.org/10.1007/s00044-011-9891-y

22 Alberto, I., Juan, R., Marcela, R., Carlos, E., Jairo, Q., *et al*. (2013). Synthesis, Antifungal and Antitumor Activity of Novel (Z)-5-Hetarylmethylidene-1,3-thiazol-4-ones and (Z)-5 Ethylidene-1,3-thiazol-4-ones. *Molecules*, *18*(5), 5482–5497. https://doi.org/10.3390/molecules18055482

23 Salem, M.A., Abbas, S.Y., Helal, M.H., & Alzahrani, A.Y. (2021). Synthesis and antimicrobial evaluation of new 2-pyridinone and 2-iminochromene derivatives containing morpholine moiety. *Journal of Heterocyclic Chemistry, 58*(11), 2117-2123. https://doi.org/10.1002/jhet.4335.

24 Muller, K., Faeh, C., & Diederch, F. (2007). Fluorine in Pharmaceuticals: Looking Beyond Intuition. *Science*, *317*(5846), 1881–1886. https://www.science.org/doi/pdf/10.1126/science.1131943

25 Zhang, L.H., Zhang, Z.H., Li, M.Y., Wei, Z.Y., Jin, X.J., & Piao, H.R. (2019). Synthesis and evaluate on of the HIF-1α inhibitory activities of novel ursolic acid tetrazole derivatives. *Bioorganic & Medicinal Chemistry Letters*, *29*, 1440-1445. https://doi.org/10.1016/j.bmcl.2019.04.028

26 Roh, J., Karabanovich, G., Vlckova, H., Carazo, A., Němeček, J., Sychra, P., Valášková, L., Pavliš, O., Stolaříková, J., Klimešová, V., Vávrová, K., Pávek, P., & Hrabále, A. (2017). Development of water-soluble 3,5-dinitrophenyl tetrazole and oxadiazole antitubercular agents. *Bioorganic & Medicinal Chemistry, 25*, 5468-5476. https://doi.org/10.1016/j.bmc.2017.08.010

27 Aruoma, O.I. (1998). Free radicals, oxidative stress, and antioxidants in human health and disease. *Journal of the American Oil Chemists' Society*, *75*(2), 199–212. https://doi.org/10.1007/s11746-998-0032-9.

28 Ames, B.N., Shigenaga, M.K., & Hagen, T.M. (1993). Oxidants, antioxidants, and the degenerative diseases of aging. *Proceedings of the National Academy of Sciences of the United States of America*, *90*(17), 7915–7922. https://doi.org/10.1073/pnas.90.17.7915.

29 Tyagi, Y.K., Kumar, A., Raj, H.G., *et al.* (2005). Synthesis of novel amino and acetyl amino-4-methylcoumarins and evaluation of their antioxidant activity. *European Journal of Medicinal Chemistry*, *40*(4), 413–420. https://doi.org/10.1016/j.ejmech.2004.09.002.

30 Karegoudar, P., Karthikeyan, M.S., Prasad, D.J., Mahalinga, M., Holla, B.S., & Kumari, N.S. (2008). Synthesis of some novel 2,4-disubstituted thiazoles as possible antimicrobial agents. *European Journal of Medicinal Chemistry*, *43*(2), 261–267. https://doi.org/10.1016/j.ejmech.2007.03.014.

31 Boddapati, S.N.M., Talari, S., Kola, A.E., & Chalapaka, B. (2022). Synthesis of 2-aryl-5-(arylsulfonyl)-1,3,4-oxadiazoles as potent antibacterial andantioxidant agents. *Turkish Journal of Chemistry, 46*, 766-776. https://doi.org/10.55730/1300-0527.3366.

32 Saketi, J.M.R., Boddapati, S.N.M., Adil, S.F., Shaik, M.R., Alduhaish, O., Siddiqui, M.R.H., & Bollikolla, H.B. (2020). Pd(PPh₃)₄ Catalyzed Synthesis of Indazole Derivatives as Potent Anticancer Drug. *Applied Sciences*, *10*, 3792. https://doi.org/10.3390/app10113792

33 Boddapati, S.N.M., Kola, A.E., Talari, S., & Arnipalli M.S. (2022). Synthesis, Docking and Antibacterial Evaluation of N-(1-(3-Fluoro-4-morpholinophenyl)-1H-tetrazol-5-yl) Amides. *Chemistry Africa*, *5*, 781–790. https://doi.org/10.1007/s42250-022-00347-y.

34 European Pharmacopoeia Commission, & European Directorate for the Quality of Medicines & Healthcare. (2010). *European pharmacopoeia* (Vol. 1). Council of Europe. Retrieved from https://file.wuxuwang.com/yaopinbz/EP7/EP7.0_01__26.pdf

35 Chew, A.L., Jessica, J.J.A., & Sasidharan, S. (2012). Antioxidant and antibacterial activity of different parts of Leucas aspera. *Asian Pacific Journal of Tropical Biomedicine*, *2*(3), 176–180. https://doi.org/10.1016/S2221-1691(12)60037-9

36 Frisch, M.J., Trucks, G.W., Schlegel, H.B., Scuseria, G.E., Robb, M.A., Cheeseman J.R., et. al. Gaussian 09, Revision E.01, Gaussian, Inc., Wallingford CT, 2009. https://gaussian.com/g09citation/.

37 Gwupuye, J.A., Gber, T.E., Edet, H.O., Zeeshan, M., Batool, S., Duke, O.E.E., Adah, P.O., Odey, J.O., & Egbung, G.E. (2023). Molecular Modeling, DFT Studies and Biological Evaluation of Methyl 2,8-Dichloro-1,2-Dihydroquinoline-3-Carboxylate. *Chemical Physics Impact, 6* (100146), 100146. https://doi.org/10.1016/j.chphi.2022.100146.

38 Mumit, M.A., Pal T.K., Alam, M.A., Islam, M.A.A.A.A., Paul, S., & Sheikh. M.C. (2020). DFT studies on vibrational and electronic spectra, HOMO-LUMO, MEP, HOMA, NBO and molecular docking analysis of benzyl-3-N-(2,4,5-trimethoxyphenylmethylene)hydrazinecarbodithioate. *Journal of Molecular Structure*, *1220*(128715), 128715. https://doi.org/10.1016/j.molstruc.2020.128715.

39 Yin, J., Zhao, M.M., Huffman, M.A., & McNamara. J.M. (2002). Pd-Catalyzed N-arylation of heteroarylamines. *Organic Letters*, *4*, 3481–3484. https://doi.org/10.1021/ol0265923.

40 McGowan, M.A., Henderson, J.L., & Buchwald, S.L. (2012). Palladium-catalyzed N-arylation of 2-aminothiazoles. *Organic Letters, 14*, 1432–1435. https://doi.org/10.1021/ol300178j.

41 Andrejević́n T.P., Nikolić́T A.M., Glišić́A B.D., Wadepohl, H., Vojnovic, S., Zlatović́B M., Petković́M M., Nikodinovic-Runic, J., Opsenica, I.M., & Djuran, M.I. (2018). Synthesis, structural characterization and antimicrobial activity of silver(I) complexes with 1-benzyl-1H-tetrazoles. *Polyhedron*, *154*, 325–333. https://doi.org/10.1016/j.poly.2018.08.001.

42 Boddapati, SN.M., Kola, A.E., Kesana, S.B., & Bollikolla, H.B. (2018). Temperature dependent regioselective synthesis of aryl tetrazole amines using copper source. *Journal of Organometallic Chemistry, 866*, 177–183. https://doi.org/10.1016/j.jorganchem.2018.04.027.

43 Boddapati, SN.M., Polam, N., Mutchu B.R., & Bollikolla, H.B. (2018). The synthesis of arylcyanamides: a copper-catalyzed consecutive desulfurization and C–N cross-coupling strategy. *New Journal of chemistry*, *42*, 918-922. https://doi.org/10.1039/C7NJ03527F.

44 Boddapati, SN.M., Kurmarayuni, C.M., Mutchu B.R., Tamminana, R., & Bollikolla, H.B. (2018). Copper-catalyzed synthesis of 2-aminophenyl benzothiazoles: A novel approach. *Organic & Bio molecular Chemistry*, *16*, 8267-8272. https://doi.org/10.1039/C8OB02018C.

45 Bencini, A., & Lippolis, V. (2010). 1,10-Phenanthroline: A versatile building block for the construction of ligands for various purposes. *Coordination Chemistry Reviews, 254*, 2096-2180. https://doi.org/10.1016/j.ccr.2010.04.008.

46 Sammes, P.G., & Yahioglu, G. (1994). 1,10-Phenanthroline: a versatile ligand. *Chemical Society Reviews, 23*, 327-334. https://doi.org/10.1039/CS9942300327.

47 Alreja, P., & Kaur, N. (2016). Recent advances in 1,10-phenanthroline ligands for chemosensing of cations and anions. *RSC Advances, 6*, 23169-23217. https://doi.org/10.1039/C6RA00150E.

48 Wu, F., Xie, J., & Zhu, Z. (2020). 1,10-Phenanthroline: A versatile ligand to promote copper-catalyzed cascade reactions. *Applied Organometallic Chemistry, 34*(11), e5926. https://doi.org/10.1002/aoc.5926.

49 Kaczmarek, J., Smagowski, H., & Grzonka, Z. (1979). A correlation of substituent effects with the acidity of aromatic tetrazolic acids. *Journal of the Chemical Society*, *Perkin Transactions* 2, *2*, 1670-1674. https://doi.org/10.1039/P29790001670.

50 Ciarkowski, J., Kaczmarek, J., & Grzonka, Z. (1979). A correlation of substituent effects with proton chemical shifts in aromatic tetrazolic acids. *Organic Magnetic Resonance*, *12*(11), 631-636. https://doi.org/10.1002/mrc.1270121107.

51 Becke, A.D. (1998). Density-functional thermochemistry. III. The role of exact exchange. *Journal of Chemical Physics, 98*(7), 5648–5652. https://doi.org/10.1063/1.464913.

Information about authors*

Boddapati, S.N. Murthy (*corresponding author*) — Associate Professor, Department of Chemistry, Sir C R Reddy College, P G Courses, Eluru, 534007, Andhra Pradesh, India; e-mail: snmurthy-boddapati@gmail.com; https://orcid.org/0000-0002-0703-9827

Johar, K. — Lecturer, Department of Chemistry, Sir C R Reddy College, Eluru, 534007, Andhra Pradesh, India; e-mail: johark3399@gmail.com

Manoj Kumar, B.V. — Lecturer, Department of Chemistry, Sir C R Reddy College, Eluru, 534007, Andhra Pradesh, India; e-mail: bvmkumar061@gmail.com

Satish, V.A.N. — Lecturer, Department of Chemistry, Sir C R Reddy College, Eluru, 534007, Andhra Pradesh, India; e-mail: vansatish82@gmail.com

Emmanuel, K.A. (*corresponding author*) — Professor, Department of Chemistry, Y.V.N.R Government Degree College, Kaikaluru, 521333, Andhra Pradesh, India.; e-mail: dr.kaekola@gmail.com; https://orcid.org/0000-0001-6498-7957

_____

*The author's name is presented in the order: *Last Name, First and Middle Names*

Article

UDC 547; 544.16

https://doi.org/10.31489/2959-0663/4-23-7

Shivani U. Chavan[1*] , Sonali A. Waghmare[1], Shraddha S. Bodke[2] , Atul R. Bendale[2]

[1]Department of Pharmaceutical Chemistry, S.N.D. College of Pharmacy, Babhulgaon, Nashik, India;
[2]Department of Pharmaceutical Chemistry, Mahavir Institute of Pharmacy, Varvandi, Nashik, India
(*Corresponding author's e-mail: Shivanichavan26@gmail.com)

Exploring 1,3,4-Oxadiazole Derivatives as Potent α-Amylase Inhibitors: Design, Synthesis, and Biological Evaluation

Diabetes mellitus is a growing global health concern, and α-amylase inhibitors have been recognized as promising therapeutic agents for its treatment. This study aimed to design, synthesize and evaluate 1,3,4-oxadiazole derivatives as potential α-amylase inhibitors. A series of 1,3,4-oxadiazole derivatives were designed and subjected to in silico ADMET, Lipinski's Rule of Five, and drug-likeness analysis. The most promising compounds, SC2 and SC8, were synthesized and their α-amylase inhibitory activity was assessed in vitro. The interactions with the human α-amylase (PDB ID: 6Z8L) which is a target protein, was analyzed through molecular docking studies. The designed compounds complied with Lipinski's Rule of Five and exhibited favourable drug-likeness properties. In silico ADMET analysis predicted good absorption and distribution profiles. SC2 and SC8 demonstrated potent α-amylase inhibitory activity with IC_{50} values of 36.5 ± 1.5 µg/mL and 45.2 ± 2.1 µg/mL, respectively, compared to acarbose (68.9 ± 3.2 µg/mL). Molecular docking revealed that both compounds formed crucial interactions with key amino acid residues in the enzyme's active site. The binding affinities of SC2 and SC8 were -10.1 kcal/mol and -9.1 kcal/mol, respectively. The 1,3,4-oxadiazole derivatives, particularly SC2 and SC8, demonstrated potential as α-amylase inhibitors with favorable ADMET properties. These findings provide a basis for further optimization and development of these compounds as novel antidiabetic agents.

Keywords: 1,3,4-oxadiazole derivatives, α-amylase inhibitors, diabetes mellitus, ADMET, molecular docking, Lipinski's Rule of Five, drug-likeness.

Abbreviation

ADMET:	Absorption, Distribution, Metabolism, Excretion and Toxicity;	SD:	Standard Deviation;
		SAR:	Structure-Activity Relationship
Mol Log P:	Partition coefficient between octanol and water;	CMC:	Critical Micelle Concentration;
		H-bond:	Hydrogen bond;
TPSA:	Topological Polar Surface Area;	Å²:	square angstrom;
Caco2:	Human colorectal adenocarcinoma cells;	GI:	Gastrointestinal;
		logBB:	Blood-Brain Barrier partition coefficient;
BBB:	Blood-Brain Barrier;	CYP:	Cytochrome P450;
PPB:	Plasma Protein Binding;	OD:	Optical Density;
PDB:	Protein Data Bank;	IC_{50}:	Half maximal inhibitory concentration;

Introduction

Diabetes mellitus is a chronic metabolic disorder characterized by elevated blood glucose levels resulting from defects in insulin secretion, insulin action, or both. The World Health Organization (WHO) estimates that worldwide diabetes affects about 422 million people, making it a major global health concern [1]. The prevalence of this disease has augmented dramatically over the past few decades, primarily due to changes in lifestyle, urbanization and an aging population. Diabetes can lead to severe complications such as cardiovascular diseases, stroke, kidney failure, blindness and lower limb amputation, significantly impacting an individual's quality of life and placing a heavy burden on healthcare systems [2].

There are two primary types of diabetes, namely type 1 and type 2. Type 1 diabetes is an autoimmune disease in which the body's immune system destroys the insulin-producing β-cells of the pancreas, resulting in an absolute insulin deficiency. Type 2 diabetes, which accounts for about 90 % of all diabetes cases, is

characterized by insulin resistance and progressive β-cell dysfunction. Although the etiology of type 2 diabetes is multifactorial, it is often associated with obesity, sedentary lifestyles, and unhealthy dietary habits [3].

α-Amylase is a crucial enzyme responsible for hydrolyzing α-1,4-glucosidic linkages in starch, glycogen and other polysaccharides, converting them into smaller, easily digestible glucose units. The modulation of α-amylase activity has been widely recognized as a potential therapeutic strategy in the management of various metabolic disorders, including type 2 diabetes mellitus and obesity. Consequently, the discovery and development of novel α-amylase inhibitors have emerged as a significant area of research in medicinal chemistry [4].

1,3,4-Oxadiazole derivatives have attracted considerable attention in recent years due to their versatile biological properties and potential applications as pharmacophores. Figure 1 shows commercially available drugs that incorporate the 1,3,4-oxadiazole nucleus within their molecular structure. This nucleus is a pivotal component in various therapeutic agents, emphasizing its significance in the realm of medicinal chemistry [5]. The presence of the 1,3,4-oxadiazole ring in these drugs highlights its potential for diverse biological activities and its role in enhancing the pharmacological profile of these compounds [6].

In this study, we present the rational design, synthesis and biological evaluation of a series of novel 1,3,4-oxadiazole derivatives as potent α-amylase inhibitors. The research aims to explore the structure-activity relationships (SAR) of these compounds, shedding light on their inhibitory mechanisms and establishing a foundation for further optimization and development. Additionally, the study assesses the selectivity and safety profiles of the synthesized derivatives through in vitro assays, providing valuable insights into their potential as therapeutic agents [7].
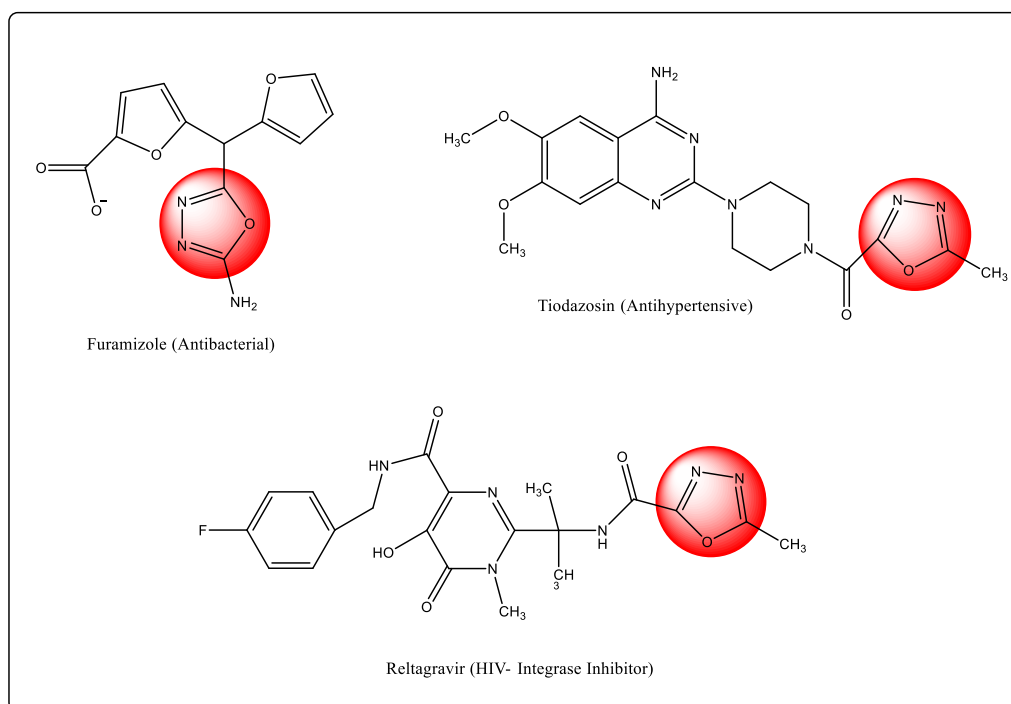

Figure 1. Commercially available drugs with the 1,3,4-oxadiazole nucleus

By uncovering the α-amylase inhibitory properties of 1,3,4-oxadiazole derivatives, this research not only contributes to the growing body of knowledge surrounding these versatile compounds but also paves the way for the development of novel, more effective therapeutic strategies to combat metabolic disorders. Ultimately, the findings of this study have the potential to significantly impact the management and treatment of conditions such as type 2 diabetes mellitus and obesity, enhancing the overall quality of life for patients affected by these prevalent health challenges [8].

Experimental

All chemicals and solvents used in the study were procured from Research Lab Fine Chem Industries (India) and Prerana Enterprises (Ahmednagar). Characterization of all synthesized compounds was per-

formed using various spectroscopic techniques. FTIR spectra were recorded on an alpha Bruker eco ATR instrument, and ^{1}H NMR spectra were obtained using a Bruker AM-300 spectrophotometer with tetramethylsilane (TMS) as the internal standard. Deuterated solvents such as chloroform and DMSO were used for recording the spectra, and chemical shifts were presented as delta values comparative to TMS. Melting points were determined using a digital Gallen Kemp melting point apparatus. The synthesized final compounds were recrystallized using suitable solvents to achieve high purity. The progress of the reactions was monitored using thin-layer chromatography (TLC) as a valuable analytical technique. A solvent system consisting of methanol and chloroform in a 1:9 ratio was used for TLC, and silica gel-60 HF254 plates served as the stationary phase for the separation of compounds.

Methods

Molecular Docking:

The molecular docking studies were performed to evaluate the binding affinity and interactions of the synthesized 1,3,4-oxadiazole derivatives with human α-amylase (PDB ID: 6Z8L) using AutoDockVina. The crystal structure of human α-amylase was obtained from the Protein Data Bank (www.rcsb.org) and prepared for docking. The protein was prepared by removing any water molecules, adding missing hydrogen atoms, and optimizing the structure using energy minimization. The ligands, i.e., the synthesized 1,3,4-oxadiazole derivatives, were prepared using Chem3D (v.16.0) and ChemDraw (v.16.0) software. The geometry of the ligands was optimized using the MM2 force field method in Chem Office. After optimization, Gasteiger charges were assigned. The docking procedure was performed using AutoDockVina tool (v.1.2.0). The active site of the protein was predicted using a grid box encompassing the catalytic site residues with dimensions of 20×20×20 Å and a grid co-ordinate selected as $x = -11.343897$, $y = 6.133868$, $z = -23.338819$. The best-docked poses were selected based on the docking scores. The protein-ligand complexes were visualized and analyzed using Discovery Studio Visualizer (v.4.5). Furthermore, 2D interactions were generated using LigPlot+ (v.2.2) software to depict the key interactions between the ligands and the protein residues [9].

In Silico ADMET, Lipinski's Rule of Five & Drug-likeness Analysis:

To assess the pharmacokinetic properties and drug-likeness of the synthesized 1,3,4-oxadiazole derivatives, in silico ADMET (Absorption, Distribution, Metabolism, Excretion and Toxicity) predictions were performed using online web servers SwissADME (http://www.swissadme.ch/) and PreADMET (https://preadmet.webservice.bmdrc.org/) [10, 11]. The compounds were evaluated for their compliance with Lipinski's Rule of Five, which is a set of criteria used to predict the drug-likeness of a compound. These criteria include molecular weight, the number of hydrogen bond donors, the number of hydrogen bond acceptors, and the octanol-water partition coefficient (LogP) [12]. The drug-likeness of the compounds was also evaluated using other relevant descriptors and rules such as the Veber's rule, Ghose filter and Egan's rule, to assess their potential for oral bioavailability and drug development. The results of the ADMET predictions and drug-likeness analysis were then integrated with the molecular docking results to prioritize the most promising 1,3,4-oxadiazole derivatives for further experimental validation and optimization [13, 14].

Synthesis

General Procedure for the Synthesis of (Z)-N-(5-((2-phenylethylidene)amino)-1,3,4-oxadiazol-2-yl)acetamide (SC1 to SC10)

A mixture of carbohydrazide (0.25 mmol) and substituted 2-phenylacetic acid (0.20 mmol) (Table 1) was refluxed in the presence of DMSO (10 mL) and ethanol (15 mL) for 2 hours. The progress of the reaction was monitored by TLC using chloroform: methanol(6:1 v/v). After 2 hours, the reaction mixture was allowed to cool, and ice was added to precipitate the product. For the next step, the obtained product (0.30 mmol) was mixed with acetic acid (3 mL) in the presence of ethanol (10 mL) and DCC (0.10 mmol). This mixture was refluxed for 1.5 hours. The progress of the reaction was again monitored by TLC using chloroform: methanol (6:1 v/v). After completion, the reaction mixture was allowed to cool to room temperature before being poured into HCl to precipitate the solid product. The precipitated solid product was collected by filtration and then recrystallized from ethanol, resulting in a slightly brown sample. The sample was dried, and its melting point was recorded to characterize the final product (Scheme in Fig. 2) [15–17, 27].
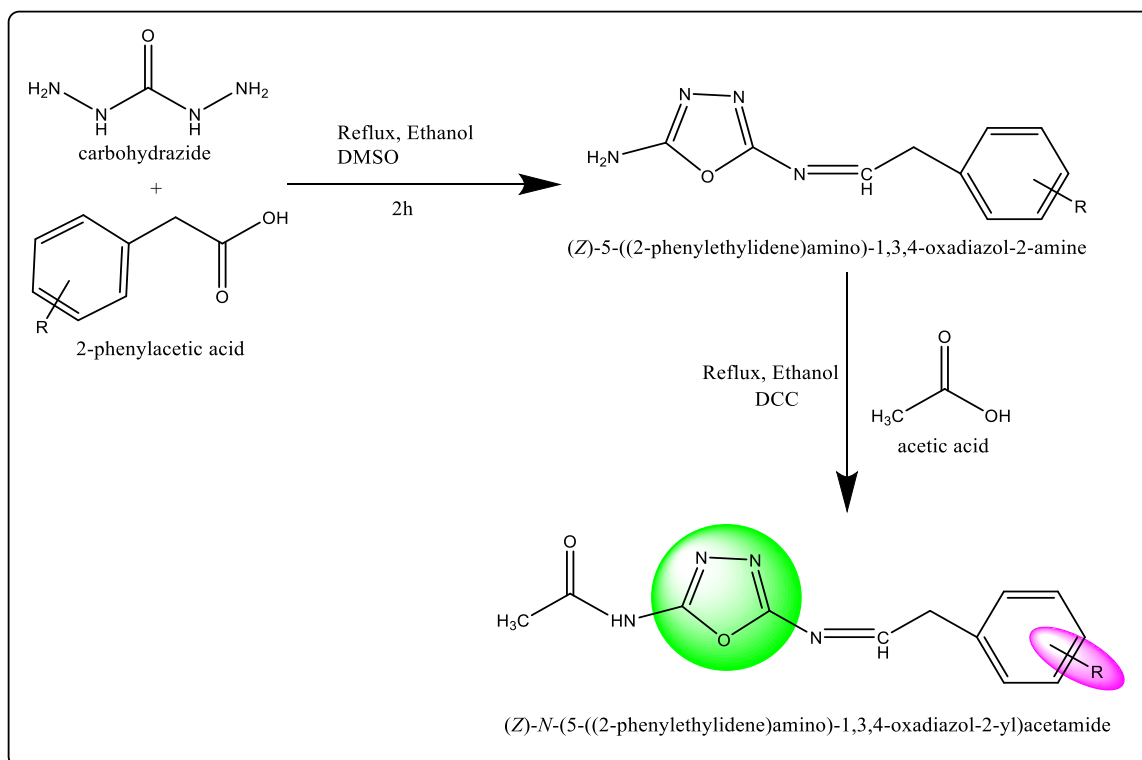
Figure 2. Proposed scheme of synthesis of 1,3,4-Oxadiazole derivatives

T a b l e 1

Designed derivatives of 1,3,4-Oxadiazole

Label	Molecular Formula	R
SC1	$C_{12}H_{11}ClN_4O_2$	-Cl
SC2	$C_{13}H_{14}N_4O_2$	-CH$_3$
SC3	$C_{12}H_{11}N_5O_4$	-NO$_2$
SC4	$C_{14}H_{16}N_4O_2$	-C$_2$H$_5$
SC5	$C_{12}H_{12}N_4O_2$	-H
SC6	$C_{12}H_{11}BrN_4O_2$	-Br
SC7	$C_{13}H_{14}N_4O_3$	-OCH$_3$
SC8	$C_{13}H_{13}ClN_4O_2$	
SC9	$C_{12}H_{11}FN_4O_2$	-F
SC10	$C_{15}H_{18}N_4O_3$	

Spectral Analysis of SC1 ─ SC10 Compounds

(Z)-N-(5-((2-(4-chlorophenyl)ethylidene)amino)-1,3,4-oxadiazol-2-yl)acetamide (SC1): Orange Solid, **Yield:** 64%, **M.p:** 178–182°C, **Rf value:** 0.78, **FTIR (cm⁻¹):** 3450–3500 (O–H stretching), 3300–3350 (N–H stretching), 3050–3100 (aromatic C–H stretching), 2900–2950 (aliphatic C–H stretching), 1680–1720 (C=O stretching), 1580–1620 (aromatic C=C stretching), **¹H NMR (δppm):** 7.50–7.60 (t, 1H, Ar-H), 7.10–7.20 (m, 2H, Ar-H), 7.00–7.10 (dt, 2H, Ar–H), 3.35–3.45 (dt, 2H, –CH$_2$–), 2.25–2.35 (d, 3H, –CH$_3$).

(Z)-N-(5-((2-(p-tolyl)ethylidene)amino)-1,3,4-oxadiazol-2-yl)acetamide (SC2): Yellow solid, **Yield:** 68 %, **M.p:** 198-202 °C, **Rf value:** 0.72, **MS (m/e):** 258.11, **FTIR (cm^{-1}):** 3492.34 (O-H stretching), 3313.17 (N-H stretching), 3191.59 (aromatic C-H stretching), 3062.55 (aliphatic C-H stretching), 1742.74 (C=O stretching), 1588.09 (aromatic C=C stretching), 1490.17 (aromatic C=C stretching), 1446.65 (CH$_2$ scissoring), 1319.33 (C-N stretching), 1295.02 (C-N stretching), 1244.24 (C-O stretching), 1206.88 (aromatic C-H in-plane bending), 1169.01 (CH$_2$ wagging), 1098.13 (aromatic C-H out-of-plane bending), 1071.43 (C-N stretching), 1020.79 (C-N stretching), 995.38 (C=N stretching), 872.05 (aromatic C-H out-of-plane bending), **^{1}H NMR (δppm):** 7.50 (t, 1H, Ar-H), 7.14-7.08 (m, 2H, Ar-H), 7.01 (dt, 2H, Ar-H), 3.39 (dt, 2H, -CH$_2$-), 2.30 (d, 3H, -CH$_3$).

(Z)-N-(5-((2-(4-nitrophenyl)ethylidene)amino)-1,3,4-oxadiazol-2-yl)acetamide (SC3): Yellow solid, **Yield:** 88 %, **M.p:** 167-170 °C, **Rf value:** 0.65, **FTIR (cm^{-1}):** 3480-3520 (O-H stretching), 3350-3390 (N-H stretching), 3150-3200 (aromatic C-H stretching), 1720-1760 (C=O stretching), 1590-1630 (aromatic C=C stretching), ^{1}H NMR (δppm): 7.55-7.65 (t, 1H, Ar-H), 7.15-7.25 (m, 2H, Ar-H), 7.05-7.15 (dt, 2H, Ar-H), 3.40-3.50 (dt, 2H, -CH$_2$-), 2.35-2.45 (d, 3H, -CH$_3$).

(Z)-N-(5-((2-(4-ethylphenyl)ethylidene)amino)-1,3,4-oxadiazol-2-yl)acetamide (SC4): Yellow solid, **Yield:** 83%, **M.p:** 168-169 °C, **Rf value:** 0.86, **FTIR (cm^{-1}):** 3490-3530 (O-H stretching), 3310-3350 (N-H stretching), 3180-3220 (aromatic C-H stretching), 1720-1760 (C=O stretching), 1570-1610 (aromatic C=C stretching), **^{1}H NMR (δppm):** 7.50-7.60 (t, 1H, Ar-H), 7.10-7.20 (m, 2H, Ar-H), 7.00-7.10 (dt, 2H, Ar-H), 3.30-3.40 (dt, 2H, -CH$_2$-), 2.20-2.30 (d, 3H, -CH$_3$).

(Z)-N-(5-((2-phenylethylidene)amino)-1,3,4-oxadiazol-2-yl)acetamide (SC5): Orange Solid, **Yield:** 70 %, **M.p:** 177-179 °C, **Rf value:** 0.68, **FTIR (cm^{-1}):** 3480-3520 (O-H stretching), 3300-3340 (N-H stretching), 3140-3180 (aromatic C-H stretching), 1720-1760 (C=O stretching), 1580-1620 (aromatic C=C stretching), **^{1}H NMR (δppm):** 7.50-7.60 (t, 1H, Ar-H), 7.15-7.25 (m, 2H, Ar-H), 7.05-7.15 (dt, 2H, Ar-H), 3.40-3.50 (dt, 2H, -CH$_2$-), 2.30-2.40 (d, 3H, -CH$_3$).

(Z)-N-(5-((2-(4-bromophenyl)ethylidene)amino)-1,3,4-oxadiazol-2-yl)acetamide (SC6): Orange solid, **Yield:** 57 %, **M.p:** 183-187°C, **Rf value:** 0.84, **FTIR (cm^{-1}):** 3490-3530 (O-H stretching), 3310-3350 (N-H stretching), 3180-3220 (aromatic C-H stretching), 1720-1760 (C=O stretching), 1570-1610 (aromatic C=C stretching), **^{1}H NMR (δppm):** 7.55-7.65 (t, 1H, Ar-H), 7.20-7.30 (m, 2H, Ar-H), 7.10-7.20 (dt, 2H, Ar-H), 3.45-3.55 (dt, 2H, -CH$_2$-), 2.35-2.45 (d, 3H, -CH$_3$).

(Z)-N-(5-((2-(4-methoxyphenyl)ethylidene)amino)-1,3,4-oxadiazol-2-yl)acetamide (SC7): Yellow solid, **Yield:** 59 %, **M.p:** 163-167 °C, **Rf value:** 0.77, **FTIR (cm^{-1}):** 3500-3540 (O-H stretching), 3320-3360 (N-H stretching), 3170-3210 (aromatic C-H stretching), 1730-1770 (C=O stretching), 1590-1630 (aromatic C=C stretching), **^{1}H NMR (δppm):** 7.55-7.65 (t, 1H, Ar-H), 7.15-7.25 (m, 2H, Ar-H), 7.05-7.15 (dt, 2H, Ar-H), 3.40-3.50 (dt, 2H, -CH$_2$-), 2.30-2.40 (d, 3H, -CH$_3$).

(Z)-N-(5-((2-(3-chloro-4-methylphenyl)ethylidene)amino)-1,3,4-oxadiazol-2-yl)acetamide (SC8): Yellow solid, **Yield:** 78 %, **M.p:** 191-194 °C, **Rf value:** 0.81, **MS (m/e):** 292.07, **FTIR (cm^{-1}):** 3535.37 (O-H stretching), 3396.54 (N-H stretching), 2931.02 (aliphatic C-H stretching), 2882.80 (aliphatic C-H stretching), 2736.02 (aromatic C-H stretching), 1686.98 (C=O stretching), 1410.64 (aromatic C=C stretching), 1304.10 (C-N stretching), 1170.35 (aromatic C-H in-plane bending), 888.99 (aromatic C-H out-of-plane bending), **^{1}H NMR (δppm):** 7.60 (t, 1H, Ar-H), 7.24-7.10 (m, 1H, Ar-H), 7.07 (dq, 1H, Ar-H), 6.98-6.66 (ddt, 1H, Ar-H), 3.13-3.08 (dt, 2H, -CH$_2$-), 2.18 (d, 6H, -CH$_3$).

(Z)-N-(5-((2-(4-fluorophenyl)ethylidene)amino)-1,3,4-oxadiazol-2-yl)acetamide (SC9): Orange solid, **Yield:** 68%, **M.p:** 162-166°C, **Rf value:** 0.79, **FTIR (cm^{-1}):** 3490-3530 (O-H stretching), 3300-3340 (N-H stretching), 3140-3180 (aromatic C-H stretching), 1720-1760 (C=O stretching), 1580-1620 (aromatic C=C stretching), **^{1}H NMR (δppm):** 7.50-7.60 (t, 1H, Ar-H), 7.10-7.20 (m, 2H, Ar-H), 7.00-7.10 (dt, 2H, Ar-H), 3.40-3.50 (dt, 2H, -CH$_2$-), 2.30-2.40 (d, 3H, -CH$_3$).

(Z)-N-(5-((2-(3-ethyl-4-methoxyphenyl)ethylidene)amino)-1,3,4-oxadiazol-2-yl)acetamide (SC10): Orange solid, **Yield:** 74%, **M.p:** 167-171°C, **Rf value:** 0.94, **FTIR (cm^{-1}):** 3510-3550 (O-H stretching), 3330-3370 (N-H stretching), 3190-3230 (aromatic C-H stretching), 1740-1780 (C=O stretching), 1600-1640 (aromatic C=C stretching), **^{1}H NMR (δppm):** 7.55-7.65 (t, 1H, Ar-H), 7.20-7.30 (m, 2H, Ar-H), 7.10-7.20 (dt, 2H, Ar-H), 3.45-3.55 (dt, 2H, -CH$_2$-), 2.35-2.45 (d, 3H, -CH$_3$).

Antidiabetic Activity

Invitro α-Amylase Inhibitory Activity

The invitro α-amylase inhibitory activity of compounds SC2 and SC8 was evaluated using a reported procedure with slight modifications (Srinivasan et al., 2018). Acarbose, a known α-amylase inhibitor, was used as a positive control. The assay was performed in triplicate.The reaction mixture was prepared by adding 70 µL of 50 mM phosphate buffer (pH 6.8) and 50 µL of the test compound (SC2 or SC8) at different concentrations (25, 50, and 100 µg/mL). To the mixture, 10 µL of α-amylase solution (0.057 units) was added and incubated for 10 minutes at 25°C. After pre-incubation, 10 µL of 0.5 mM *p*-nitrophenyl glucopyranoside was added to the reaction mixture and further incubated at 25°C for 10 minutes. The reaction was terminated by adding 100 µL of 0.1 M Na_2CO_3, and the absorbance was measured at 400 nm using a 96-well plate reader [18–20].

The residual activity was calculated using the following formula:

$$\text{Residual activity (\%)} = \frac{\text{(Absorbance (sample)}}{\text{(Absorbance (control)}} \times 100 \text{ \%}, \tag{1}$$

The % inhibition was calculated using the following formula:

$$\% \: Inhibition \: = \frac{(1 - (Residual \: activity \: of \: the \: sample)}{Residual \: activity \: of \: the \: control} \times 100\%. \tag{2}$$

The IC_{50} values were calculated using linear regression analysis of the % inhibition data plotted against the logarithm of the concentration of the test compound. The mean ± standard deviation (SD) of the IC_{50} values were calculated from three independent experiments [21].

Results and Discussion
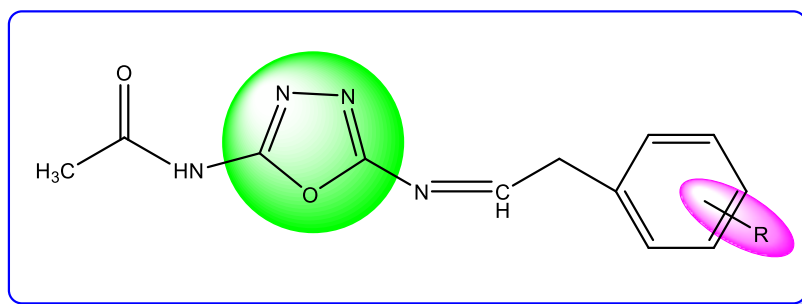
Figure 3. Chemistry of (Z)-N-(5-((2-phenylethylidene)amino)-1,3,4-oxadiazol-2-yl)acetamide (SC)

The compound (Z)-N-(5-((2-phenylethylidene)amino)-1,3,4-oxadiazol-2-yl)acetamide belongs to the 1,3,4-oxadiazole family of heterocyclic compounds. As depicted in Figure 3, this compound showcases the chemistry of the 1,3,4-oxadiazole family, a five-membered heterocyclic ring containing two nitrogen atoms and one oxygen atom. The 1,3,4-oxadiazole ring is renowned for its diverse biological activities and serves as a pivotal scaffold in medicinal chemistry. The (Z)-2-Phenylethylidene amine group contains a double bond between a carbon atom (from the 2-phenylethyl moiety) and a nitrogen atom. The "Z" configuration indicates that the two highest priority substituents are on the same side of the double bond. In this case, the phenyl ring and the 1,3,4-oxadiazole ring are on the same side. The phenyl ring contributes to the compound's hydrophobicity and can potentially participate in π-π stacking interactions with other aromatic moieties. The acetamide functional group consists of a carbonyl group (C=O) bonded to a nitrogen atom, which in turn is connected to the 1,3,4-oxadiazole ring. This group can act as a hydrogen bond acceptor through the carbonyl oxygen and as a hydrogen bond donor via the amide nitrogen [22, 26].

The substitution of different functional groups at the phenyl ring (R) in the (Z)-N-(5-((2-phenylethylidene)amino)-1,3,4-oxadiazol-2-yl)acetamide compound can significantly affect its chemical properties, biological activities and interactions with its target enzyme. By altering the electronic and steric properties of the phenyl ring, substituted derivatives can exhibit different binding affinities, selectivity and potency toward the target enzyme. Electron-donating groups (EDGs) such as alkyl groups (e.g., methyl, ethyl), hydroxyl (-OH), amino (-NH$_2$) and methoxy (-OCH$_3$) groups can increase the electron density on the phenyl ring, probably enhancing its ability to form π-π stacking interactions and hydrogen bonding with target enzyme residues [23]. Electron-withdrawing groups (EWGs) such as halogens (e.g., F, Cl, Br), nitro (-NO$_2$), cyano

(-CN) and carbonyl groups decrease the electron density on the phenyl ring, altering its electronic properties and potentially affecting its interactions with target enzyme residues [24, 25].

Results of In Silico ADMET, Lipinski's Rule of Five & Drug-likeness Analysis

Table 2 presents a comprehensive drug-likeness analysis of the designed 1,3,4-Oxadiazole derivatives based on Lipinski's rule of five and other relevant physicochemical parameters.

T a b l e 2

Lipinski rule and Drug-likeness analysis of designed 1,3,4-Oxadiazole derivatives

Comp.	Molecular Formulae	Molecular weight (g/mol)	CMC rule violation	Lipinski's rule violation	Mol Log P	H bond donor	H bond acceptor	No. of rotatable bonds	TPSA (Å^2)
SC1	$C_{12}H_{11}ClN_4O_2$	278.69	0	0	2.32	1	5	5	80.38
SC2	$C_{13}H_{14}N_4O_2$	258.28	0	0	2.05	1	5	4	80.38
SC3	$C_{12}H_{11}N_5O_4$	289.25	0	0	0.89	1	7	6	126.20
SC4	$C_{14}H_{16}N_4O_2$	272.30	0	0	1.91	1	5	6	80.38
SC5	$C_{12}H_{12}N_4O_2$	244.25	0	0	1.78	1	5	5	80.38
SC6	$C_{12}H_{11}BrN_4O_2$	323.15	0	0	2.45	1	5	5	80.38
SC7	$C_{13}H_{14}N_4O_3$	274.28	0	0	1.11	1	6	6	89.61
SC8	$C_{13}H_{13}ClN_4O_2$	292.72	0	0	2.58	1	5	5	80.38
SC9	$C_{12}H_{11}FN_4O_2$	262.24	0	0	2.18	1	6	5	80.38
SC10	$C_{15}H_{18}N_4O_3$	302.33	0	0	1.63	1	6	7	89.61

As can be seen in Table 2, molecular weight of all, from SC1 to SC10, lies within the acceptable range for drug-likeness, with values ranging from 244.25 g/mol (SC5) to 323.15 g/mol (SC6). Notably, none of the compounds violate the CMC (Congreve, Murray & Carr) rule or Lipinski's rule, indicating their potential as drug candidates. The partition coefficient (Log P) is a measure of a compound's lipophilicity, which can influence its absorption and distribution in the body. The Log P values of the derivatives vary, with SC8 exhibiting the highest value of 2.58 and SC3 showing the lowest at 0.89. These values suggest that the compounds possess a balanced hydrophilic-lipophilic profile, which is crucial for optimal bioavailability. Hydrogen bond donors and acceptors play a significant role in molecular interactions with biological targets. All results have a single hydrogen bond donor, while the number of hydrogen bond acceptors ranges from 5 to 7. SC3 and SC10, with 7 hydrogen bond acceptors, might exhibit enhanced interactions with their biological targets due to their potential to form multiple hydrogen bonds. The number of rotatable bonds in a molecule can influence its conformational flexibility. Most of the derivatives have either 5 or 6 rotatable bonds, with SC10 being an exception with 7. A higher number of rotatable bonds can increase the conformational flexibility, which might be advantageous in certain drug-target interactions.

The Topological Polar Surface Area (TPSA) is a predictor of a molecule's ability to cross biological membranes. The TPSA values for the derivatives are predominantly 80.38 Å^2, with SC3 and SC10 having slightly higher values of 126.20 Å^2 and 89.61 Å^2, respectively. These values suggest that the compounds have a favorable balance of polar and non-polar surface areas, which can influence their absorption and distribution profiles. In conclusion, the 1,3,4-Oxadiazole derivatives, as presented in Table 2, exhibit promising drug-likeness properties, making them potential candidates for further biological evaluations and optimizations.

Table 3 provides an in-depth analysis of the in silico ADME (Absorption, Distribution, Metabolism and Excretion) properties of the designed 1,3,4-Oxadiazole derivatives. The Caco2 permeability values are indicative of a compound's potential to be absorbed in the intestines.

As can be seen in Table 3, all byproducts, from SC1 to SC10, show varying degrees of Caco2 permeability, with SC8 having the highest value of 21.8737 and SC9 having a notably low value. High Caco2 permeability, as observed in most compounds, suggests good intestinal absorption potential. Additionally, all compounds are classified as having high gastrointestinal (GI) absorption, further emphasizing their potential for good oral bioavailability. The Blood-Brain Barrier (BBB) permeability, represented by logBB values, provides insights into a compound's ability to cross the BBB and reach the central nervous system. Most of the derivatives such as SC1, SC3, SC5, SC6, SC7 and SC9 are not permeable to the BBB. However, SC2, SC4, SC8 and SC10 are poorly permeable, suggesting they might have limited access to the brain. The Plasma Protein Binding (PPB) percentage indicates the fraction of the drug bound to plasma proteins. High PPB

values, as seen in the derivatives, suggest that a significant portion of the drug might be bound to proteins, potentially affecting its free concentration and pharmacological activity.

In silico ADME properties of designed 1,3,4-Oxadiazole derivatives

Comp.	Absorption		Distribution			Metabolism				
	Caco2 permeability	GI absorption	BBB perm. (logBB)	BBB Permeant	PPB (%)	CYP3A4 substrate	CYP1A2 inhibitor	CYP2C9 inhibitor,	CYP3A4 inhibitor	CYP2C19 inhibitor
SC1	18.6072	High	0.06724	No	79.77	No	Yes	No	No	Yes
SC2	20.305	High	0.0920	No	73.43	Weakly	Yes	No	No	No
SC3	19.427	High	0.0724	No	80.93	No	No	No	No	No
SC4	20.2128	High	0.134913	No	80.41	Weakly	Yes	No	No	Yes
SC5	19.7145	High	0.0893237	No	67.85	No	Yes	No	No	No
SC6	20.1718	High	0.0517618	No	79.95	No	Yes	No	No	Yes
SC7	15.8186	High	0.0920033	No	58.96	No	Yes	No	No	No
SC8	21.8737	High	0.105363	No	80.22	Weakly	Yes	No	No	No
SC9	0.0515124	High	0.0515124	No	64.94	No	Yes	No	No	No
SC10	16.4202	High	0.0576984	No	75.07	Weakly	Yes	No	No	No

Cytochrome P450 (CYP) enzymes play a pivotal role in drug metabolism. The table provides information on the interaction of the derivatives with various CYP isoforms. Most of the compounds, including SC1, SC2, SC4, SC5, SC6, SC7, SC8, SC9 and SC10, are substrates for CYP3A4, indicating that they might be metabolized by this enzyme. Additionally, SC1, SC4 and SC6 are inhibitors of CYP3A4, suggesting potential drug-drug interactions if co-administered with other drugs metabolized by CYP3A4. It is noteworthy that only SC1 is an inhibitor of CYP2C9, while none of the compounds inhibit CYP1A2 or CYP2C19. In conclusion, the 1,3,4-Oxadiazole derivatives exhibit a diverse range of ADME properties. While they generally show promising absorption characteristics, their distribution and metabolism profiles suggest the need for further investigation, especially concerning potential drug-drug interactions and brain accessibility.

Table 4 provides a comprehensive overview of the amino acid interactions, bond types and binding affinities of the designed 1,3,4-Oxadiazole derivatives with the target protein, human α-amylase (PDB ID: 6Z8L).

A summary of the amino acid interactions, bond types & binding affinities (kcal/mol)
for designed compounds

Compound	Amino acid interactions	Bond type	Binding Affinity (Kcal/mol)
1	2	3	4
SC1	GLU233, ASP300, ASP197, TRP59, TRP59, TRP59, TRP59, ALA198, ILE235, GLU233, VAL234, GLY306, LEU165, LEU162	H-bond, H-bond, Electrostatic, π-π Stacked, π-π Stacked, π-Alkyl, π-Alkyl, π-Alkyl, H-bond, H-bond, H-bond, H-bond, Hydrophobic, π-Alkyl	-7.3
SC2	ILE235, GLU233, VAL234, GLY306, LEU165, LEU162	H-bond, H-bond, H-bond, H-bond, Hydrophobic, π-Alkyl	-10.1
SC3	GLN63, ILE235, GLU233, VAL234, GLY306, LEU162	H-bond, H-bond, H-bond, H-bond, H-bond, π-Alkyl	-7.9
SC4	GLY306, GLY306, LEU165, TRP59, LEU162	H-bond, H-bond, Hydrophobic, π-Alkyl, π-Alkyl	-7.8
SC5	GLU233, ASP300, ASP197, TRP59, TRP59, ALA198	H-bond, H-bond, Electrostatic, π-π Stacked, π-π Stacked, π-Alkyl	-7.5
SC6	GLU233, GLY306, ASP300, LEU165, UNL1	H-bond, H-bond, Electrostatic, π-Sigma, π-π Stacked	-7.4
SC7	GLN63, GLU233, GLY306, THR163, ASP300, LEU165, LEU165	H-bond, H-bond, H-bond, H-bond, Electrostatic, π-Sigma, Hydrophobic	-7.6

1	2	3	4
SC8	GLU233, ASP197, TRP59, TRP59, TRP59, LEU165, TRP59, ALA198	H-bond, Electrostatic, π-Sigma, π-π Stacked, π-π Stacked, Hydrophobic, π-Alkyl, π-Alkyl	-9.1
SC9	GLN63, GLU233, ASP300, ASP197, TRP59, TRP59, ALA198	H-bond, H-bond, H-bond, Electrostatic, π-π Stacked, π-π Stacked, π-Alkyl	-7.5
SC10	GLN63, GLU233, ASP300, ASP197, TRP59, TRP59, TRP59, TRP59, LEU165, TRP59, ALA198, LEU165	H-bond, H-bond, H-bond, Electrostatic, π-Sigma, π-Sigma, π-π Stacked, π-π Stacked, Hydrophobic, π-Alkyl, π-Alkyl, π-Alkyl	-7.8
Acarbose	GLN63, GLN63, HIS305, THR163, ASP300, HIS305, TRP59, HIS305, TYR62, LEU165	H-bond, H-bond, H-bond, H-bond, Electrostatic, π-Donor H-bond, π-π Stacked, π-π T-shaped, π-π T-shaped, π-Alkyl	-10.5

Table 4 shows, that amino acid interactions and bond types are crucial in understanding the binding mechanism and specificity of the compounds. For instance, compound SC1 exhibits interactions with a wide range of amino acids, including GLU233, ASP300 and TRP59, through various bond types such as hydrogen bonds, electrostatic interactions and π-π stacking. This diversity in interactions might contribute to its binding affinity of -7.3 kcal/mol. Similarly, compound SC2, which has a notably high binding affinity of -10.1 kcal/mol, interacts predominantly through hydrogen bonds with amino acids like ILE235 and GLU233. The presence of π-alkyl and hydrophobic interactions further stabilizes the binding.The binding affinities represented in kcal/mol provide insights into the strength of the interaction between the compounds and the target protein. A more negative value indicates a stronger binding affinity. Among the designed compounds, SC2 stands out with a binding affinity of -10.1 kcal/mol, suggesting a strong interaction with the target protein. This is closely followed by SC8 with a binding affinity of -9.1 kcal/mol. For comparison, the native ligand Acarbose exhibits a binding affinity of -10.5 kcal/mol, indicating its strong binding potential.

Figures 4, 5 and 6 provide visual representations of the interactions of compounds SC2, SC8 and the native ligand Acarbose, respectively, with the target protein. The 2D (A) interactions offer a detailed view of the specific amino acids involved and the type of bonds formed, while the 3D (B) interactions provide a spatial perspective of the compound's orientation and positioning within the active site of the protein.

For instance, the 2D and 3D interactions of compound SC2 (Fig. 4) might reveal the spatial arrangement of the compound within the active site and its proximity to key amino acids, which could be crucial for its high binding affinity. In conclusion, the designed 1,3,4-Oxadiazole derivatives exhibit diverse interactions with the target protein, human α-amylase. The combination of amino acid interactions, bond types and binding affinities provides valuable insights into the potential of these compounds as effective inhibitors. The visual representations further enhance our understanding of the binding mechanisms and can guide future modifications to improve the efficacy of these compounds.
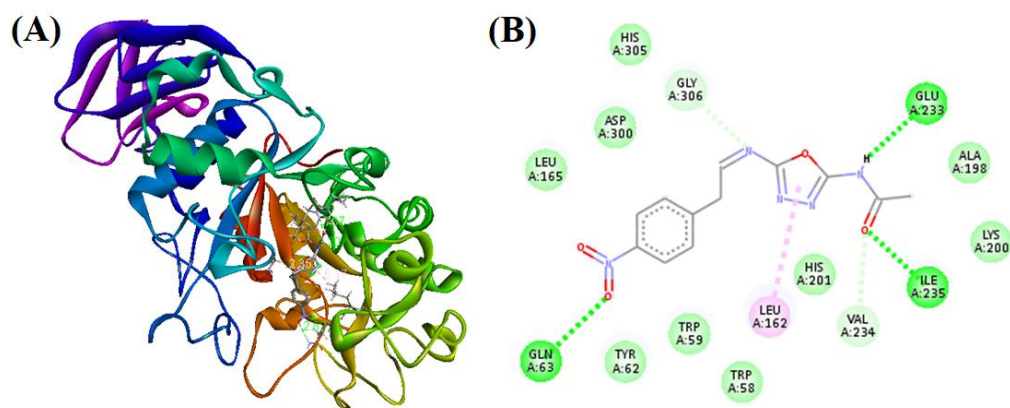
Figure 4. 2D (A) and 3D (B) interaction of compound SC2
with the target protein, human α-amylase (PDB ID: 6Z8L)
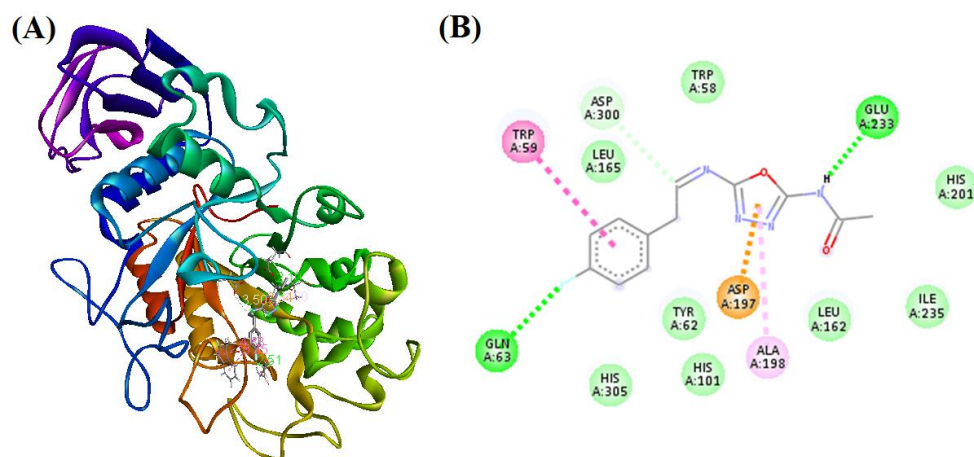
Figure 5. 2D (A) and 3D (B) interaction of compound SC8
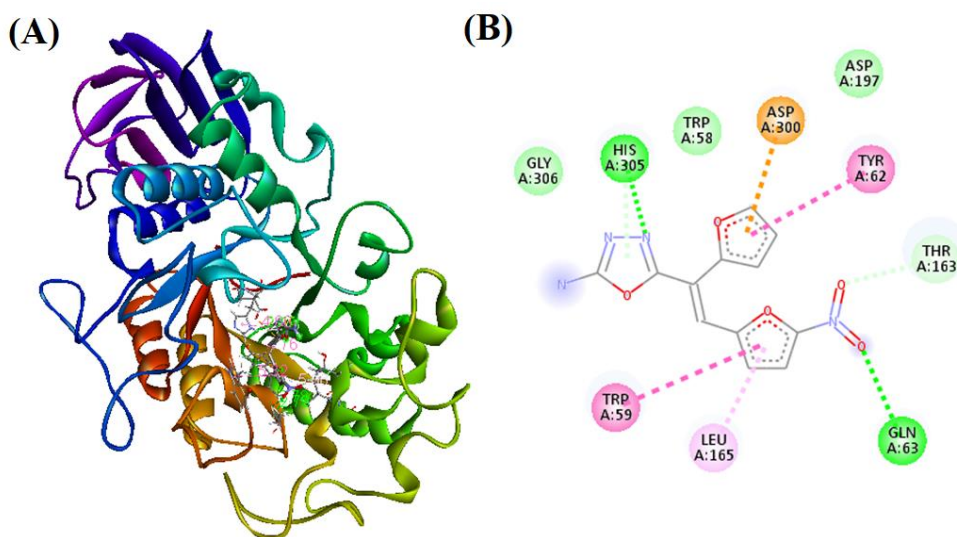with the target protein, human α-amylase (PDB ID: 6Z8L)

Figure 6. 2D (A) and 3D (B) interaction of Native Ligand (Acarbose)
with the target protein, human α-amylase (PDB ID: 6Z8L)

Results of α-Amylase Inhibition Activity

The result of α-amylase inhibition activity of the compounds SC2, SC8 and Acarbose based on the data presented in Table 5, Table 6 and Figure 7.

T a b l e 5

α-Amylase inhibition activity of compounds

Compound	Concentration (μg/mL)	OD at 400 nm	Residual activity	% Inhibition
SC2	100	0.180±0.010	20±2	80±2**
	50	0.290±0.010	35±2	65±2
	25	0.400±0.010	45±3	55±3
SC8	100	0.160±0.010	18±1	82±1
	50	0.270±0.010	30±2	70±2**
	25	0.390±0.010	40±3	60±3*
Acarbose	100	0.220±0.010	25±2	75±2
	50	0.320±0.010	40±3	60±3
	25	0.460±0.010	55±3	45±3
Values are expressed in mean±SD, (*n* = 3)				

Table 5 shows the α-amylase inhibition activity of SC2, SC8 and Acarbose at different concentrations (100, 50, and 25 µg/mL). At a concentration of 100 µg/mL, SC2 exhibits an inhibition of 80±2 %, while SC8 has slightly higher inhibition at 82±1%. In comparison, Acarbose demonstrates lower inhibition at 75±2 %. This indicates that SC2 and SC8 have a more potent inhibitory effect on α-amylase than Acarbose at the highest concentration tested. At lower concentrations (50 µg/mL and 25 µg/mL), SC2 and SC8 continue to display higher α-amylase inhibition than Acarbose. At 50 µg/mL, SC2 has an inhibition of 65±2% and SC8 exhibits an inhibition of 70±2 % compared to Acarbose with 60±3 % inhibition. Similarly, at 25 µg/mL, SC2 and SC8 inhibit α-amylase by 55±3 % and 60±3 %, respectively, while Acarbose shows a lower inhibition of 45±3 %.

Table 6

IC_{50} values for α-amylase inhibition activity of compounds SC2, SC8 and Acarbose

Compound	IC_{50} Value (µg/mL)
SC2	36.5±1.5
SC8	45.2±2.1
Acarbose	68.9±3.2
Values are expressed in mean±standard deviation ($n = 3$)	

Table 6 presents the IC_{50} values for α-amylase inhibition activity of SC2, SC8 and Acarbose. The IC_{50} value represents the concentration of the compound required to inhibit 50 % of the enzyme activity. SC2 has the lowest IC_{50} value of 36.5±1.5 µg/mL, followed by SC8 at 45.2±2.1 µg/mL, and Acarbose with the highest IC_{50} value of 68.9±3.2 µg/mL. These results indicate that SC2 is the most potent inhibitor among the three compounds, requiring a lower concentration to achieve 50% inhibition of α-amylase activity.
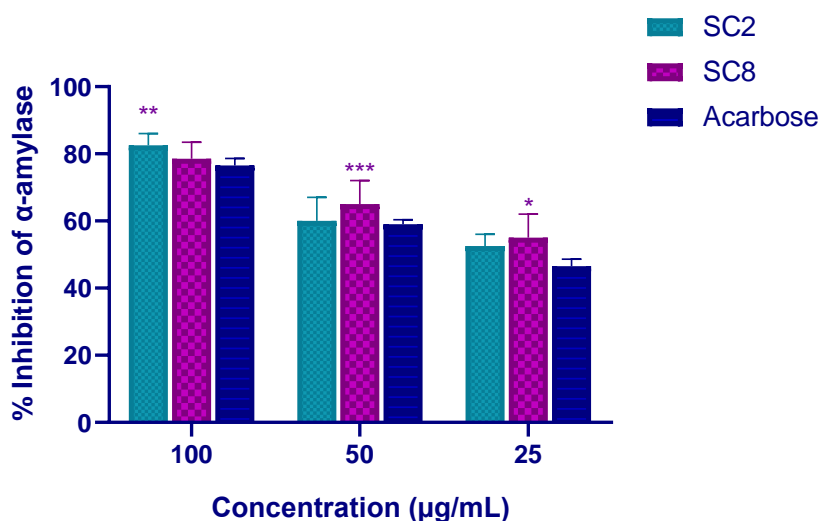
Figure 7. Graphical Representation of α-amylase inhibition activity of compounds SC2, SC8 and Acarbose

Figure 7 graphically represents the α-amylase inhibition activity of SC2, SC8 and Acarbose at different concentrations. The plot further illustrates that SC2 and SC8 exhibit superior inhibition compared to Acarbose across all tested concentrations. In conclusion, the results of the α-amylase inhibition activity assay indicate that SC2 and SC8 are more potent inhibitors of α-amylase than Acarbose at all tested concentrations. Furthermore, SC2 displays the highest potency among the three compounds, with the lowest IC_{50} value of 36.5±1.5 µg/mL. These findings suggest that SC2 and SC8 hold promise as potential therapeutic agents for the inhibition of α-amylase, with SC2 being the most effective. Further studies are needed to assess the in vivo efficacy and safety profile of these compounds as potential therapeutics for conditions that could benefit from α-amylase inhibition, such as diabetes.

Conclusions

In conclusion, this research article has successfully designed and analyzed a series of 1,3,4-oxadiazole derivatives as potential α-amylase inhibitors. Through in silico ADMET analysis, Lipinski's Rule of Five and drug-likeness evaluation, the study has identified two promising candidates, SC2 and SC8 that exhibit favorable pharmacokinetic properties and drug-likeness characteristics. Molecular docking studies reveal strong binding affinities of these compounds to the target protein, human α-amylase (PDB ID: 6Z8L), and provide insights into the key interactions responsible for their inhibitory activities. The in vitro α-amylase inhibition assay demonstrates that both SC2 and SC8 exhibit more potent inhibitory activities against α-amylase than the reference compound Acarbose across all tested concentrations. Notably, SC2 is the most effective inhibitor, with the lowest IC_{50} value of 36.5±1.5 µg/mL. These findings suggest that SC2 and SC8 hold significant potential as therapeutic agents for the inhibition of α-amylase and could serve as a basis for the advancement in novel therapies for diabetes. Despite these promising results, further investigations are required to confirm the in vivo efficacy and safety profile of SC2 and SC8 as potential therapeutic agents. Future studies should focus on evaluating the pharmacodynamic properties, toxicity and long-term effects of these compounds in animal models, followed by human clinical trials. Additionally, structure-activity relationship (SAR) studies could be conducted to optimize the molecular structures of these compounds for enhanced potency, selectivity and reduced side effects. Overall, this research article presents valuable findings that contribute to the ongoing search for novel and effective α-amylase inhibitors in the treatment of diabetes and other related disorders.

Acknowledgments

References

1   American Diabetes Association (2014). Diagnosis and classification of diabetes mellitus. *Diabetes care*, *37 Suppl 1*, S81–S90. https://doi.org/10.2337/dc14-S08

2   Kaul, K., Tarr, J. M., Ahmad, S. I., Kohner, E. M., & Chibber, R. (2012). Introduction to diabetes mellitus. *Advances in experimental medicine and biology*, *771*, 1–11. https://doi.org/10.1007/978-1-4614-5441-0_1

3   Alam, U., Asghar, O., Azmi, S., & Malik, R. A. (2014). General aspects of diabetes mellitus. *Handbook of clinical neurology*, *126*, 211–222. https://doi.org/10.1016/B978-0-444-53480-4.00015-1

4   Bashary, R., Vyas, M., Nayak, S. K., Suttee, A., Verma, S., Narang, R., & Khatik, G. L. (2020). An Insight of Alpha-amylase Inhibitors as a Valuable Tool in the Management of Type 2 Diabetes Mellitus. *Current diabetes reviews*, *16*(2), 117–136. https://doi.org/10.2174/1573399815666190618093315

5   Yakkala, P. A., Khan, I. A., Dannarm, S. R., Aboti, J., Sonti, R., Shafi, S., & Kamal, A. (2023). Multicomponent Domino Reaction for Concise Access to 2-Amino-Substituted 1,3,4 Oxadiazoles via Smiles Rearrangement. *The Journal of Organic Chemistry, 88*(17), 12216–12223. https://doi.org/10.1021/acs.joc.3c00516

6   Bukhari, A., Nadeem, H., Imran, M., & Muhammad, S. A. (2021). Novel oxadiazole derivatives as potent inhibitors of α-amylase and α-glucosidase enzymes: Synthesis, *in vitro* evaluation, and molecular docking studies. *Iranian journal of basic medical sciences*, *24*(12), 1632–1642. https://doi.org/10.22038/IJBMS.2021.58429.12977

7   Hamdani, S. S., Khan, B. A., Ahmed, M. N., Hameed, S., Akhter, K., Ayub, K., & Mahmood, T. (2020). Synthesis, crystal structures, computational studies and α-amylase inhibition of three novel 1, 3, 4-oxadiazole derivatives. *Journal of Molecular Structure*, 1200, 127085, https://doi.org/10.1016/j.molstruc.2019.127085.

8   Badithapuram, V., Nukala, S. K., Thirukovela, N. S., Dasari, G., Manchal, R., & Bandari, S. (2022). Design, synthesis, and molecular docking studies of some new quinoxaline derivatives as EGFR targeting agents. *Russian Journal of Bioorganic Chemistry, 48*(3), 565-575. https://doi.org/10.1134/S106816202203022

9   Zhang, S., Luo, Y., He, L. Q., Liu, Z. J., Jiang, A. Q., Yang, Y. H., & Zhu, H. L. (2013). Synthesis, biological evaluation, and molecular docking studies of novel 1,3,4-oxadiazole derivatives possessing benzotriazole moiety as FAK inhibitors with anticancer activity. *Bioorganic & medicinal chemistry*, *21*(13), 3723–3729. https://doi.org/10.1016/j.bmc.2013.04.043

10   Bitla, S., Sagurthi, S. R., Dhanavath, R., Puchakayala, M. R., Birudaraju, S., Gayatri, A. A., ... & Atcha, K. R. (2020). Design and synthesis of triazole conjugated novel 2, 5-diaryl substituted 1, 3, 4-oxadiazoles as potential antimicrobial and anti-fungal agents. *Journal of Molecular Structure, 1220*, 128705, https://doi.org/10.1016/j.molstruc.2020.128705

11 Perla, P., Seelam, N., & Bera, R. (2020). Design and synthesis of novel 1a, 3, 4-oxadiazole derivatives as cytotoxic agents: a combined experimental and docking study. *Russian Journal of Organic Chemistry, 56*, 924-934 https://doi.org/10.1134/S1070428020050280

12 Srinivasa, M.G., Paithankar, J.G., SahebBirangal, S.R., Pai, A., Pai, V., Deshpande, S.N., & Revanasiddappa, B.C. (2023). Novel hybrids of thiazolidinedione-1,3,4-oxadiazole derivatives: synthesis, molecular docking, MD simulations, ADMET study, in vitro, and in vivo anti-diabetic assessment. *RSC Advances, 13*(3), 1567–1579. https://doi.org/10.1039/d2ra07247e

13 Wang, Y., Xing, J., Xu, Y., Zhou, N., Peng, J., Xiong, Z., Liu, X., Luo, X., Luo, C., Chen, K., Zheng, M., & Jiang, H. (2015). In silico ADME/T modelling for rational drug design. *Quarterly reviews of biophysics*, *48*(4), 488–515. https://doi.org/10.1017/S0033583515000190

14 Jafari, E., Mohammadi, T., Jahanian-Najafabadi, A., & Hassanzadeh, F. (2017). Synthesis and antimicrobial evaluation of some 2,5 disubstituted 1,3,4-oxadiazole derivatives. *Research in pharmaceutical sciences*, *12*(4), 330–336. https://doi.org/10.4103/1735-5362.212051

15 Radia, A.J., Lalpara, J.N., Modasiya, I.J., & Dubal, G.G. (2021). Design and synthesis of novel 1, 3, 4-oxadiazole based azaspirocyclescatalyzed by NaI under mild condition and evaluated their antidiabetic and antibacterial activities. *Journal of Heterocyclic Chemistry, 58*(2), 612-621. https://doi.org/10.1002/jhet.4200

16 Zhou, L., Wang, P.Y., Zhou, J., Shao, W.B., Fang, H.S., Wu, Z.B., & Yang, S. (2017). Antimicrobial activities of pyridinium-tailored pyrazoles bearing 1, 3, 4-oxadiazole scaffolds. *Journal of Saudi Chemical Society, 21*(7), 852-860, https://doi.org/10.1016/j.jscs.2017.04.005

17 Li, Y., Luo, Y., Hu, Y., Zhu, D.D., Zhang, S., Liu, Z.J., Gong, H.B., & Zhu, H.L. (2012). Design, synthesis and antimicrobial activities of nitroimidazole derivatives containing 1,3,4-oxadiazole scaffold as FabH inhibitors. *Bioorganic & medicinal chemistry*, *20*(14), 4316–4322. https://doi.org/10.1016/j.bmc.2012.05.050

18 Khalilullah, H., Ahsan, M.J., Hedaitullah, M., Khan, S., & Ahmed, B. (2012). 1,3,4-oxadiazole: a biologically active scaffold. *Mini reviews in medicinal chemistry*, *12*(8), 789–801. https://doi.org/10.2174/138955712801264800

19 Acar Çevik, U., Celik, I., Paşayeva, L., Fatullayev, H., Bostancı, H. E., Özkay, Y., & Kaplancıklı, Z. A. (2023). New benzimidazole-oxadiazole derivatives: Synthesis, α-glucosidase, α-amylase activity, and molecular modeling studies as potential antidiabetic agents. *Archiv der Pharmazie*, *356*(5), e2200663. https://doi.org/10.1002/ardp.202200663

20 Khan, B.A., Hamdani, S.S., Ahmed, M.N., Hameed, S., Ashfaq, M., Shawky, A.M., Ibrahim, M.A.A., & Sidhom, P.A. (2022). Synthesis, X-ray diffraction analysis, quantum chemical studies and α-amylase inhibition of probenecid derived *S*-alkylphthalimide-oxadiazole-benzenesulfonamide hybrids. *Journal of enzyme inhibition and medicinal chemistry*, *37*(1), 1464–1478. https://doi.org/10.1080/14756366.2022.2078969

21 Lima, L.R., Bastos, R.S., Ferreira, E.F.B., Leão, R.P., Araújo, P.H.F., Pita, S.S.D.R., De Freitas, H.F., Espejo-Román, J.M., Dos Santos, E.L.V.S., Ramos, R.D.S., Macêdo, W.J.C., & Santos, C.B.R. (2022). Identification of Potential New *Aedes aegypti* Juvenile Hormone Inhibitors from N-Acyl Piperidine Derivatives: A Bioinformatics Approach. *International journal of molecular sciences*, *23*(17), 9927. https://doi.org/10.3390/ijms23179927

22 Al-Wahaibi, L.H., Mohamed, A.A.B., Tawfik, S.S., Hassan, H.M., & El-Emam, A.A. (2021). 1,3,4-Oxadiazole *N*-Mannich Bases: Synthesis, Antimicrobial, and Anti-Proliferative Activities. *Molecules (Basel, Switzerland), 26*(8), 2110. https://doi.org/10.3390/molecules26082110

23 SarveAhrabi, Y., Ahrabi, N.Z., & Souldozi, A. (2021). Synthesis and antimicrobial evaluation of new series of 1,3,4-oxadiazole containing cinnamic acid derivatives. *Avicenna Journal of Clinical Microbiology and Infection, 8*(1), 11–16. https://doi.org/10.34172/ajcmi.2021.03

24 Glomb, T., & Świątek, P. (2021). Antimicrobial activity of 1,3,4-oxadiazole derivatives. *International journal of molecular sciences, 22*(13), 6979. https://doi.org/10.3390/ijms22136979

25 Bala, S., Kamboj, S., Kajal, A., Saini, V., & Prasad, D.N. (2014). 1,3,4-oxadiazole derivatives: synthesis, characterization, antimicrobial potential, and computational studies. *BioMed research international*, *2014*, 172791. https://doi.org/10.1155/2014/172791

26 Karande, N.A., Rathi, L.G., Kamble, K.S., et al. (2023) Synthesis, Anti-Inflammatory Activity and Molecular Docking Studies of New 1,2,4-Triazolo[3,4-b][1,3,4]Thiadiazine Derivatives. *Pharm Chem J, 57*, 234–242. https://doi.org/10.1007/s11094-023-02873-6

27 Bendale, A.R., Bhatt, R., Nagar, A., Jadhav, A.G., & Vidyasagar, G. (2011). Schiff base synthesis by unconventional route: *An innovative green approach. Der Pharma Chemica, 3*(2), 34–38.

Information about authors*

Chavan, Shivani U. (*corresponding author*) — Research Student, Department of Pharmaceutical Chemistry, S.N.D. College of Pharmacy, Babhulgaon, 423401, Nashik, India; e-mail: shivani-chavan26@gmail.com, https://orcid.org/0009-0009-8805-8699

Waghmare, Sonali A. — Assistant Professor, Department of Pharmaceutical Chemistry, S.N.D. College of Pharmacy, Babhulgaon, 423401, Nashik, India; e-mail: waghmaresonali877@gmail.com

Bodke, Shraddha S. — Research Student, Department of Pharmaceutical Chemistry, Mahavir Institute of Pharmacy, Varvandi, 422004, Nashik, India; e-mail: shraddhabodke32@gmail.com, https://orcid.org/0000-0002-0765-7553

Bendale, Atul R. — Professor, Department of Pharmaceutical Chemistry, Mahavir Institute of Pharmacy, Varvandi, 422004, Nashik, India; e-mail: atulbendale123@gmail.com, https://orcid.org/0000-0002-3219-0377

*The author's name is presented in the order: *Last Name, First and Middle Names*

Mariya N. Grigor'eva ⅈD, Sergey A. Stelmakh* ⅈD

Baikal Institute of Nature Management SB RAS, Ulan-Ude, Russia;
*(*Corresponding author's e-mail: s_stelmakh@bk.ru)*

Doped Proton-Conducting Membranes
Based on Heat-Resistant Heterochain Polymers

Fuel cells with solid polymer electrolytes are the most popular chemical current sources and versatile sources of energy today. Proton-conducting membranes based on a guanidine-containing polymer of the cationic type on a polybenzimidazole matrix were obtained in this work. The membranes were created by doping film materials with orthophosphoric acid from a polymer-polymer mixture of N-phenyl-substituted polyhexamethylene guanidine (10 %) and polybenzimidazole. In this case, phosphoric acid remains in the membrane due to hydrogen bonds with the functional groups of the polymer and electrostatic interactions resulting from the doping of polyguanidine, which transforms into a polycationic form. As the content of polyguanidine increases in the polymer-polymeric mixture, the proton conductivity of the membrane increases. It was discovered that these membranes possess high thermal stability, with only a 20% mass loss occurring at 350 °C. Additionally, they exhibit high proton conductivity of $0.3 \cdot 10^{-1}$ mS/cm at temperatures of 130°C and higher, as well as satisfactory mechanical properties, with a tensile strength (σp) of 21-27 MPa and elongation at break (εp) of 7–11 %. The value of activation energy (E_a) is also low, at 0.145 eV, which suggests that these membranes have potential for using them in solid polymer electrolyte fuel cells.

Keywords: polymer films, polymer mixtures, proton-conducting membrane, polyguanidines, polybenzimidazoles, polycationic form, orthophosphoric acid, activation energy.

Introduction

Currently, a large number of proton-conducting membranes (PCM), including sulfonated aromatic polymer membranes, composite polymer-inorganic membranes, polymer-polymer mixture (PPM) membranes, and acid-base PCMs have been developed [1–3]. The main challenge in operating most of these membranes is maintaining satisfactory performance characteristics within the working temperature range of solid polymer electrolyte fuel cells (SPEFC) (100–200 °C) [4, 5]. Acid-base membranes, particularly phosphoric acid-doped polybenzimidazole (PBI) membranes, are of interest due to their potential for high performance [6–8]. However, the conductivity of such membranes decreases during prolonged operation because of acid leaching and other destructive processes, limiting their commercial use [9–11]. In addition to these PCM, membranes combining the characteristics of different groups are being created and studied to create highly efficient PCM that meet reliability requirements at a relatively low cost.

In this study, doped proton-conducting membranes were produced using a method based on [12]. These membranes contain phosphoric acid due to both weak hydrogen bonds with the polymer's functional groups and electrostatic interactions. The process involves creating a PPM N-phenyl-substituted polyhexamethylene guanidine/polybenzimidazole mixture, which results in the polyguanidine transforming into a polycationic form upon doping. As the content of polyguanidine in the PPM increases, the proton conductivity of the membrane sharply increases.

This study focuses on creating new doped proton-conducting membranes using a polymer-polymeric mixture of polyguanidines with a heat-resistant aromatic heterochain polymer.

Experimental

Classic methods of organic synthesis, isolation, and purification of reaction products have been used in this study. A complex of physicochemical methods of analysis (IR and NMR spectroscopy, elemental, thermogravimetric analysis, differential scanning calorimetry, microscopy) was used to characterize the obtained compounds. Studies of IR ATR spectroscopy were performed on ALPHA (Bruker, Germany), ATR attachment (ZnSe crystal), 4000–600 cm⁻¹, resolution 4 cm⁻¹. Studies of thermal decomposition of samples were performed on a NETZSCH STA 449 C synchronization thermal analyzer using air as a purge gas. The sam-

ples were recorded in the 25 ÷ 1000 °C temperature range at a heating rate of 5 °C/min. Proton conductivity was determined by the van der Pauw 4-probe method (the film of a square of 10×10 mm, at 500 Hz frequency, the amplitude voltage of 6 mV) [12] and impedance spectroscopy. The measurements were carried out by impedance spectroscopy using a Z-3000 impedance meter from Elins (Russia) in the frequency range 1 Hz–3 MHz. The amplitude of the measuring signal is 10–100 mV. Mechanical properties of the obtained film materials were tested using an Instron-3367 electromechanical rupture machine. TG, IR and mechanical properties were obtained using the equipment of the Collective Use Center of Buryat Scientific Center, Siberian branch, Russian Academy of Sciences.

The polymer-polymer mixture was prepared by mixing a 10 % solution of PHMGP in DMF and a 10 % solution of PBI in DMF at the ratios shown in the Table 1.

T a b l e 1

Ratio of polymer-polymer mixture of 10% solution of PHMGP and 10% solution of polybenzimidazole

№	PHMGP content, %	V (PHMGP10 %), ml	V(PBI, 10 %), ml
1	5.0	0.10	1.90
2	7.5	0.15	1.85
3	10.0	0.20	1.80

As the polyguanidine content increases, PPM-based film materials become brittle.

Film Doping

The dopant used was orthophosphoric acid at a concentration of 60%. The doping process involved placing a pre-weighed film into the acid solution, followed by transferring it to filter paper, removing any excess acid, and air-drying it for 24 hours at room temperature until a constant weight was achieved. The average thickness of the PCM was found to be 55±10 μm. The mass fraction of the dopant in the membrane composition of PCM (ω_{dop}) was determined using the following formula:

$$\omega_{dop} = \frac{m_{PCM} - m_{film}}{m_{PCM}} \cdot 100 \% .$$

where m_{PCM} — the mass of the PCM; m_{film} — the mass of film material before doping.

Data on the composition of PCM based on PPM PHMGP/PBI are summarized in Table 2.

T a b l e 2

Composition of PCM

№	PHMGP content in PPM, %	Mass fraction of dopant, %
1	0.0	50
2	5.0	52
3	7.5	54
4	10.0	58

Results and Discussion

The synthesis of PHMGP was performed using a two-stage process with equimolar ratios of monomers, as described in reference [13], according to the scheme:
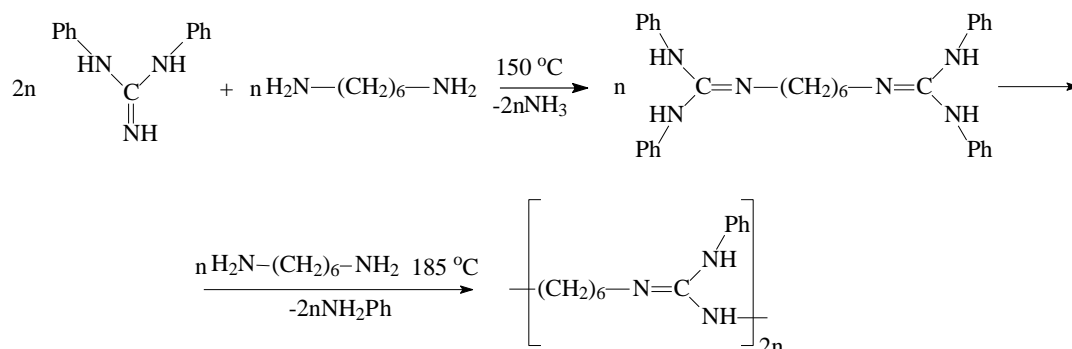
Polybenzimidazole was synthesized previously by reacting hydroxamic acid with isocyanate, as described in reference [14].

PHMGP and PBI can form single-phase stable solutions in DMF, similar to phenylone, allowing for the production of PCMs using the same method. However, increasing the content of PHMGP to more than 10% resulted in a significant deterioration of the physical and mechanical properties of the film materials, making it impossible to create PCMs based on them due to the average molecular weight of the obtained PBI. Therefore, the content of polyguanidine in PPM with PBI was limited to 10 %.
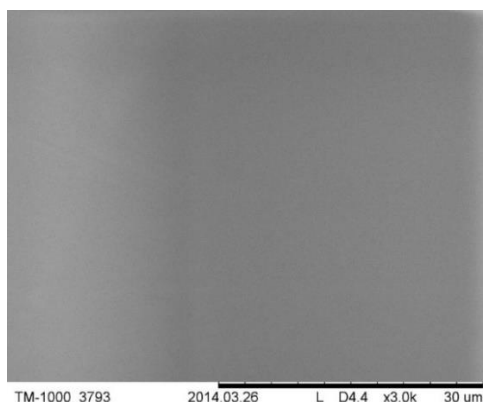
Figure 1. Micrograph of the film surface based on PPM PBI/PHMGP

On the micrograph of the film based on PBI/PHMGP PPM (Fig. 1), it can be seen that there are no defects or associates, indicating satisfactory thermodynamic compatibility between the components of PPM.

Doping films containing 5 %, 7.5 %, and 10 % wt. of polyguanidine (Table 3) with similar doping levels led to an increase in conductivity, as determined by the 4-probe van der Pauw method [15, 16], indicating the influence of the polycation content.

T a b l e   3

PCM conductivity based on PBI/PGMGP

PHMGP content, wt %	σ, mS/cm after doping
–	2.8
5.0	3.1
7.5	3.4
10.0	3.8

Despite the lower content of PHMGP, the membrane's conductivity, as determined by the van der Pauw method, was $3.8 \cdot 10^{-3}$ mS/cm, which is comparable to samples obtained from PPM with phenylon with a high content of polyguanidine [12]. This behavior is likely due to partially positive and negative charges in the elementary link of PBI, which are free vacancies targeted by ions resulting from orthophosphoric acid dissociation [17]. Therefore, phenylon should be considered an "inert matrix" that does not contribute to PCM conductivity, unlike PBI. Comparing the conductivity of PCMs doped with PBI and PBI/PHMGP at room temperature and the same dopant content revealed that PPM-based membranes had a specific volumetric conductivity more than 1.5 times higher ($1.69 \cdot 10^{-3}$ and $2.82 \cdot 10^{-3}$ mS/cm, respectively), indicating a significant contribution of polyguanidine to PCM conductivity. Macromolecules of polycation are likely evenly distributed, forming a zone with high concentrations of hydrophilic components (H_2O and dissociated H_3PO_4), characterized by low resistivity. The interaction between the mixture's components is similar to that of the above-described system based on aromatic polyamide (APA):
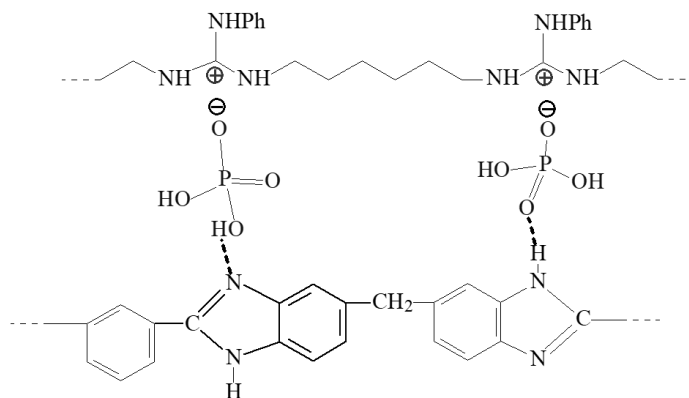
TG/DSC analysis of the doped PBI (Fig. 2) and PBI/PGMGP-based PPM (Fig. 3) samples shows a rather similar decomposition pattern.
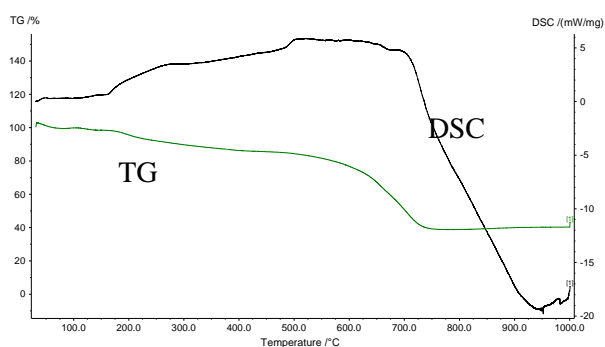
Figure 2. TG/DSC curves of PBI doped
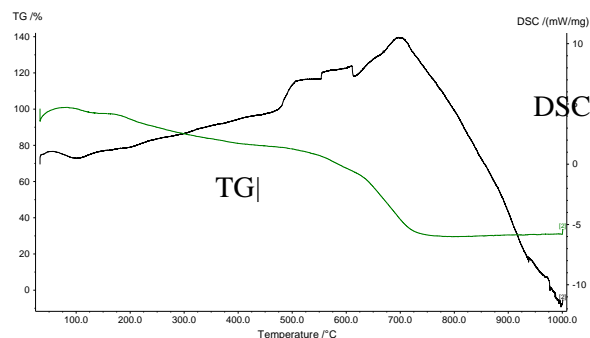
Figure 3. TG/DSC curves of the doped
PPM PBI/PHMGP 10 % mass sample

There is no well-defined stepwise mass loss in the TG curves over a wide range up to 450 °C. This is due to the high resistance of PBI to thermal and thermo-oxidative destruction even in aggressive environments. Heating up to 700 °C leads to mass loss of both samples up to 35-40% and is accompanied by pronounced exothermic effects. For the doped PBI sample it is a one-step process, whereas for PBI/PGMGP two steps and a more complex pattern on DSC can be distinguished. The first step can be conventionally designated in the range of 450–600 °C and the second step — one 600–700 °C. This can be attributed to the presence of another polymer. The combination of exothermic effects and abrupt mass loss suggests intensive thermo-oxidative oxidation processes of the organic components of these systems. However, the low-temperature region is of most interest for study because it partly mimics the membrane operation in fuel cell. For the PBI/PGMGP sample (Fig. 3), an endothermic effect is observed with a peak at ~100 °C and accompanied by mass loss in the range of 100–150 °C. This is due to the partial loss of bound water. For the PBI sample (Fig. 2), this effect is practically not observed. This may be due to the presence of more hygroscopic PGMGF in the composition of the system in Figure 3, and leads to more intense sorption of moisture from the atmosphere by the membrane surface due to its easy detachment (desorption) even at low temperature. In the temperature range of ~185–250 °C for both samples, the TG curves show a step of mass loss up to 90–85 % and its subsequent smooth decrease up to 80–75 % when reaching 450 °C. However, there are differences in the DSC curves. For PBI sample in the range 190-300 °C there is a prolonged endothermic effect. Similar behavior was not observed for the second system. It is associated with oxidative reactions starting to occur perhaps for PBI sample. For the PBI/PGMGP sample (Fig. 3) the absence of a similar region on DSC presumably be explained by competing endothermic processes, such as desorption of bound water. In addition, the presence of PGMHP in its composition can lead to a marked change in the behavior of these systems with respect to sorption-desorption. The analysis of the obtained data allows us to assume that these systems (investigated PBI/PGMGP system) demonstrate high thermal stability in oxidizing atmosphere at typical temperatures of fuel cell operation in spite of the fact that some questions of thermal stability of such membranes remain not completely solved.

The sample with the maximum content of PHMGP (10% by weight) is the most interesting among the obtained membranes, therefore, other PCM-based PPMs are not further considered.

Based on PPM PHMGP/PBI, the temperature dependence of PCM was examined (Fig. 4).
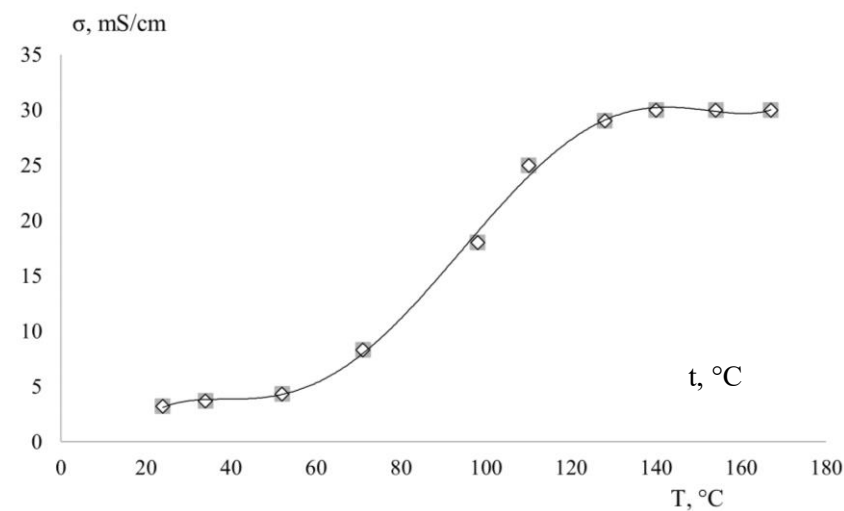
Figure 4 Temperature dependence of the specific conductivity of PCM
based on PPM PHMGP/PBI (4-probe van der Pauw method)

The behavior indicator of conductivity of membrane differs in the low and high-temperature areas. At low temperatures, the membrane's conductivity gradually increases from 3.2 mS/cm at room temperature and humidity to 8.3 mS/cm at 70 °C. In the future, due to the loss of free water by the film and subsequent temperature increase, the dependence becomes more pronounced, which is associated with the increased contribution of the Grootgus mechanism [18, 19] to the membrane's conductivity, similar to the dependence for PCM based on PPM polyguanidine with phenylone [12]. However, the membrane's further behavior is significantly different; from a temperature of 130 °C, the dependence reaches a plateau. At first glance, it may seem that the contribution of temperature increase is leveled by the destruction of the membrane; however, a detailed study of the IR spectra of the membrane before and after measurements (Fig. 5), as well as the preservation of the original color and elasticity of the film, indicates the absence of destructive changes.
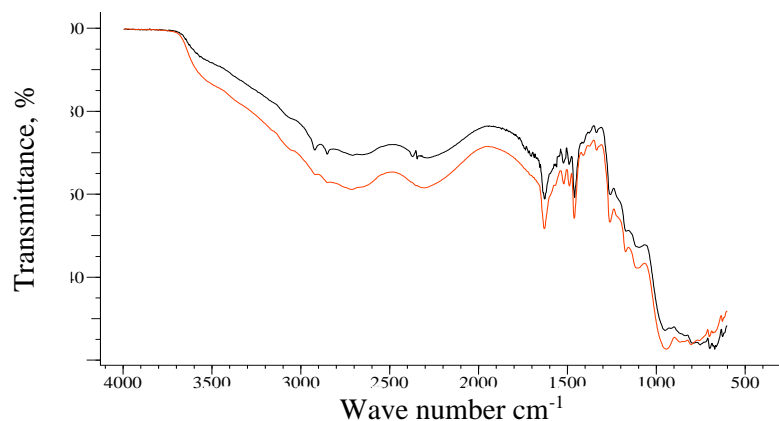
Figure 5. IR spectrum of the membrane based on PPM PHMGP/PBI
before and after measuring the temperature dependence of the conductivity

In the IR spectra, a wide absorption region in the range of 3700–2500 cm^{-1} is characteristic of strong hydrogen bonds, which partly mask the strong (intense) bands of asymmetric and symmetric oscillations of the CH_2 groups at 2920 and 2850 cm^{-1}, respectively. Peaks at 2700 cm^{-1} and 2330 cm^{-1} refer to the oscillations of the hydroxyl group of the dihydrogen phosphate anion. Their origin may be caused by the Fermi resonance $\nu(OH)$-$2\delta(OH)$ [12]. The band at 1630 cm^{-1} was indicated as a characteristic peak of guanidine salts. The group of bands at 1550–1400 cm^{-1} obviously refers to oscillations of the imidazole ring of PBI. Also,

characteristic signals of oscillations of the benzene ring are in this region at 1450 cm^{-1}. This oscillation is overlapped by deformation oscillations of CH$_2$, therefore, in this case, it is not possible to reliably identify the signals of cyclic fragments related to a specific compound in the composition of PPM seems possible. The peaks in the region of 1240-1180 cm^{-1} are attributed to the P=O oscillations. Absorptions in the region of 1100–970 cm^{-1} belong to orthophosphoric acid anions [20]. Signals in the region of 900–710 cm^{-1} are characteristic of non-planar deformation oscillations of hydrogen atoms in the benzene ring (mono-substituted for PGMHP, 1,3- and 1,2,4- for PBI), however, as in the case of pulsation oscillations of the ring it is impossible to correlate them reliably for this system. Analysis of the IR spectrum of the PPM confirms the presence of the declared structural fragments according to the scheme given above. The presence of water can also lead to increased signals in the regions of 3000–3600 cm^{-1}, 2100 cm^{-1}, near 1640 cm^{-1} and below 800 cm^{-1}.

Several reasons may explain this behavior. The membrane's resistance consists of the resistance caused by the potential barrier during the migration of the proton from one acid residue to another (Rp) and the resistance of the membrane defects (Rd). If, in the first case, the resistance decreases significantly with increasing temperature, then in the second case, it does not depend on temperature. In the region of low temperatures, Rp and Rd decrease; however, with an increase in temperature, Rp decreases, and in the high-temperature region, Rd begins to prevail, and the membrane's conductivity ceases to change significantly.

Physical and mechanical tests of the obtained film materials at break — ultimate strength (σ_p) and relative elongation (ε_p) were carried out (Table 4).

T a b l e 4

Physical and mechanical properties of film materials and PCM based on them

№	Sample	Mechanical properties	
		σ_p, MPa	ε_p, %
1	PBI nondop.	75–93	4–7
2	PBI dop.	65–80	10–14
3	PBI/PHMGP nondop.	41–46	3–6
4	PBI/PHMGP dop.	21–27	7–11

It has been shown that the addition of polyguanidine worsens the mechanical performance of the samples; however, the resulting membranes meet the requirements for PCMs [21, 22].

In addition, such membranes are characterized by low E_a values (Fig. 6, Table 5).
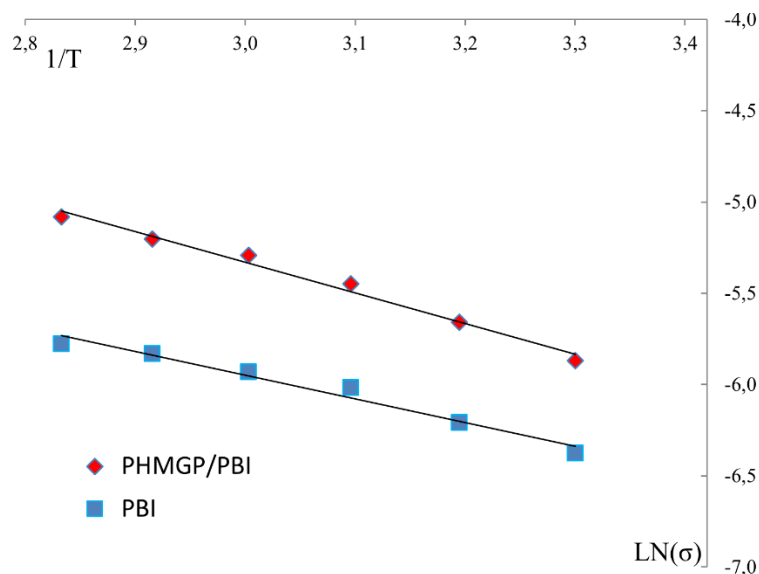
Figure 6. The dependence of conductivity on temperature (up to 80 ºC). Composition of PBI/PHMGP film

E_a for PCM based on PBI and PPM PHMGP/BI

Sample	tg angle	Activation energy (E_a) eV	E_a kJ/mol
PBI	1.299	0.1123635	10.84308
PHMGP/BI	1,675	0.1448875	13.98164

Conclusions

Using the previously developed approach to the creation of PCM [12], membranes with improved characteristics based on PPM PHMGP/BI were obtained. The maximum specific conductivity of such membranes reaches 2.82^{10-3} mS/cm at room temperature and 0.3^{10-1} mS/cm at 130-170 °C, and 20 % weight loss is observed at a temperature of ~350°C. In addition, the membranes are characterized by satisfactory mechanical performance (σ_p = 21–27 MPa, ε_p = 7–11 %) and low activation energy (E_a = 0.145 eV).

Thus, the combination of good performance in the temperature range of SPEFC, good temperature resistance, satisfactory physical and mechanical characteristics, and relatively low cost of the obtained membranes allows us to consider them as promising materials for creating SPEFC.

Acknowledgments

References

1 Jiang, S., Sun, H., Wang, H., Ladewig, B.P., & Yao, Z. (2021). A comprehensive review on the synthesis and applications of ion exchange membranes. *Chemosphere*, 282:130817. https://doi.org/10.1016/j.chemosphere.2021.130817

2 Tellez-Cruz, M.M., Escorihuela, J., Solorza-Feria, O., & Compañ, V. (2021). Proton Exchange Membrane Fuel Cells (PEM-FCs): Advances and Challenges. *Polymers (Basel),* 10, 13(18), 3064. https://www.doi.org/10.3390/polym13183064

3 Qu, E., Hao, X., Xiao, M., Han, D., Huang, S., Huang, Z., et al. (2022). Proton exchange membranes for high temperature proton exchange membrane fuel cells: Challenges and perspectives. *Journal of Power Sources*, 533, 231386. https://doi.org/10.1016/j.jpowsour.2022.231386

4 Liu, H., Chen, J., Ouyang, Q., & Su, H. (2016). A Review on Prognostics of Proton Exchange Membrane Fuel Cells. 2016 IEEE Vehicle Power and Propulsion Conference (VPPC), 1-6.

5 Tang, H., Aili, D., Geng, K., Gao, J., Li, Q., & Li, N. (2021). On the stability of imidazolium and benzimidazolium salts in phosphoric acid based fuel cell electrolytes. *Journal of Power Sources*, 515, 230642. https://doi.org/10.1016/j.jpowsour.2021.230642

6 Peng, J., Fu, X., Liu, D., Luo, J., Wang, L., & Peng, X. (2022). An Effective Strategy to Enhance Dimensional-Mechanical Stability of Phosphoric Acid Doped Polybenzimidazole Membranes by Introducing in Situ Grown Covalent Organic Frameworks. *Journal of Membrane Science*, 655, 120603. https://doi.org/10.2139/ssrn.4046609

7 Yu, S., Xiao, L., & Benicewicz, B.C. (2008). Durability Studies of PBI-based High Temperature PEMFCs. *Fuel Cells,* 8, 165–174. https://doi.org/10.1002/fuce.200800024

8 Hjuler, H.A., Azizi, K., Šešelj, N., Martinez Alfaro, S., Garcia, H.R., Gromadskyi, D.G., Hromadska, L., Primdahl, S., Jensen, J.O., Li, Q., Celenk, S., & Cleemann, L.N. (2021). Durability Studies on PBI Based High Temperature PEMFC. *ECS Transactions,* 104, 403. https://doi.org/10.1149/10408.0403ecst

9 Ahmad, S., Nawaz, T., Ali, A., Orhan, M.F., Samreen, A., & Kannan, A.N. (2022). An overview of proton exchange membranes for fuel cells: Materials and manufacturing. *International Journal of Hydrogen Energy,* 47, 44, 19086-19131. https://doi.org/10.1016/j.ijhydene.2022.04.099

10 Azizi, K., Hjuler, H., Seselj, N., Jensen, J. O., Li, Q., & Cleemann, L.N. (2022). PBI-Membrane for High-Temperature PEMFC. ECS Meeting Abstracts, MA2022-02(40), 1496–1496. https://doi.org/10.1149/ma2022-02401496mtgabs

11 Park, H., Kim, H., Kim, D.-K., Lee, W. J., Choi, I., Kim, H.-J., et al. (2020). Performance deterioration and recovery in high-temperature polymer electrolyte membrane fuel cells: Effects of deliquescence of phosphoric acid. *International Journal of Hydrogen Energy, 45*(57), 32844–32855. https://doi.org/10.1016/j.ijhydene.2020.03.039

12 Stelmakh, S.A., Ukshe, A.E., Mognonov, D.M., Novikova, K.S., Grigor'eva, M.N., Kayumov, R.R., et al. (2016). Proton conductivity of new type medium-temperature proton exchange membranes. *Ionics*, *22*(10), 1873–1880. https://doi.org/10.1007/s11581-016-1722-1

13 Bazaron, L. U., & Stel'makh, S. A. (2008). Molecular-weight characteristics of polyhexamethyleneguanidine hydrochloride. *Russian Journal of Applied Chemistry*, *81*(11), 2021–2025. https://doi.org/10.1134/s1070427208110293

14 Grigor'eva, M.N., Mognonov, D.M., Tonevitskii, Yu.V., Stel'makh, S.A., & Ochirov, O.S. (2018). Aromatic Polybenzimidazoles on the Basis of 4,4′-Diphenylmethane Diisocyanate and Bis(arylene)hydroxamic Acids. *Polymer Science, Series B*, 60(1), 16–19. https://doi.org/10.1134/s1560090418010050

15 Bissessur, R., White, W., & Dahn, D.C. (2006). Electrical characterization of conductive polymers and their intercalated nanocomposites with molybdenum disulfide. *Materials Letters*, *60*(2), 248–251. https://doi.org/10.1016/j.matlet.2005.08.026

16 van der PAUW, L.J. (1991). A method of measuring specific resistivity and hall effect of discs of arbitrary shape. *Semiconductor Devices: Pioneering Papers*, 174–182. https://doi.org/10.1142/9789814503464_0017

17 Zuo, Z., Fu, Y., & Manthiram, A. (2012). Novel Blend Membranes Based on Acid-Base Interactions for Fuel Cells. Polymers, *4*(4), 1627–1644. https://doi.org/10.3390/polym4041627

18 Vilčiauskas, L., Tuckerman, M.E., Bester, G., Paddison, S.J., & Kreuer, K.-D. (2012). The mechanism of proton conduction in phosphoric acid. *Nature Chemistry*, *4*(6), 461–466. https://doi.org/10.1038/nchem.1329

19 Li, Q. (2004). Water uptake and acid doping of polybenzimidazoles as electrolyte membranes for fuel cells. *Solid State Ionics, 168*(1–2), 177–185. https://doi.org/10.1016/j.ssi.2004.02.013

20 Goto, T., Nakanishi, K., & Ohashi, M. (1957). An Account on the Infrared Absorption of Guanidiniums. *Bulletin of the Chemical Society of Japan*, 30, 723-725.

21 Aricò, A.S., Srinivasan, S., & Antonucci, V. (2001). DMFCs: From Fundamental Aspects to Technology Development. *Fuel Cells*, *1*(2), 133–161. https://doi.org/10.1002/1615-6854(200107)1:2<133::aid-fuce133>3.0.co;2-5

22 Kalhammer, F.R. (1998). Status and prospects of fuel cells as automobile engines. A Report of the Fuel Cell Technical Advisory Panel. Retrieved from https://ininet.org/fcta-p-fuel-cell-technical-advisory-panel.html

Information about authors*

Grigor'eva, Mariya Nikolaevna — Candidate of Sciences in Pharmacy, Lead Engineer of the Polymer Chemistry Laboratory, Baikal Institute of Nature Management of the Siberian Branch of the Russian Academy of Sciences (Ulan-Ude, Russia), Sakhyanova street, 6, 670047, Ulan-Ude, Russia; e-mail: Gmn_07@bk.ru; https://orcid.org/0000-0003-4184-2805

Stelmakh, Sergey Alexandrovich (*corresponding author*) — Candidate of Sciences in Chemistry, senior researcher of the Polymer Chemistry Laboratory, Baikal Institute of Nature Management of the Siberian Branch of the Russian Academy of Sciences (Ulan-Ude, Russia), Sakhyanova street, 6, 670047, Ulan-Ude, Russia; e-mail: s_stelmakh@bk.ru; https://orcid.org/0000-0003-3392-5600

_____
*The author's name is presented in the order: *Last Name, First and Middle Names*

Vijaya R. Mandale, Asha B. Thomas[*] [iD], Pranali A. Jadhav [iD],
Chandrajyoti Y. Patil [iD], Ritesh P. Bhole [iD]

*Department of Pharmaceutical Chemistry, Dr. D.Y. Patil Institute of Pharmaceutical Sciences and Research,
Pimpri, Pune, Maharashtra, India*
(*Corresponding author′s e-mail: asha.thomas@dypvp.edu.in)

Design and Synthesis of Folic Acid-Phytochemical Conjugates
as Anti-Cancer Agents

Cancer treatment continues to be a major challenge for the medical community mainly due to non-specificity, leading to serious toxic effects. The use of vitamins such as folic acid and biotin are presently being studied through the synthesis of vitamin-drug conjugates as a new approach to improve the affinity of the drug molecules with cancer cells. Current research emphasizes on the design and synthesis of novel phytochemical vitamin conjugates as anticancer agents through *in silico* studies. Conjugates of quercetin (QC), curcumin (CUR) and berberine (BER) with folic acid (FA) were evaluated through docking experiments using Autodock Vina. Quercetin-folic acid conjugate 1 (QC-FA 1) demonstrated the highest binding affinity (-12.0 kcal/mol) to the human folate receptor (PDB ID: 4LRH) indicating the possibility of rapid uptake leading to internalization within the cells, improving the specificity to cancer tissues. The conjugates were further examined for their pharmacokinetic properties using AdmetSAR and SMARTcyp tools, which implied the incapability of these conjugates to cross the blood brain barrier but with favorable pharmacokinetic and CYP450 potential indicating their ability to act as drug-like molecules. Further QC-FA 1 was synthesized and effectively characterized. This conjugate will be further tested for its efficacy in treatment of cancer.

Keywords: Vitamin-drug conjugate, Folic acid, Anticancer, Quercetin, Curcumin, Berberine, In silico study, Cancer treatment.

Introduction

One in every six deaths worldwide is caused by cancer, making it a key concern for global public health [1]. The WHO cancer estimates that about 10 million people died from the disease in 2020 [2]. Cancer is abnormal cell growth that can grow out of control and, in many cases, may spread to other body parts [3]. The most popular treatment for cancer is chemotherapy, but its disadvantage is that it is not selective, which leads to serious, often fatal side effects [4, 5]. The drawback of widely used cytotoxic medications like doxorubicin, cisplatin, paclitaxel, is that they are unable to distinguish between healthy and abnormal cells. This nonspecificity causes systemic toxicity, which in turn leads to a cascade of other negative side effects, including hair thinning, damage of the kidney, lung, and bone marrow [6].

Further, it is extremely difficult to deliver anticancer drugs to the tumor site. It is necessary to develop tailored drug delivery system so that pharmaceuticals can act exclusively on actively growing malignant cells with minimal side effects [7]. Such targeted medications, which are preferentially absorbed by tumor cells, are expected to significantly improve the effectiveness of cancer therapy. Recent research has focused on developing medications with different targeted ligands, including use of polysaccharides, peptides, and folate, to improve efficacy of anticancer drugs [8–12]. The best way to improve the safety and efficacy is to use a targeting ligand to deliver a therapeutic drug with high affinity for malignant tumours but low affinity for healthy cells [13].

Tumour targeting moiety and chemotherapeutic drug should be directly coupled through a linker so as to enable efficient tumor-specific drug delivery. Additionally, the targeted drugs can deliver therapeutic doses precisely into the cancer cell, blocking nonspecific absorption and associated damage of healthy cells [14, 15]. As a result, a conjugate acting "prodrug" can be developed that will quickly dissociate when incorporated into a malignant cell and restore the activity of the anticancer drug [16]. Due to the rapid growth, cancer cells have an enhanced demand for essential vitamins, which is a physiological trait shared by all living cells [17, 18]. Recent studies in the literature have demonstrated that receptors required for vitamin absorp-

tion are overexpressed in malignant cells. Essential vitamins such as folic acid, riboflavin, vitamin B12, and biotin are required for efficient tumor growth. Combining pharmaceuticals with vitamins that target tumor-associated antigens is one way to boost the sensitivity of malignant cells to ligand-targeted therapies while decreasing the susceptibility of normal cells to medications.

Recently, it was found that cancer cells have higher levels of overexpressed folate receptors than normal, healthy cells. Thus, it is recognized that folate receptors function as excellent targets [19–22]. Folate receptor alpha (FRA) protein is overexpressed on the exterior of several forms of tumours, including ovarian, breast, pancreatic, and liver malignancies. Thus folate and anticancer drugs can be combined. The optimal approach is to combine therapeutic probes with folic acid to prepare conjugates targeting FRA-positive tumour cells. Folate conjugates make it possible to administer cancer-specific medications with little or no harm to the healthy cells [23–25]. This conjugation scaffold can increase the bioavailability and efficacy of cytotoxic substances. Since such vitamin-anticancer medication conjugates can provide a large amount of the cytotoxic agents to the target malignant cell, the essential vitamins including biotin, folic acid, vitamin B12, and riboflavin may act as a promising approach to kill the malignant cells.

Folic acid-drug conjugates, biotin-drug conjugates, vitamin B12-drug conjugates, vitamin E-drug conjugates, and vitamin C-drug conjugates are now being extensively studied [26]. Over the past few decades, innovative lead compounds derived from natural sources have increased [27]. New research has also confirmed that the natural molecules are useful in making cancer cells more susceptible to chemotherapy, assisting to defeat multi drug resistance (MDR) [28]. Among the reported phytomolecules; quercetin (QC), curcumin (CUR), and berberine (BER) have gained large attention in the last decade due to their multifaceted therapeutic activities. The anti-proliferative, anti-metastatic, anti-migratory, and pro-apoptotic properties of these molecules have proven their potential in the treatment of a variety of malignancies [29-35]. However, since these molecules have very low bioavailability due to poor solubility, their use in cancer therapy is limited.

The present study attempted to design and evaluate folic acid (FA) conjugates with these identified phytomolecules with proven efficacy in various types of cancer through systematic in silico and synthetic studies. Conjugation of folic acid with these anticancer agents is hypothesized to provide targeted drug delivery of these phytomolecules with increased efficacy and fewer side effects.

Experimental

Materials: All chemicals used in this study were of analytical grade. Quercetin was obtained as a gift sample from Cayman Chemical Company, USA, whereas biotin and folic acid were procured from Sigma Aldrich, Merck KGaA, Darmstadt, Germany. DCC, dimethyl amino pyridine, N-hydroxy succinimide were obtained from SD Fine Chem. Mumbai, Maharashtra, India. All other laboratory solvents and regents used in the study were purchased from Loba Chemie Pvt Ltd, Mumbai, Maharashtra, India.

Instruments used: The docking studies were carried out by using Autodock Tools and Discovery Studio was applied for the visualization and interpretation of the docking results. Melting point apparatus (Veego) was used to find melting point. Spectral analysis of the synthesized compound was carried out using UV-Visible spectrophotometer 1800 and FTIR 8400S, Make-Shimadzu. ^{1}H-NMR spectra was recorded on a Bruker Avance 400 MHz spectrometer using DMSO-d_6 as a solvent with Tetra Methyl Silane (TMS) as internal standard. The reaction completion was monitored by TLC using readymade F254 silica plates.

In Silico study:

Protein preparation: Human folate receptor (PDB ID: 4LRH) was downloaded in PDB format from RCSB protein data bank with 2.80Å resolution. The protein structure was prepared, processed and verified for missing atoms, bonds and contacts using protein preparation wizard in AutoDock 1.5.6. Then hydrogen atoms were added to the protein structure. All water molecules were erased from the protein along with ligand molecules and heteroatoms. Kolman charges were added to remove non integral charges present on amino acid in the polypeptides, 7.0 pH range was set and charged fields were added using AutoDock. Finally, the structures were refined and saved as PDBQT files for further docking studies [36, 39].

Ligand Preparation: 3D structure of phytoconstituent-vitamin conjugates were drawn using ChemDraw 18.1. 3D ligand energy minimization was performed using the MM2 method of Chem3D 18.1, and the results were saved in a PDB file. PDB file for folic acid was converted to PDBQT format using the Open Babel GUI program. The energy-minimized ligand PDBQT file was used for further docking studies [37].

Receptor grid generation: Using H-bond interactions from the PDBsum, the active pocket was located, and grid settings were determined. Grid was created by grid box in Autodock. The targeted molecule's active

location was enclosed by a cubic box. The receptor grid was then created using the following coordinates: 5.69, 20.79, and 4.05 for X, Y, and Z, respectively (by calculation method). Grid points were separated by 0.375. Maximum 10 conformers were taken into account throughout the docking process [38, 39].

Docking studies: Human folate receptor alpha (PDB ID: 4LRH) was chosen as the target protein because this receptor is overexpressed on breast cancer cells. Folic acid was selected as a reference drug, and 6 phytochemical-vitamin conjugates were chosen as ligands. The reference drug selected for docking acts as a folate receptor inhibitor. Lamarckian genetic algorithm method was used for docking. The docking process was carried out using the Autodock Vina software, and the outcomes were visualized and analyzed using the Discovery Studio Visualizer. Analysis was done based on the binding energy, bond length, interactions bond length, and participation of amino acid residues.

Pharmacokinetic predictions:

ADME/T property: To estimate each ligand's pharmacokinetic features, such as human abdominal absorption, carcinogenicity, cytochrome P inhibitory promiscuity, etc., the ADME/T profile of each ligand has been examined using the ADME/T SAR server [40-42].

P450 site of metabolism prediction: SMARTcyp web server was utilized to predict the P450 site of metabolism for each ligand molecule. This prediction provides information on the metabolism of the cytochrome P450 family of enzymes, like CYP2C9, CYP3A4, CYP2D6 [43].

Synthesis of Quercetin- Folic Acid Conjugate 1:

Scheme for synthesis of QC-FA 1 conjugate is presented in Figure 1.
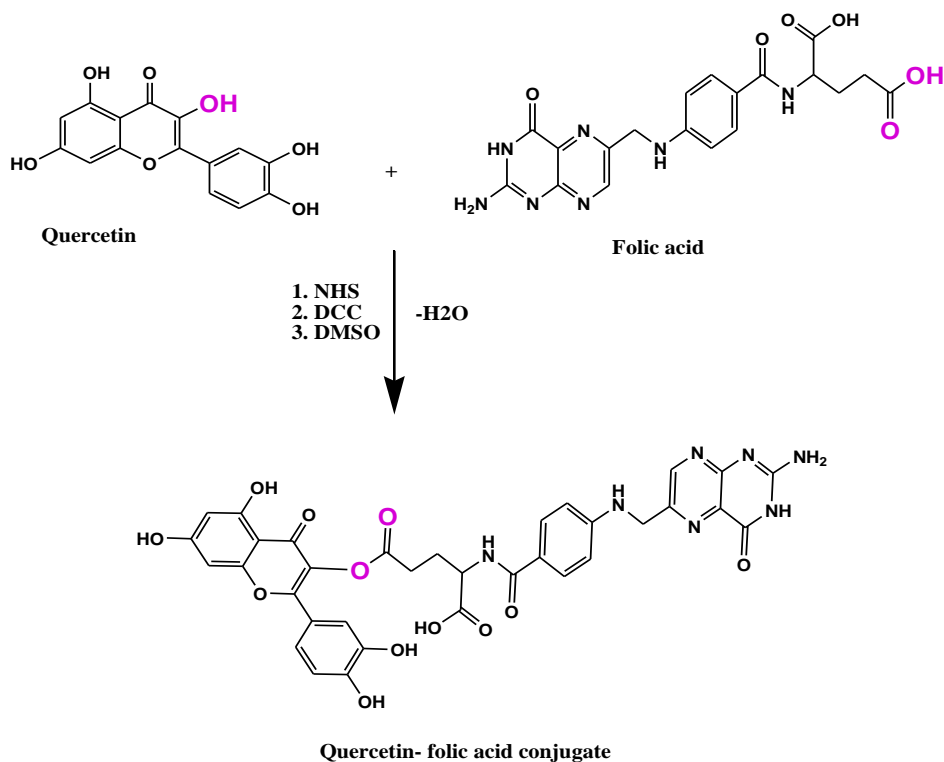
Figure 1. Reaction scheme for the synthesis of Quercetin-Folic Acid Conjugate 1

STEP 1: Activation of folic acid (FA): In a clean, dry 50 ml round bottom flask, 1.34 mmol folic acid was dissolved in 10 ml of dimethylsulphoxide (DMSO) with mild heating for about 10–15 min (time may vary as per dissolution of FA in DMSO). Then equivalent amount of N-Hydroxysuccinamide and Dicyclohexylcarbodiimide (DCC) was added in the above mixture. Reaction mixture was then stirred for 16 hours at room temperature. After which urea precipitated as dicyclohexyl urea (DCU) was filtered off to get activated folic acid.

STEP 2: Conjugation of QC and activated FA: In a round bottom flask, activated FA was added with solvent from Step 1 followed by the addition of equivalent amount of triethylamine and QC. This mixture

was then kept under continuous stirring overnight in the presence of molecular sieves, which ensure the entrapment of the water molecules generated during the synthesis process.

Physical and Spectral data of QC-FA Conjugate 1:

The physical characteristics of the synthesized conjugate, including its color, percentage yield, and melting point, were documented. Additionally, an absorption UV spectrum was obtained using a Shimadzu UV-Visible spectrophotometer-1800. The infrared (IR) spectra of the synthesized compounds were recorded using a Shimadzu 8400-S FT-IR spectrophotometer with potassium bromide. The synthesis of the conjugate was further validated through analysis using 1H-NMR and mass spectrometry techniques. The ^{1}H NMR spectra were recorded in DMSO using NMR spectrometer Bruker 400 MHz. The chemical shift values are given in parts per million, downfield from Tetra Methyl Silane (TMS) used as the internal standard. The mass spectra were recorded using BRUKER IMPACT mass analyser.

Results and Discussion

Physical and Spectral data of QC-FA Conjugate 1:

Folic acid binds to the folate receptor through the α-carboxylic acid of a glutamate residue, thus it should be free for its metabolism and function. The γ-carboxylic acid, located away from the binding site, can be modified. In order to leave the α-position unmodified, conjugation of pharmacophores to folic acid must be specific to the γ-carboxylic acid in order to maintain ligand binding affinity, thus we have selected terminal carboxyl group for modification [44]. To increase the acidic strength of folic acid as well as to ensure esterification at γ carboxyl group, we have activated folic acid as per the method described by Figliola, et al. [45]. The quercetin molecule offers five hydroxyl groups that can be modified through esterification reactions. Among these, the hydroxyl group at position 3 displays higher reactivity owing to its proximity to an adjacent carbonyl group. Existing literature supports the idea that modifying the enol hydroxyl group at position 3 enhances the stabilization of the pharmacophore, all while maintaining the antioxidant and anticancer properties of quercetin [46, 47]. Additionally, naturally occurring glycosides of quercetin utilize the 3-OH group to form glycosidic linkages [48, 49]. The above literature helps to support our hypothesis of enhanced reactivity of the 3-OH group in our study.
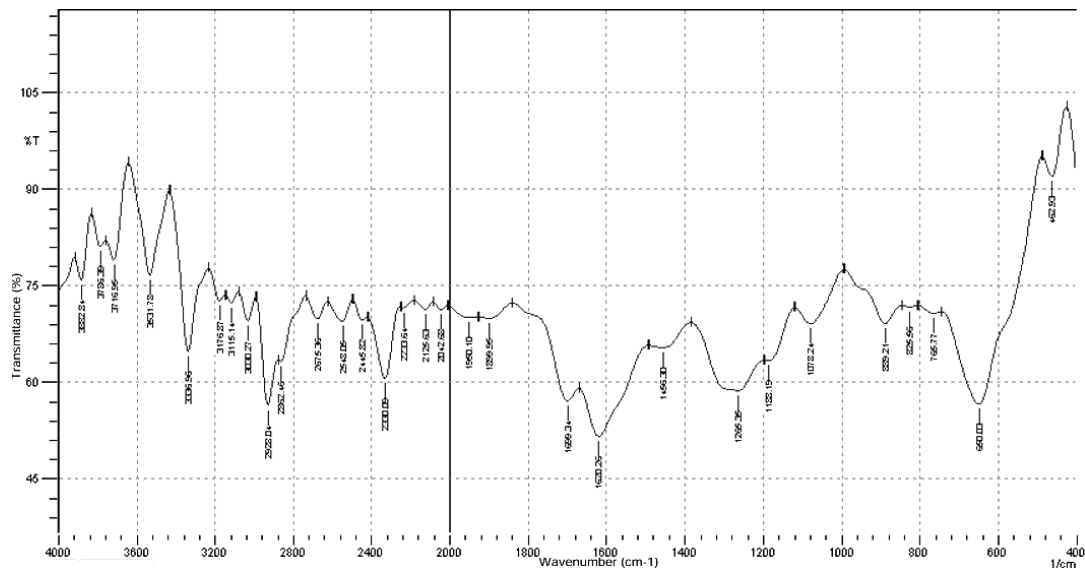
Figure 2. IR Spectrum of Quercetin-Folic Acid Conjugate 1

QC-FA Conjugate 1 was obtained as yellowish-brown powder with the yield of 67 % and melting point 213 °C. UV spectrum of the conjugate showed λ_{max} at 254.60 nm (0.669). IR (KBr, 4000–400 cm^{-1}): 3531.78 (Phenolic, O-H), 3336.96 (Amide, Asymmetrical N-H stretching), 3176.87 (Amide, Symmetrical N-H stretching), 3030.27 (Aromatic, C-H), 2938.04 (Aliphatic, C-H stretching), 1780 (Ester, C=O stretching), 1699.34 (Acid, C=O stretching), 1620.25 (Amide, C=O stretching), 1562.39 (N-H bending), 1496.30 (Aromatic, C=C), 1266 (Ester, C-O stretching), 1188.19 1078.24 (C-N stretching). The peak observed at 1780 cm^{-1} and 1266 cm^{-1} indicates the C=O ester stretching and C-O ester stretching respectively (Fig. 2). The peak of ester C=O stretching appears to be broadened due to the overlapping with the broad peak of the

acid C=O, due to the dimeric nature of carboxylic acid with intermolecular hydrogen bond formation. These two peaks give high assurance of formation of ester bond. Other functional groups are present in this spectrum confirm the formation of the QC-folic acid conjugate.

^{1}H NMR of synthesized conjugate displayed multiplet (m) from 6.2 to 7.9 ppm, representing 9 aromatic hydrogens (Ar-H) and 1 hydrogen on a pyrazine ring (pyrazine CH). A singlet (s) at 10.9 ppm, indicates a carboxylic hydroxyl group (carboxylic OH). Two singlets at 5.2 and 5.6 ppm correspond to 4 hydroxyl protons attached to the aromatic rings (Ar-OH). A multiplet from 2.08–2.24 ppm, representing 6 methylene hydrogens (Methylene CH). A triplet (t) at 4.87 ppm, revealing 1 methine hydrogen. A singlet (s) each at 4.00, 4.2 and 8.00 pm indicates the presence of the -NH$_2$, two -NH and one ring NH protons respectively. The presence of only one carboxylic hydroxyl group indicates the formation of linkage between quercetin O-H and carboxylic group of folic acid, confirming the formation of target compound.

MS: m/z (%) =725 (M+), 726 (M$^+$+1).

Molecular docking: All chosen ligands docked well with the folate receptor, demonstrating the necessary binding affinities and good binding energies. Six ligand molecules, including the BER-FA conjugate, the QC-FA conjugates 1, 2 and the CUR-FA conjugates 1, 2, and 3 was used for docking studies (Fig. 3).
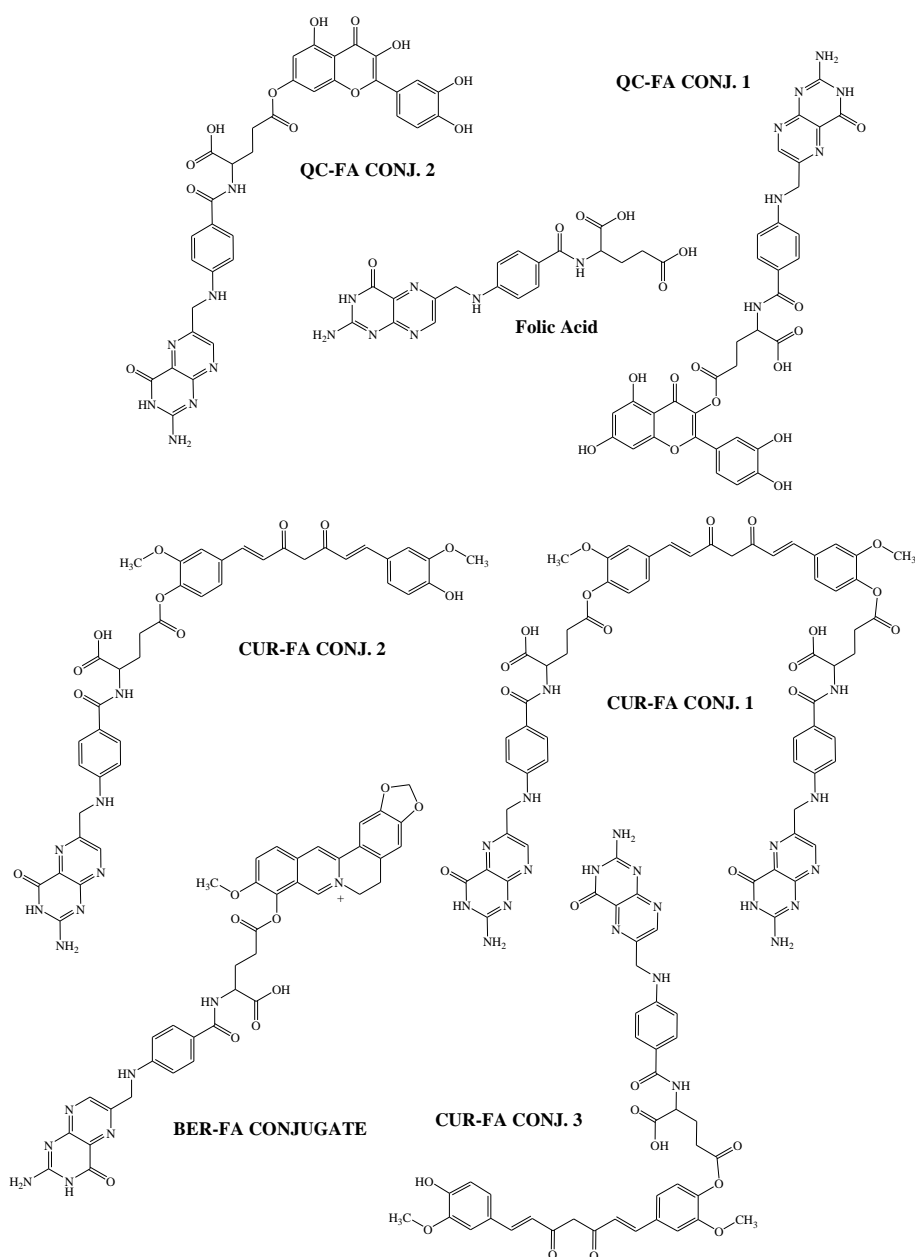
Figure 3. Structures of ligands

Reference drug FA docked in the binding site of the folate receptor with a binding energy of -10.6 kcal/mol by forming Pi-Pi bonding with amino acid Tyr60, Trp140 and hydrogen bonding with the amino acid residues Tyr60, Thr82, Arg103, Arg106, Ser 174. QC-FA conjugate 1 and BER-FA conjugate displayed highest binding energy of -12.0 and -11.2 kcal/mol respectively. QC-FA conjugate1 forms Pi-Pi bonding with Trp64, Tyr85, Trp140, Trp171 and hydrogen bonding with the amino acid residues Trp 102, Trp138 and Thr141. BER-FA conjugate displays Pi-Pi bonding with amino acid residues Tyr60, Arg61, Phe62, Trp102, Trp140, Trp171 and conventional hydrogen bonding with Arg61 and Trp102. Good binding energy through increased Pi-Pi bonding of QC-FA conjugate 1 and BER-FA conjugate indicates their affinity to the target. Other ligands showed binding energy lesser than FA, indicating lower affinity to the target. Binding energies of all ligands are summarized in Table. Figure 4 represents the docking positions and interactions with amino acids, bond distance, and type of bond.

T a b l e

Ligands with their binding energy

Sr. No.	Ligands	Target	Binding energy (kcal/mol)
1.	Folic acid (reference drug)		−10.6
2.	BER-FA conjugate		−11.2
3.	QC- FA conjugate 1		−12.0
4.	QC- FA conjugate 2	Folate receptor (PDB ID: 4LRH)	−10.3
5.	CUR- FA conjugate1		−10.4
6.	CUR- FA conjugate 2		−10.2
7.	CUR- FA conjugate 3		−10.2

Pharmacokinetic property prediction: QC-FA 1conjugate and BER-FA conjugate showed high binding energy and greater binding affinity to folate receptor. These conjugates were compared with respective phytochemicals for pharmacokinetic profile and analyzed to assess whether the conjugates showed enhanced pharmacokinetic activity than individual phytochemicals.

ADME/T Prediction: Both QC and QC-FA 1 conjugate showed impermeability to the Blood Brain Barrier (BBB). BER showed permeability to BBB while BER-FA conjugate demonstrated impermeability to the BBB, indicating absence of Central Nervous System (CNS) side effects. Both the conjugates showed non-substrate activity to CYP450 2C9 and 2D6 enzymes, non- inhibitor activity to CYP450 2C9, 2C19, and 3A4 enzymes indicating slower metabolism and increased half life. CYP Inhibitory Promiscuity (capacity for a drug to bind to and decrease or diminished the activity of multiple different CYP450 isoform) of both the conjugates was found to be satisfactory. All of them showed no AMES toxicity and were non-carcinogenic. QC exhibited type II acute oral toxicity which was not exhibited by its conjugate indicating its safety.

Prediction of the P450 site of metabolism: P450 metabolism prediction of QC and BER was compared with their conjugates, QC-FA 1 and BER-FA conjugate respectively. Carbon 13, 15 and 2 of QC were the most prominent atoms with low enzyme score for all three enzymes of CYP450 family, which gives strong knowledge of being catalyzed by using 3A4, 2D6 and 2C9 enzyme. On other hand, carbon 28, nitrogen 37 and 27 of QC-FA 1 conjugate molecule shows lowest enzyme score. However, the site for metabolism of QC-FA 1 involved carbon atoms present on FA structure indicating the metabolite stability of amide linkage in the complex. For BER, carbon 22, 1 and 25 represent lowest enzyme score. Considering enzyme score, energy and 2D solvent accessible surface area (2DSASA), these atoms are responsible for BER metabolism. Carbon 20, 29 and 46 of BER-FA conjugate shows lowest enzyme score of which carbon 46 is present in BER structure and carbon 20, 29 presents in folic acid structure. While, carbon 1 and 25 were absent in conjugate's metabolism data indicating metabolic stability of conjugate. This supports the hypothesis that the designed conjugates will internalize into the tumor cells through endocytosis after binding to the receptor, thereby improving specificity to the tumor cells.
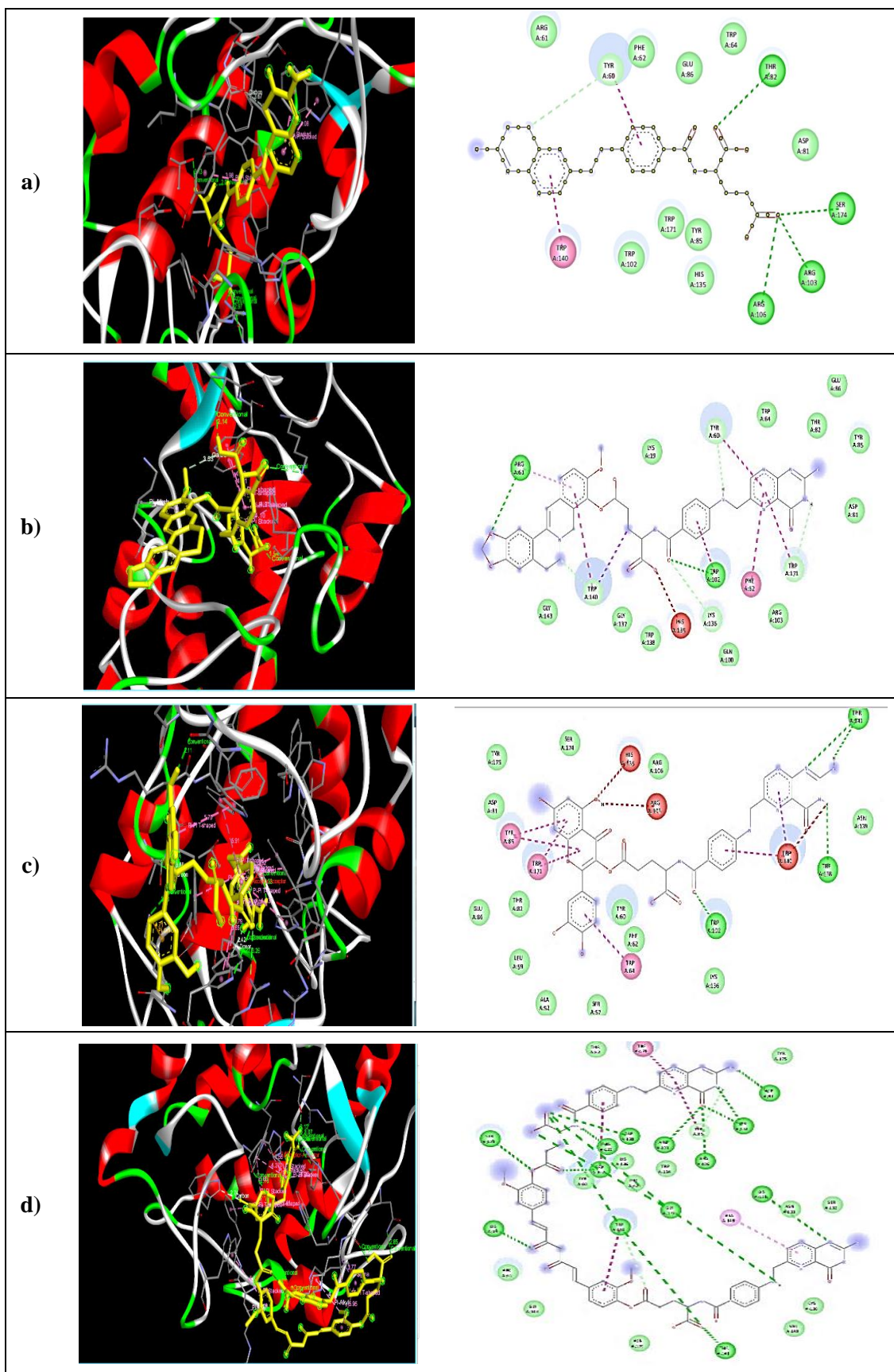
Figure 4. *a*) Standard FA docked to Human folate receptor alpha; *b*) Human folate receptor alpha is docked with a BER-FA conjugate; *c*) Human folate receptor alpha is docked with QC-FA conjugate 1; *d*) Human folate receptor alpha is docked CUR- FA conjugate 1

Conclusions

The conventional chemotherapeutic drugs exhibit undesirable side effects that may damage the healthy cells, including those in the gastrointestinal tract, bone marrow, and hair follicles. However, phytomolecules like curcumin, quercetin and berberine with proven anti-cancer potential can be employed for cancer therapeutics. However, their utilization is limited due to their poor bioavailability. Therefore, higher doses of phytomolecules required to achieve a therapeutic response may lead to toxicity and other side effects. To achieve improved bioavailability with improved tumor cells specificity, quercetin, berberine and curcumin were complexed with folic acid. The conjugates demonstrated favorable affinity for the human folate receptor, with the QC-FA1 conjugate showing higher binding affinity (–12 kcal/mol) than standard folic acid (–10.6 kcal/mol). The QC-FA1 conjugate also displayed satisfactory pharmacokinetic and safety predictions with reduced cytochrome susceptibility indicating stability of complex, supporting the concept of receptor mediated endocytosis in tumor cells. Further QC-FA1 conjugate was successfully synthesized, characterized using suitable chromatographic and spectroscopic tools and will be subsequently tested for its anti-cancer potential.

The successful design and synthesis of the QC-FA1 conjugate may act as a novel pro-drug, improving specificity to cancer cells, thereby reducing the undesirable side effects and bioavailability problems associated with its use. This study open development prospects for the identification and synthesis of newer phytomolecules based therapeutics for addressing the rising concerns associated with chemical-based agents. This novel but simplified approach of design of vitamin-phytomolecule conjugates can be further explored and studied to better understand its effective role in revolutionizing cancer therapeutics.

Acknowledgments

References

1   Debela, D.T., Muzazu, S.G., Heraro, K.D., Ndalama, M.T., Mesele, B.W., Haile, D.C., Kitui, S.K., & Manyazewal, T. (2021) New approaches and procedures for cancer treatment: Current perspectives. *SAGE open medicine, 9.* https://doi.org/10.1177/20503121211034366

2   Sung, H., Ferlay, J., Siegel, R. L., Laversanne, M., Soerjomataram, I., Jemal, A., et al. (2021). Global Cancer Statistics 2020: GLOBOCAN Estimates of Incidence and Mortality Worldwide for 36 Cancers in 185 Countries. *CA Cancer J. Clin. 71*, 209–249. https://doi.org/10.3322/caac.21660

3   What is Cancer? https://www.cancer.gov/about-cancer/understanding/what-is-cancer, Accessed on October 10, 2023.

4   Allen, T.M. (2002). Ligand-targeted therapeutics in anticancer therapy. *Nature Reviews Cancer, 2(10)*, 750–763. https://doi.org/10.1038/nrc903

5   Chari, R.V.J. (1998). Targeted delivery of chemotherapeutics: Tumor-activated prodrug therapy. *Advanced Drug Delivery Reviews, 31(1)*, 89–104. https://doi.org/10.1016/S0169-409X(97)00095-1

6   Ojima, I., Geng, X., Wu, X., Qu, C., Borella, C.P., & Xie, H.et al. (2002). Tumor-Specific Novel Taxoid−Monoclonal Antibody Conjugates. *Journal of Medicinal Chemistry, 45(26)*, 5620–5623. https://doi.org/10.1021/jm025540g

7   Jaracz, S., Chen, J., Kuznetsova, L. V., & Ojima, I. (2005). Recent advances in tumor-targeting anticancer drug conjugates. *Bioorganic & Medicinal Chemistry, 13(17)*, 5043–5054. https://doi.org/10.1016/j.bmc.2005.04.084

8   Yan, Y., Dong, Y., Yue, S., Qiu, X., Sun, H., & Zhong, Z. (2019). Dually Active Targeting Nanomedicines Based on a Direct Conjugate of Two Purely Natural Ligands for Potent Chemotherapy of Ovarian Tumors. *ACS Applied Materials & Interfaces, 11(50)*, 46548–46557. https://doi.org/10.1021/acsami.9b17223

9   Zhong, Y., Meng, F., Deng, C., & Zhong, Z. (2014). Ligand-Directed Active Tumor-Targeting Polymeric Nanoparticles for Cancer Chemotherapy. *Biomacromolecules, 15(6)*, 1955–1969. https://doi.org/10.1021/bm5003009

10   Zagami, R., Rapozzi, V., Piperno, A., Scala, A., Triolo, C., & Trapani, M.et al. (2019). Folate-Decorated Amphiphilic Cyclodextrins as Cell-Targeted Nanophototherapeutics. *Biomacromolecules, 20(7)*, 2530–2544. https://doi.org/10.1021/acs.biomac.9b00306

11   Sun, H., Dong, Y., Feijen, J., & Zhong, Z. (2018). Peptide-decorated polymeric nanomedicines for precision cancer therapy. *Journal of Controlled Release, 290*, 11–27. https://doi.org/10.1016/j.jconrel.2018.09.029

12   Jiang, Z., Guan, J., Qian, J., & Zhan, C. (2019). Peptide ligand-mediated targeted drug delivery of nanomedicines. *Biomaterials Science, 7(2)*, 461–471. https://doi.org/10.1039/C8BM01340C

13   Srinivasarao, M., Galliford, C.V., & Low, P.S. (2015). Principles in the design of ligand-targeted cancer therapeutics and imaging agents. *Nature Reviews Drug Discovery, 14(3)*, 203–219. https://doi.org/10.1038/nrd4519

14 Srinivasarao, M., & Low, P.S. (2017). Ligand-Targeted Drug Delivery (world) [Review-article]. *American Chemical Society.* https://doi.org/10.1021/acs.chemrev.7b00013

15 Muro, S. (2012). Challenges in design and characterization of ligand-targeted drug delivery systems. *Journal of Controlled Release, 164(2)*, 125–137. https://doi.org/10.1016/j.jconrel.2012.05.052

16 Ojima, I. (2008). Guided Molecular Missiles for Tumor-Targeting Chemotherapy — Case Studies Using the SecondGeneration Taxoids as Warheads. *Accounts of Chemical Research, 41(1)*, 108–119. https://doi.org/10.1021/ar700093f

17 Russell-Jones, G., McTavish, K., McEwan, J., Rice, J., & Nowotnik, D. (2004). Vitamin-mediated targeting as a potential mechanism to increase drug uptake by tumours. *Journal of Inorganic Biochemistry, 98(10)*, 1625–1633. https://doi.org/10.1016/j.jinorgbio.2004.07.009

18 Chen, S., Zhao, X., Chen, J., Chen, J., Kuznetsova, L., Wong, S.S., & Ojima, I. (2010). Mechanism-Based Tumor-Targeting Drug Delivery System. Validation of Efficient Vitamin Receptor-Mediated Endocytosis and Drug Release. *Bioconjugate Chemistry, 21(5)*, 979–987. https://doi.org/10.1021/bc9005656

19 Leamon, C.P., & Reddy, J.A. (2004). Folate-targeted chemotherapy. *Advanced Drug Delivery Reviews, 56(8)*, 1127–1141. https://doi.org/10.1016/j.addr.2004.01.008

20 Lu, Y., & Low, P.S. (2002). Folate-mediated delivery of macromolecular anticancer therapeutic agents. *Advanced Drug Delivery Reviews, 54(5)*, 675–693. https://doi.org/10.1016/S0169-409X(02)00042-X

21 Reddy, J.A., Westrick, E., Vlahov, I., Howard, S.J., Santhapuram, H.K., & Leamon, C.P. (2006). Folate receptor specific antitumor activity of folate–mitomycin conjugates. *Cancer Chemotherapy and Pharmacology, 58(2)*, 229–236. https://doi.org/10.1007/s00280-005-0151-z

22 Leamon, C.P., Reddy, J.A., Vlahov, I.R., Vetzel, M., Parker, N., Nicoson, J.S., Xu, L.-C., & Westrick, E. (2005). Synthesis and Biological Evaluation of EC72: A New Folate-Targeted Chemotherapeutic. *Bioconjugate Chemistry, 16(4)*, 803–811. https://doi.org/10.1021/bc049709b

23 Shi, H., Guo, J., Li, C., & Wang, Z. (2015). A current review of folate receptor alpha as a potential tumor target in non-smallcell lung cancer. *Drug Design, Development and Therapy, 9*, 4989–4996. https://doi.org/10.2147/DDDT.S90670

24 Zhao, X., Li, H., & Lee, R.J. (2008). Targeted drug delivery via folate receptors. *Expert Opinion on Drug Delivery, 5(3)*, 309–319. https://doi.org/10.1517/17425247.5.3.309

25 Low, Philip Stewart, & Kularatne, S.A. (2009). Folate-targeted therapeutic and imaging agents for cancer. *Current Opinion in Chemical Biology, 13(3)*, 256–262. https://doi.org/10.1016/j.cbpa.2009.03.022

26 Bhole, R. P., Yogita, S., Bonde, C. G., & Wavhale, R. D. (2021). Vitamin Drug conjugate: a systematic review of pharmacological potential. *Bulletin of the University of Karaganda — Chemistry*, *(1)*, 27–52. https://doi.org/10.31489/2021Ch1/27-52

27 Newman, D. J., & Cragg, G. M. (2016). Natural products as sources of new drugs from 1981 to 2014. *Journal of natural products*, *79*(3), 629-661.https://doi.org/10.1021/acs.jnatprod.5b01055

28 Shaikh, S., Shaikh, J., Naba, Y. S., Doke, K., Ahmed, K., & Yusufi, M. (2021). Curcumin: Reclaiming the lost ground against cancer resistance. *Cancer Drug Resistance*, *4*(2), 298. http://dx.doi.org/10.20517/cdr.2020.92

29 Kashyap, A., Umar, S. M., Mendiratta, M., & Prasad, C. P. (2022). In vitro anticancer efficacy of a polyphenolic combination of Quercetin, Curcumin, and Berberine in triple negative breast cancer (TNBC) cells. *Phytomedicine Plus*, *2*(2), 100265. https://doi.org/10.1016/j.phyplu.2022.100265

30 Shaikh, S., Shaikh, J., Naba, Y. S., Doke, K., Ahmed, K., & Yusufi, M. (2021). Curcumin: Reclaiming the lost ground against cancer resistance. *Cancer Drug Resistance*, *4*(2), 298. https://doi.org/10.20517 %2Fcdr.2020.92

31 Vyas, A., Dandawate, P., Padhye, S., Ahmad, A., & Sarkar, F. (2013). Perspectives on new synthetic curcumin analogs and their potential anticancer properties. *Current pharmaceutical design*, *19*(11), 2047–2069. https://doi.org/10.2174/138161213805289309

32 Dandawate, P. R., Vyas, A., Ahmad, A., Banerjee, S., Deshpande, J., Swamy, K. V.,... & Sarkar, F. H. (2012). Inclusion complex of novel curcumin analogue CDF and β-cyclodextrin (1: 2) and its enhanced in vivo anticancer activity against pancreatic cancer. *Pharmaceutical research*, *29*, 1775-1786. https://doi.org/10.1007/s11095-012-0700-1

33 De Paz, E., Martin, A., Every, H., & Cocero, M. J. (2015). Production of water-soluble quercetin formulations by antisolvent precipitation and supercritical drying. *The Journal of Supercritical Fluids*, *104*, 281–290.https://doi.org/10.1016/j.supflu.2015.07.006

34 Wong, M. Y., & Chiu, G. N. (2011). Liposome formulation of co-encapsulated vincristine and quercetin enhanced antitumor activity in a trastuzumab-insensitive breast tumor xenograft model. *Nanomedicine: Nanotechnology, Biology and Medicine*, *7*(6), 834-840. https://doi.org/10.1016/j.nano.2011.02.001

35 Xiong, R. G., Huang, S. Y., Wu, S. X., Zhou, D. D., Yang, Z. J., Saimaiti, A., ... & Li, H. B. (2022). Anticancer effects and mechanisms of berberine from medicinal herbs: An update review. *Molecules*, *27*(14), 4523. https://doi.org/10.3390/molecules27144523

36 Trott, O., & Olson, A. J. (2010). AutoDock Vina: improving the speed and accuracy of docking with a new scoring function, efficient optimization, and multithreading. *Journal of computational chemistry*, *31*(2), 455-461. https://doi.org/10.1002/jcc.21334

37 Spessard, G.O. (1998) ACD Labs/LogP dB 3.5 and ChemSketch 3.5. *Journal of Chemical Information and Computer Sciences, 38*, 1250–1253. https://doi.org/10.1021/ci980264t

38 Ullah, A., Prottoy, N. I., Araf, Y., Hossain, S., Sarkar, B., & Saha, A. (2019). Molecular docking and pharmacological property analysis of phytochemicals from Clitoria ternatea as potent inhibitors of cell cycle checkpoint proteins in the cyclin/CDK pathway in cancer cells. *Computational Molecular Bioscience*, *9(03),* 81.http://dx.doi.org/10.4236/cmb.2019.93007

39 Zeleke, D., Eswaramoorthy, R., Belay, Z., & Melaku, Y. (2020). Synthesis and antibacterial, antioxidant, and molecular docking analysis of some novel quinoline derivatives. *Journal of Chemistry*, 1–16. https://doi.org/10.1155/2020/1324096

40 Daina, A., Michielin, O., & Zoete, V. (2017). SwissADME: a free web tool to evaluate pharmacokinetics, drug-likeness and medicinal chemistry friendliness of small molecules. *Scientific reports*, *7(1)*, 42717. https://doi.org/10.1038/srep42717

41 Lipinski, C.A. (2004) Lead-and Drug-Like Compounds: The Rule-of-Five Revolution. *Drug Discovery Today: Technologies, 1*, 337-341. https://doi.org/10.1016/j.ddtec.2004.11.007

42 Li, A.P. (2001) Screening for human ADME/Tox drug properties in drug discovery. *Drug Discovery Today, 6*, 357–366. https://doi.org/10.1016/S1359-6446(01)01712-3

43 Guengerich, F.P. (1999) Cytochrome P-450 3A4: Regulation and role in drug metabolism. *Annual Review of Pharmacology and Toxicology, 39*, 1-17. https://doi.org/10.1146/annurev.pharmtox.39.1.1

44 Geersing, A., de Vries, R. H., Jansen, G., Rots, M. G., Roelfes, G. (2019) Folic acid conjugates of a bleomycin mimic for selective targeting of folate receptor positive cancer cells. *Bioorganic & medicinal chemistry letters, 29(15)*, 1922–1927. https://doi.org/10.1016/j.bmcl.2019.05.047

45 Figliola, C., Marchal, E., Groves, B. R., Thompson, A. (2019) A step-wise synthetic approach is necessary to access γ-conjugates of folate: folate-conjugated prodigiosenes. *RSC advances, 9(25),* 14078–14092. https://doi.org/10.1039/c9ra01435g

46 Pechinskii, S.V., Kuregyan, A. G., Oganesyan, E. T. (2023) Regioselective synthesis of quercetin and myricetin derivatives. *Russ J Gen Chem*. *93*, 245-252. https://doi.org/10.1134/s1070363223020032

47 Elmegerhi, S., Su, C., Buglewicz, D. J., Aizawa, Y., Kato, T. A. (2018) Effect of hydroxyl group position in flavonoids on inducing single-stranded DNA damage mediated by cupric ions. *International journal of molecular medicine, 42(1)*, 658–664. https://doi.org/10.3892/ijmm.2018.3615

48 Dueñas, M., Surco-Laos, F., González-Manzano, S., González-Paramás, A. M., Gómez-Orte, E., Cabello, J., Santos-Buelga, C. (2013) Deglycosylation is a key step in biotransformation and lifespan effects of quercetin-3-O-glucoside in Caenorhabditis elegans. *Pharmacological research, 76*, 41–48. https://doi.org/10.1016/j.phrs.2013.07.001

49 Panda, S., Kar, A. (2007) Antidiabetic and antioxidative effects of Annona squamosa leaves are possibly mediated through quercetin-3-O-glucoside. *BioFactors, 31(3-4)*, 201–210. https://doi.org/10.1002/biof.5520310307

Information about authors*

Mandale, Vijaya R. — Post Graduate Research Scholar, Department of Pharmaceutical Chemistry, Dr. D.Y. Patil Institute of Pharmaceutical Sciences and Research, Pimpri, Pune-411018, Maharashtra, India

Thomas, Asha Byju (*corresponding author*) — Professor and Head, Department of Pharmaceutical Chemistry, Dr. D.Y. Patil Institute of Pharmaceutical Sciences and Research, Pimpri, Pune-411018, Maharashtra, India; e-mail:asha.thomas@dypvp.edu.in; https://orcid.org/0000-0003-1058-8779

Jadhav, Pranali A. — PhD Scholar, Department of Pharmaceutical Chemistry, Dr. D.Y. Patil Institute of Pharmaceutical Sciences and Research, Pimpri, Pune-411018, Maharashtra, India; e-mail: pranali.jadhav@dypvp.edu.in, https://orcid.org/0000-0001-7956-3268

Patil, Chandrajyoti Y. — Post Graduate Research Scholar, Department of Pharmaceutical Chemistry, Dr. D.Y. Patil Institute of Pharmaceutical Sciences and Research, Pimpri, Pune-411018, Maharashtra, India; e-mail:patilchandrajyoti@gmail.com, https://orcid.org/0000-0002-6030-1353

Bhole, Ritesh Prakash — Associate Professor, Department of Pharmaceutical Chemistry, Dr. D.Y. Patil Institute of Pharmaceutical Sciences and Research, Pimpri, Pune-411018, Maharashtra, India; e-mail: ritesh.bhole@dypvp.edu.in; https://orcid.org/0000-0003-4088-7470

*The author's name is presented in the order: *Last Name, First and Middle Names*

PHYSICAL AND ANALYTICAL CHEMISTRY

Abel K. Oyebamiji[1*] [ID], Faith E. Olujinmi[1] [ID], Emmanuel T. Akintayo[1,2] [ID],
Cecilia O. Akintayo[1,3] [ID], Sunday A. Akintelu [4] [ID], Banjo Semire[5] [ID],
Jonathan O. Babalola[1,6] [ID], Felix Okunlola[7] [ID], Bolanle M. Olawoye[8] [ID]

[1]Industrial Chemistry Programme, Bowen University, Iwo, Osun State, Nigeria;
[2]Department of Chemistry, Ekiti State University, Ado-Ekiti, Ekiti State, Nigeria;
[3]Department of Chemistry, Federal University, Oye-Ekiti, Ekiti State, Nigeria;
[4]School of Chemistry and Chemical Engineering, Beijing Institute of Technology, Beijing, China;
[5]Computational Chemistry Research Laboratory, Department of Pure and Applied Chemistry,
Ladoke Akintola University of Technology, Ogbomoso, Oyo State, Nigeria;
[6]Department of Chemistry, University of Ibadan, Ibadan, Oyo State, Nigeria;
[7]Department of Natural Sciences, Faculty of Pure and Applied Sciences, Precious Cornerstone University, Ibadan, Nigeria;
[8]Department of Basic Sciences, Adeleke University, Ede, Nigeria
(Corresponding author's e-mail: abel.oyebamiji@bowen.edu.ng)

Potential Inhibiting activities of Phytochemicals from *Enantia chlorantia* Bark Against Lactate Dehydrogenase: *in Silico* Approach

Malaria is a serious ailment, and it remains a serious challenge for global health organisations. The establishment of unconventional drugs to fight this ailment has drawn the attention of several researchers. In this work, selected phytochemicals from *Enantia chlorantia* bark as potential anti-lactate dehydrogenase were investigated using *in silico* approach. A number of softwares were used in this study namely: Spartan 14 for optimization, Pymol for treating the downloaded receptor, Autodock tool for identifying the active site of the target, Autodock Vina for docking calculation and Discovery Studio visualizer for observing the non-bonding interaction of the studied complex. The calculated descriptors from the optimized *Enantia chlorantia* bark phytochemicals described their anti-lactate dehydrogenase activities. Compounds **2, 4, 9, 15, 16** and **17** demonstrated higher binding affinity (in terms of negativity) than other studied compounds and the reference drug (Quinine). This predicts that they have a higher ability to inhibit lactate dehydrogenase downregulate malaria. Also, (1*R*,4*aS*,8*aS*)-7-methyl-4-methylidene-1-propan-2-yl-2,3,4*a*,5,6,8*a*-hexahydro-1*H*-naphthalene (compound **15**) showed higher values inhibition of lactate dehydrogenase than other studied compounds and reference drug Quinine. The developed quantitative structure-activity relationship model using binding affinity as a dependent variable proved to be predictive and this can help in the subsequent study.

Keywords: Lactate Dehydrogenase, Phytochemicals, *Enantia chlorantia*, *In Silico*, Malaria, Docking, Bark, Drug.

Introduction

Malaria, one of the most difficult to dare parasitic sicknesses, remains the disease with devastating effects in many countries globally [1]. A few years ago, above 210 million malaria cases and hundreds of thousands of malaria death cases were observed and reported by scientists [2, 3]. According to Schlitzer, 2008 [4], malaria in human beings could be attributed to *P. falciparum*, *P. knowlesi, P. ovale*, *P. vivax*, and *P. malariae*. Several synthesized drugs to cure malaria have significantly reduced malaria mortality [5]. According to Mutabingwa, 2005 [6], Artemisinin Combination therapy was recommended by World Health

Organization for proper combat against malaria, and in recent time, the call to overcome drug resistivity has attracted the attention of researchers, leading to the development of several potent antimalaria drugs such as artemether, lumefantrine [7]. Despite the efficiency of the synthesized drugs to fight the existence of malaria among humans, the case of anti-malaria drug resistivity in many part of Africa is still on the high side and this has necessitated the development of more potent antimalaria agents than the commercial drugs [8]. Moreover, the production of hundreds of drugs from over eighty-five medicinal plants has been carried out, which may be due to its easy accessibility, efficiency, as well as their mode of action in the human body system [9–11].

Two *Plasmodium* genus (*P. falciparum* and *P. vivax*) were the root cause of many malaria among humans [12–14]. Meanwhile, the mode of action of *P. falciparum* has led to the highest mortality compared to others [15]. Several malaria cases with the greatest number of mortality due to malaria have been observed and reported in Africa. The use of chemical compounds to combat this life-threatening disease (Malaria) has been employed by many scientists; however, resistance to antimalarial drugs remains a serious challenge, and this has called for more potent drug-like compounds as a lasting solution to this menace in the medical world [16–20].

Lactate dehydrogenase is a crucial proteinous compound that plays a significant role in all living cells [21]. It has been observed to be a usual target in malaria and it played a crucial role in the anaerobic existence of Plasmodium falciparum [22]. Any molecular drug-like compound with enough potency to hinder Plasmodium falciparum lactate dehydrogenase will destroy the Plasmodium falciparum in human body system [23]. It helps in transporting hydride among molecular compounds, and a series of health conditions such as liver disease, anemia, heart attack, muscle trauma, cancers, and HIV have been reported to increase lactate dehydrogenase in any living cell [24]. According to Garcia *et al*., 2014 [25], lactate in living beings can be increased by raising the level of glucose absorption, and this has attracted the attention of researchers globally.

Enantia chlorantha has been classified to the annonaceae family. Different names have been given to this tree based on different cultures, such as Dokitaigbo, Kakerim and Erenba-vbogo Yoruba, Boki, and Benin, respectively [26, 27]. It is a tree with yellow wood, 28 m high, and many researchers report that in Africa it can be found in tropical forests [28]. Every part (leaves, root and bark) of the tree has been observed and reported to be medicinal in treating diseases like malaria, typhoid fever, etc. [29]. Also, several biologically active compounds were found in *Enantia chlorantha,* which has reportedly given it exceptional medicinal value for humans [30]. Thus, the purpose of this work is to study the inhibiting capacity of phytochemicals from *Enantia chlorantia* bark against lactate dehydrogenase [31], as well as to identify their descriptors responsible for anti-lactate dehydrogenase activity.
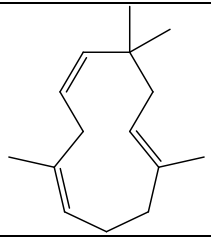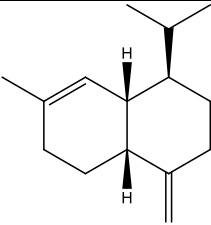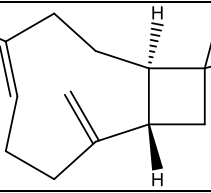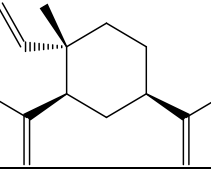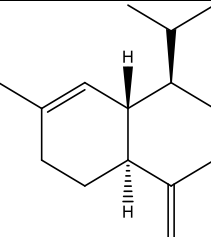
Experimental

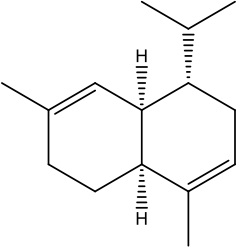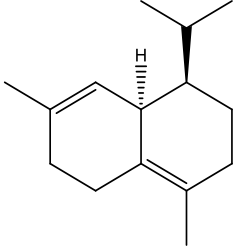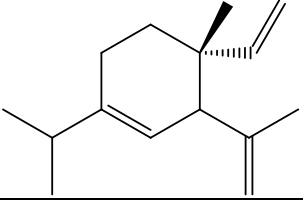### *Ligand Preparation via Quantum chemical method*

Eighteen phytochemicals (Table 1) from *Enantia chlorantia* bark were subjected to Spartan 14 software for geometry optimization [32]. The appropriate elements were bonded together according to the chemical formula for each compound using 6-31G* as basis set. The time required to complete processing of each compound is a function of the composition of each compound coupled with the basis set used. A series of activity descriptors for the studied compounds were obtained using Spartan 14 software and included: highest occupied molecular orbital energy (E_{HOMO}), lowest unoccupied molecular orbital energy (E_{LUMO}), bandgap (BG), dipole moment (DM), molecular weight (MW), lipophilicity (LogP), ovality, polar surface area (PSA), polarizability, hydrogen bond donor (HBD), and hydrogen bond acceptor (HBA). The studied compounds are presented in Table 1.

Studied phytochemicals obtained from *Enantia chlorantia* bark
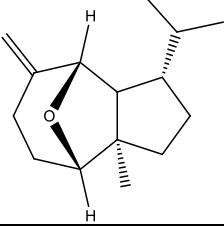
No.	Structures	IUPAC Names
1		(1*S*,2*R*,5*S*,7*S*)-2-methyl-8-methylidene-5-propan-2-yl-11-oxatricyclo[5.3.1.0^{2,6}]undecane
2		1,6-dimethyl-4-propan-2-ylnaphthalene
3		(1*R*,4*R*,6*R*,10*S*)-4,12,12-trimethyl-9-methylidene-5-oxatricyclo[8.2.0.0^{4,6}]dodecane
4		(1*E*,6*E*)-1-methyl-5-methylidene-8-propan-2-ylcyclodeca-1,6-diene
5		(1*R*,3*E*,7*E*,11*R*)-1,5,5,8-tetramethyl-12-oxabicyclo[9.1.0]dodeca-3,7-diene
6		(1*S*,3*aR*,8*aS*)-3*a*-methyl-7-methylidene-1-propan-2-yl-2,3,5,6,8,8*a*-hexahydro-1*H*-azulen-4-one
7		(1*aR*,4*aR*,7*S*,7*aR*,7*bR*)-1,1,7-trimethyl-4-methylidene-1*a*,2,3,4*a*,5,6,7*a*,7*b*-octahydrocyclopropa[h]azulen-7-ol
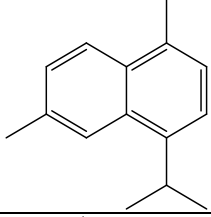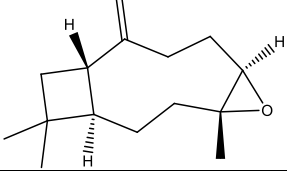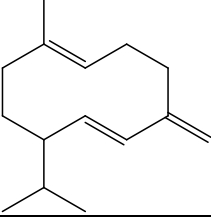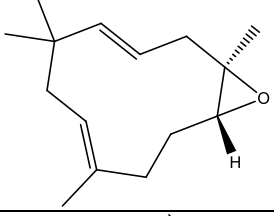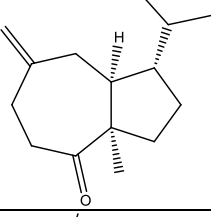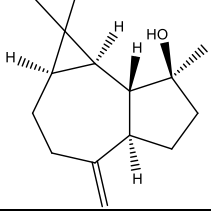
No.	Structures	IUPAC Names
8		(1*R*,4*S*,4*aR*,8*aR*)-1,6-dimethyl-4-propan-2-yl-3,4,4*a*,7,8,8*a*-hexahydro-2*H*-naphthalen-1-ol
9		(1*R*,5*S*,6*R*,7*S*,10*R*)-4,10-dimethyl-7-propan-2-yltricyclo[4.4.0.0^{1,5}]dec-3-ene
10		(1*aR*,4*R*,4*aR*,7*bS*)-1,1,4,7-tetramethyl-1*a*,2,3,4,4*a*,5,6,7*b*-octahydrocyclopropa[e]azulene
11		(1*Z*,4*Z*,8*E*)-2,6,6,9-tetramethylcycloundeca-1,4,8-triene
12		(1*R*,4*aR*,8*aS*)-7-methyl-4-methylidene-1-propan-2-yl-2,3,4*a*,5,6,8*a*-hexahydro-1*H*-naphthalene
13		(1*R*,4*E*,9*S*)-4,11,11-trimethyl-8-methylidenebicyclo[7.2.0]undec-4-ene
14		(1*S*,2*S*,4*R*)-1-ethenyl-1-methyl-2,4-bis(prop-1-en-2-yl)cyclohexane
15		(1*R*,4*aS*,8*aS*)-7-methyl-4-methylidene-1-propan-2-yl-2,3,4*a*,5,6,8*a*-hexahydro-1*H*-naphthalene
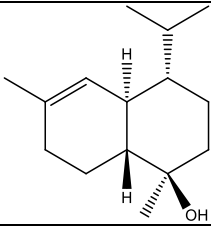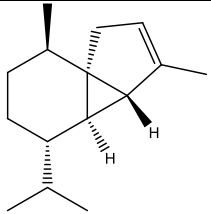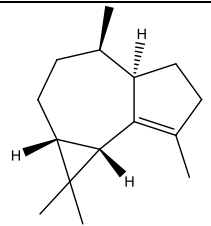
No.	Structures	IUPAC Names
16		(1*S*,4a*S*,8a*R*)-4,7-dimethyl-1-propan-2-yl-1,2,4a,5,6,8a-hexahydronaphthalene
17		(1*R*,8a*R*)-4,7-dimethyl-1-propan-2-yl-1,2,3,5,6,8a-hexahydronaphthalene
18		(4*R*)-4-ethenyl-4-methyl-1-propan-2-yl-3-prop-1-en-2-ylcyclohexene

Preparation of Studied Ligands and Receptor for Molecular Docking
Preparation of the Studied Phytochemicals

The optimized structures were converted from .spartan to .pdb format using Spartan software. Before Autodock Vina docking calculation the .pdb format of the studied phytochemicals was converted to the .pdbqt format using Autodock Tool software.

Preparation of the Lactate Dehydrogenase for Docking Study

The downloaded lactate dehydrogenase structure (PDB ID: 1LDG) (Fig. 1) [31] from the Protein Data Bank was processed using Pymol software to identify any extraneous molecules (small molecules and water molecules) downloaded with the desired protein. Other molecules downloaded with lactate dehydrogenase were removed and subjected to Autodock Tool software to locate the appropriate binding site for the studied compounds. The calculated value for the centre and binding site in X, Y and Z directions that show the located binding site were 27.729 Å, 16.305 Å, and 36.464 Å for the centre and 66Å, 56 Å and 66 Å for site (Fig. 2). The binding affinity for the studied complex was determined using Autodock Vina software.
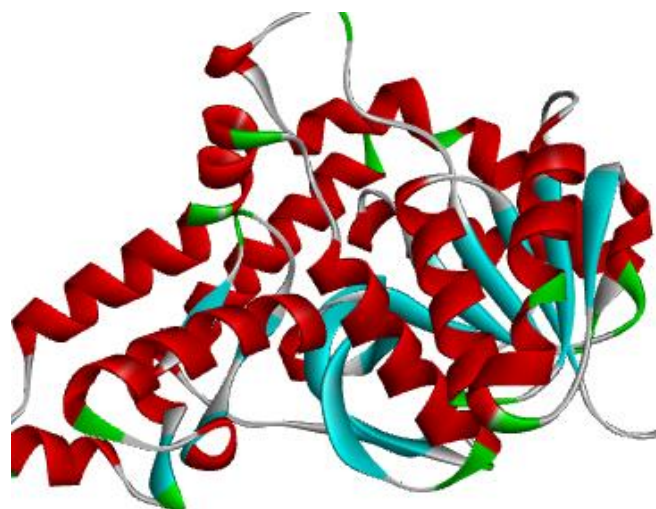
Figure 1. 3D structure of lactate dehydrogenase (PDB ID: 1LDG)

Figure 2. 3D structure of lactate dehydrogenase (PDB ID: 1LDG) with binding site located

Molecular Dynamic Simulation Study

In this work, compound **15** with the lowest binding affinity and reference drug (quinine) were subjected to molecular dynamics simulation using AMBER14 molecular dynamics package [33]. Hydrogen atoms were added to the complexes under study via a leap sector of AMBER14. AMBER force field 99SB was used for the protein while general AMBER force field was used for ligand [34, 35]. Appropriate number of counterions were added so as to neutralize the investigated complexes before solvation which was executed in a condensed octahedral cell of TIP3P [36] water molecules, and 12˚A was overextended beyond the protein.

Moreover, 5000 frames of steepest descent minimization were used for minimization, and 10000 frames of conjugated gradient minimization were also employed in order to eradicate unwanted atom interactions. The temperature used for the entire system was 300K at 100ns and the study was executed at 1 atm via the particle mesh Ewald method [37]. Also, molecular dynamics trajectories analysis was executed via CPPTRAJ module [34].

Quantitative Structure-activity Relationship (QSAR) Study

The optimized compounds were converted to .sdf format before subjecting to PaDEL (Pharmaceutical Data Exploration Laboratory) version 2.21 to generate 2D descriptors [38, 39]. For reliability, the studied compounds were divided into two different sets ((training set (80%) and test set (20%)), and the training set compounds were subjected to Material Studio software to develop a valid QSAR model via genetic function algorithm (Equation 1):

$$Y = 0.117614842(ALogp2) + 0.006900712 (ATS1m) + 0.002645580 (ATS7m) -$$
$$- 0.007905861 (ATS0v) + 29.444475533. \tag{1}$$

The studied QSAR model was validated by considering CVR^2, adjusted R^2, and F-value.
R-squared = 0.80602900, Adjusted R-squared = 0.72844100,
Cross validated R-squared = 0.61235600, Significance-of-regression F-value = 10.38855500

Result and Discussion

Calculated Descriptors for Obtained Phytochemicals from Enantia chlorantia Bark

In this work, a series of descriptors were obtained, and four descriptors were selected using Lipinski rule of five, i.e. Molecular Weight ≤ 500 amu, Log P ≤ 5, Hydrogen Bond Donor (HBD) ≤ 5 and Hydrogen Bond Acceptor (HBA) ≤ 10 [40] (Table 2).

Calculated descriptors for studied compounds

	MW	LogP	HBD	HBA
1	220.35	3.47	0	1
2	198.30	2.87	0	0
3	220.35	3.29	0	1
4	204.35	4.69	0	0
5	220.35	3.6	0	1
6	220.356	4.35	0	1
7	220.356	3.01	1	1
8	222.372	3.49	1	1
9	204.357	4.23	0	0
10	204.357	4.08	0	0
11	204.357	4.78	0	0
12	204.357	4.34	0	0
13	204.357	4.48	0	0
14	204.357	4.76	0	0
15	204.357	4.34	0	0
16	204.357	4.29	0	0
17	204.357	4.14	0	0
18	204.357	4.71	0	0

According to Lien, 1982 [41], the calculated molecular weight from optimized molecular structures using computational tools remains an important characteristic that reveals the state (solubility, Van der Waals forces, molar refraction, steric factors, molecular connectivity, thermodynamic activity, partition coefficient, etc.) of such compound. The oral bioavailability of any compounds is a function of molecular weight in the range of 150–500 amu [42]; thus, all the calculated compounds proved to be orally bioavailable.

Moreover, the solubility of molecular compounds in lipophilic phase reveals the role of Log P in drug design [43]. Also, the report by Meanwell 2011 [44] showed that there may be possible complications which human body system may experience if the calculated Log P value is higher than 5 for oral absorption of drug-like molecule; therefore, all the calculated Log P value were within the accepted range for Log P (Log $P \leq 5$). This implies that the studied compounds have the ability to be taken orally without any complication.

It was observed that all the studied compounds obeyed the Lipinski rule of five, and this shows that all they have the potential ability to act as a drug.

Molecular Docking Studies on Phytochemicals from Enantia chlorantia Bark and Lactate dehydrogenase

The studied compounds obtained from *Enantia chlorantia* bark were screened for inhibitory activities against Lactate dehydrogenase using the molecular docking method. As reported in several literature sources, the higher binding affinity (in terms of negativity) corresponds to the better ability of the compound to inhibit the receptor [45]. The inhibitory activity of the individual studied ligand was compared with the inhibitory activity of the reference drug (quinine) and presented in Table 3.

Calculated binding affinity for Phytochemicals from *Enantia chlorantia* Bark–Lactate dehydrogenase complex

No	Binding Affinity (kcal/mol)	Residues involved in the interactions	Types of Non-bonding interaction involved
1	–6.4	PHE52, ILE54, ALA98, ILE119	Pi-Alkyl, Alkyl
2	–7.4	PHE100, ILE119, VAL26, ILE54, PHE52, ALA98	Pi-Alkyl, Alkyl, Pi-Sigma
3	–5.9	LEU201, VAL200, LYS314, PHE229, LEU202, LYS203	Pi-Alkyl, Alkyl
4	–7.0	ILE119, VAL55, ALA98, VAL26, TYR85, PHE52, ILE123, ILE54	Pi-Alkyl, Alkyl
5	–6.0	LYS203, LEU201, PHE229, LEU202, VAL200, LYS314	Pi-Alkyl, Alkyl
6	–6.2	LYS314, LYS198, VAL200, VAL233	Alkyl

No	Binding Affinity (kcal/mol)	Residues involved in the interactions	Types of Non-bonding interaction involved
7	−6.6	VAL233, LYS314, VAL200, LEU201	Unfavorable Donor-Donor, Alkyl
8	−6.3	VAL55, ALA98, PHE52, ILE119, ILE54, VAL26	Pi-Alkyl, Alkyl
9	−7.3	ILE54, PHE100, ILE119, VAL26, ALA98, PHE52, TYR85, ILE123	Pi-Alkyl, Alkyl
10	−6.4	ALA98, ILE54, ILE119, PHE100	Pi-Alkyl, Alkyl
11	−5.8	LYS314, VAL200, LEU202, PHE229, ARG204, LY203	Pi-Alkyl, Alkyl
12	−5.8	TYR174, TYR175, ILE239, ARG171, ALA249	Pi-Alkyl, Alkyl
13	−5.9	ILE54, ILE119, ALA98	Alkyl
14	−6.1	ILE119, ALA98, PHE52, ILE54, PHE100, LYS118	Pi-Alkyl, Alkyl
15	−7.8	ALA98, ILE123, VAL26, ILE54, ILE119, TYR85, PHE52	Pi-Alkyl, Alkyl
16	−7.0	ILE54, ILE119, PHE100, VAL26, ILE123, TYR85, PHE52, ALA98	Pi-Alkyl, Alkyl
17	−7.0	PHE52, ALA98, ILE54, ILE119, PHE100	Pi-Alkyl, Alkyl
18	−6.4	PHE52, VAL26, ALA98, ILE54, ILE123, TYR85, ILE119, PHE100	Pi-Alkyl, Alkyl
Quinine	−6.7	-	-

According to the data in Table 3, compound **15,** with the highest binding affinity value in terms of negative, has the highest tendency to inhibit Lactate dehydrogenase compared with other studied compounds and the reference drug (Fig. 3).

It can also be seen from Table 3 that six compounds (**2, 4, 9, 15, 16** and **17**) have better binding affinities than the other studied compounds and the reference drug. This showed that these phytochemicals enhanced the biological activities of *Enantia chlorantia* bark as a potential antimalaria agent. The reference drug with -6.7 kcal/mol binding affinity showed a greater tendency to inhibit Lactate dehydrogenase than compounds **1**, **3**, **5**, **6**, **7**, **8**, **10**, **11**, **12**, **13**, **14** and **18**.

a) 2D structure   *b*) 3D structure
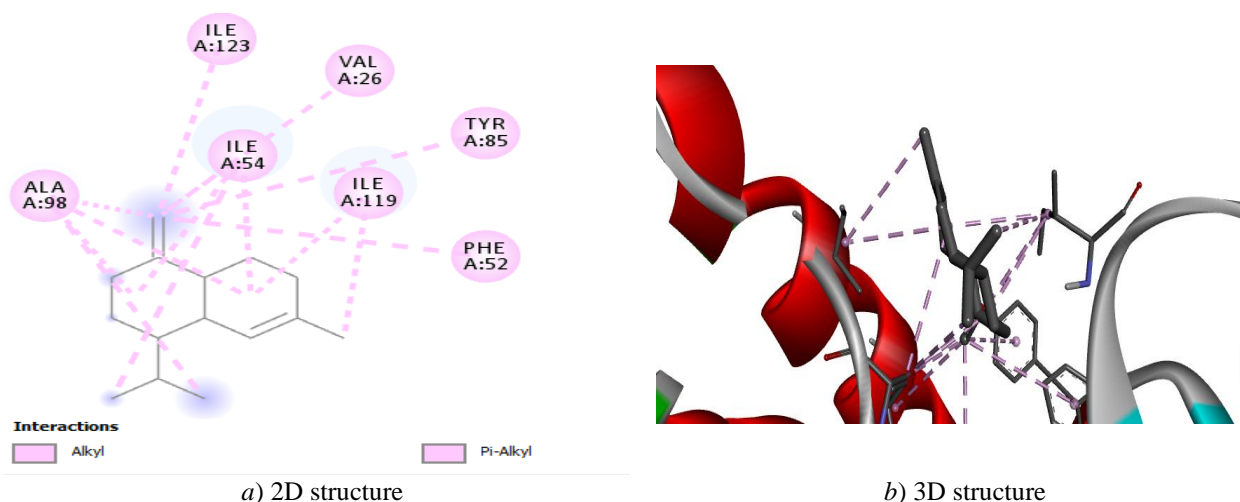
Figure 3. Binding site of Lactate dehydrogenase amino acid residues with compound **15**

Molecular Dynamic Simulation Analysis
Root of Mean Square Deviation (RMSD)

Root of mean square deviation of Lactate dehydrogenase backbone atoms in connection to the initial structure of the studied enzyme in forming complexes with compounds **15** and quinine during the 100 ns MD simulation is presented in Figure 4.
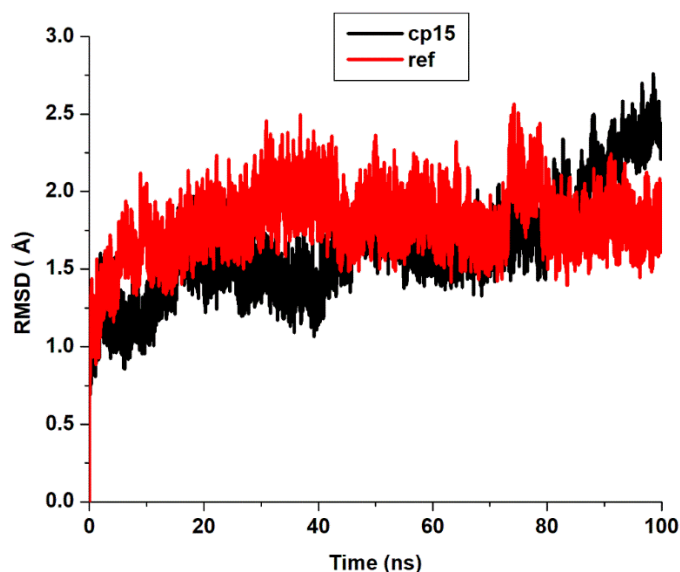
Figure 4. RMSD of **Compound 15-**1LDG (black) and **Quinine-ILDG** (red) complexes
during the 100 ns MD simulations

This study was carried out to investigate the rate of deviation of the initial studied compounds upon binding, as well as the stability of the simulated complexes. Therefore, as shown in Figure 4, compound **15-**Lactate dehydrogenase complex proved to be more stable after sixty nanoseconds (60 ns) of the simulation time than quinine- Lactate dehydrogenase complex.

Binding Energy Calculation
Table 4 presents the calculated binding energy components (total binding energy; van der Waals energy; electrostatic energy; gas-phase energy; solvation energy).

T a b l e 4

**Binding energy profiles of Compound 15-Lactate dehydrogenase complex
and Quinine-Lactate dehydrogenase complex**

Complexes	Binding Energy Components (kcal/mol)				
	ΔE_{vdw}	ΔE_{ele}	ΔG_{gas}	ΔG_{sol}	ΔG_{bind}
CP15-protein	-26.95 ± 0.08	-1.30 ± 0.01	-28.25 ± 0.08	3.08 ± 0.02	-25.17 ± 0.08
REF-protein	-13.34 ± 0.17	10.69 ± 0.18	-2.65 ± 0.44	-7.51 ± 0.44	-10.17 ± 0.13
Note: ΔG_{bind} = total binding energy; ΔE_{vdw} = van der Waals energy; ΔE_{ele} = electrostatic energy; ΔG_{gas} = gas-phase energy; ΔG_{sol} = solvation energy.					

The calculated binding free energy for compound **15**–Lactate dehydrogenase complex (–25.17 kJ/mol) confirmed the outstanding activity of compound **15** as potential Lactate dehydrogenase inhibitor. The presented molecular dynamic simulation result revealed that van der Waal energy, electrostatic energy, and gas-phase energy were favourable while polar solvation energy was not favourable for the binding of compound **15** to lactate dehydrogenase.

Quantitative Structure Activities Relationship Study
The obtained descriptors were screened, and the selected descriptors were divided into two sets, i.e. training and test sets. Compounds **2**, **6** and **10** were used as test sets, while other compounds obtained from *Enantia chlorantia* bark were used as the training set. The descriptors from the training set were used as the independent variable, while calculated binding affinity was used as the dependent variable. The 2D-QSAR model shown in Equation 1 included four descriptors which align with ratio 1:4 of the descriptors to the entire studied compounds as described in several reports [46]. The developed model was used to predict the calculated binding affinity. It was observed that the predicted binding affinity of the training set was closer to the original binding affinity. This is proof that the developed QSAR model is predictive, and its reliability was confirmed via the test set, which also goes in line with the squared correlation coefficient (R^2). Also,

according to Adegoke *et al*., 2020 [47], the predictive ability of any developed QSAR model is not enough to justify its potency; thus, this calls for 2D-QSAR validation. Adjusted R-squared, Cross validated R-squared and Significance-of-regression F-value were considered for QSAR validation. According to Oyebamiji *et al*., 2022 [48], Adjusted R-squared must be less than or equal to 0.6 while Cross validated R-squared must be less than or equal to 0.5 for any developed QSAR model to be considered valid; thus, the developed 2D-QSAR model can be considered valid and efficient (Table 5).

T a b l e 5

Observed and predicted binding affinity

	Original Binding Affinity	Predicted Binding Affinity
1	−6.4	−6.4
2*	−7.4	−0.6
3	−5.9	−5.9
4	−7.0	−7.0
5	−6.0	−6.0
6*	−6.2	2.9
7	−6.6	−6.6
8	−6.3	−6.3
9	−7.3	−7.3
10*	−6.4	2.2
11	−5.8	−5.8
12	−5.8	−5.8
13	−5.9	−5.9
14	−6.1	−6.1
15	−7.8	−7.8
16	−7.0	−7.0
17	−7.0	−7.0
18	−6.4	−6.4
Note: *Denote test set.		

Conclusions

Eighteen phytochemicals were selected from the entire compounds in *Enantia chlorantia* bark for *in silico* study. The structure of the selected compounds was subjected to optimization using Spartan 14 software, and a series of descriptors describing the antimalaria activities of the studied plant were obtained. Compound **15** (1*R*,4*aS*,8*aS*)-7-methyl-4-methylidene-1-propan-2-yl-2,3,4*a*,5,6,8*a*-hexahydro-1*H*-naphthalene) showed −7.8 kcal/mol binding affinity, that is higher than all other studied compounds, as well as the reference drug. This proves that Compound **15** has better ability to inhibit Lactate dehydrogenase, thereby downregulating malaria. Also, the QSAR model developed using binding affinity as the dependent variable showed good prediction, and was found to be reliable and valid.

Acknowledgements

References

1   Uzor, P.F. (2020). Alkaloids from Plants with Antimalarial Activity: A Review of Recent Studies. *Evidence-Based Complementary and Alternative Medicine*, 17 pages. https://doi.org/10.1155/2020/8749083

2   Kaur, K., Jain, M., Khan, S.I., et al. (2011). Synthesis, antiprotozoal, antimicrobial, β-hematin inhibition, cytotoxicity and methemoglobin (MetHb) formation activities of bis(8-aminoquinolines). *Bioorganic & Medicinal Chemistry*, *19*(1), 197–210. https://doi.org/10.1016/j.bmc.2010.11.036

3   Ashok, P., Ganguly, S., & Murugesan, S. (2013). Review on in-vitro antimalarial activity of natural β-carboline alkaloid. *Mini-Reviews in Medicinal Chemistry*, *13*(12), 1778–1791. https://doi.org/10.2174/1389557511313120008

4   Schlitzer, M. (2008). Antimalarial Drugs—what is in use and what is in the pipeline. *Archiv der Pharmazie*, *341*(3), 149–163. https://doi.org/10.1002/ardp.200700184

5   Nwanosike Dominic, U., Orji, A., Okafor, J.C., & Umesiobi, S. (2015). Progressive health spending and health outcomes in Nigeria: the case of malaria. *International Journal of Academic Research in Business and Social Sciences*, *5*(12), 2222–6990. https://doi.org/10.6007/IJARBSS/v5-i12/1924

6   Mutabingwa, T.K. (2005). Artemisinin-based combination therapies (ACTs): best hope for malaria treatment but inaccessible to the needy! *Acta Tropica*, *95*(3), 305–315. https://doi.org/10.1016/j.actatropica.2005.06.009

7   Udu, R., Oyweri, J., & Gathirwa, J. (2021). Antimalarial Activity of Nigella sativa L. Seed Extracts and Selection of Resistance in Plasmodium berghei ANKA in a Mouse Model. *Journal of Pathogens*, 2021, 1-10. https://doi.org/10.1155/2021/6165950

8   Nyandwaro, K., Oyweri, J., Kimani, F., & Mbugua, A. (2020). Evaluating Antiplasmodial and Antimalarial Activities of Soybean (Glycine max) Seed Extracts on *P. falciparum* Parasite Cultures and P. berghei-Infected Mice. *Journal of Pathogens*, *2020*, 1-8. https://doi.org/10.1155/2020/7605730

9   Kinghorn, A.D., Pan, L., Fletcher, J.N., & Chai, H. (2011). The relevance of higher plants in lead compound discovery programs. *Journal of Natural Products*, *74*(6), 1539–1555. https://doi.org/10.1021/np200391c

10   Ridley, R.G. (2002). Medical need, scientific opportunity and the drive for antimalarial drugs. *Nature*, *415*(6872), 686–693. https://doi.org/10.1038/415686a

11   Ginsburg, H., & Deharo, E. (2011). A call for using natural compounds in the development of new antimalarial treatments–an introduction. *Malaria Journal, 10*(1), (S1). https://doi.org/10.1186/1475-2875-10-S1-S1

12   Kuznetsov, G., Dyke, K.T., Towle, M.J., Cheng, H., Liu, J., Marsh, J.P., Schiller, S.E, Spyvee, M.R., Yang, H., Seletsky, B.M., Shaffer, C.J., Marceau, V., Yao, Y., Suh, E.M., Campagna, S., Fang, F.G., Kowalczyk, J.J., & Littlefield, B.A. (2009). Tubulin-based antimitotic mechanism of E7974, a novel analogue of the marine sponge natural product hemiasterlin. *Mol. Cancer. Ther. 8*, 2852-2860. https://doi.org/10.1158/1535-7163.mct-09-0301

13   Guinovart, C., Navia, M., Tanner, M., & Alonso, P. (2006). Malaria: burden of disease. *Curr. Mol. Med*. 6(2), 137–140. https://doi.org/10.2174/156652406776055131

14   Abdel-Sattara E, Abdallaha HM, El-Mekkawy S, Ichinod C, Kiyoharad H, & Yamada H (2020). Antimalarial alkaloid from Hypoestes forskaolii. *Experimental Parasitology*, *211*, 107851. https://doi.org/10.1016/j.exppara.2020.107851

15   Onguéné, PA., Ntie-Kang, F., Lifongo, L.L., Ndom, J.C., Sippl, W., & Mbaze, L.M. (2013). The potential of antimalarial compounds derived from African medicinal plants. Part I: A pharmacological evaluation of alkaloids and Terpenoids. *Malaria Journal*, *12*, 449. https://doi.org/10.1186/1475-2875-12-449

16   Tajbakhsh, E., Kwenti, T.E., Kheyri, P., Nezaratizade, S., Lindsay, D.S., & Khamesipour, F. (2021). Antiplasmodial, antimalarial activities and toxicity of African medicinal plants: a systematic review of literature. *Malaria Journal*, *20*, 349 https://doi.org/10.1186/s12936-021-03866-0

17   Kwenti, E.T. (2018). Malaria and HIV coinfection in sub-Saharan Africa: prevalence, impact, and treatment strategies. *Res Rep Trop Med*. 9, 123–36. https://doi.org/10.2147/rrtm.s154501

18   Kwenti, E.T., Kukwah, T.A., Kwenti, T.D.B., Nyassa, B.R., Dilonga, M.H., Enow-Orock, G., et al. (2019). Comparative analysis of IgG and IgG subclasses against Plasmodium falciparum MSP-119 in children from five contrasting bioecological zones of Cameroon. *Malar J.*, *18*, 16. https://doi.org/10.1186/s12936-019-2654-9

19   Dondorp, AM., Nosten, F., Yi, P., Das, D., Phyo, AP., Tarning, J, et al. (2009). Artemisinin resistance in Plasmodium falciparum malaria. *N Engl J Med*., *361*, 455–67. https://doi.org/10.1128/microbiolspec.EI10-0013-2016

20   Murray, C.J., Rosenfeld, L.C., Lim, S.S., Andrews, K.G., Foreman, K.J., Haring, et al. (2012). Global malaria mortality between 1980 and 2010: a systematic analysis. *Lancet*., *379*, 413–31. https://doi.org/10.1016/s0140-6736(12)60034-8

21   Schumann, G., Bonora, R., Ceriotti, F., Férard, G., Ferrero, C. A., Franck, P.F.H., Gella, F.-J., Hoelzel, W., Jørgensen, P.J., Kanno, T., Kessner, A., Klauke, R., Kristiansen, N., Lessinger, J.-M., Linsinger, T.P.J., Misaki, H., Panteghini, M., Pauwels, J., Schiele, F., & Schimmel, H. G. (2002). IFCC Primary Reference Procedures for the Measurement of Catalytic Activity Concentrations of Enzymes at 37 °C. Part 5. Reference Procedure for the Measurement of Catalytic Concentration of Aspartate Aminotransferase. Clinical Chemistry and Laboratory Medicine, 40(7). https://doi.org/10.1515/cclm.2002.125

22   Bzik, D.J., Fox, B.A., & Gonyer, K. (1993). Expression of *Plasmodium falciparum* lactate dehydrogenase in *Escherichia coli*. *Molecular and Biochemical Parasitology, 59*(1): 155–166. https://doi.org/10.1016/0166-6851(93)90016-q

23   Simpalipan, P., Pattaradilokrat, S., & Harnyuttanakorn, P. (2018). Global sequence diversity of the lactate dehydrogenase gene in *Plasmodium falciparum*. *Malar J., 17*, 16. https://doi.org/10.1186/s12936-017-2157-5

24   Holmes, R.S., & Goldberg, E. (2009). Computational analyses of mammalian lactate dehydrogenases: human, mouse, opossum and platypus LDHs. *Comput Biol Chem*., *33*(5), 379-85.https://doi.org/10.1016/j.compbiolchem.2009.07.006

25   Garcia, A.M., Marik, P., & Bellomo, R. (2014). Sepsis-associated hyperlactatemia. Crit Care. *18*(5), 503. https://doi.org/10.1186/s13054-014-0503-3

26   Tcheghebe, O.T., Tatong, F.N., & Seukep, A.J. (2016). Traditional uses, phytochemical and pharmacological profiles, and toxicity of Enantia chlorantha (Oliver): An overview. *Edorium J Med, 3*, 12–18. https://doi.org/10.5348/m05-2016-4-ra-2

27   Adesokan, A.A, Akanji, I.A. (2003). Effect of administration of aqueous extract of Enantia chlorantha on the activity of some enzymes in the small intestines of rats. *Nigeria biochem Mol Biol, 18*(2), 103–5. ISSN 1684–5315

28   Apkulu, I.N., Dada, J.D., Odama, E.L., & Galadima, O. (1994). Antibacterial activity of aqueous extract of some Nigerian medicinal plants. *Nigeria Journal of Botany*, *7*, 45–8.

29 Tsabang, N., Fokou, P.V., Tchokouaha, L.R., et al. (2012). Ethnopharmacological survey of Annonaceae medicinal plants used to treat malaria in four areas of Cameroon. *J Ethnopharmacol.*, *139*(1), 171– 80. https://doi.org/10.1016/j.jep.2011.10.035

30 Dawodu, A.O., Moses, U.D., Apena, A., Adetoro, A., & Dairo, J.O. (2014). The proximate evaluation and phytochemistry of Enantia chlorantha stem bark in aqueous and ethanolic extract. *Middle-East Journal of Scientific Research*, *21*(11), 2145–2148.

31 Dunn, C.R., Banfield, M.J., Barker, J.J., Higham, C.W., Moreton, K.M., Turgut-Balik, D., Brady, R.L., & Holbrook, J.J. (1996). The structure of lactate dehydrogenase from Plasmodium falciparum reveals a new target for antimalarial design. *Nat Struct Biol.*, *3*, 912–915. https://doi.org/10.1038/nsb1196-912

32 Wang, J., Wolf, R.M., Caldwell, J.W., Kollman, P.A., & Case, D.A. (2004). Development and testing of a general amber forcefield. *Journal of Computational Chemistry*, *25*(9), 1157–1174. https://doi.org/10.1002/jcc.20035

33 Nyeguea, M., Amvam-Zollo, P.-H., Etoa, F.-X., Agnaniet, H., & Menut C. (2008). Chemical and Biological Investigations of Essential Oils from Stem Barks of Enantia chlorantha *Oliv.* and *Polyalthia suaveolens* Engler. & Diels. from Cameroon. *Natural Product Communications*, *3* (7), 1089–1096. https://doi.org/10.1177/1934578X0800300711

34 Roe, D.R., & Cheatham, T.E. (2013). PTRAJ and CPPTRAJ: Software for Processing and Analysis of Molecular Dynamics Trajectory Data. *Journal of Chemical Theory and Computation, 9*(7), 3084–3095. https://doi.org/10.1021/ct400341p

35 Jorgensen, W.L., Chandrasekhar, J., Madura, J.D., Impey, R.W., & Klein, M.L. (1983). Comparison of simple potential functions for simulating liquid water. *The Journal of Chemical Physics*, *79*(2), 926–935. https://doi.org/10.1063/1.445869

36 Darden, T., York, D., & Pedersen, L. (1993). Particle mesh Ewald: an N.log(N) method for Ewald sums in large systems. *The Journal of Chemical Physics*, *98*(12), 10089–10092. https://doi.org/10.1063/1.464397

37 Roe, D.R., & Cheatham, III T.E. (2013). PTRAJ and CPPTRAJ: software for processing and analysis of molecular dynamics trajectory data. *Journal of Chemical Theory and Computation*, *9*(7): 3084–3095. https://doi.org/10.1021/ct400341p

38 Oyebamiji, A.K., Kaka, O.M., Akintelu, S.A., Semire, B., & Adelowo, J.M. (2020). Theoretical Bio-evaluation of 3,5-dimethoxy-N-vinylbenzenamine Analogues as Potential anti-Sclerotinia sclerotiorum. *Pharmacologyonline*, *3*, 427-439. ISSN: 1827-8620

39 Oyebamiji, A.K., Tolufashe, G.F., Oyawoye, O.M., Oyedepo, T.A., & Semire, B. (2020). Biological Activity of Selected Compounds from Annona muricata Seed as Antibreast Cancer Agents: Theoretical Study. *Journal of Chemistry,* 2020, Article ID 6735232, 10 pages. https://doi.org/10.1155/2020/6735232

40 Adeoye, D., Olarinoye, E.F., Oyebamiji, A.K., & Latona, D.F. (2022). Theoretical Evaluation of Potential Anti-Alanine Dehydrogenase Activities of Acetamide Derivatives. *Biointerface Research in Applied Chemistry*, *12*(6), 7469–7477. https://doi.org/10.33263/BRIAC126.74697477

41 Lien, E.J. (1982). Molecular weight and therapeutic dose of drug. *Journal of Clinical and Hospital Pharmacy, 7*, 101–106. https://doi.org/10.1111/j.1365-2710.1982.tb01009.x

42 Ibrahim, Z., Uzairu, A., Shallangwa, G., & Abechi, S. (2020). Molecular docking studies, drug-likeness and *in-silico* ADMET prediction of some novel β-Amino alcohol grafted 1,4,5-trisubstituted 1,2,3-triazoles derivatives as elevators of p53 protein levels. *Scientific African, 10*, e00570. https://doi.org/10.1016/j.sciaf.2020.e00570

43 Oyebamiji, A,K., Fadare, O.A., Akintelu, S,A, & Semire, B. (2021). Biological Studies on Anthra[1,9-cd]pyrazol-6(2D)-one Analogues as Anti-vascular Endothelial Growth Factor Via In silico Mechanisms. *Chemistry Africa*, *4(4)*, 955–963. https://doi.org/10.1007/s42250-021-00276-2

44 Meanwell, N.A. (2011). Synopsis of some recent tactical application of bioisosteres in drug design. *Journal of Medicinal Chemistry*, *54*(8), 2529–2591. https://doi.org/10.1021/jm1013693

45 Oyebamiji, A.K., Josiah, O.M., Akintelu, S.A., Adeoye, M.D., Sabitu, B.O., Latona, D.F., Esan, A.O., Soetan, E.A., & Semire, B. (2021). Dataset on Insightful Bio-Evaluation of 2-(quinoline-4-yloxy)acetamide Analogues as Potential Anti-Mycobacterium tuberculosis Catalase-Peroxidase Agents Via In silico Mechanisms. *Data in Brief*, *38*, 107441. https://doi.org/10.1016/j.dib.2021.107441

46 Erazua, E.A., Akintelu, S.A., Adelowo, J.M., Odoemene, S.N., Josiah, O.M., Raheem, S.F., Latona, D.F., Adeoye, M.D., Esan, A.O., & Oyebamiji, A.K. (2021). QSAR and Molecular Docking Studies on Nitro(Triazole/Imidazole)-Based Compounds as Anti-Tubercular Agents. *Trop J Nat Prod Res.*, *5*(11), 2022-2029. https://doi.org/10.26538/tjnpr/v5i11.22

47 Adegoke, R.O., Oyebamiji, A.K., & Semire, B. (2020). Dataset on the DFT-QSAR, and docking approaches for anticancer activities of 1,2,3-triazole-pyrimidine derivatives against Human Esophageal Carcinoma (EC-109). *Data in Brief, 31*, 105963. https://doi.org/10.1016/j.dib.2020.105963

48 Oyebamiji, A.K., Soetan, E.A., Akintelu, S.A., Ayeleso, A.O., & Mukwevho, E. (2022). Alpha-glucosidase activity of phytochemicals from *Phyllanthus amarus* leaves via *in-silico* approaches. *Pharmacological Research ─ Modern Chinese Medicine*, *2*, 100054. https://doi.org/10.1016/j.prmcm.2022.100054

Information about authors*

Oyebamiji, Abel Kolawole (*corresponding author*) — PhD, Assistant Professor, Industrial Chemistry Programme, Bowen University, Iwo, Osun State, Nigeria; e-mail: abel.oyebamiji@bowen.edu.ng; https://orcid.org/0000-0002-8932-6327

Olujinmi, Faith Eniola — Technologist, Industrial Chemistry Programme, Bowen University, Iwo, Osun State, Nigeria; e-mail: olujinmieniola@gmail.com; https://orcid.org/0000-0002-0655-4018

Akintayo, Emmanuel T. — Professor, Industrial Chemistry Programme, Bowen University, Iwo, Osun State; Department of Chemistry, Ekiti State University, Ado-Ekiti, Ekiti State, Nigeria Nigeria; e-mail: emmanuel.akintayo@bowen.edu.ng; https://orcid.org/0000-0001-8543-9554

Akintayo, Cecilia Olufunke — Professor, Industrial Chemistry Programme, Bowen University, Iwo, Osun State; Department of Chemistry, Federal University, Oye-Ekiti, Ekiti State, Nigeria; e-mail: cecilia.akintayo@bowen.edu.ng ; https://orcid.org/0000-0002-6023-5405

Akintelu, Sunday Adewale — PhD Candidate, School of Chemistry and Chemical Engineering, Beijing Institute of Technology, Beijing, 100811, China; e-mail: akintelusundayadewale@gmail.com; https://orcid.org/0000-0001-8919-3029

Semire, Banjo — PhD, Professor, Candidate of Computational Chemistry Laboratory, Department of Pure and Applied Chemistry, Ladoke Akintola University of Technology, P.M.B. 4000, Ogbomoso, Oyo State, Nigeria; e-mail: bsemire@lautech.edu.ng; https://orcid.org/0000-0002-4173-9165

Babalola, Jonathan Oyebamiji — Professor, Department of Chemistry, University of Ibadan, Ibadan, Oyo State, Nigeria; e-mail: bamijibabalola@yahoo.co.uk; https://orcid.org/0000-0002-1407-6677

Okunlola, Felix — Lecturer, Department of Natural Sciences, Faculty of Pure and Applied Sciences, Precious Cornerstone University, Ibadan, Nigeria; https://orcid.org/0000-0002-5471-2375

Olawoye, Bolanle Mary — PhD Candidate, Department of Basic Sciences, Adeleke University, Ede, Nigeria; e-mail: blessedbolanlemary@gmail.com; https://orcid.org/0009-0008-2981-133X

_____

*The author's name is presented in the order: *Last Name, First and Middle Names*

Article

UDC 621.793; 541.138

Igor V. Petukhov[1*] , Anna M. Popova[2], Vladimir I. Kichigin[1]

[1]Perm State University, Perm, Russia;
[2]Perm Scientific-Industrial Instrument-Making Company, Perm, Russia
(*Corresponding author's e-mail: Petukhov-309@yandex.ru)

Electrochemical Processes in Sulfite Gold Plating Solutions and Some Properties of Gold Coatings

The kinetics of gold electrodeposition from Au(I) sulfite solutions have been studied by impedance spectroscopy and polarization measurements on a rotating disk electrode. Two solutions were used: a $Na_3Au(SO_3)_2$-based electrolyte with 2,2′-bipyridine as stabilizing additive and an electrolyte containing $(NH_4)_3Au(SO_3)_2$. The polarization curves show a rise in current with increasing rotation speed of the electrode up to 300 rpm. It was found that contributions to the impedance spectra come from the steps of charge transfer and gold adatom incorporation into the crystal lattice, as well as from the relaxation of surface coverage with adsorbed species in an inhibiting layer. An equivalent electrical circuit was suggested to describe the impedance spectra. This circuit provides good approximation of impedance plots for both electrolytes at all electrode potentials. The overall cathodic reaction in both electrolytes appears to consist of the steps of the same nature. Some properties of the Au coatings (micro hardness, size of crystallites) were also determined. Soft gold coatings with micro hardness of 0.66 GPa are obtained from the electrolyte based on $(NH_4)_3Au(SO_3)_2$, the coatings with a higher micro hardness (~0.85 GPa) are deposited from the electrolyte containing 2,2′-bipyridine.

Keywords: gold plating, sulfite electrolyte, 2,2′-bipyridine, ethylenediamine, inhibiting layer, impedance spectroscopy, polarization curve, rotating disk electrode, micro hardness.

Introduction

Sulfite solutions are used for the electrolytic deposition of thick gold coatings in microelectronics, optoelectronics, integrated optics [1–5], for fabricating X-ray gratings [6, 7] and other microstructures [8]. These electrolytes have near-neutral pH value which enables to deposit rather thick (≥ 20 μm) gold layers through photoresist patterns for fabricating different devices operating in microwave band.

From the sulfite electrolytes, bright and soft coatings that have low internal stress even at considerable thickness are obtained [2, 9] if the optimal deposition regime and electrolyte composition were selected. Stabilizing additives are required for stable and long work of sulfite electrolytes.

Another aspect concerning the sulfite gold plating solutions is the need to adjust the bath regularly because sulfite ions are consumed during bath operation at elevated temperature and are oxidized by oxygen in the electrolyte open to the air. For this reason, the electrolytes based on ammonium sulfite have some advantages over the electrolytes based on sodium sulfite since the former are characterized by a much higher concentration of sulfite ions. These circumstances determined the choice of the electrolytes in this work. The aim of this work is to study the effect of sulfite electrolyte composition on the kinetics and mechanism of gold electrodeposition and on some properties of gold coatings.

Experimental

The electrolytic deposition of Au coatings was performed in stirred solutions at a temperature of 50 °C on specimens of copper foil (M0). The copper surface was pre-activated in a 10 % H_2SO_4 solution for 30 s.

Two gold plating electrolytes were studied in this work:

1. Electrolyte No.1 based on sodium sulfite with addition of 2,2′-bipyridine as a stabilizer. The composition is as follows: gold as metal — 8.5 g L^{-1}, sodium sulfite — 40 g L^{-1}, ethylenediamine — 32 g L^{-1}, 2,2′-bipyridine — 0.1 g L^{-1}, pH 7.2. In this electrolyte gold is present as complex compound $Na_3Au(SO_3)_2$. Current density is 20–25 A m^{-2}, current efficiency is 96–98 %.

2. Electrolyte No. 2 based on ammonium sulfite. The composition is as follows: gold as metal — 9.0 g L^{-1}, ammonium sulfite — 100 g L^{-1}, pH 6.8. In this electrolyte gold is present as complex compound $(NH_4)_3Au(SO_3)_2$. Current density is 20–40 A m^{-2}, current efficiency is 94–95 %.

The electrolytes were prepared using deionized water and the following chemicals: sodium sulfite of chemically pure grade, ammonium sulfite monohydrate (Sigma Aldrich), 2,2′-bipyridine of analytical reagent grade, ethylenediamine of analytical reagent grade purified additionally by distillation. Sulfite complexes of gold, $Na_3Au(SO_2)_2$ and $(NH_4)_3Au(SO_3)_2$, were prepared from $HAuCl_4 \cdot H_2O$ (chemically pure) as described in [10].

Electrochemical measurements were carried out on a rotating disk Pt electrode at rotation speeds of 100–300 rpm. To this end a RDE-2 rotating disk electrode unit (Metrohm, Autolab B.V.) was used. Polarization curves were measured in a three-electrode thermostatted cell (at 50 ℃) using Autolab potentiostat, model PGSTAT302N. Before measurements, a gold layer of ~1 μm in thickness was deposited on the electrode surface from the electrolyte under study at a current density of 20 A m^{-2} for 8 min. The electrode surface area was 0.07 cm^2. A Pt electrode was used as anode since gold does not dissolve in sulfite electrolytes. The main anodic reaction is the electrooxidation of sulfite ion. All potentials are referred to the NHE scale.

Impedance spectra were measured over a frequency range from 10 kHz to 0.01 Hz at an a.c. signal amplitude of 10 mV using a Solartron 1280Z system. In the course of measurements, the electrode potential was changed in the cathodic direction by steps of 0.02–0.04 V; each potential was held for 10 min to achieve the steady state. Impedance spectra were obtained under the following conditions: 50 ℃, rotating electrode, 300 rpm.

The structure of the coatings was studied using scanning electron microscopy (Hitachi S-3400N). The coating micro hardness was measured by the Vickers method using micro hardness tester DM-8 Affri with applied load of 3 g.

Results and Discussion

From the electrolyte No. 1, the coatings were obtained at 2,2′-bipyridine concentration of 0.1 g L^{-1}. When the additive concentration was lower, the stability of electrolyte was insufficient, metallic gold particles appeared in bulk solution; at higher concentrations coatings of poorer quality were obtained: the dendrite growth and coating discontinuities were observed. Addition of 2,2′-bipyridine increased to some extent the coating hardness (up to ~0.85 GPa) and the coating roughness (Fig. 1).
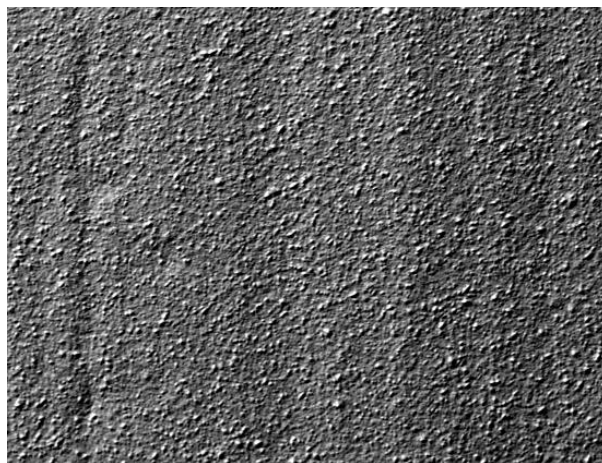
Figure 1. Micrograph of the surface of a coating obtained from the electrolyte No.1.
Magnification ×1000

The currents in the electrolyte No.1 increase with rotation speed up to 300 rpm (Fig. 2*a*) while further enhancement of the rotation of the electrode has only slight effect on polarization curve. The polarization curves have three regions of clearly different slope (Fig. 2*a*), with the slope of the first region being 0.08–0.11 V/decade. The adsorption of 2,2′-bipyridine inhibits the electrode process thus resulting in considerably larger magnitudes of cathodic polarization.

From the electrolyte Nao. 2, bright coatings with low hardness (0.66 ± 0.05 GPa) were deposited. To stabilize the electrolyte further, ethylenediamine was added (32 g L^{-1}); this resulted in increasing current efficiency (up to 97–98 %) and micro hardness (up to 0.82 ± 0.04 GPa). As evidenced by electron microscopy, the average size of crystallites decreased from 37 nm to 27 nm (Fig. 3).

The polarization curves in electrolyte No.2 have also a complex shape (Fig. 2*b*). In particular, a larger slope of the polarization curve is observed at moderate current densities. This suggests that an inhibiting layer forms on the electrode surface. At further rise of the polarization, desorption of adsorbed species occurs and the slope decreases again. The electrode rotation has a marked effect only at rather high polarizations, this appears to be related to diffusion limitations in that polarization region. Figure 2 shows typical polarization curves. The relative standard deviation of the current density was about 10–15 %.

a)

b)
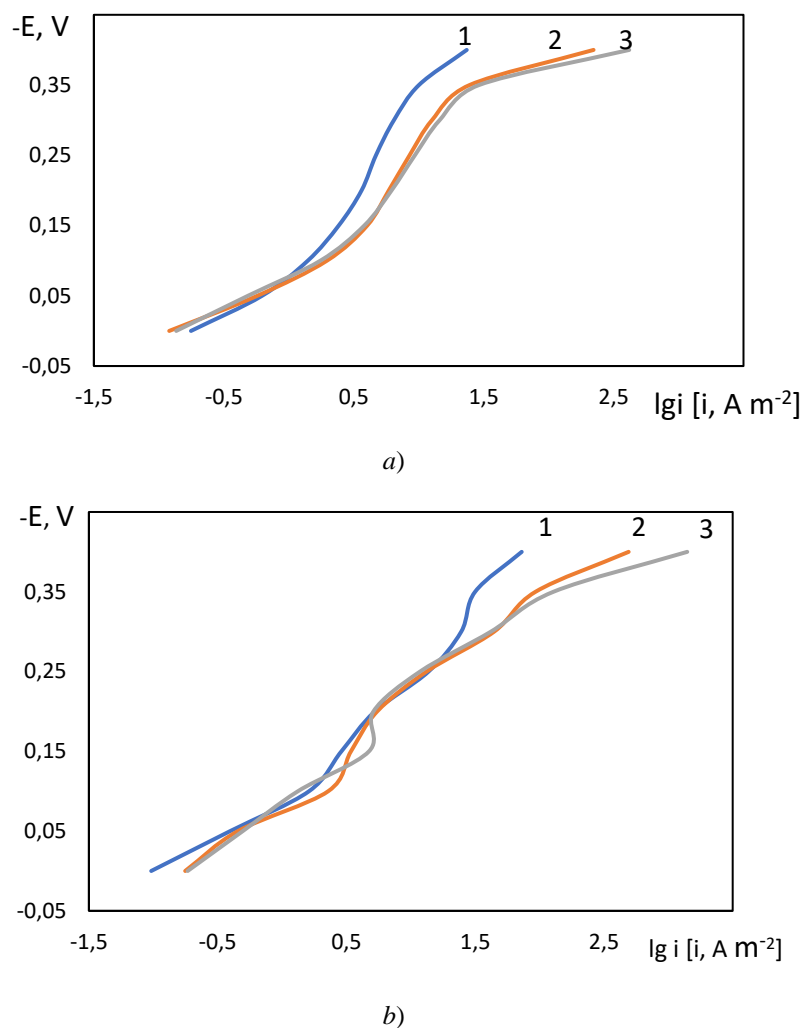
Figure 2. Cathodic polarization curves (*a*) in the electrolyte No. 1 and (*b*) in the electrolyte No. 2 at rotation speeds of 0 (1), 100 (2) and 300 (3) rpm

The overall electrode reaction is:

$$[Au(SO_3)_2]^{3-} + e^- = Au + 2SO_3^{2-}$$
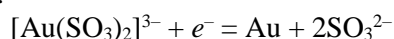
and it can contain several steps (mass transfer, electron transfer, complex ion dissociation, ad-atom incorporation into the crystal lattice) and can be affected by the adsorption of different species. In order to determine the nature of steps in the process under study, the impedance measurements were performed.

For the electrodes on which the gold electrodeposition occurs, two types of the complex plane impedance plots (Fig. 4, 5) were obtained depending on the electrode potential. At low cathodic polarizations, the impedance plot consists of a capacitive arc at high frequencies and an inductive arc at low frequencies (Fig. 4*a*, 5*a*). At higher cathodic polarizations, the impedance plots display two capacitive arcs followed by an inductive arc (Figures 4*b*, 5*b*).

a)   *b)*
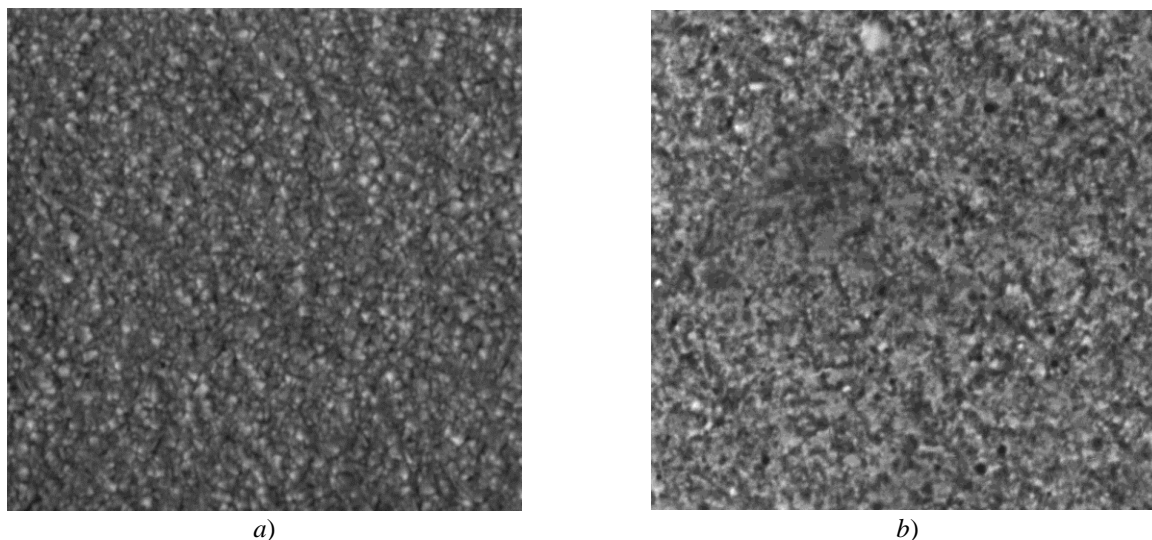
Figure 3. Micrographs of the surface of coatings obtained from the electrolyte No. 2 (*a*)
without ethylenediamine and (*b*) with ethylenediamine additive. Magnification ×100 000
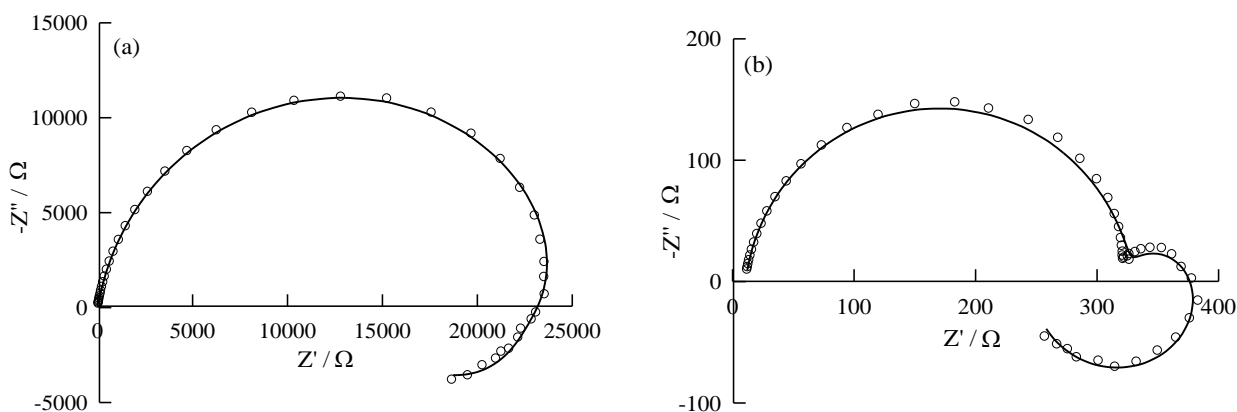
Figure 4. The impedance spectra in electrolyte No. 1. Circles are experimental points, solid lines are fitted curves
obtained using the equivalent circuit presented in Figure 6. Electrode potential: (*a*) –0.04 V; (*b*) –0.36 V
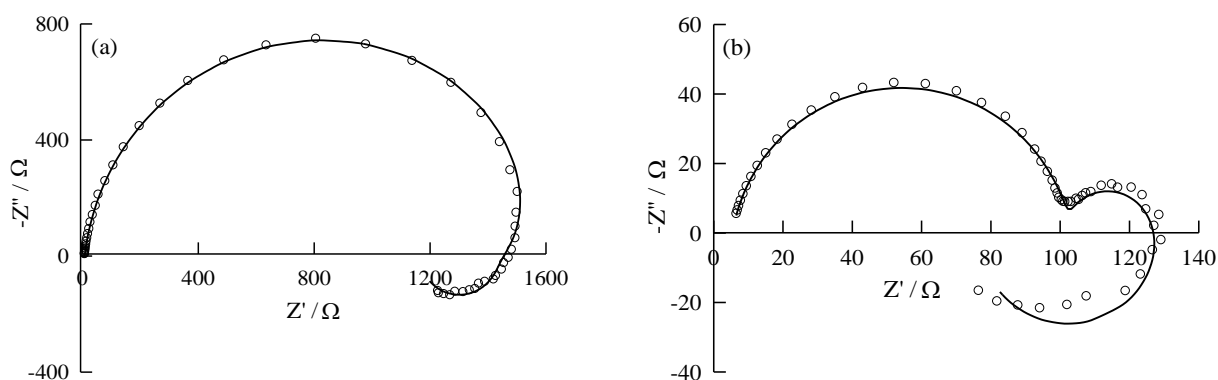
Figure 5. The impedance spectra in electrolyte No. 2. Circles are experimental points, solid lines are fitted curves
obtained using the equivalent circuit presented in Figure 6. Electrode potential: (*a*) –0.18 V; (*b*) –0.28 V

The first (high-frequency) capacitive arc corresponds to the charge transfer resistance in parallel with the double layer capacitance. The second capacitive arc is assumed to be related to the incorporation of gold ad-atoms into the crystal lattice. It should be noted that, depending on the conditions, the reagent diffusion in solution can also contribute to the second capacitive arc. However, the impedance was measured at the rota-

tion speed of 300 rpm, when the current, as mentioned above, ceases to change with further increasing rotation speed. Consequently, the diffusion contribution to the impedance is small. The inductive arc can be explained with the following assumptions: additives to the electrolyte adsorb on the electrode surface; adsorption of the additives inhibits the discharge of Au(I) complex ions; adsorption of the additives depends on the electrode potential and decreases as the cathodic polarization increases. The possibility of inductive arc appearing for the charge transfer reaction coupled with inhibitor adsorption has been demonstrated by Mészáros et al. [11].

At gold electrode in sulfite electrolyte, the inhibiting (passivating) layer with which the inductive arc is associated can have a complex composition. The layer supposedly contains chemisorbed sulfite ions and sulfur [12], chemisorbed OH groups, adsorbed molecules of organic compounds (ethylenediamine, bipyridine, etc.). The adsorption in this layer must not be very strong in order that the amount of adsorbate could respond to a sinusoidal potential perturbation used in impedance measurement.

Bipyridine adsorbs well at electrodes from aqueous solutions, and in particular, at Au electrodes from neutral electrolytes [13–16]. The adsorption of 2,2′-bipyridine is potential dependent [14, 15], decreases as the potential is lowered; in a neutral perchlorate solution, desorption of 2,2′-bipyridine from the Au(111) surface is completed at $E \approx -0.65$ V [14]. Such features of bipyridine adsorption are favorable for an inductive arc to appear in impedance plots.

Taking into account possible steps of the process, an equivalent electrical circuit (Fig. 6) is suggested. The elements of this circuit have the following physical meaning: R_s is the solution resistance, R_1 is the charge transfer resistance, R_2C_2 elements describe the ad-atom incorporation step, and R_3C_3 elements (with negative R and C) are related to the inductive arc. The frequency responses of a negative resistance in parallel with a negative capacitance and of a positive resistance in parallel with a positive inductance are identical at certain relations between the parameter values [17]. Because of this RC couple is also used in the equivalent circuit to model inductive arc. The charge transfer resistance R_1 and R_2C_2 elements (for the ad-atom incorporation step) have the positive sign for the process of metal deposition.
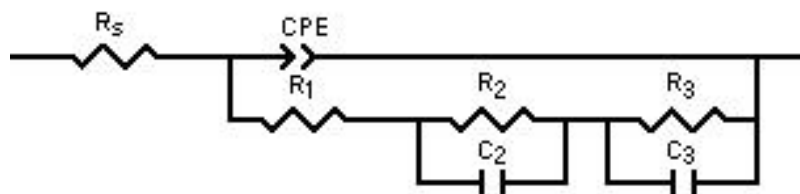
Figure 6. Equivalent electrical circuit

The constant phase element (CPE) is used in equivalent circuit instead of the double layer capacitance. The CPE originates generally from a distribution in the current density along the electrode surface as a result of surface inhomogeneity (geometric, structural, and energetic) [18–20]. The impedance of CPE is $Z_{CPE} = [Q(j\omega)^p]^{-1}$ where j is the imaginary unit, ω is the angular frequency of alternating current, Q is the CPE coefficient, p is the CPE exponent. For gold plating electrolytes studied, $p = 0.90$–0.91 (electrolyte No. 1) and $p = 0.92$–0.94 (electrolyte No. 2); the p value depends only slightly on the electrode potential.

The equivalent circuit shown in Figure 6 provides good approximation of both types of impedance spectra (Fig. 4, 5).

At low cathodic polarizations, there is no second capacitive arc (Fig. 4, 5); it can be supposed that the charge transfer is the rate-limiting step under these conditions. The relaxation of the surface coverage in the inhibiting layer is also manifested in this polarization range. When the potential shifts in the negative direction and the charge transfer becomes faster, kinetic limitations arise in the ad-atom incorporation step and the second capacitive arc appears in the impedance plot. The rate-determining step seems still to be the charge transfer as evidenced by the size of two capacitive arcs.

Despite the variations in electrolyte composition, the impedance plots are similar (Fig. 4, 5) and the experimental impedance spectra can be fitted using the same equivalent circuit for both electrolytes. Thus, the steps comprising the mechanism for the overall cathodic reaction are of the same nature in electrolyte No.1 and No.2. Some differences between the impedance spectra in the investigated electrolytes are mainly due to the variations in the values of rate constants of the steps and in the properties of inhibiting layers on the electrode surface.

Conclusions

The kinetics and mechanism of gold electrodeposition were studied in two sulfite electrolytes: (i) an electrolyte containing $Na_3Au(SO_3)_2$ and 2,2′-bipyridine additive; (ii) an electrolyte containing $(NH_4)_3Au(SO_3)_2$. Bipyridine adsorbs well at Au electrode, inhibits the electrode process and has an appreciable effect on the properties of Au coatings. In particular, addition of 2,2′-bipyridine increases the coating hardness up to ~0.85 GPa. From the electrolyte based on ammonium sulfite, the coatings with a lower hardness (0.66 ± 0.05 GPa) are deposited.

The impedance spectroscopy data suggest that the overall cathodic process in both electrolytes involves the steps of charge transfer and gold ad-atom incorporation into the crystal lattice; the relaxation of surface coverage with adsorbed species also affects the impedance spectra.

Acknowledgements

References

1 Osaka, T., Okinaka, Y., Sasano J., & Kato, M. (2006). Development of new electrolytic and electroless gold plating processes for electronics applications. *Science and Technology of Advanced Materials,* 7, 425–437. https://doi.org/10.1016/j.stam.2006.05.003

2 Green, T.A. (2007). Gold electrodeposition for microelectronic, optpelectronic and microsystem applications. *Gold Bulletin*, *40* (2), 105–114. https://doi.org/10.1007/BF03215566

3 Dimitrijević, S., Rajčić-Vujasinović, M., & Trujić, V. (2013). Non-cyanide electrolytes for gold plating — a review. *Int. J. Electrochem. Sci.*, 8, 6620–6646.

4 Josell, D., & Moffat, T. P. (2019). Bottom-up filling of damascene trenches with gold in a sulfite electrolyte. *J. Electrochem. Soc.*, 166, D3022–D3034. https://doi.org/10.1149/2.0041901jes

5 Lintao Liu, Xiaoli Zhu, Shuhua Wei, Jing Zhang, M.R. Baklanov, A.B. da Silva Fanta, Jiebin Niu, & Changqing Xie. (2019). Influence of current density on orientation-controllable growth and characteristics of electrochemically deposited Au films. *J. Electrochem. Soc.* 166, D3232–D3237. https://doi.org/10.1149/2.0291901jes

6 Josell, D., & Moffat, T.P. (2023). Extreme bottom-up gold filling of high aspect ratio features. *Acc. Chem. Res. 56*(6), 677–688. https://doi.org/10.1021/acs.accounts.2c00826

7 Ohlin, H., Frisk, T., Åstrand, M., & Vogt, U. (2022). Miniaturized sulfite-based gold bath for controlled electroplating of zone plate nanostructures. *Micromachines 13*(3), 452. https://doi.org/10.3390/mi13030452

8 Schürch, P., Osenberg, D., Testa, P., Bürki, G., Schwiedrzik, J., Michler, J., & Koelmans, W.W. (2023). Direct 3D microprinting of highly conductive gold structures via localized electrodeposition. *Materials & Design*, 227, 111780. https://doi.org/10.1016/j.matdes.2023.111780

9 Kichigin, V.I., Petukhov, I.V., Shevtsov, D.I., & Permyakova M.A. (2015). Electrodeposition of coatings from sulfite gold-plating electrolyte and their properties. *Russ. J. Appl. Chem.,* 88, 1950–1957. https://doi.org/10.1134/S10704272150120083

10 Karyakin, Yu.V., & Angelov, I.I. (1974). *Chistye Khimicheskie Veshchestva [Pure Chemical Substances]*. Moscow: Khimiia [in Russian].

11 Mészáros, L., Lengyel, B., & Garai, T. (1982). Study of inhibitors by electrode impedance measurements. *Acta Chim. Acad. Sci. Hung.,* 110, 57–65.

12 Baltrūnas, G., Valiūnienė, A., Vienožinskis, J., Gaidamauskas, E., Jankauskas, T., & Margarian, Ž. (2008). Electrochemical gold deposition from sulfite solution: application for subsequent polyaniline layer formation. *J. Appl. Electrochem.*, 38, 1519–1526. https://doi.org/10.1007/s10800-008-9596-1

13 Mambetkaziev, E.A., Zhdanov, S.I., & Damaskin, B.B. (1972). Uchet vliianiia adsorbtsii ligandov i kompleksov pri issledovanii kompleksoobrazovaniia poliaroficheskim metodom. I. Issledovanie adsorbtsii 2,2′-dipiridila na rtuti iz vodnykh rastvorov KNO_3 [Account of the adsorption of ligands and complexes in complexation study by polarographic method. I. A study of 2,2′-bipyridine adsorption on mercury from aqueous KNO_3 solutions]. *Elektrokhimiia — Electrochemistry*, *8*(11), 1650–1654 [in Russian].

14 Dretschke, Th., & Wandlowski, Th. (1999). An order-disorder-order adlayer transition of 2,2′-bipyridine on Au(III). *Electrochim. Acta*, 45, 731–740. https://doi.org/10.1016/S0013-4686(99)00252-2

15 Zeng, X., & Hatton, R. (2000). EQCM study of adsorption of bipyridine on Au polycrystalline electrode using underpotential deposition of Pb as a probe. *Electrochim. Acta*, 45, 3629–3638. https://doi.org/10.1016/S0013-4686(00)00446-1

16 Ren, X., Song, Y., Liu, A., Zhang, J., Yuan, G., Yang, P., et al. (2015). Computational chemistry and electrochemical studies of adsorption behavior of organic additives during gold deposition in cyanide-free electrolytes. *Electrochim. Acta*, 176, 10–17. https://doi.org/10.1016/j.electacta.2015.06.147

17 Lasia, A. (2014). Electrochemical Impedance Spectroscopy and its Applications. Springer Science + Business Media, New York.

18 Córdoba-Torres, P., Mesquita, T.J., & Nogueira, R.P. (2015). On the relationship between the origin of constant-phase element behavior in electrochemical impedance spectroscopy and electrode surface structure. *J. Phys. Chem. C.*, 119(8), 4136–4147. https://doi.org/10.1021/jp512063f

19 Alexander, C.L., Tribollet, B., & Orazem, M.E. (2015). Contribution of surface distributions to constant-phase-element (CPE) behavior: 1. Influence of roughness. *Electrochim. Acta*, 173, 416–424. https://doi.org/10.1016/j.electacta.2015.05.010

20 Pajkossy, T., & Jurczakowski, R. (2017). Electrochemical impedance spectroscopy in interfacial studies. *Current Opinion in Electrochemistry*, 1, 53–58. https://doi.org/10.1016/j.coelec.2017.01.006

Information about authors*

Petukhov, Igor Valentinovich (*corresponding author*) — Candidate of chemical sciences, Associate Professor, Perm State University, Bukireva st., 15,, 614097, Perm, Russia; e-mail: Petukhov-309@yandex.ru, https://orcid.org/0000-0002-3110-668x

Popova, Anna Mikhailovna — Head of the Laboratory, Perm Scientific-Industrial Instrument-Making Company, 25th October st., 106, 614007, Perm, Russia; e-mail: AMPopova@pnppk.ru

Kichigin, Vladimir Ivanovich — Candidate of chemical sciences, Senior Researcher, Perm State University, Bukireva st., 15, 614097, Perm, Russia; e-mail: kichigin@psu.ru, https://orcid.org/0000-0002-4668-0756

_____

*The author's name is presented in the order: *Last Name, First and Middle Names*

INORGANIC CHEMISTRY

Daniil B. Gogol[1] ID, Ivan E. Rozhkovoy[1] ID, Daniyar T. Sadyrbekov[2] ID, Astra M. Makasheva[3*] ID

[1]Institute of Problems of Complex Development of Mineral Resources, Karaganda, Kazakhstan;
[2]Karaganda Buketov University, Karaganda, Kazakhstan;
[3]Abishev Chemical and Metallurgical Institute, Karaganda, Kazakhstan
(*Corresponding author's e-mail: astra_mun@mail.ru)

Deposition of Transition Metal onto Carbonate Materials Surface: Theoretical Evaluation of Optimal Parameters

Deposition probabilities of transition metal ions on carbonate materials have been discussed in this paper. The deterministic and probabilistic design of the experiment has been used to obtain the optimal deposition parameters. The special features of deposition of copper, nickel, cobalt and zinc cations on surface of marble have been analyzed. Based on this research, the authors proposed the generalized multiple factor equations to predict the behavior of the selected metals on a marble surface. It was demonstrated that copper deposition is affected only by concentration of copper sulfate solution. For nickel, the strength of a complex with transition metal ion affects the deposition of an insoluble compound on carbonate surface. Deposition of cobalt under the specified conditions is very weak and an impact is exerted by the basicity and concentration of cobalt sulfate. For zinc, deposition under specified conditions has a strong dependence on the influencing factors, and the amount of deposited zinc varies within a wide range. The obtained results permit to use the application method of the protective and decorative coatings on products made of the natural minerals and inorganic materials such as marble, concrete, dolomite, limestone, gypsum, etc.

Keywords: transition metals, carbonate materials, deposition, marble surface, hardly soluble compounds, complexing agents, deterministic and probabilistic design of the experiment, optimal parameters.

Introduction

Marble is one of the frequently used natural materials in construction [1–11]. It has been used as a building cladding material in construction of monuments, various types of works of art, cultural heritage sites, etc. [10, 12, 13]. However, marble is a fragile and heterogeneous material and its composition depends on its deposit [4, 8, 12]. During the operation, marble is exposed to various natural water phenomena, temperature changes, weathering, etc. Therefore, the protection of such material from the external influences is relevant and of interest from beginning of its use [10, 13]. The authors [2, 14] developed methods for obtaining of coatings from various organic substances based on the density functional theory. Various types of complexing agents are also applied and they slow down the deposition rate and improve the quality of the marble coating [15–17]. Processes of the chemical deposition of transition metal ions on carbonate materials have been studied in some papers [18–20]. This is primarily related to water treatment and recovery of trace metals. Mechanism of a chemical deposition of copper on calcite has been described in [21]. We have showed before the deposition probability of malachite and azurite minerals from the organic complex copper compounds on carbonate materials [22, 23]. Moreover, the paper described the stabilization of the unstable polymorphic forms of minerals under copper ion influence [24]. An approach closest to this project is described in [25], where the electrokinetic methods have been applied for deposition of calcium oxalate on the

marble surface. This paper focuses on substitution of cations (instead of anions) on a surface of the treated materials.

The research purpose is to find the optimal conditions of deposition processes of the selected transition metals (copper, nickel, cobalt and zinc) as applied to carbonate inorganic construction material.

A series of experiments using the deterministic and probabilistic design of the experiment have been carried out to study the deposition methods of the insoluble transition metal compounds on the surface of a carbonate reservoir [26, 27].

Experimental

In order to select d-elements, the main criteria were availability and price of salts of these metals, and also stability of an element in the valence state of 2+. Cu, Ni, Co and Zn compiled with the relevant criteria and they were selected for the research.

Marble was chosen as a carbonate reservoir. The experiments used the cubic samples of the cubic polycrystalline marble with a side of 2.5 cm and a polished surface. This was done to exclude a factor of the difference in the specific area of the rough cube surface for deposition intensity of the main carbonate transition metal on it.

For all experiments, a five-factor experiment matrix has been developed with four levels for each factor. The factors influencing on deposition intensity have been selected as below:

– concentration of transition metal salt;

– concentration of a strong electrolyte salt with an anion similar to transition metal salt to study an effect of an ionic strength of solution;

– amount of KOH in solution to study an effect of basicity of medium;

– holding time of cube in solution;

– vacancy factor required for calculations.

The amount of transition metal deposited on surface of a marble sample has been taken as the result of the experiment. For this purpose, a surface layer of the extracted sample has been dissolved in a 1:100 sulfuric acid solution. Then the obtained solution has been brought to 50 ml. Concentration of transition metal has been measured by the photometric methods.

The experiment matrix for deposition of copper, nickel, cobalt and zinc as their basic carbonates has been generally described. Table 1 summarizes the selected factors and levels. In this case, differences for four metals are the first and second factors.

The factor designations are as follows:

factor 1 — $CuSO_4$ concentration (mol/l) for Cu; $Ni(NO_3)_2$ concentration for Ni; $CoSO_4$ concentration for Co and $ZnSO_4$ concentration for Zn;

factor 2 — Na_2SO_4 concentration (mol/l) for Cu, Co and Zn; Na_2NO_3 concentration for Ni.

factor 3 — the amount of 0.1 M KOH solution (ml);

factor 4 — the holding time of the marble sample in solution (a week);

factor 5 — vacant.

The volume of solution was 300 ml.

T a b l e   1

Factors and levels

Factor No.	Factor	Designation	Level 1	Level 2	Level 3	Level 4
1	Factor 1	X1	0.01	0.02	0.03	0.04
2	Factor 2	X2	0	0.1	0.15	0.2
3	Factor 3	X3	4.2	8.4	12.5	16.8
4	Factor 4	X4	1	2	3	4
5	Factor 5	X5	1	2	3	4

The volume of solution was 300 ml.

In order to exclude deposition of $Cu(OH)_2$, $Ni(OH)_2$, $Co(OH)_2$ and $Zn(OH)_2$ with increasing basicity of a solution and possible increase in activity of ions of Cu^{2+}, Ni^{2+}, Co^{2+} and Zn^{2+}, a complexing agents have been added to the solution, i.e. Na-EDTA for copper, sodium acetate for nickel, sodium citrate for cobalt and lactate ion for zinc. All substances have been added in concentrations equivalent to the concentrations of Cu^{2+}, Ni^{2+}, Co^{2+} and Zn^{2+} ions.

Analysis of the solutions obtained by the above approach has been performed photometrically according to the method of analysis of Cu^{2+} ions with Na-DDTC (sodium diethyldithiocarbamate); Ni^{2+} with dimethylglyoxime and Co^{2+} with nitroso-r-salt. The content of Zn^{2+} ions has been analyzed by the atomic absorption spectroscopy.

For copper, the obtained optical density of the analyzed samples relative to a pure solvent has been taken as the result. For nickel and cobalt, the result contained the received optical density of the analyzed samples relative to a blank sample. For zinc, the result included the obtained values of zinc content in the analyzed samples.

The amount of deposited metal has been used as a comparative measure of Y.

MS Excel program has been applied for calculations and graphs. Table 2 summarizes the design of the experiment for all explored metals.

Table 2

The design of the experiment by factors

No.	Factor 1	Factor 2	Factor 3	Factor 4	Factor 5
1	0.01	0	4.2	1	1
2	0.01	0.1	8.4	2	2
3	0.01	0.15	12.5	3	3
4	0.01	0.2	16.6	4	4
5	0.02	0	8.4	3	4
6	0.02	0.1	4.2	4	3
7	0.02	0.15	16.6	1	2
8	0.02	0.2	12.5	2	1
9	0.03	0	12.5	4	2
10	0.03	0.1	16.6	3	1
11	0.03	0.15	4.2	2	4
12	0.03	0.2	8.4	1	3
13	0.04	0	16.6	2	3
14	0.04	0.1	12.5	1	4
15	0.04	0.15	8.4	4	1
16	0.04	0.2	4.2	3	2

Results and Discussion

Table 3 demonstrates the obtained results of factors for the studied transition metals.

Table 3

The results of calculations for Cu^{2+}, Ni^{2+}, Co^{2+} and Zn^{2+}

No	Calculation results, kg/m²			
	Cu^{2+}	Ni^{2+}	Co^{2+}	Zn^{2+}
1	0.107	0.189	0.04	33.141
2	0.469	0.487	0.06	339.9
3	0.047	0.56	0.023	1084.4
4	0.081	0.489	0.06	1427.7
5	0.16	0.339	0.027	63.7
6	0.065	0.402	0.047	2.1
7	0.156	0.212	0.047	123
8	0.284	0.39	0.081	359.4
9	0.090	0.449	0.097	38.2
10	0.086	0.132	0.022	30.1
11	0.567	0.300	0.088	0.2
12	0.180	0.322	0.079	0.6
13	0.590	0.181	0.089	28.5
14	0.223	0.174	0.042	1.8
15	0.249	0.844	0.121	4.5
16	0.153	1.153	0.034	1.5

Results of the computational calculations are shown by the partial dependencies. The graphical data are also presented for them.

For factors of 1-4, the results for Cu^{2+}, Ni^{2+}, Co^{2+} and Zn^{2+} are illustrated in Figures of 1-4. It should be stated that the graphical data are presented only for the significant factors.

Correlation coefficients of all factors for all metals are shown in Table 4. Table 4 demonstrates that only factor 1 was significant for copper, i.e., the amount of copper deposited on marble surface is affected only by concentration of copper sulfate solution.

For nickel and zinc, all factors are significant. For cobalt, factors of 1 and 3 are relevant.

T a b l e 4

Correlation coefficients by factors 1-5 for Cu^{2+}, Ni^{2+}, Co^{2+} and Zn^{2+} metals

Factor	Correlation coefficients			
	Cu^{2+}	Ni^{2+}	Co^{2+}	Zn^{2+}
X1	$R = 0.9766$	$R = 0.8001$	$R = 0.9104$	$R = 0.9968$
X2	$R = 0.5211$	$R = 0.9632$	$R = 0.6704$	$R = 0.9879$
X3	$R = 0.5683$	$R = 0.9834$	$R = 0.8617$	$R = 0.9788$
X4	$R = 0.6380$	$R = 0.9998$	$R = 0.6606$	$R = 0.9712$
X5	$R = 0.5376$	$R = 0.8087$	$R = 0.9959$	$R = 0.8427$
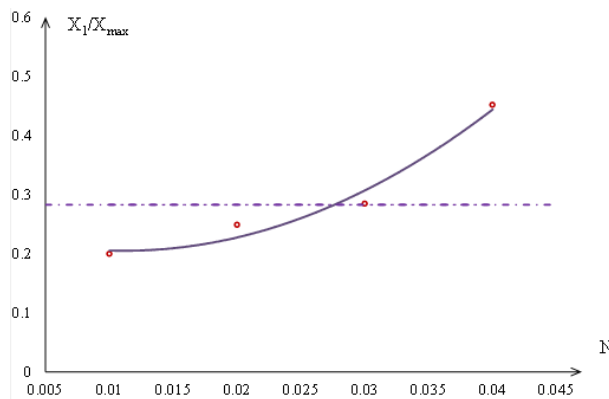
a) for copper (II)
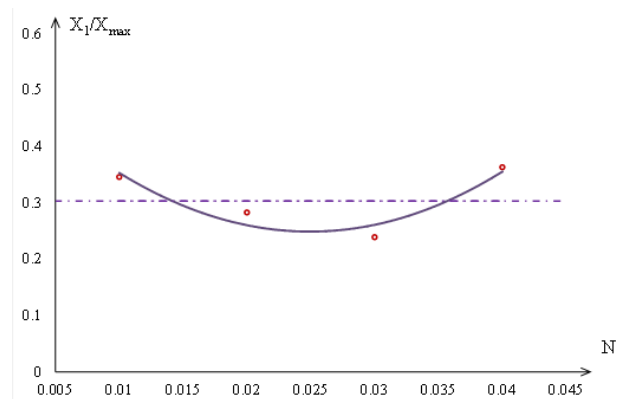
b) for nickel (II)
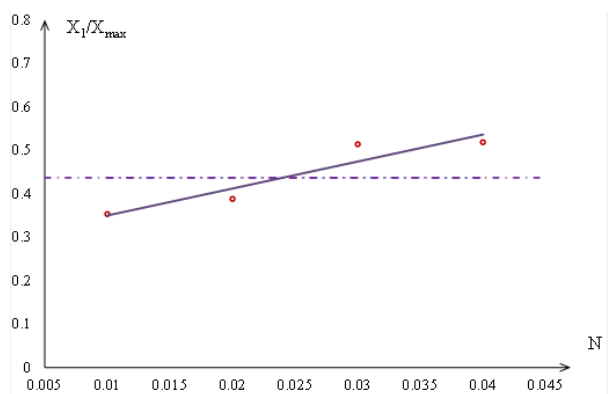
c) for cobalt (II)
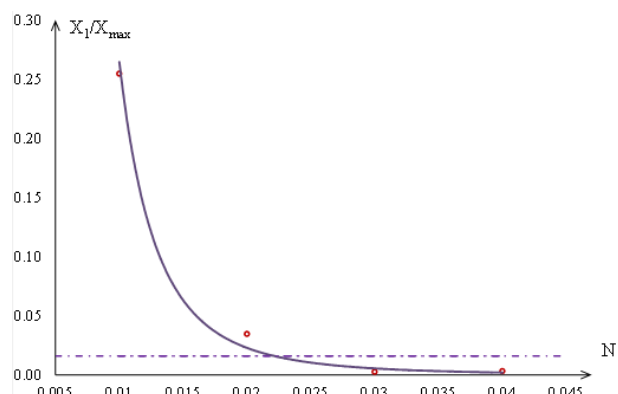
d) for zinc (II)

Figure1. Dependence of factor 1 on the amount of deposited metal

The equations for all studied metals are described. For copper, the significant factor is 1, thus, the equation is showed only for it:

$$Y_1 = 0.00751e^{48.45X_1}X_1^{-0.4953}, \text{ kg/m}^2 \qquad (1)$$

For nickel, all factors were relevant, so the overall multiple factor equation is as follows:

$$Y = Y_{av}^{-3} \cdot \left(0.0004032 e^{62.19 X_1} X_1^{-1.367}\right)\left(11.05 X_2^2 - 0.8843 X_2 + 0.2641\right) \times$$
$$\times \left(-0.04898 X_3^2 + 0.0832 X_3 + 0.4084\right)\left(0.19 e^{0.1219 X_4} X_4^{0.3646}\right), \text{ kg/m}^2 \qquad (2)$$

a) for nickel (II)
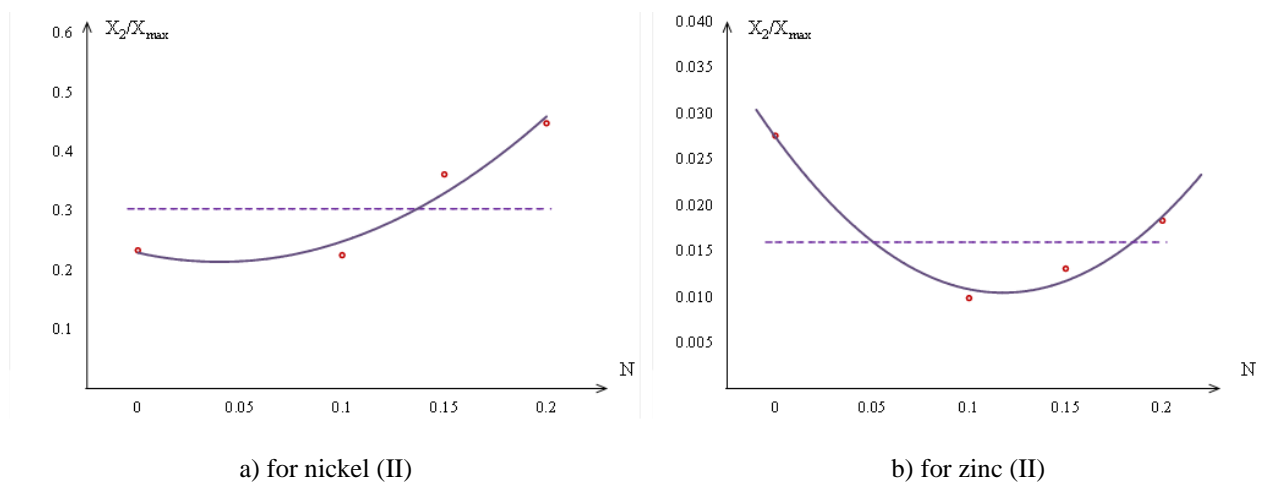
b) for zinc (II)

Figure 2. Dependence of factor 2 on the amount of deposited metal

a) for nickel (II)

b) for cobalt (II)
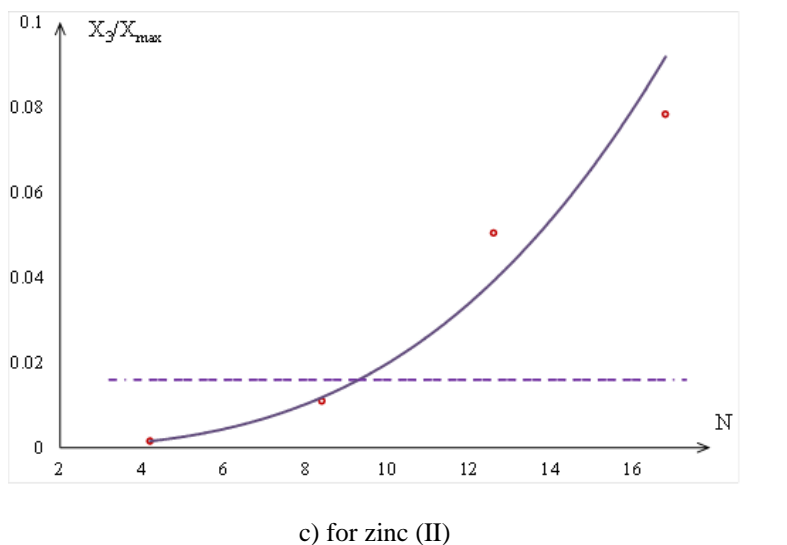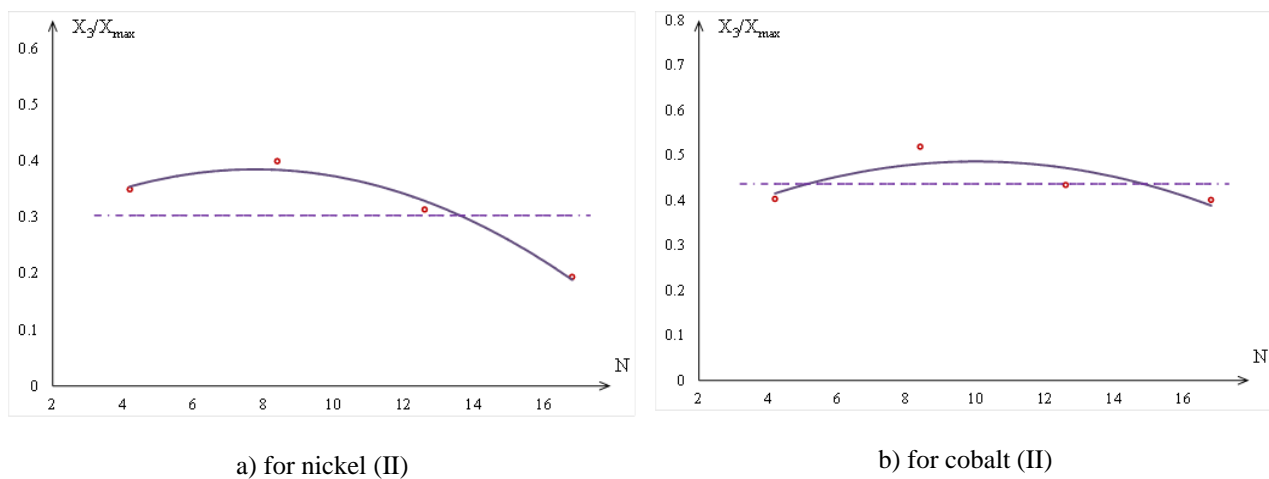
c) for zinc (II)

Figure 3. Dependence of factor 3 on the amount of deposited metal
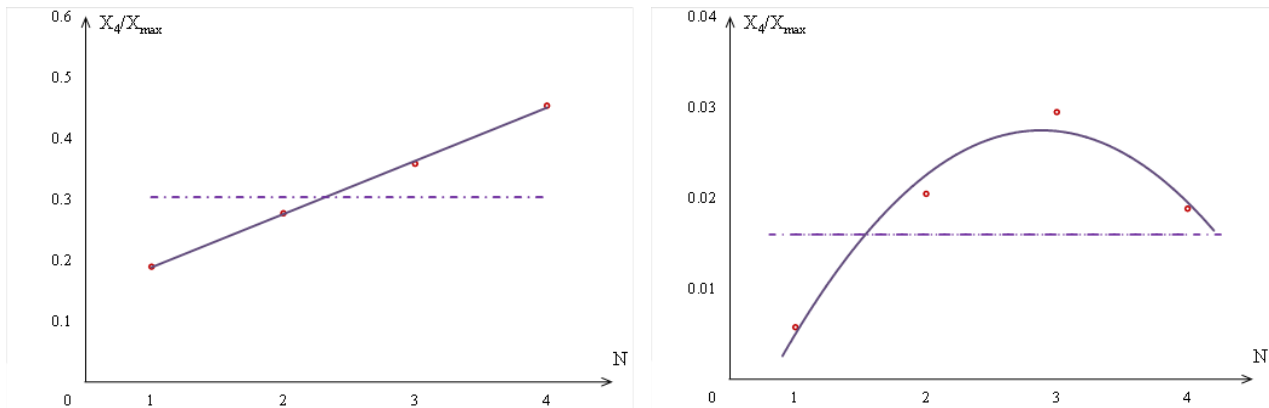
a) for nickel (II)   b) for zinc (II)

Figure 4. Dependence of factor 4 on the amount of deposited metal

For cobalt, we describe a generalized multiple factor equation for factors of 1 and 3:

$$Y = Y_{av}^{-1} \cdot \left(0.03485 + 0.749 X_1\right)\left(0.02087 e^{-0.102 X_3} X_3^{0.8965}\right), \text{ kg/m}^2. \tag{3}$$

For zinc, generalized multiple factor equation for all studied factors:

$$Y = Y_{av}^{-3} \cdot \left(3.194 \cdot 10^{-5} X_1^{-3.536}\right)\left(1748 X_2^2 - 410.9 X_2 + 39.04\right) \times$$
$$\times \left(0.01672 e^{-0.06677 X_3} X_3^{3.55}\right)\left(35,5 e^{-1.49 X_4} X_4^{4.127}\right), \text{ kg/m}^2. \tag{4}$$

After obtaining of the multiple factor equations, the additional experiments have been performed. Results of the experimental data are summarized in Table 5. A correlation coefficient compared to the experimental data is present in a bottom line of Table 5. This table includes the results for cobalt which are not significant.

T a b l e   5

Obtained experimental data for Cu²⁺, Ni²⁺, Co²⁺ and Zn²⁺

No	Calculation results, kg/m²			
	Cu²⁺	Ni²⁺	Co²⁺	Zn²⁺
1	0.1439	0.2007	0.03948	21.6699
2	0.2129	0.4629	0.03951	250.8943
3	0.1323	0.6166	0.0386	1071.8711
4	0.05735	0.4599	0.03678	2637.4584
5	0.1589	0.2743	0.0478	73.0732
6	0.06992	0.4667	0.03525	2.7565
7	0.1539	0.1558	0.04178	49.6374
8	0.237	0.3926	0.05878	138.4649
9	0.09267	0.4719	0.05615	40.839
10	0.2045	0.1722	0.04058	46.3329
11	0.3302	0.2998	0.04467	0.7753
12	0.2056	0.4229	0.07192	2.7098
13	0.4639	0.1844	0.05382	34.7992
14	0.2931	0.1822	0.05179	1.8646
15	0.1265	0.7322	0.06328	2.0041
16	0.2905	1.038	0.06751	0.5478
R	**0.6718**	**0.9636**	**0.4764**	**0.6117**

Conclusions

Thus, matrix experiments have been performed for each type of the inorganic transition metal salt using the mathematical design of the experiment.

The amount of copper deposited on a marble surface has been established to be affected only by the concentration of copper sulfate solution. The other factors are not significant. Hypothetically, the weak deposition of basic copper carbonate has been particularly influenced by the presence of Trilon B in solution, binding copper ions in a sufficiently strong complex.

For nickel, the obtained results can be used to predetermine the effect of strength of the complex with a transition metal ion on deposition of an insoluble compound on the carbonate surface.

Acetate forms a less strong complex with nickel and prevents its deposition in the form of hydroxide in the presence of KOH. Thus, acetate does not prevent the Ni^{2+} ion to react with calcium carbonate in the basic medium. This feature is confirmed by the fact that nickel hydroxide deposits with increasing KOH concentration. In addition, the complex of copper with Trilon B does not deposit at a high KOH content in solution. The solution concentration has the least effect on the amount of the deposited basic nickel carbonate. Thus, it indicates a low reaction rate, which is limited by the specific surface of calcium carbonate.

Deposition of cobalt under the specific conditions is very weak, i.e., it is confirmed by very low concentration of cobalt in all analyzed solutions. The cobalt citrate complex has the sufficient strength to prevent the formation of cobalt hydroxide deposit at the high concentrations of KOH in the solution. The strong complex is also thought to slow down the reaction of cobalt with calcium carbonate. However, in model solutions, cobalt without the extraneous ions showed a much lower deposition rate on the $CaCO_3$ surface than ions of nickel or copper. Therefore, the influence of a complexing agent is not significant. The conducted research described that the significant factors are the basicity of solution and concentration of cobalt sulfate.

For zinc, deposition under the specific conditions is highly dependent on the influencing factors. The amount of the deposited zinc varies within a wide range. Zinc deposition elevates with increasing concentration of the complexing agent. However, zinc deposition is maximized in the absence of a complexing agent. Thus, it indicates that the strength of zinc complexes is high to slow down the reaction of zinc with calcium carbonate. All studied factors are significant. The most significant factors are the basicity of solution and concentration of zinc sulfate. However, the basicity of solution has a positive correlation with the amount of the deposited zinc, but the concentration of zinc sulfate has a negative correlation.

References

1 Popelka, A., Padmanabhan, A.C., Elgendy, A.S., Sobolciak, P., Krupa, I., Bin Yousaf, A., Sebesta, M., Tkac, J., & Kasak, P. (2023). Perfluoroctylsilane grafted Ti3C2X-based hydrogel liquid marble for controlled movement, self-assembly, light-induced release, and water evaporation system. *Materials Today Communications*, 35, 105529. http://dx.doi.org/10.1016/j.mtcomm.2023.105529

2 Papasergio, A.E., Ugolotti, G., Sassoni, E., & Lessio, M. (2023). Adsorption of water and organic solvents on the calcite [1014] surface: Implications for marble conservation treatments. *Applied Surface Science*, 616, 156438. http://dx.doi.org/10.1016/j.apsusc.2023.156438

3 Vrochidou, E., Sidiropoulos, G.K., Ouzounis, A.G., Lampoglou, A., Tsimperidis, I., Papakostas, G.A, Sarafis, I.T, Kalpakis, V., & Stamkos, A. (2022). Towards Robotic Marble Resin Application: Crack Detection on Marble Using Deep Learning. *Electronics*, 11, 20, 3289. http://dx.doi.org/10.3390/electronics11203289

4 Hammouda, M., Ghienne, M., Dion, J.L., & Ben Yahia, N. (2022). Linear regression and artificial neural network models for predicting abrasive water jet marble drilling quality. *Advances in Mechanical Engineering*, 14, 9, 16878132221123426. http://dx.doi.org/10.1177/16878132221123426

5 Singha, P., Nguyen, N.K., Nguyen, V., Sreejith, K.R., Tran, D., Nguyen, A.V., Nguyen, N.T., & Ooi, C.H. (2022). Investigation of liquid marble shell using X-ray: shell thickness and effective surface tension. *Chemnanomat*, 8, 1, 423-428. http://dx.doi.org/10.1002/cnma.202100423

6 Zha, J.R., Wei, S.Y., Han, H.R., Wang, F., & Ma, Q.L. (2020). Two-step method for preparing calcium oxalate film on marble surface for stone protective. *Materials Research Express*, 7, 12. http://dx.doi.org/10.1088/2053-1591/abce22

7 Lopez, R., Li, H., Norret, M., Iyer, S., Biggs, S., & Atkin, R. (2020). Hydrophobic Coatings Using Polymer Blends for the Surface Protection of Marble. *Colloids And Surfaces A-Physicochemical And Engineering Aspects*, 599, 124796. http://dx.doi.org/10.1016/j.colsurfa.2020.124796

8 Pappu, A., Chaturvedi, R., & Tyagi, P. (2020). Sustainable approach towards utilizing Makrana marble waste for making water resistant green composite materials. *SN Applied Sciences*, 2, 3, 347. http://dx.doi.org/10.1007/s42452-020-2133-5

9 Huang, S.G., Lu, J., Chen, S.H., Huang, H., Xu, X.P., & Cui, C.C. (2019). Study on the surface quality of marble tiles polished with Sol-Gel derived pads. *Journal of Sol-Gel Science and Technology*, 91, 3, 485-495. http://dx.doi.org/10.1007/s10971-019-05041-z

10 Melquiades, F.L., Appoloni, C.R., Andrello, A.C., & Spagnuolo, E. (2019). Non-destructive analytical techniques for the evaluation of cleaning and protection processes on white marble surfaces. *Journal of Cultural Heritage*, 37, 54-62. http://dx.doi.org/10.1016/j.culher.2018.10.013

11 Athirah, A.A., Saad, N.A., Akhir, M.F.M., & Zakaria, N.A. (2019). Manganese Removal in Groundwater Treatment Using Marble. *International Journal of Integrated Engineering*, 11, 2, 53-60. http://dx.doi.org/10.30880/ijie.2019.11.01.006

12 Garg, S., Agarwal, P., Ranawat, P.S., Kaur, P., Singh, A., Saini, J., Pandit, M.K., Acharya, K., & Kaur, G.R. (2022). Marble: a Prominent Heritage Stone from Rajasthan, NW India. *Geoheritage*, 14, 1, 4. http://dx.doi.org/10.1007/s12371-021-00621-4

13 Fermo, P., Colella, M., Malagodi, M., Fiocco, G., Albano, M., Marchioron, S., Guglielmi, V., & Comite, V. (2022). Study of a surface coating present on a Renaissance Piety from the Museum of Ancient Art (Castello Sforzesco, Milan). *Environmental Science and Pollution Research*, 29, 20, 29498-29509. http://dx.doi.org/10.1007/s11356-021-16244-9

14 Hu, L.J., Zhang, X.B., Wang, H., Zhang, J.L., Xia, R.Y., Cao, J.W., & Pan, G.F. (2021). Experimental and density functional theory study of complexing agents on cobalt dissolution in alkaline solutions. *Electrochimica Acta*, 375, 137977. http://dx.doi.org/10.1016/j.electacta.2021.137977

15 Li, Y.P., Xi, M.F., Jiang, B.W., Li, X.A., Zhang, Y.F., & Zhang, Z.F. (2023). Structure-Performance Relationships of Complexing Agents on the Chemical Mechanical Polishing of 6063 Aluminum Alloy. *Journal of Solid State Science and Technology*, 12, 4, 044001. http://dx.doi.org/10.1149/2162-8777/acbedc

16 Zhang, W., Lei, H., Liu, W.Q., & Zhang, Z.F. (2023). Effect of the carboxyl group number of the complexing agent on polishing performance of alumina slurry in sapphire CMP. *Ceramics International*, 49, 9, 13687-13697. http://dx.doi.org/10.1016/j.ceramint.2022.12.246

17 Kumaran, T.M., Jothilakshmi, S., & Rekha, S. (2020). Influences of bath chemistry and complexing agent on plating rate in electroless copper methane sulphonate bath. *Journal of the Indian Chemical Society*, 97, 11B, 2427-2432.

18 Borzenko, S.V., & Fedorov, I.A. (2019). Basic forms of metals migration in the presence of humic substances in soda lakes of Eastern Transbaikalia. *Bull. Tomsk Polytech. Univ., Geo Assets Eng.*, 303(3), 18-27. http://dx.doi.org/10.18799/24131830/2019/3/155

19 Potysz, M., Grybos, J., Kierczak, G., Guibaud, P., Fondaneche, P.N.L., & Lens, E.D. van Hullebusch. (2017). Metal mobilization from metallurgical wastes by soil organic acids. *Chemosphere*, 178, 197-211. http://dx.doi.org/10.1016/j.chemosphere.2017.03.015

20 Seda, N.N., Koenigsmark, F., & Vadas, T.M. (2016). Sorption and coprecipitation of copper to ferrihydrite and humic acid organomineral complexes and controls on copper availability. *Chemosphere*, 147, 272-278. http://dx.doi.org/10.1016/j.chemosphere.2015.12.106

21 Zhizhaev, A.M., Merkulova, E.N., & Bragin, I.V. (2007). Copper precipitation from sulfate solutions with calcium carbonates. *Russian Journal of Applied Chemistry*, 80, 10, 1632-1635.

22 Fomin, V.N., Rozhkovoy, I.E., Gogol, D.B., & Ponomarev, D.L. (2015). Thermodynamic parameters of reactions of basic copper carbonates formation with participation of organic complexing agents. *Bulletin of the Karaganda University Chemistry*, 4(80), 22-26.

23 Fomin, V.N., Gogol, D.B., Rozhkovoy, I.E., & Ponomarev, D.L. (2017). Quantum-chemical and thermodynamic calculation of parameters of fulvate and humate copper complexes and malachite formation reactions with their involving. *Applied Geochemistry*, 79, 9-16.

24 Nassrallah-Aboukaïs, N., Boughriet, A., Laureyns, J., Gengembre, L., & Aboukaïs A. (1999). Stabilization of the vaterite structure in the presence of copper(II): Thermodynamic and spectroscopic studies. *Chemistry of Materials*, 11, 1, 44-51.

25 Meloni, P., Manca, F., & Carcangiu, G. (2013). Marble protection: An inorganic electrokinetic approach. *Applied Surface Science*, 273, 377-385.

26 Malyshev, V.P. (1994). *Veroiatnostno-determinirovannoe otobrazhenie [Probabilistic and Deterministic Mapping]*. Almaty, Gylym, 376 p. [in Russian]

27 Malyshev, V.P., Makasheva, A.M., & Bekbayeva, L.A. (2021). Invariants of ratio of crystal-mobile, liquid-mobile, and vaporized chaotized particles in solid, liquid, and gas states of substance. *Bulletin of the University of Karaganda Chemistry*, 104(4), 69-78. https://doi.org/10.31489/2021Ch4/69-78

Information about authors*

Gogol, Daniil Borisovich — Candidate of chemical sciences, Associate Professor, Chief Researcher, Institute of Problems of Complex Development of Mineral Resources, Ippodromnaya Str. 5, 100019, Karaganda, Kazakhstan; e-mail: d.gogol@ipkon.kz; https://orcid.org/0000-0002-1319-5818

Rozhkovoy, Ivan Evgenjevich — Researcher, Institute of Problems of Complex Development of Mineral Resources, Ippodromnaya Str. 5, 100019, Karaganda, Kazakhstan; e-mail: rozhkovoy@inbox.ru; https://orcid.org/0000-0001-5193-5904

Sadyrbekov, Daniyar Tleuzhanovich — Candidate of chemical sciences, Leading Researcher, Karaganda Buketov University, Universitetskaya Str. 28, 100026, Karaganda, Kazakhstan; e-mail: acid-bear@mail.ru; https://orcid.org/0000-0002-3047-9142

Makasheva, Astra Mundukovna (*corresponding author*) — Doctor of Technical Sciences, Professor, Head of the Laboratory, Abishev Chemical and Metallurgical Institute, Ermekov street, 63, 100009, Karaganda, Kazakhstan; e-mail: astra_mun@mail.ru; https://orcid.org/0000-0003-2249-3435

_____
*The author's name is presented in the order: *Last Name, First and Middle Names*

Article

https://doi.org/10.31489/2959-0663/4-23-9

Maria D. Plotnikova [iD], Marina G. Shcherban′* [iD], Anastasia D. Shitoeva [iD],
Alexander N. Vasyanin [iD], Anatoly B. Shein [iD]

Perm State National Research University, Perm, Russia
(*Corresponding author′s e-mail: ma-sher74@mail.ru)

The Role of Surface Hydrophobization of Mild Steel by Some Triazole Derivatives in Acidic Medium

Triazole derivatives (4,5-diphenyl-4H-1,2,4-triazole-3-thiol (4,5-PhTAT) and 3,4-diphenyl-5-(prop-2-yn-1-ylthio)-4H-1,2,4-triazole (3,4-PhPTTA) have been researched as corrosion inhibitors for mild steel in 0.1 N sulfuric acid solution. Electrochemical methods were used to estimate the corrosion rate and the inhibition efficiency: potentiodynamic polarization and impedance spectroscopy. The semi-empirical GFN2-xTB method, taking into account their implicit solvation in water using the ALPB method in the XTB program have been used for Geometry optimization of the structures of individual compounds and protomers in solution. Quantum chemical calculations suppose predominantly protonated structure for 3,4-PHPTTA molecules and neutral form of molecules for 4,5-PhTAT. According to electrochemical measurements the best inhibition efficiency for 4,5-PhTAT achieved at 50 mg·l^{-1} and 200 mg·l^{-1} for 3,4-PhPTTA. 4,5-PhTAT and 3,4-PHPTTA are the mix-type inhibitors in 0.1 N sulfuric acid solution, but rate of cathodic process is decreased more than anodic. Contact angle measurements were carried out by the sessile drop method. Hydrophobization of the steel surface occurs in the blank acid and inhibited solution. The contact angle measurements by two test liquids (water and diethylene glycol) after corrosion with presents 4,5-Pstat and 3,4-PHPTTA show that the protective film formed in inhibited solution.

Keywords: corrosion, inhibitor, triazoles, polarization curves, surface tension, impedance spectroscopy, quantum chemical calculations, sessile drop method.

Introduction

Corrosion is a widely studied field of science. The use of inhibitors to control the corrosion in acid medium was found to have widespread applications [1–4]. The corrosion inhibition of steel in acidic medium by organic inhibitors was studied in considerable detail. Triazoles derivatives are N-heterocyclic compounds containing a five-member ring with three nitrogen atoms. Their molecules play important roles in biology due to their extensive biological interactions [4] and in chemistry due to their ability to inhibit corrosion of metals and alloys [1–3]. Today heterocycles inhibitors leading to minimize the corrosion process in metals [5–7]. The use of heterocycles inhibitors is of significant interest because of their economical synthesis methods and high protection efficiency [8, 9]. Among them, triazole derivatives have been researched as effective corrosion inhibitors for steel in acidic media [6, 7]. The inhibition efficiency depends on many factors: the nature of the metal surface, the inhibitor molecular structure — the number of adsorption active centers in the molecule, the charge density, the molecular size, and the ability of this molecule to interact with a metal surface. In order to understand action mechanisms of corrosion inhibitors, there are numerous experimental (electrochemical) [8, 9] and theoretical (quantum chemical) [10, 11] studies. One of the key approaches is the film theory of inhibitors [12, 13], according to the inhibition efficiency is due to the formation of a hydrophobic film on the metal surface. This film can be investigated by the sessile drop method [12–18]. The energy of the surface changes when the inhibitor film is formed and some adsorption centers appear and disappear on it. This can be measured by the method of steel surface contact angles with tested liquids and calculated the components (polar and dispersion) of the free surface energy with increase in the inhibitor concentration. The purpose of this work is to study the protective effect of some triazole derivatives against corrosion of low-carbon steel and to confirm the film theory of adsorption of organic heterocyclic corrosion inhibitors by both experimental electrochemical, surface physico-chemical methods and theoretical quantum chemical calculations.

Experimental

The tested inhibitors, namely 4,5-diphenyl-4H-1,2,4-triazole-3-thiol (4,5-PhTAT) and 3,4-diphenyl-5-(prop-2-yn-1-ylthio)-4H-1,2,4-triazole (3,4-PhPTTA), were synthesized according to a previously described experimental procedure [6, 18]. The concentration range of both inhibitors was 10–200 mg·l^{-1}.

Geometry optimization of the structures of individual compounds was carried out using the semi-empirical GFN2-xTB method, taking into account their implicit solvation in water using the ALPB method in the XTB program [19, 20]. The calculation of the mole fractions of individual protomers in solution at 298.15 K was performed using the Boltzmann distribution based on the computed Gibbs energies of the optimized structures. The estimation of the protonation constants of compounds was done using the ChemAxon Marvin pK$_a$ Plugin [21].

Electrochemical measurements were carried out using the electrochemical system Solatron 1280C. Steel potentials were measured relative to a silver chloride electrode. Potentiodynamic polarization and impedance measurements were performed using a glass electrochemical cell with an external space for silver chloride and counter platinum electrodes. Voltammetric studies were performed according to a three-electrode scheme in potentiodynamic mode at a working electrode potential sweep rate of 0.5 mV·s^{-1}. Prior to polarization, the electrode was kept in the test solution for 30 min to establish a free corrosion potential, Ecor. Impedance measurements were recorded in the range of frequencies f from 20 kHz to 0.1 Hz, a sine wave with 5 mV amplitude was used to perturb the system. The criterion for estimating equivalent electrical circuits was the χ^2 parameter calculated in ZView2. A satisfactory equivalent scheme is for χ^2 less than 10^{-3} when weight coefficients calculated from experimental values of the impedance modulus. All potentials are reported vs standard hydrogen electrode.

Working electrodes with the composition, wt.%: Fe — 98.27; C — 0.20; Mn — 0.50; Si — 0.30; P — 0.04; S — 0.04; Cr — 0.15; Ni — 0.30; Cu — 0.20, were used in the study. The experiments were conducted in 0.1 N solution were prepared from chemically pure H_2SO_4 and distilled water.

The corrosion rate, *ICR* (cm·s^{-1}), was estimated through the following equation combining Stern-Geary and Faraday equations:

$$ICR = (MB)/(zFS\rho R_p),$$

where *M* is average molecular weight of the metal or metal alloy (g·mol^{-1}), *S* is the surface area (cm^2), *F* is the Faraday constant [96 485 A·s·mol^{-1}], *z* is the average charge of the metal, and ρ is the density of the metal (g·cm^3), *B* is the Stern-Geary constant (V) defined as $B = b_ab_c/2.3(b_a + b_c)$, R_p is polarization resistance, (Ω). Units of corrosion rate in this paper are given in mm·year^{-1}.

According to the theory of polarization resistance the R_p method is based on charge balance and the current-potential relationship (Tafel relationship) for electron-transfer reactions. R_p is defined as the differential of the overpotential, ΔE (volt), over the withdrawn current, i_{corr} (amp), when the slope of polarization curves at the corrosion potential:

$$R_p = dE/di = b_ab_c/2.3i_{cor}(b_a + b_c) = B/i_{corr},$$

where b_a and b_c are anodic and cathodic Tafel constants (volt), i_{corr} is the corrosion current (A·cm^{-2}) [22, 23].

The inhibition efficiency for each concentration of inhibitors was calculated according to the equation,

$$IE(\%) = (1 - i_{corr}/i_{0corr})\cdot 100,$$

where *IE*, is the inhibition efficiency, i_{corr} and i_{0corr} are the corrosion current densities (A·cm^{-2}) with and without inhibitor, respectively. The corrosion current density (i_{corr}) was determined by extrapolating the Tafel lines.

On the basis of Young's equation plus Owen-Wendt's theory, the surface free energies of the steel surface can be calculated using the contact angles between the two test liquids (water and diethylene glycol) and steel surface [24, 25]. Contact angle measurements were carried out using a tensiometer DSA 25E (KRUSS) by the sessile drop method [26]. Test liquids (liquid with known the value of surface tension) were dropped to the surface of the sample using a dispenser, after that the angle between three phases (steel, test liquid and air) was measured. The volume of test liquids was 1–2 µl. All the experiments were carried out after immersion of mild steel for 24 hours in 0.1 N H_2SO_4 in absence and presence of different concentrations of inhibitors. After immersion samples were cleaned with distilled water repeatedly and dried in hot air, then the contact angles were measured.

Results and Discussion

Based on the structural characteristics of 4,5-PhTAT, it is reasonable to posit that this compound exhibits amphiprotic behavior in aqueous systems, where it can undergo both protonation and deprotonation reactions. According to free energy calculations, the tautomeric form with proton moved to the N atom dominates in the neutral state (Fig. 1).
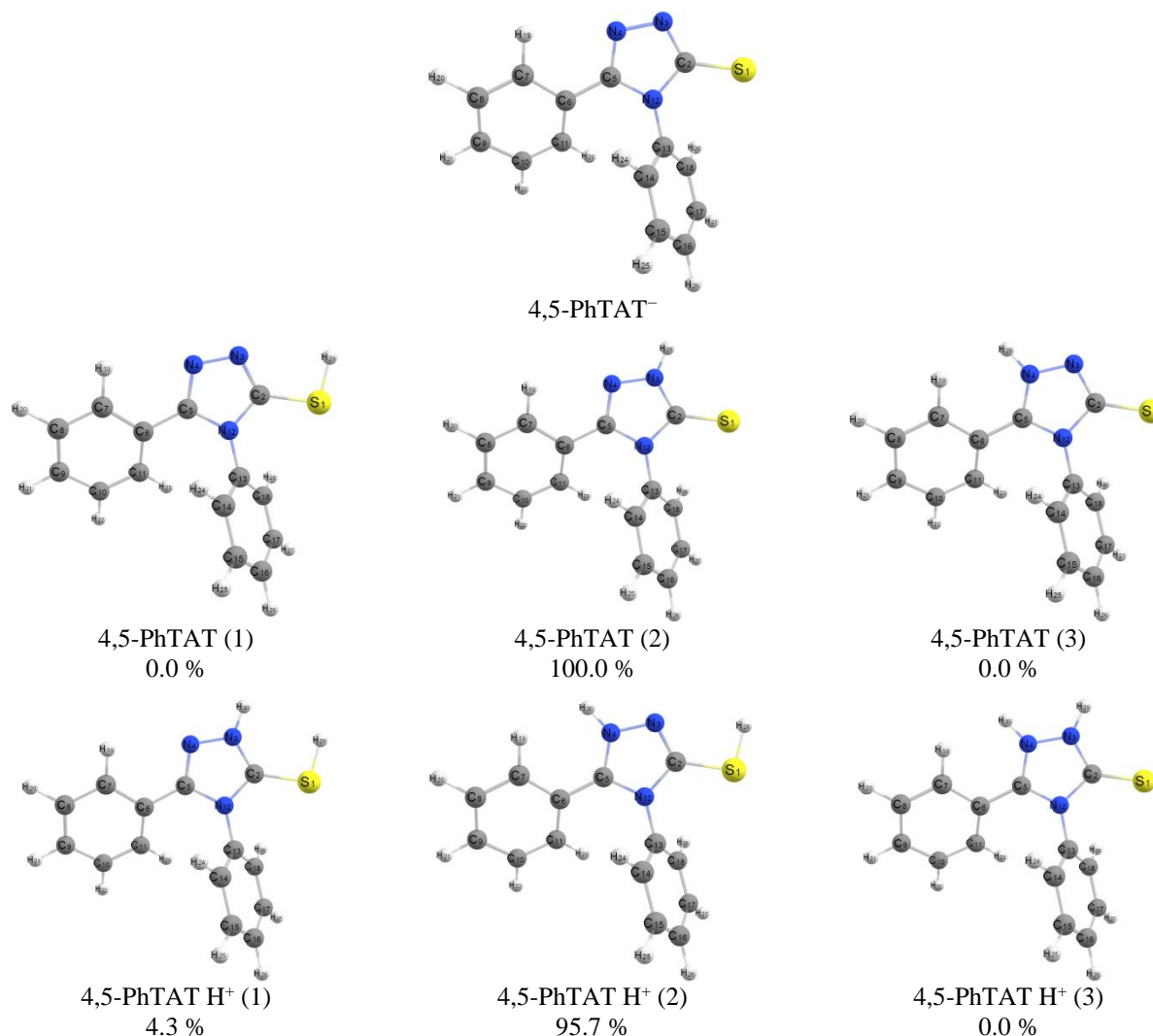

4,5-PhTAT⁻

4,5-PhTAT (1)	4,5-PhTAT (2)	4,5-PhTAT (3)
0.0 %	100.0 %	0.0 %

4,5-PhTAT H⁺ (1)	4,5-PhTAT H⁺ (2)	4,5-PhTAT H⁺ (3)
4.3 %	95.7 %	0.0 %

Figure 1. The optimized geometries of the deprotonated molecule (anion) 4,5-PhTAT,
as well as the tautomers of the neutral molecule and its mono-protonated form obtained
at the GFN2-xTB[ALPB(H_2O)] theory level with their relative fractions (%) in solution at 298.15 K

The protonation/deprotonation equilibrium constants were computed using the Marvin pK_a Plugin program, taking into account tautomerization. The results indicate that deprotonation is the only feasible outcome in solutions with weakly alkaline properties (pK_a = 7.21). Conversely, the calculations strongly suggest that protonation is practically unattainable, as evidenced by the extremely low predicted value of the corresponding equilibrium constant (pK_a = –4.65). Notably, the calculations reveal that among the three feasible tautomers of the protonated form present in solution, the 4,5-PhTAT H⁺ (2) tautomer is expected to be the predominant species.

Protonation of 3,4-PHPTTA

Only protonation processes are possible for 3,4-PHPTTA. In contrast to 4,5-PhTAT, protonation of 3,4-PHPTTA is entirely possible in strongly acidic aqueous solutions (with a pKa value of 0.97 for the 3,4-PHPTTA H⁺(1) form and 0.22 for the 3,4-PHPTTA H⁺(2) form). The calculation of the molar fraction of monoprotonated forms using the GFN2-xTB[ALPB(H_2O)] method agrees well with the results obtained from the Marvin pK_a Plugin and confirms the predominance of the 3,4-PHPTTA H⁺ (1) protomer (Fig. 2).

3,4-PHPTTA

3,4-PHPTTA H$^+$(1)
89.3 %
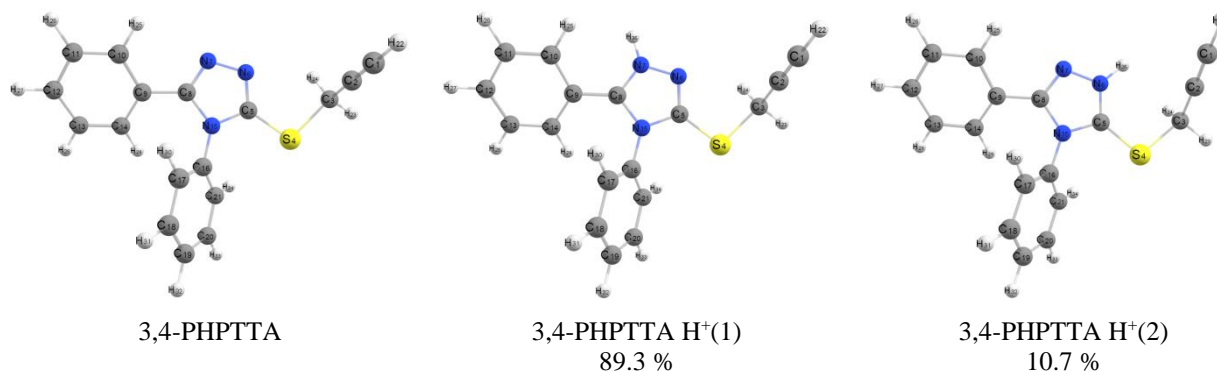
3,4-PHPTTA H$^+$(2)
10.7 %

Figure 2. The optimized geometries of the neutral molecule 3,4-PHPTTA and its monoprotonated tautomers obtained at the GFN2-xTB[ALPB(H$_2$O)] level of theory with their relative fractions (%) in solution at 298.15 K

Based on the results of the calculations, it was shown that in acidic H$_2$SO$_4$ solutions, inhibitors 4,5-PhTAT and 3,4-PHPTTA exist in different forms: 3,4-PHPTTA molecules are predominantly protonated, while 4,5-PhTAT exists as neutral molecules.

Polarization curves for mild steel in 0.1 N H$_2$SO$_4$ solution without and with addition of 100 mg·l^{-1} of 4,5-PhTAT and 3,4-PhPTTA are shown in Figure 3.
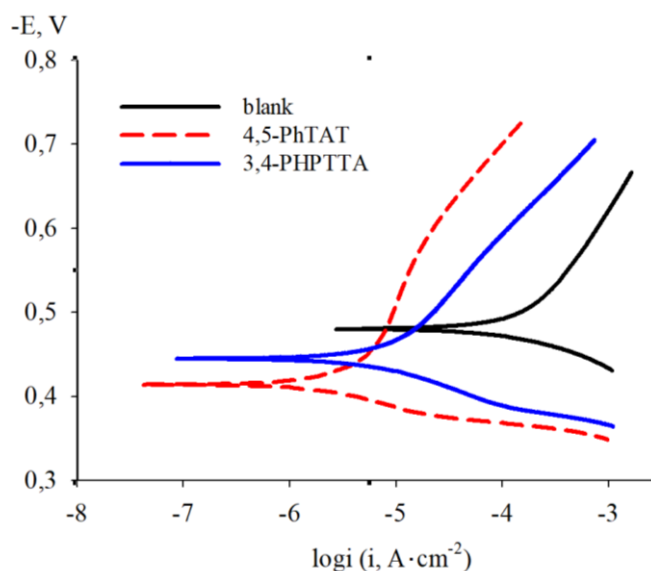
Figure 3. Potentiodynamic polarization curves for mild steel
in 0.1 N H$_2$SO$_4$ with different triazole derivatives

Analysis of Figure 3 and Table 1 reveals that the presence of both triazoles resulted in a shift of the corrosion potential towards the anodic direction in comparison with the result obtained in the blank acid solution (Table 1). The anodic and the cathodic current densities were decreased, indicating that 4,5-PhTAT and 3,4-PhPTTA suppressed both the anodic and cathodic reactions (Fig. 3).

Table 1 shows that in the case of 4,5-PhTAT corrosion current decreased already at 10 mg·l^{-1} and had minimal value at 50 mg·l^{-1}, then it slightly increased with the growth concentration. If added to the system 3,4-PhPTTA, corrosion currents slowly decrease with increasing concentration, it appears from 50 mg·l^{-1}.

Figure 3 demonstrates that polarization curves show two linear parts in the anode region in the presence of inhibitors, but Table 1 shows only Tafel coefficients near by corrosion potential. It is shown that, the injection of inhibitors decreased the rate of cathode process greater than anodic, as the b$_c$ has increased with raising concentration. According to linear polarization results, the corrosion rate decreases from 1.13 mm·year^{-1} to 0.023 and 0.049 mm·year^{-1} (47 and 23 times) with presence 4,5-PhTAT and 3,4-PhPTTA respectively.

Polarization Parameters for Mild Steel in 0.1 N H₂SO₄ Solution
Containing Different Concentrations of 4,5-PhTAT and 3,4-PhPTTA at 298 K

Inhibitor	C, mg·l⁻¹	Tafel polarization				Linear polarization	
		$-E_{corr}$, mV	i_{corr}, A·cm⁻²	b_a, mV	b_c, mV	R_p, Ω	ICR, mm·year⁻¹
–	–	677	$8.34 \cdot 10^{-5}$	51	125	190	1.13
4,5-PhTAT	10	625	$3.56 \cdot 10^{-5}$	53	132	2994	0.041
	50	619	$2.45 \cdot 10^{-6}$	55	140	5154	0.023
	100	614	$2.09 \cdot 10^{-6}$	54	160	4831	0.024
	200	604	$2.87 \cdot 10^{-6}$	51	189	4466	0.033
3,4-PhPTTA	10	672	$8.10 \cdot 10^{-5}$	48	120	200	1.25
	50	654	$9.19 \cdot 10^{-6}$	45	130	1603	0.11
	100	645	$7.15 \cdot 10^{-6}$	47	158	1943	0.083
	200	601	$4.18 \cdot 10^{-6}$	50	157	2493	0.049

Figure 4 shows the Nyquist diagrams of impedance data of mild steel in 0.1 N sulfuric acid solution with different concentrations 4,5-PhTAT and 3,4-PhPTTA. Impedance spectra in pure acid solution are presented as the insertion on one of the diagrams. These diagrams (Fig. 4) at E_{corr} are characterized by a depressed capacitive semicircle at high to medium frequencies. The dispersion is explained by surface heterogeneity due to surface roughness [26, 27]. Hence the inhibition efficiency has a tendency to grow as the values of R_{ct} increase.

(*a*)

(*b*)
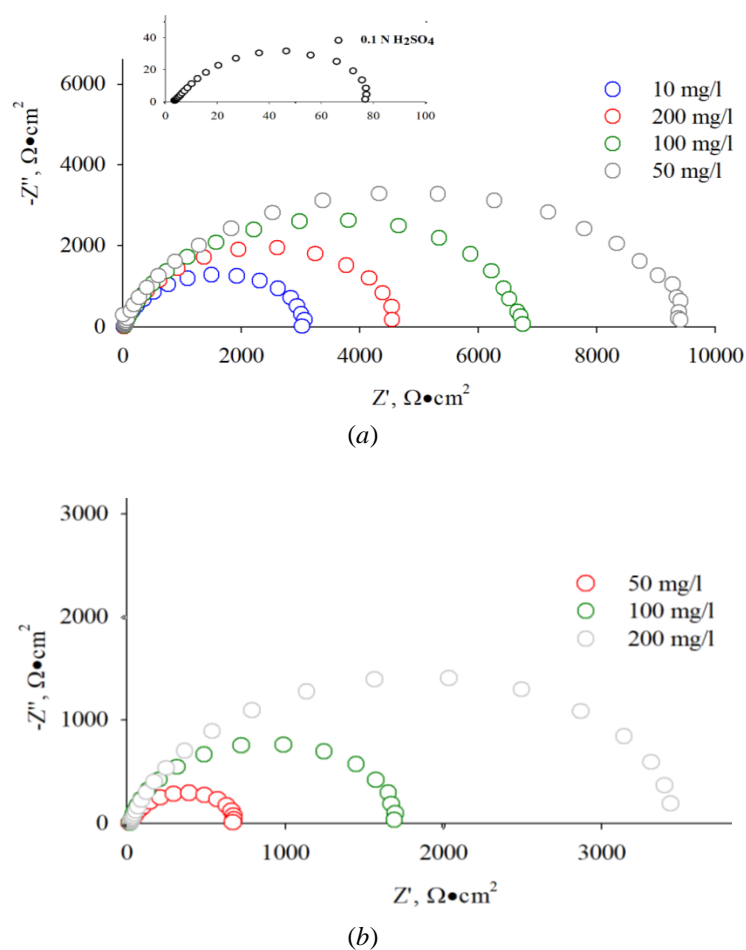
Figure 4. Nyquist diagrams of mild steel in a solution of 0.1 N H₂SO₄ at E_{corr}
with addition of various concentration of (*a*) and (*b*) 3,4-PhPTTA

The calculation results correlate with the electrochemical results. 4,5-PhTAT gives a greater inhibition efficiency than 3,4-PhPTTA at low concentration due to the neutral form of molecules. The protonated form of 3,4-PhPTTA molecules at low concentration are pushed off the surface of mild steel with positive charge in sulfuric acid solution.

The calculation of the free surface energy (SFE) of steel was carried out before and after contact with a corrosive medium to confirm the assumptions about the formation of the protective film and the chemical nature of adsorption. The value of SFE due to the isolation of its polar (γ^p) and dispersion (γ^d) components can indicate the direction of further modification to increase resistance of the corrosion system.

The surface energy parameters were calculated based on the analysis of the Owen-Wendt's equation:

$$W_a = \gamma_{LG}(1 + \cos\theta_C) = 2(\gamma^d_{SG} \gamma^d_{LG})^{0,5} + 2(\gamma^p_{SG} \gamma^p_{LG})^{0,5},$$

where W_a — work of adhesion, γ_{LG} — the liquid/air interfacial tension, γ^d_{SG}, γ^p_{SG} — polar and dispersive component of surface energies of steel, γ^p_{LG}, γ^d_{LG} — polar and dispersive component of surface tension of test liquids, $\cos\theta_C$ — the contact angle for test liquids at steel surface after corrosion.

Figure 5 demonstrates images of test liquids drops on the steel surface after exposition in corrosion medium with inhibitors during 24 hours.

(*a*)

(*b*)
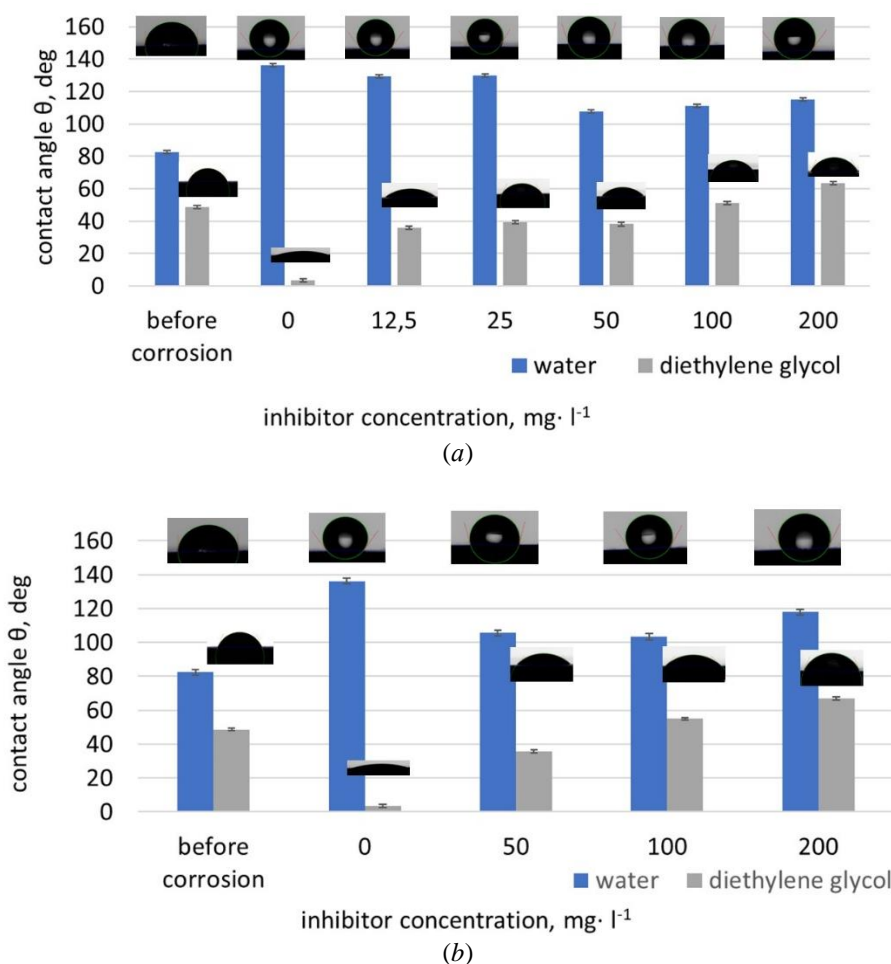
Figure 5. Surface wettability of steel surface after corrosion in 0.1 N H_2SO_4 solution with (*a*) 4,5-PhTAT and (*b*) 3,4-PhPTTA

In general, the steel surface before corrosion has a hydrophilic character, since metals and metal alloys have high surface energy values and wettability by liquids with lower surface tensions. Thus, the surface energies of ferrite and cementite are 2482 and 2050 mJ·m^{-2} [25], these steel phases are wetted by water with surface tension 72 mJ·m^{-2} [28]. According to [29], the contact angle of mild steels by water is about 64° [30]. In our case, the contact angle is 82°, this value is close to the contact angle on pyrolytic graphite (83.9°). This allows to propose that the surface is enriched by carbon.

The contact angle increased to 136° after exposure of samples in pure sulfuric acid that leads to surface hydrophobization significantly. After that surface roughness increased as a result of iron dissolution and surface enrichment by carbon — the contact angles are close to those of fine-dispersed graphite and graphene [28, 29]. The hydrophobicity is also shown by the wettability of the steel by less polar liquid after immersion in pure acid. The contact angles decrease from 48° to 3°, if the test liquid is changed from water to diethylene glycol.

The steel surface is also hydrophobized in the presence of the inhibitors (contact angles range from 105° to 130°); however, this is caused by other reasons. In this case, the hydrophobicity increased probably due to the formation of a protective film of inhibitor on the steel surface. The contact angle of the primary steel surface is 48,7°±0,9°, then after corrosion in sulfuric acid it is decreased to 3,6°±0,5° and finally the contact angle in presence of inhibitors changes in the range of 35–70°. There is a tendency to growth with increasing inhibitor concentration.

These changes in the wettability of test liquids after corrosion indicate a different state of steel surface. Figure 6 demonstrates the redistribution of the polar and dispersion components of the free surface energy, its values and the inhibition efficiency are given in Table 2.

The immersion of the samples in blank sulfuric acid leads to significant hydrophobization of the steel surface, the contact angle increases to 136̊ as a result of the dissolution of iron and the surface enrichment with carbon [31-33].

The steel surface in the presence of an inhibitor is also hydrophobized — the contact angles are in the range of 105̊ — 130̊. Probably, the effect of hydrophobization of the surface is associated with the formation of a protective film of the inhibitor, and not with the increase of the carbon concentration on the steel surface.

Also the ratio of the polar and dispersion components of the free surface energy changes when samples are kept in inhibited acid. Calculated SFE values and the degrees of protection calculated from the results of weight loss testing are presented in Table 2.

T a b l e 2

Surface energies for test liquids (22° C) and degree of protection of St3 after weight loss tests in the presence of triazole derivatives in 0.1 N H₂SO₄ solution

Conc., mg·l⁻¹	γ^p_{SG}, mJ·m⁻²	γ^d_{SG}, mJ·m⁻²	γ_{SG}, mJ·m⁻²	$\gamma^d_{SG}/\gamma^p_{SG}$	Z, %
Before immersion	6,2	24,98	31,18	4,0	
0	43,4	149,96	193,32	3,5	
4,5-PhTAT					
50	3,73	70,19	73,92	18,8	96
100	6,40	78,18	84,58	12,2	92
200	9,25	83,96	93,21	9,1	92
3,4-PhPTTA					
50	1,13	53,40	54,53	47,3	94
100	1,06	42,12	43,18	39,7	95
200	2,53	43,28	45,82	17,3	95
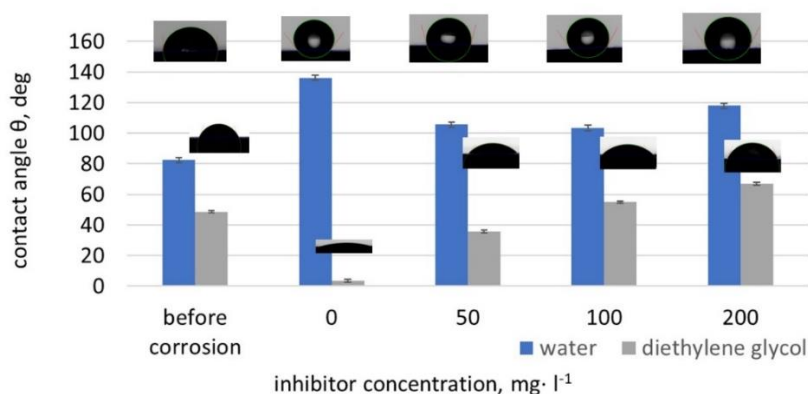
Figure 6. The effect of redistribution of the free surface energy with increasing concentration of inhibitors

4,5-PhTAT has higher value of ratio dispersion and polar components of the free surface energy (Table 2). 4,5-PhTAT forms hydrophobic film at low concentration and, due to this, has inhibition properties already at 10 mg·l⁻¹. 3,4-PhPTTA doesn't have inhibition activity at low concentration.

Conclusions

1. 4,5-diphenyl-4H-1,2,4-triazole-3-thiol (4,5-PhTAT) and 3,4-diphenyl-5-(prop-2-yn-1-ylthio)-4H-1,2,4-triazole (3,4-PhPTTA) act as good inhibitors for mild steel in 0.1 N H_2SO_4, the rate of corrosion is reduced by 47 and 23 times, respectively. The inhibition efficiency depended from concentration: 4,5-PhTAT has the best inhibition efficiency value at 50 mg·l⁻¹ and 3,4-PhPTTA only at 200 mg·l⁻¹.

2. Polarization curves proved that 4,5-PhTAT and 3,4-PhPTTA were mixed type inhibitors, but which can suppress cathodic reactions more. Impedance plots indicated that Rct values increase as well as shown in polarization results. Theoretical calculations provide good support to experimental electrochemical results.

3. The steel surface in the presence of both compounds becomes more hydrophobic, as the contact angle increases from 82° to 120° — 130° depending on the inhibitor concentration. Also, the free surface energy of steel decreases in the presence of inhibitors compared to pure acid (from 193 mJ·m⁻² to 46 — 74 mJ·m⁻²), and the SFE components are redistributed: the contribution of the dispersion component with adding triazole derivatives in corrosion media to the total value of SFE increases by 3-4 times compared to the test steel surface.

4. Redistribution in polar and dispersion components consist of different forms of molecular existence: 3,4-PHPTTA is predominantly protonated, while 4,5-PhTAT is neutral molecules according to quantum chemical calculation.

Acknowledgments

References

1 Awad, M.K., Mustafa, M.R., & Elnga, M.M.A. (2010). Computational simulation of the molecular structure of some triazoles as inhibitors for the corrosion of metal surface. *Journal of molecular structure: theochem*, *959*(1-3), 66-74. https://doi.org/10.1016/j.theochem.2010.08.008

2 Ouicia, H., Tourabib, M., Benalic, O., Sellesd, C., Jamae, C., Zarroukf, A., & Bentiss, F. (2017). Adsorption and corrosion inhibition properties of 5-amino 1,3,4-thiadiazole-2-thiol on the mild steel in hydrochloric acid medium: Thermodynamic, surface and electrochemical studies. *Journal of Electroanalytical Chemistry*, *803*, 125-134. http://dx.doi.org/10.1016/j.jelechem.2017.09.

3 Hrimla, M., Bahsis, L., Laamari, M. R., Julve, M., & Stiriba, S. E. (2021). An overview on the performance of 1, 2, 3-triazole derivatives as corrosion inhibitors for metal surfaces. *International Journal of Molecular Sciences, 23*(1), 16. https://doi.org/10.3390/ijms23010016

4 Bozorov, K., Zhao, J., & Aisa, H.A. (2019) 1,2,3-Triazole-containing hybrids as leads in medicinal chemistry: A recent overview. *Bioorg. Med. Chem., 27 (16)*, 3511–3531. https://doi.org/10.1016/j.bmc.2019.07.005

5 Plotnikova, M.D., Solovyev, A.D., Shein, A.B., Bakiev, A.N., & Sofronov, A.S. (2021). New inhibitors based on substituted 1, 2, 4-triazoles for mild steel in hydrochloric acid solutions. *International Journal of Corrosion and Scale Inhibition*, *10*(3), 1230-1244. https://doi.org/10.17675/2305-6894-2021-10-3-23

6 Plotnikova, M.D., Shitoeva, A.D., Solovyev, A.D., Shein, A.B., & Bakiev, A.N. (2023). Some aspects of the of the mechanism of C1018 steel protection in hydrochloric acid solutions by triazole derivatives. *Int. J. Corros. Scale Inhib., 2023, 12*, no. 2, 511–530. https://doi.org/10.17675/2305-6894-2023-12-2-8

7 Hrimla, M., Bahsis, L., Boutouil, A., Laamari, M.R., Julve, M., & Stiriba, S.E. (2021). Corrosion inhibition performance of a structurally well-defined 1, 2, 3-triazole derivative on mild steel-hydrochloric acid interface. *Journal of Molecular Structure*, *1231*, 129895. doi.org/10.1016/j.molstruc.2021.129895

8 Carranza, M.S.S., Reyes, Y.I.A., Gonzales, E.C., Arcon, D.P., & Franco, F.C. (2021). Electrochemical and quantum mechanical investigation of various small molecule organic compounds as corrosion inhibitors in mild steel. *Heliyon, 7*(9). doi: 10.1016/j.heliyon.2021.e07952

9 Fouda, A.S., Wahba, A.M., & Al-Bonayan, A.M. (2021). Corrosion inhibition of stainless steel in 1.0 M hydrochloric acid solution using novel nonionic surfactant: electrochemical and density functional Theory/B3LYP/6-31G* analysis. *Surface Engineering and Applied Electrochemistry, 57*, 689-702. https://doi.org/10.3103/S1068375521060041

10 Hamani, H., Daoud, D., Benabid, S., & Douadi, T. (2022). Electrochemical, density functional theory (DFT) and molecular dynamic (MD) simulations studies of synthesized three news Schiff bases as corrosion inhibitors on mild steel in the acidic environment. *Journal of the Indian Chemical Society, 99*(7), 100492. https://doi.org/10.1016/j.jics.2022.100492

11 Akpan, E.D., Oladipo, S.D., Quadri, T.W., Olasunkanmi, L.O., Nwanna, E.E., Omondi, B., & Ebenso, E.E. (2022). Formamidine-Based Thiuram Disulfides as Efficient Inhibitors of Acid Corrosion of Mild Steel: Electrochemical, Surface, and Density Functional Theory/Monte Carlo Simulation Studies. *ACS omega, 7*(30), 26076-26091. https://doi.org/10.1021/acsomega.2c00985

12 Liu, P., Huang, X., & Guo Zh. (2023). Superhydrophobic Corrosion Inhibitor Intercalated Hydrotalcite Coating for Enhanced Corrosion Resistance of the Aluminum. *ACS Applied Engineering Materials, 1*(1), 486-494. https://doi.org/10.1021/acsaenm.2c00117

13 Kai An, Wei Tong, Youqiang Wang, Yongquan Qing, Yi Sui, Ying Xu, & Chenbing Ni. (2023). Eco-Friendly Superhydrophobic Coupling Conversion Coating with Corrosion Resistance on Magnesium Alloy. *Langmuir*, *39*(18), 6355-6365. https://doi.org/10.1021/acs.langmuir.3c00025

14 Barkhudarov, P.M., Shah, P.B., Watkins, E.B., Doshi, D.A., Brinker, C.J., & Majewski, J. (2008). Corrosion inhibition using superhydrophobic films. *Corrosion Science*, *50*(3), 897-902. https://doi.org/10.1016/j.corsci.2007.10.005

15 Pandarinathan, V., Lepkova, K., Bailey, S., Becker, T., & Gubner, R. (2014). Adsorption of corrosion inhibitor 1-dodecylpyridinium chloride on carbon steel studied by in situ AFM and electrochemical methods. *Industrial and Engineering Chemistry Research*, *53*(14), 5858-5865. https://doi.org/10.1021/ie402784y

16 Umoren, S.A., Obot, I.B., Madhankumar, A., & Gasem, Z.M. (2015). Performance evaluation of pectin as ecofriendly corrosion inhibitor for X60 pipeline steel in acid medium: Experimental and theoretical approaches. *Carbohydrate Polymers*, *100*(124), 280-291. https://doi.org/10.1016/j.carbpol.2015.02.036

17 Ma, X., Dang, R., Kang, Y. H., Gong, Y., Luo, J., Zhang, Y. Y.,... & Ma, Y. J. (2020). Electrochemical studies of expired drug (formoterol) as oilfield corrosion inhibitor for mild steel in H2SO4 media. *International Journal of Electrochemical Science*, *15*, 1964-1981. https://doi.org/10.20964/2020.03.65

18 Plotnikova, M.D., Solovyev, A.D., Shein, A.B., Vasyanin, A.N. & Sofronov, A.S. (2021). Corrosion inhibition of mild steel by triazole and thiadiazole derivatives in 5 M hydrochloric acid medium. *Int. J. Corros. Scale Inhib., 9*(3), 1336–1354. https://doi.org/10.17675/2305-6894-2021-10-3-29

19 C. Bannwarth, E. Caldeweyher, S. Ehlert, A. Hansen, P. Pracht, J. Seibert, S. Spicher, & S. Grimme. (2021). Extended tight-binding quantum chemistry methods. *WIREs Computational Molecular Science*, 11, 1493. https://doi.org/10.1002/wcms.1493

20 C. Bannwarth, S. Ehlert, & S. Grimme. (2019). GFN2-xTB—An Accurate and Broadly Parametrized Self-Consistent Tight-Binding Quantum Chemical Method with Multipole Electrostatics and Density-Dependent Dispersion Contributions, *J. Chem. Theory Comput*, 15, 1652–1671. https://doi.org/10.1021/acs.jctc.8b01176.

21 Caine, B.A., Dardonville, Ch., & Popelier, L.A. (2018). Prediction of Aqueous pKa Values for Guanidine-Containing Compounds Using Ab Initio Gas-Phase Equilibrium Bond. *ACS Omega*, 3, 3835−3850. https://doi.org/10.1021/acsomega.8b00142

22 Ma, I.W., Ammar, S., Kumar, S.S., Ramesh, K., & Ramesh, S. (2022). A concise review on corrosion inhibitors: types, mechanisms and electrochemical evaluation studies. *Journal of Coatings Technology and Research*, 1-28. https://doi.org/10.1007/s11998-021-00547-0

23 Hsieh, M.-K., Dzombak, D.A., & Vidic, R.D. (2010). Bridging Gravimetric and Electrochemical Approaches To Determine the Corrosion Rate of Metals and Metal Alloys in Cooling Systems: Bench Scale Evaluation Method. Industrial & amp; *Engineering Chemistry Research, 49*(19), 9117–9123. https://doi.org/10.1021/ie100217k

24 Owens, D.K. & Wendt, R.C. (1969). Estimation of the Surface Free Energy of Polymers. *J. Appl. Polym. Sci., 13*(8), 1741–1747. https://doi.org/10.1016/0006-2952(75)90009-x

25 Ponomar, M., Krasnyuk, E., Butylskii, D., Nikonenko, V., Wang, Y., Jiang, C.,... & Pismenskaya, N. (2022). Sessile drop method: critical analysis and optimization for measuring the contact angle of an ion-exchange membrane surface. *Membranes*, *12*(8), 765. https://doi.org/10.3390/membranes12080765

26 Growcock, F.B., & Jasinski, R.J. (1989). Time-resolved impedance spectroscopy of mild steel in concentrated hydrochloric acid. *Journal of the Electrochemical Society*, *136*(8), 2310. https://doi.org/10.1149/1.2097847

27 Popova, A., & Christov, M. (2006). Evaluation of impedance measurements on mild steel corrosion in acid media in the presence of heterocyclic compounds. *Corrosion Science*, *48*(10), 3208-3221. https://doi.org/10.1016/j.corsci.2005.11.001

28 Song, E.J., Bhadeshia, H.K.D.H., & Suh, D.W. (2013). Effect of hydrogen on the surface energy of ferrite and austenite. *Corrosion Science*, *77*, 379-384. https://doi.org/10.1016/j.corsci.2013.07.043

29 Kalová, J., & Mareš, R. (2015). Reference values of surface tension of water. *International Journal of Thermophysics*, *36*, 1396-1404. https://doi.org/10.1007/s10765-015-1907-2

30 Duan, C., Zhu, Y., Gu, W., Li, M., Zhao, D., Zhao, Z.,... & Wang, Y. (2018). Atomic coupling growth of graphene on carbon steel for exceptional anti-icing performance. *ACS Sustainable Chemistry & Engineering*, *6*(12), 17359-17367. https://doi.org/10.1021/acssuschemeng.8b04913

31 Bañon, F., Montaño, R., Vazquez-Martinez, J. M., & Salguero, J. (2022). Free surface energy evaluation in the laser texturing of a carbon steel s275. *Procedia CIRP*, *108*, 72-76. https://doi.org/10.1016/j.procir.2022.03.016

32 Shin, Y.J., Wang, Y., Huang, H., Kalon, G., Wee, A.T.S., Shen, Z.,... & Yang, H. (2010). Surface-energy engineering of graphene. *Langmuir*, *26*(6), 3798-3802. https://doi.org/10.1021/la100231u

33 Kozbial, A., Li, Z., Conaway, C., McGinley, R., Dhingra, S., Vahdat, V., … & Li, L. (2014). Study on the surface energy of graphene by contact angle measurements. *Langmuir*, *30*(28), 8598-8606. https://doi.org/10.1021/la5018328

Information about authors*

Plotnikova, Maria Dmitrievna — Candidate of chemical sciences, Assistant Professor of Physical Chemistry Department, Perm State National Research University, Bukireva st., 15, 614990, Perm, Russia; e-mail: plotnikova-md@mail.ru; https://orcid.org/0000-0002-4050-5682

Shcherban', Marina Grigoryevna (*corresponding author*) — Candidate of chemical sciences, Assistant professor of Physical Chemistry Department, Perm State National Research University, Bukireva st., 15, 614990, Perm, Russia; e-mail: ma-sher74@mail.ru; https://orcid.org/0000-0002-6905-6622

Shitoeva, Anastasia Dmitrievna — First-Year Master Student, Perm State National Research University, Bukireva st., 15, 614990, Perm, Russia; e-mail: shitoeva0910@gmail.com; https://orcid.org/0009-0005-9611-7848

Vasyanin, Alexander Nikolaevich — Candidate of chemical sciences, Assistant professor of Physical Chemistry Department, Perm State National Research University, Bukireva st., 15, 614990, Perm, Russia; e-mail: avasyanin@psu.ru; https://orcid.org/0000-0002-1991-094X

Shein, Anatoly Borisovich — Doctor of chemical sciences, Professor of Physical Chemistry Department, Perm State National Research University, Bukireva st., 15, 614990, Perm, Russia; e-mail: ashein@psu.ru; https://orcid.org/0000-0002-2102-0436

_____

*The author's name is presented in the order: *Last Name, First and Middle Names*

Article

UDC 544.774

https://doi.org/10.31489/2959-0663/4-23-14

Dana M-K. Ibraimova[1*] [iD], Olga V. Rozhkova[2,3] [iD], Kuanyshbek B. Musabekov[1] [iD], Sagdat M. Tazhibayeva[1] [iD], Vitaly I. Rozhkov[2,4] [iD], Marat T. Yermekov [iD][3]

[1]*Al-Farabi Kazakh National University, Almaty, Kazakhstan;*
[2]*Saken Seifullin Kazakh Agrotechnical University, Astana, Kazakhstan;*
[3]*JSC "Science and Technology Solutions", Almaty, Kazakhstan*
[4]*LLP "Altai Geological and Ecological Institute", Ust-Kamenogorsk, Kazakhstan*
(*Corresponding author's e-mail: dana_kereevna@kaznu.kz)

Development of Methods to Obtain Composite Materials from Organoclays

The paper presents methods to obtain a bionanocomposite from hydrophobic halloysite with bacteridic properties. During the study using TEM analysis, it was established that Karaganda halloysite has a natural nanostructured material and has a cylindrical in shape (halloysite nanotube HNT). It was shown that bactericidal properties of nanoclays are due to exchange reactions between Ag^+ and with active groups of nanoclay, where free H^+ ions are present. The presence of several peaks characteristic of silver was detected by energy-dispersive X-ray spectroscopy, indicating exchange reactions involving silver. The bactericidal properties of silver-modified halloysite were proven using in situ analysis with live bacteria. The observed displacements of interlayer spaces from values of 9.997 Å to 17.51 Å in the diffraction patterns confirmed the successful intercalation of octadecylamine into the nanohalloisite galleries. Such medicinal bionanocomposite materials can be used as carriers of various vitamins and drugs due to their high adsorption properties. A study to obtain bactericidal oleophilic (hydrophobic) bionanocomposites based on Karaganda halloysite was carried out for the first time and it includes the stages of processing halloysite with silver ions and the stage of hydrophobization of bactericidal halloysite.

Keywords: bionanocomposite, halloysite nanoclay, silver clay, bacteridic properties, hydrophobization, organoclay, silver-modified, composite material.

Introduction

Clays are used as bleaching material in the manufacture of fabrics [1]. In the rubber industry, bentonite clays, along with kaolin, are used as an active filler to give hardness to products, increase their acid resistance and strength. In the soap and cosmetics industry, kaolins are used as filler in the production of cheap soap varieties, in the production of powder, makeup, lipstick, tooth powder, paste and other cosmetics [2]. In the food industry, montmorillonite clays are used to purify water and food products (wine, juices, and vegetable oils). In agriculture, clays are effectively used in the production of animal feed, and in soil reclamation. Montmorillonite clays are used in ceramics as a binder in molding mixtures, in the production of iron ore granules, as well as a waterproofing and adsorption material [3]. In medicine, montmorillonite and halloysites are used in the manufacture of medicines, mainly as a binder in tablets, also have applications in cases as adsorbent of harmful substances in stomach diseases (bioadsorber), ulcers, poisoning with alkaloids, etc. [4].

Halloysite is a clay mineral of the subclass of layered silicates consisting of silicon oxide and aluminosilicates, which is not toxic to living organisms and harmless to the environment. The composition is close to kaolinite, which contains a large amount of water. It crystallizes in monoclinic syngony. The mineral halloysite clay is mainly mined in kaolinite deposits and has a multilayer nanotube structure with an outer diameter of about 50 nm – 700 nm and 2 microns in length. It is a tube-packed kaolin, which finds practical applications in ceramics and polymer composites [1], fabric engineering [1, 3], antimicrobial coatings [2, 5], and microvesicle in cosmetology [3, 5]. It is also used to regulate various strength and mechanical properties of drugs and enzymes. This review summarizes the latest data on the structure of halloysite with an insight into its applications in various fields [4].

Currently, methods of creating a variety of drugs and new forms are daily developing [5–9]. Organo-modified bionanocomposites from clay minerals were obtained by the authors [6–8] and as an organically modifiers were used cetyltrimethylammonium bromide, but currently cationic surfactants are not always able

to give superhydrophobicity to clay minerals [6, 8]. Medicines and forms of a new type can perform several functional in one, and medicines of this type can be in high demand in production facilities and pharmacology. If the drugs are biodegradable with bactericidal properties, have prolonged effect and high ion exchange capacity, which can sorb from a non-aqueous medium, then such an object is a unique drug. In this regard, the development of technology for the production of multifunctional medicines is an urgent problem today [5–7].

The focus of this work was to obtain a biodegradable nanocomposite based on nanotubes halloysite with prolongation and bactericidal properties, as well as a high sorption capacity, which can be used for ion exchange process to absorb harmful ions from the body [6].

Experimental

Materials

The halloysite clay used in this work has been obtained from the Beloye Glinishche deposit of the Karaganda region. It is known that these halloysite clays are by nature hollow nanotubes [5].

Octadecylamine $C_{18}H_{39}N$ (Sigma Aldrich. CAS No 124-30-1, 99 % chemical pure), a surfactant solution, was used to produce the organomodified clay mineral.

Silver nitrate (Sigma Aldrich. CAS No 7761-88-8, 99,9999 % pure) was used to obtain bionanocomposites from clay mineral.

Methods

X-ray diffractometric analysis was carried out on an automated diffractometer Drone-3 with *CuK* radiation and a β-filter under capturing diffractograms conditions of: $U = 35$ kV; $I = 20$ mA; θ-2θ capture; detector 2 grad/min. X-ray phase analysis was performed on diffractograms of powder samples using the method of equal suspensions and artificial mixtures on a semi-quantitative basis.

A scanning electron microscope was necessary to obtain acceptable images of at least 2.5 nm in size and to conduct quantitative and qualitative analysis of objects made of nanomaterials. The images were obtained under vacuum using a Quanta 200 3d scanning electron microscope (FEI Company, USA).

The transmission electron microscopy (TEM) method was used to describe the structure of a material, both in the sample size and on its surface. The morphology of the particle shape of HNTs was studied using transmission electron microscopy, TEM-301 Philips (USA) with an accelerating voltage of 80 kV.

Infrared spectroscopy was used to indicate presence surfactants after hydrophobization of clay minerals by ODA.

To measure the contact angle of water drops with the surface of the samples under study, the Goniometer LK-1 (Russia) was used by the sessile drop measurements method.

Chlorides were determined as a result of titration of the analyzed sample and water with silver nitrate in the presence of potassium chromate is used as an indicator [10].

For indicating bactericidal properties of modified clay samples were put on Petri dish the studying samples of clays and 10 ml of distilled water was added on top and mixed well. In a Petri dish, a test culture of *Escherichia coli* was sowed on a flat surface over a nutritious Agar. Then grooves were made on the agar, as in Figure 6, and 0.2 ml of the studied suspension was poured. Grown in a petri dish at 37 °C thermostat at intervals of 3 days. The bactericidal property of Clay can be found if there is inhibit the growth of the bacterium *Escherichia coli*.

Results and Discussion

The main purpose of this study is to develop a method for creating a multifunctional drug — a self-biodegradable and environmentally friendly drug. Thus, the research will be implemented in the following directions:

− introduction of bactericidal properties into the dosage form halloysite nanotube clays;
− organomodification of HNTs;
− checking and achieving prolongation properties of the modified HNSs;
− characterization of the modified HTNSs to investigate if the initial components for the production of biodegradable nanocomposite are achieved through the use of environmentally friendly products. These are clay nanoparticles, silver ions, organoclay nanoparticles.

In this study, silvered halloysite clay and silvered organohalloysite were obtained from the Beloye Glinishche halloysite deposits.

In the Republic of Kazakhstan there are halloysite deposits in two places. They are halloysite of the Beloye Glinishche deposit near the Karaganda city and the Aizin-Tamarskoye halloysite deposit in the Akmola region [10-12]. The main reason for the selection of halloysite from the Beloye Glinishche deposit is that the mineral of this deposit is very finely dispersed and the main composition is halloysite. Chemical formula is $Al_4[Si_4O_{10}][OH]_8 \cdot 4H_2O$ or $Al_2O_3 \cdot 2SiO_2 \cdot 4H_2O$. The halloysite mineral does not occur in pure state and is mainly found in nature with kaolinite and quartz, as well as a mixture of other aluminosilicate minerals. In order to determine the composition of the Karaganda halloysite mineral, the mineral was washed, ground and micron-sieved in laboratory conditions by decantation to separate the selected deposit from quartz particles and the composition of the resulting powder was characterized by X-ray diffraction analysis as shown in Figure 1.
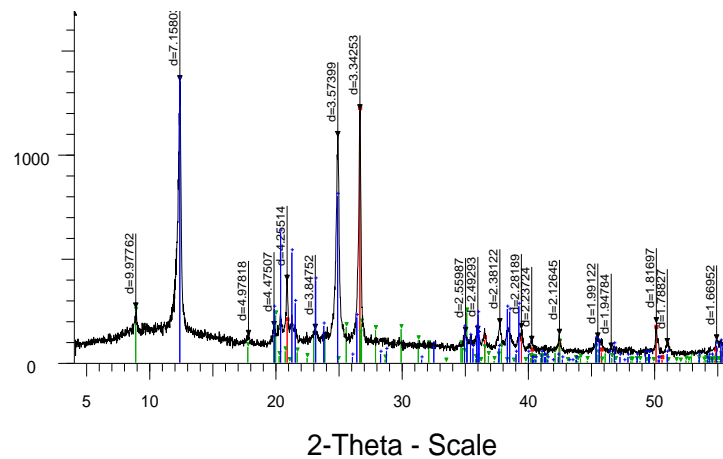
Figure 1. Diffractogram of the halloysite

The analysis of the mineral composition of the sample was carried out according to semi-digital X-ray phase analysis and quantitative indicators were obtained. All diffraction peaks corresponding to different phases shown in Figure 1 are listed in Table 1.

T a b l e 1

Results of semi-digital X-ray phase analysis

Mineral	Formula	Concentration, %
Halloysite	$Al_2(Si_2O_5)(OH)_4$	81.2
Quartz	SiO_2	15.1
Mica	$KAl_2(AlSi_3O_{10})(OH)_2$	3.8

In particular, the mineral halloysite is known to be in the form of rolled sheets [6]. For example, this diagram on below can show 3D structure of halloysites:
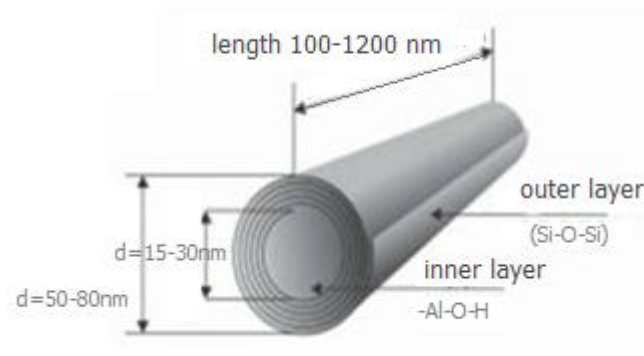
Figure 2. Diffractogram of the halloysite. Adapted and redrawn from [6]

The result of XRD analysis if the Beloye Glinishche deposit), shows that 81.2 % of the bulk of the mineralis is halloysite. Two types of halloysite are known in nature. There are halloysite 10A and halloysite 7A. As a result of this analysis, it is seen that Beloye Glinishche halloysite belongs to the halloysite 10A type, because the interlayer space is equal to 9,997 Å. The next type of analysis of interest is the demonstration of the presence of halloysite nanotubes by scanning electron microscopy, this analysis was ordered to the "National nanotechnological Laboratory of open type" of RSE on Al-Farabi Kazakh National University. The results of the scanning electron microscope (SEM) analysis are shown in Figure 2
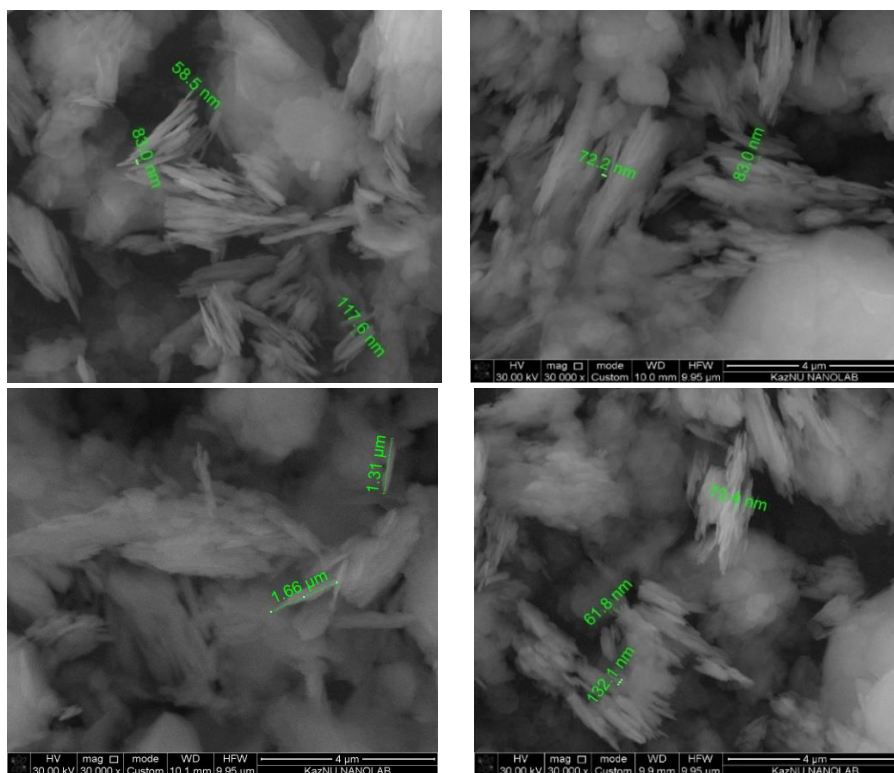
Figure 2. SEM figures of the mineral halloysite

Figure 2 shows SEM-figures of halloysite. It has been observed that the halloysite particles consist of fibrous-shaped particles, the particle length is about 500–1000 nm and the tube diameters fluctuate between 50–80 nm. It is known that halloysite exists in the form of a hollow nanotube [3, 6]. SEM analysis method was able to determine the magnitude of nanotubes, it cannot prove that the tubes are in the form of a hollow tube. Consequently, TEM analysis can show the halloysite particles are a hollow nanotube shape. The TEM analysis was performed in the nanolaboratory of the Kazakh-Japanese innovation center (KJIC) at the Kazakh National Agrarian Research University. The result obtained is presented in Figure 3.
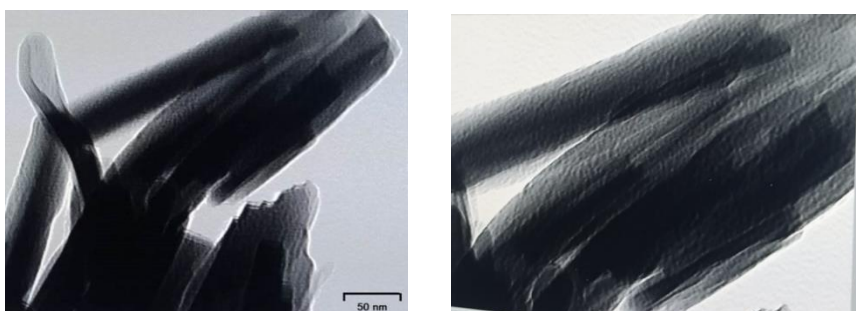
Figure 3. Shape of nanotubes obtained by Transmission Electron Microscopy

Figure 3 shows that the HNTs are in The Shape of spherical tubes wrapped, and each tube has between 20 and 50 nm in diameter. The difference between halloysite and kaolinite is that it contains a small amount

of water molecule. Accordingly, halloysite has in their structures two layers and it belongs to the kaolinite group. The scheme of the cristal grid has a 1:1 ratio by type of clays. Therefore, one of them consists of aluminum oxide, the other of silicon oxide [6]. The folding of plates into tubes is carried out due to a sharp difference in the amount of silicon and aluminum ions. In this case, when the tube is folded type, the aluminum oxide layer is inside it, and the silicium oxide layer is located outside. With different ionization of silicium oxide with aluminum oxide, the dielectric properties are different. Aluminum oxide, for example, has a positive charge when placed in a solution with pH=8.5. The presence of different charges in the outer and inner parts of the tubes of halloysite is associated with the possibility of filling the inner parts of the tubes with negatively charged molecules. The peculiarity of using halloysite in comparison with other clays is due to the fact that it has a large surface specific area.

It is known today that silver ions have bactericidal and antiseptic properties and can resist 650 types of bacteria [8]. But when modifying halloysite with silver ions, it was necessary not to change the morphological nature of HNTs. Since the intercalation of a medicinal product into the hollow part of the nanotube has a main future in science and technology the creation of SEM images of silvered halloysite particles has of great interest (Fig. 4).
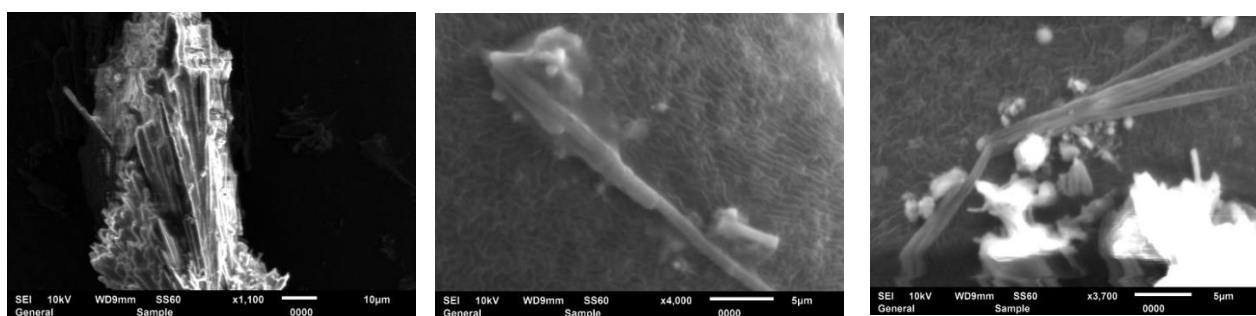
Figure 4. Results of scanning electron microscope analysis of modified clay mineral

Firstly, the halloysite was modified with silver ions. The conversion process was carried out in a simple way. Silver nitrate solutions were prepared with concentration $C(AgNO_3) = 0.4$ mg/l. Modification by silver ions of halloysite samples was carried out by static method and left for 24 hours in dark place. The resulting clay sample was washed by the decantation method until a pure solution was obtained. After that, the liquid medium was separated and qualitative and quantitative analyses for silver ions were performed.
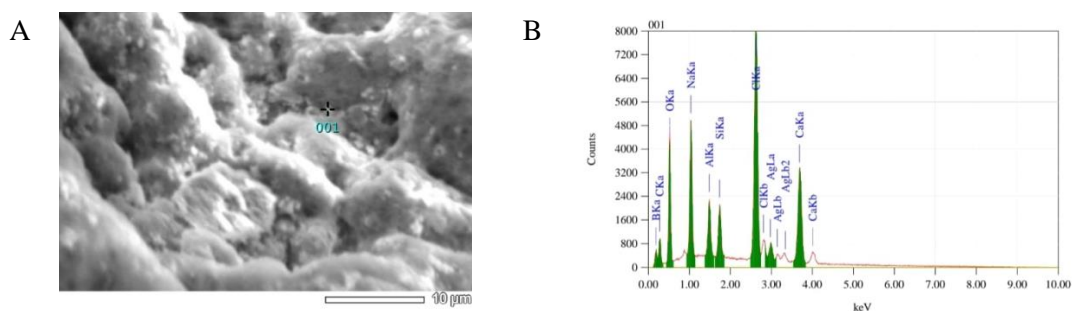
Figure 5. Determination of silver ions by energy dispersive X-ray spectroscopy

As can be seen in Figure 5, halloysite has been proven to contain silver ions using energy dispersive spectroscopy. A SEM image is created first to carry out the process of detecting silver ions. Afterwards the study area is selected (point 001 in Fig. 5A) by placing a dot on any section of the understudy sample and then spectra are obtained on this section. As the Figure 5B shows, the spectra that are colored green are responsible for the clay mineral and the silver ion. It will be right if there is not pay attention to the coal and chlorine signals shown as a result of the analysis, as this also takes into account the composition of the substrate used. Mass fraction of the found ions of the composition is listed in the Table 2.

The result of the elemental analysis of the sample

Elements	X-ray energy (keV)	Mass fraction, %	X-ray counts	Deviations, %	Atomic share, %	K
C K$_\alpha$	0.277	2.61	2972.03	0.01	6.67	1.9354
O K$_\alpha$	0.525	9.65	27693.86	0.00	18.52	0.7683
Na K$_\alpha$	1.041	9.71	34731.10	0.01	12.97	0.6167
Al K$_\alpha$	1.486	4.49	15106.39	0.02	5.11	0.6556
Si K$_\alpha$	1.739	4.66	15007.89	0.02	5.10	0.6852
Cl K$_\alpha$	2.621	36.16	79748.70	0.00	31.32	1.0000
K K$_\alpha$	3.312	1.42	2547.63	0.14	1.12	1.2316
Ca K$_\alpha$	3.690	21.36	34514.20	0.01	16.37	1.2316
Ag L$_\alpha$	2.984	9.93	6378.77	0.05	2.83	3.4349
Summary		100.00			100.00	

It is recommended the modified halloysite with silver ions and medicinal preparations from this object to keep away from sunlight, for silver ions oxidize from the sun and turn into silver oxide. For this reason, all the samples obtained were stored in tinted glass containers. The bactericidal properties of the resulting silver halloysite were tested. Testing of bactericidal properties was carried out by order in private enterprise *in vitro* microbiological laboratories of Almaty.
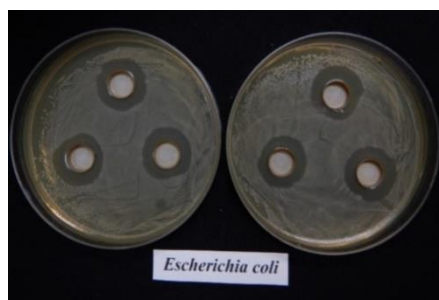
Figure 6. Zones of inhibition of the growth of *Escerichia coli* shoots of silver ion planted clay (21–23 mm)

The bacterium *Escherichia coli* (*E.coli*) was used in this work. As shown in Figure 5, 0.4 g of the studied clay was placed in a test tube and according to the results of the analysis, the bactericidal properties of the silver ion modified clay were revealed.

After organomodification of silvered halloysite, the composition of the study sample should not change, and if the interlayer spaces gallery expandes, it can indicate that large molecules have entered it, that is, either intercalation or exfoliation has occurred. In this regard, after stage of organomodification of silvered halloysite, repeated X-ray diffractometric analysis was performed.
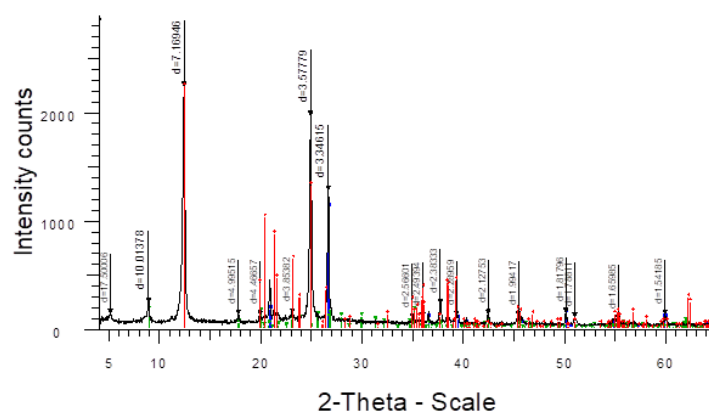
Figure 7. Diffractogram of organomodified halloysite mineral

As a result of the analysis, we observed that the interlayer spaces changed from $d = 9.98$ Å (Fig. 7) to $d = 17.50$ Å. This is an indicator that adsorption is taking place.

For the hydrophobization of halloysite, it is necessary to have a substance with a diphilic structure in a molecule that should have a long saturated hydrocarbon chain around 17 or 18 carbon atoms or more and in this bond octadecylamine (ODA) was chosen. During organomodification by ODA, the process of flushing the excess ODA was carried out and the amount of ODA could be completely flushed out, as the washing process was performed in three returns. For this reason, using the IR spectroscopy method, ODA molecules were performed in order to prove that they exist on the surface of halloysite.
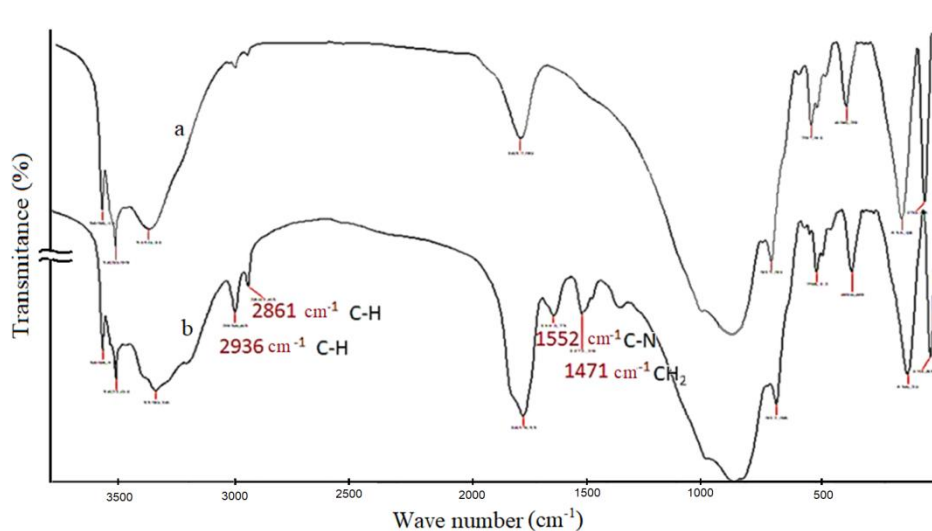
Figure 8. IR-spectra of clay samples. a-halloysite; b-organohalloysite

Data on the IR spectrum of the halloysite clay of the Beloye Glinishche deposit (*a*) and its ODA-modified hydrophobic clay (*b*) are shown in Figure 8. Thus, in halloysite, the peaks from of 3699 cm^{-1} to 3696 cm^{-1} determine the presence of the non free OH-group to which the absorption bands are connected. In the ODA-modified halloysite spectrum in the 3550-3150cm^{-1} region and in the enriched natural halloysite spectrum, the absorption of the free OH-group corresponds to the medium intensity short band frequency of 3620.99–3621.38 cm^{-1}. The location of this band indicates that, according to its nature, an OH-group is strongly linked from the interaction of halloysite [9–16].

In the spectrum of ODA-modified halloysite compound, the absorption of the trans-N-H bond of the secondary amide is determined by 3317.80 and 3323.97 cm^{-1} bands. The absorption band shows moderate intensity, with these bands showing at a very high frequency compared to the ODA-modified halloysite spectrum (*b*), whereas in a halloysite compound these bonds show at a lower frequency (*a*).

In a given region, absorption of the spectra under consideration is observed at very high intensity. The sample is taken in the form of a film (or tablets with KBr), the absorption area of various symmetric C–H bonds in the ODA-modified halloysite spectrum is observed in areas 2936 and 2861 cm^{-1}.

Absorption bands of deformation vibrations of the hydroxyl group in the spectrum of natural halloysite and its modified form with ODA bands are manifested at frequencies 1639.33, 1639.76, 1637.90 cm^{-1}. The CH_2-group in deformation oscillations is in the region of 1500–1300 cm^{-1} of the research spectrum.

The valence oscillations of the natural anti- and symmetrical C–N bond associated with different particles in the molecule are reflected in the absorption band 1129 cm^{-1} and 1150 cm^{-1} in the ODA-modified halloysite spectrum. In the spectrum of enriched natural halloysite, this area is not observed. Thus, from the results of the IR spectrum of natural halloysite and ODA-modified halloysite, the following conclusion is drawn: there is a significant reduction in free O-H bonds in the ODA-modified halloysite. It testifies to a decrease in the number of bands in the corresponding spectrum region, and also indicates the mixing of the remaining bands at a lower frequency. The spectrum picture varies in a known way in the region of 1120–1000 cm^{-1}.

Figure 9 below shows that organomodified halloysite can float on the surface of water, and the first glass is a picture taken at $t = 0$ sec, and the second glass is a picture taken after $t = 120$ days.

Figure 9. Organoclay powder newly placed on the surface of the water
after $t = 0$ SEC (*a*) and $t = 120$ days (*b*)

The organophilic halloysite obtained from halloysite is hydrophobic and has a stable chemical composition.

T a b l e 3

**Values of water absorption angles for samples of organoclay powders
obtained at different concentrations of ODA**

№	Concentration of ODA spent on modification, mol/L	Angles of incidence, degrees	Oda-modified and bactericidal organoclay names with different concentrations ODA
1	Silvered halloysite	9°	BOMC0
2	0,000625	122°	BOMC1
3	0,00125	129°	BOMC2
4	0,0025	130°	BOMC3
5	0,005	131°	BOMC4
6	0,01	132°	BOMC5

Thus, by modifying silvered halloysite with octadecylamine, as shown in Table 3, 6 type of bactericidal organoclays were obtained and they were assigned the relevant names from BOMC0 to BOMC5. Production facilities will also be provided with this model. Since the oranomodification process is carried out at a certain temperature operation mode, it is important to perform morphological analysis of the particles of the resulting hydrophobic organohalloysite, as it is the most necessary for us to keep the organohalloysite intact in space as a nanotube during the work. Therefore, by the SEM method, a SEM photo of organohalloysite was obtained (Fig. 10).

In order to study the nanotube structure of the mineral organohalloysite, SEM analysis of the mineral sample was carried out and the following results were obtained (Fig. 10).
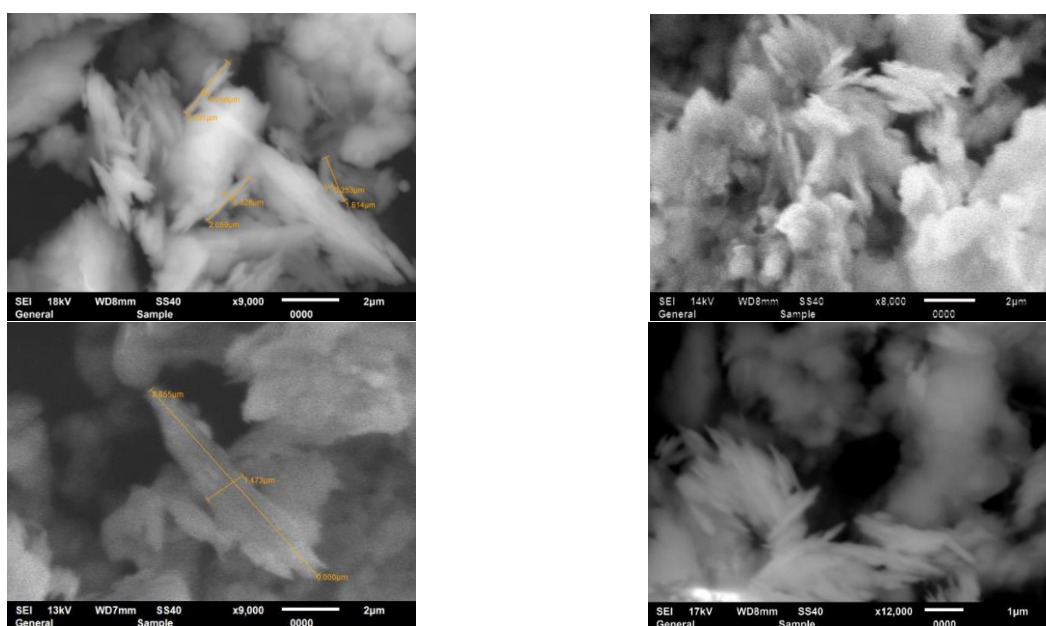
Figure 10. SEM images of organomodified silvered halloysite mineral

SEM analysis measured the width and length of the nanotubes of the halloysite mineral, found that the width is between 10–100 nm, and the length is up to ~1000 nm, and proved not to disturb the type of rolled sheet.

The last step of the performed research work is proving stabilities obtained hydrophobic bionanocomposite in an organic medium. For this reason, sunflower oil was chosen as the organic medium because of its dielectric constant equal to 3.2 and because it is an eco-friendly object for the human body. The kinetics of sedimentation in the sunflower oil medium BOMC0-BOMC5 of the bionanocomposite samples obtained below were studied by the result of a time-dependent change in the amount of light transmittance (T, %). If it considers as a dispersion system, the particles of the dispersed phase begin to settle at the bottom of test tube over time and during the time the light transmittance begins to increase. The results obtained explain if the turbidity stops at one value, there is a certain amount of stability. The results obtained are shown in the Figure 11.

1 — BOMC1; *2* — BOMC2; *3* — BOMC3; *4* — BOMC4; *5* — BOMC5; *6* — BOMC0
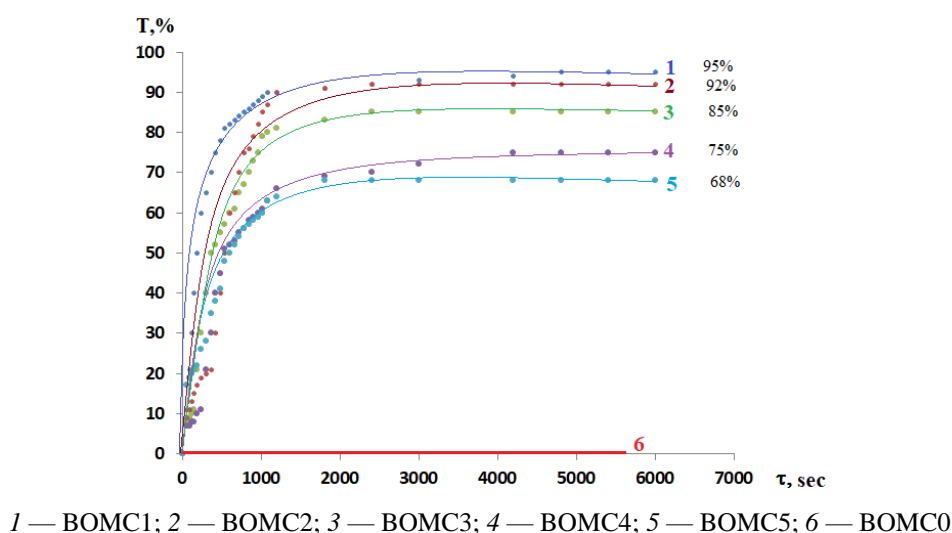
Figure 11. Stability of organo halloysite samples in the sunlight oil

As shown in Figure 11, the 6 curves are typical of the non-organomodified halloysite. During the experiment, BOMC0 immediately settles under the test tube and does not show any mechanical interference with the oily medium. Therefore, its light conductivity is equal to 100 percent homogeneous or has no turbidity. From this Figure 11 (curve 5), the lowest value of light transmittance corresponds to BOMC1 and its value equals to T = 65 % and it remains stable of dispersed phase in the medium at this value. It has been proven that this sample can physically interact with BOMC1 sunflower oil, due to which it shows better stability in the oil medium than other (BOMC0-BOMC4) samples. In other words, our samples are recommended to be used as bionanocomposite for a special nonpolar medium. Because currently, the direction of creating bionanocomposite adapted to a polar medium (aquatic medium) has been studied in detail, but the direction of creating bionanocomposite adapted to a nonpolar environment is just being developed.

Conclusions

Thus, recently, the number of works performed as part of the creation of bionanocomposites has been increasing [1–5, 14–17]. The provided results can actually indicate ways to obtain a drug of a new type from a clay mineral, expanding the scope of application of organomodified clay. At the same time, nanotechnology can determine a great scientific direction, creating nanoclays in the direction of science, creating nanobiocomposites based on it and increasing the scope of its application. Thanks to scientific work in this direction, the prospects for the creation and application of nanoclay types are well increasing. The work in this direction is promising and can expand the scope of creating various forms of drugs by creating a form of halloysite with oleophilic and bactericidal properties, structuring and microcapsulating halloysite-based bionanocomposite.

References

1 Yassin JM, Shiferaw Y, Tedla A. (2022) Application of acid activated natural clays for improving quality of Niger (Guizotia abyssinica Cass) oil. *Heliyon*, 8, (4), e09241. http://dx.doi.org/10.1016/j.heliyon.2022.e09241

2 Amari A., Gannouni H., Khan M.I., Almesfer M.K., Elkhaleefa A.M., Gannouni A. (2018). Effect of structure and chemical activation on the adsorption properties of green clay minerals for the removal of cationic dye. *Appl. Sci., 8*(11), 2302; http://dx.doi.org/10.3390/app8112302

3 Parolo, M. E., Pettinari, G. R., Musso, T. B., Sánchez-Izquierdo, M. P., & Fernández, L. G. (2014). Characterization of organo-modified bentonite sorbents: The effect of modification conditions on adsorption performance. *Applied Surface Science*, *320*, 356–363. http://dx.doi.org/10.1016/j.apsusc.2014.09.105

4 Musabekov, K., Zhakyp, B., Tazhibayeva, S., Musabekov, N., & Yergaliyeva, A. (2020).A research of colloidal silver immobilization in bionanocomposites of natural polymers and montmorillonite. *Eastern-European Journal of Enterprise Technologies*, 6 (6–108), 93–101. http://dx.doi.org/10.15587/1729-4061.2020.216995

5 Villegas, Carolina & et al. (2019). PLA/organoclay bionanocomposites impregnated with thymol and cinnamaldehyde by supercritical impregnation for active and sustainable food packaging. *Composites Part B Engineering,* 176, 107336. http://dx.doi.org/10.1016/j.compositesb.2019.107336

6 Kamal, N., Kochkodan, V., Zekri, A., Ahzi, S. (2020). Polysulfone Membranes Embedded with Halloysites Nanotubes: Preparation and Properties. *Membranes*, *10,* 2. http://dx.doi.org/10.3390/membranes10010002

7 Fernández Solarte, A. M., Blanco Massani, M. R., Molina, V. M., Benítez Guerrero, M., & Torres Sánchez, R. M. (2018). Correlating Antimicrobial activity and Structure in Montmorillonite modified with Hexadecyltrimethylammonium and Silver. *International Journal of ChemTech Research, 11(6)*, 209–223. http://dx.doi.org/10.20902/IJCTR.2018.110627

8 Rhim, J.-W., Park, H.-M., & Ha, C.-S. (2013). Bio-nanocomposites for food packaging applications. *Progress in Polymer Science,* 38(10), 1629–1652. http://dx.doi.org//https://doi.org/10.1016/j.progpolymsci.2013.05.008

9 Pessanha, N. F. N., Kawase, K. Y. F., & Coelho, G. L. V. (2014). Preparation and characterization of silver/organo-clay nanocomposites. *Chemical and Materials Engineering, 2(8)*, 173–178. http://dx.doi.org/10.13189/cme.2014.020802

10 Korkmaz, D. (2011). Determination of Chloride Ion Concentration by Titration (Mohr's Method). *University of Cantearbury*, 1-2. Retrieved from https://www.canterbury.ac.nz/media/documents/science-outreach/chloride_mohr.pdf

11 Bakenov, M.M. (2008) Netradicionnye i novye vidy poleznyh iskopaemyh Kazahstana [Unconventional and new types of Kazakhstan's minerals'] K.I. Satpayev KazNTU: Satbayev University https://www.geokniga.org. Retrieved from https://www.geokniga.org/bookfiles/geokniga-netradicionnye-i-novye-vidy-poleznyh-iskopaemyh-kazahstana.pdf, [in Russian]

12 Isagulov A.Z., Kulikov, V., Kwon, S. S., Shcherbakova, E., Kovaleva, T., & Isagulova D. (2015). Opredelenie frakcionnogo sostava galluazita na fotosedimentometre FSH-6K [Determination of the fractional constituent of halloysite by the photosedimentometer FSX-6K] *Trudy Universiteta — Proceedings of the University,* 3, 29-40. Retrieved from https://www.kstu.kz/tu/2015/trudy_universiteta_3.pdf [in Russian].

13 Sidorina, E.A., Isagulov, A.Z., Kashcheev, I.D. et al. (2022). Production and Development of Superdense Slag-Resistant Aluminosilicate Refractories. *Refractories and Industrial Ceramics,* 63, 280–282. http://dx.doi.org/10.1007/s11148-022-00724-7

14 Arellano, Sofia & et al. (2012). Sorption of Naringin from Aqueous Solution by Modified Clay. *Clays and Clay Minerals,* 60, 153–161. http://dx.doi.org/10.1346/CCMN.2012.0600205

15 Abdullayev, E., Lvov, Y. (2011). Halloysite Clay Nanotubes for Controlled Release of Protective Agents. *Journal of Nanoscience and Nanotechnology*, 11(11), 10007–10026(20). http://dx.doi.org/10.1166/jnn.2011.5724

16 Roy, S., & Chakraborty, C. (2020). Sub-second electrochromic switching and ultra-high coloration efficiency in halloysite nanoclay incorporated metallo-supramolecular polymer nano-hybrid based electrochromic device. *Solar Energy Materials and Solar Cells*, 208, 110392. http://dx.doi.org/10.1016/j.solmat.2019.110392

17 Ahmed, H.B. (2019). Cluster growth adaptor for generation of bactericide Ag-Au bimetallic nanostructures: substantiation through spectral mapping data. *International Journal of Biological Macromolecules*, 121, 774–783. http://dx.doi.org/10.1016/j.ijbiomac.2018.10.088

Information about authors*

Ibraimova, Dana Mykty-Kereevna (*corresponding author*) — Candidate of chemical sciences, Senior Lecturer, Al-Farabi Kazakh National University; Al-Farabi ave., 71, 050040, Almaty, Kazakhstan; e-mail: dana_kereevna@kaznu.kz; https://orcid.org/0000-0002-1761-9745

Rozhkova, Olga Vladimirovna — Doctor of chemical sciences, Professor, Academician of the National Academy of Natural Sciences of the Republic of Kazakhstan, NAO "Saken Seifullin Kazakh Agrotechnical University", Zhenis street, 62, 100011, Astana, Kazakhstan; JSC "Science and Technology Solutions", Satbayev street, 22/5, 050013, Almaty, Kazakhstan. e-mail: rozhkova.o@stsolutions.kz; https://orcid.org/0000-0001-8163-7035

Musabekov, Kuanyshbek Bituovich — Doctor of chemical sciences, Academician of the National Academy of Natural Sciences of the Republic of Kazakhstan, Professor, Al-Farabi Kazakh National University; Al-Farabi ave., 71, 050040, Almaty, Kazakhstan; e-mail: kuanyshbek.musabekov@kaznu.kz; https://orcid.org/0000-0003-1114-1901

Tazhibayeva, Sagdat Mederbekovna — Doctor of chemical sciences, Professor, Al-Farabi Kazakh National University; Al-Farabi ave., 71, 050040, Almaty, Kazakhstan; e-mail: tazhibayeva_s@mail.ru; https://orcid.org/0000-0003-3300-3235

Rozhkov, Vitaly Igorevich — Candidate of technical sciences, LLP "Altai Geological and Ecological Institute", Ust-Kamenogorsk, Kazakhstan; NAO "Saken Seifullin Kazakh Agrotechnical University", Zhenis street, 62, 100011, Astana, Kazakhstan; e-mail: vitalrza1983@gmail.com; https://orcid.org/0000-0002-3232-5972

Yermekov, Marat Teginbaevich — Head of the Project and Management Department, JSC "Science and Technology Solutions", Satbayev street, 22/5, 050013, Almaty, Kazakhstan; e-mail: yermekov.m@stsolutions.kz; https://orcid.org/0000-0002-5226-2710

_____

*The author's name is presented in the order: *Last Name, First and Middle Names*

CHEMICAL TECHNOLOGY

Aigerim Ospanova[1], Aida Ardakkyzy[1], Aliya Kurbanova[2] (iD), Yernar Kanagat[3],
Munziya Abutalip[2] (iD), Zhexenbek Toktarbay[4*] (iD), Nurxat Nuraje[1,2*] (iD)

[1]*Department of Chemical & Materials Engineering, School of Engineering & Digital Science,
Nazarbayev University, Astana, Kazakhstan;*
[2]*Renewable Energy Laboratory, National Laboratory Astana, Nazarbayev University, Astana, Kazakhstan;*
[3]*Department of Chemistry, Faculty of Natural Sciecnes, L.N. Gumilyov Eurasian National University, Astana, Kazakhstan;*
[4]*Laboratory of Engineering Profile, Satbayev University, Almaty, Kazakhstan*
(*Corresponding authors' e-mail: nurxat.nuraje@nu.edu.kz; zhexenbek.toktarbay@gmail.com)

Pervaporative Desulfurization: A Comprehensive Review of Principles, Advances, and Applications

Pervaporative desulfurization is a potential method for removing sulfur compounds from liquid hydrocarbon streams, having many advantages over existing methods. This overview covers the fundamentals, recent breakthroughs, and different applications of pervaporative desulfurization. The paper begins by explaining pervaporative desulfurization's core concepts, focusing on how polymeric membranes selectively separate sulfur molecules from liquid hydrocarbons. It explores membrane properties, operating conditions, and feed composition in pervaporative separation. It highlights how pervaporative desulfurization may reduce sulfur content to ultra-low levels and meet strict environmental and fuel quality standards. Finally, this comprehensive review paper concludes with a discussion on the future prospects and research directions in the field of pervaporative desulfurization. It highlights the need for continued innovation in membrane materials, module design, and process optimization, as well as the importance of addressing challenges related to scale-up and industrial implementation. Overall, this review paper provides valuable insights into the advancements, challenges, and potential applications of pervaporative desulfurization, offering a comprehensive understanding of this technology for researchers, engineers, and all parties involved in the development and implementation of sustainable sulfur removal processes.

Keywords: pervaporative desulfurization, membrane desulfurization, trace sulfur removal, thiophene removal, dibenzothiophene, acid rain, sulfur-containing oils, hydrodesulfurization, oxidative desulfurization.

Contents

Acknowledgements
References

Review plan

The present review is devoted to pervaporative desulfurization and principles, membrane fabrication techniques, process optimization of pervaporative desulfurization, storing sulfur-containing oils after desulfurization, limitations of pervaporative desulfurization and conclusion. Each section covered necessary information and data to be easily understood by the readers. Online available references from trustworthy sources were used. This review has focused on all aspects of PVD, including its optimization, the storage of sulfur-containing oils, and the limitations of PVD, which were not fully discussed in other review papers.

Introduction

Sulfur compounds in crude oil can cause serious environmental and health problems, such as acid rain [1–5], respiratory diseases [6, 7] and cancer [8]. Therefore, the removal of sulfur from crude oil has become a critical issue in the petroleum industry. Conventional desulfurization technologies, such as hydrodesulfurization (HDS) and oxidative desulfurization (ODS), have been widely used to remove sulfur compounds from crude oil [9–16]. However, these methods have some limitations, such as high energy consumption, high capital and operating costs, and low selectivity for certain sulfur compounds. Therefore, alternative desulfurization technologies, such as pervaporative desulfurization (PVD), have attracted increasing attention in recent years.

Compared to other desulfurization methods, such as extractive desulfurization, oxidative desulfurization, bio-desulfurization, and adsorptive desulfurization, pervaporative desulfurization is considered a promising method for desulfurization of fuels due to its low cost, low energy consumption, high yield, and easy processing [17, 18]. It offers advantages such as higher selectivity, lower investment and operating costs, and scalability [19]. Therefore, pervaporative desulfurization has various applications in different industries. One of the main applications is in gasoline desulfurization. The stringent regulations on sulfur content in gasoline have led to a growing interest in the use of pervaporation for this purpose [20]. Pervaporation is a promising separation technology for removing sulfur compounds from gasoline while maintaining its octane number [21]. Compared to traditional hydrodesulfurization methods, pervaporation can be carried out at normal pressure and temperature without the need for hydrogen and catalysts, resulting in lower operating costs [21]. Pervaporation is also used for the separation of azeotropic mixtures, solutions with similar boiling points, and thermally sensitive compounds. It is an effective method for removing dilute organics from aqueous solutions [20].

Pervaporative desulfurization has several applications in environmental protection. One of the main applications is in the removal of sulfur dioxide (SO_2) from flue gas. Wet flue gas desulfurization using phosphate rock slurry has been employed successfully in industrial applications for the elimination of SO_2 from phosphorus chemical processes. This technology offers an efficient and cost-effective method for SO_2 abatement. The use of phosphate rock as the raw material reduces the desulfurization cost [22]. Pervaporation is also used for the desulfurization of transport fuels, such as gasoline.

This article aims to provide a comprehensive review of the principles, mechanisms, and applications of pervaporation in desulfurization (PVD). While many other review articles focus on pervaporation characteristics and membranes, this review article also presents membrane fabrication methods and the optimization process of pervaporation desulfurization. The study on the optimization process of PVD enables readers to gain a better understanding of the procedure and to overcome obstacles for large-scale applications in industries.

Principles of Pervaporation

Pervaporation (PV) is a membrane-based separation process that utilizes the differences in the solubility, diffusivity, and vapor pressure of different components in a liquid mixture to selectively permeate through a membrane. PV involves the following steps (Fig 1.):
The liquid mixture is fed to the upstream side of a membrane module.
The membrane selectively permeates the more volatile component (usually water or organic solvents) from the liquid mixture through the membrane pores by evaporation or diffusion. The permeated component

is condensed or adsorbed on the downstream side of the membrane. The non-permeated component is collected as the retentate [23, 24].
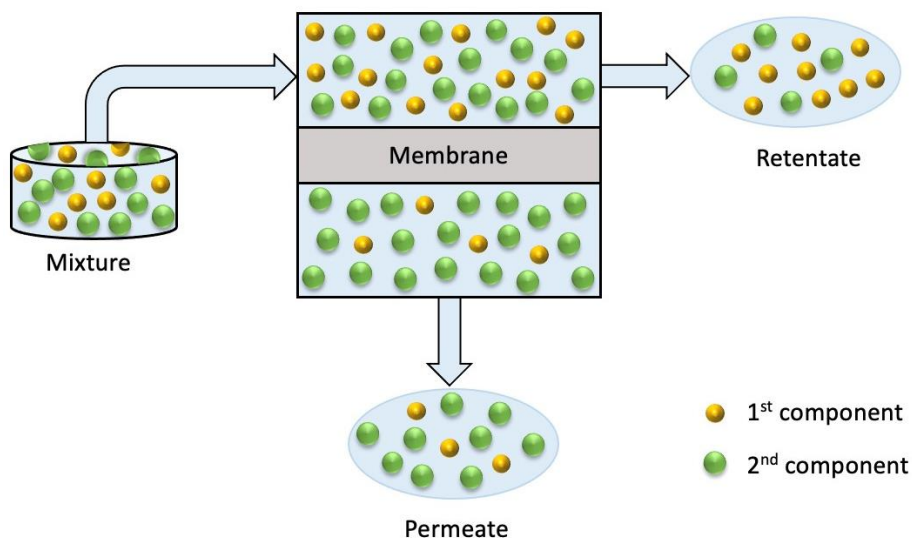
Figure 1. Schematic illustration of pervaporation process

PV is a promising separation technology for various applications, such as dehydration, concentration, and purification of organic and aqueous solutions. PV has several advantages over conventional separation methods, such as low energy consumption, high selectivity, and high recovery. PV membranes can be classified into two main categories: dense membranes and porous membranes. Dense membranes are made of polymer or ceramic materials that have low permeability but high selectivity for certain components. Porous membranes are made of materials that have high permeability but low selectivity for all components. The performance of PV membranes depends on various factors, such as membrane material, membrane structure, membrane morphology, membrane surface properties, feed composition, operating temperature, and pressure [24-28].

Mechanisms of PVD

Pervaporative desulfurization (PVD) is a combination of PV and selective permeation to remove sulfur compounds from crude oil. PVD involves the following steps:

The crude oil is mixed with a solvent that can dissolve the sulfur compounds but not the hydrocarbons.

The mixture is fed to the upstream side of a pervaporation membrane module.

The membrane selectively permeates the solvent and the dissolved sulfur compounds from the mixture through the membrane pores by evaporation or diffusion.

The permeated solvent and sulfur compounds are condensed or adsorbed on the downstream side of the membrane.

The retentate, which contains the hydrocarbons, is collected.

The selection of solvents is crucial for PVD because the solvent should have high solubility and selectivity for sulfur compounds but low solubility and selectivity for hydrocarbons. The choice of membrane materials is also important for PVD because the membrane should have high selectivity for sulfur compounds but low selectivity for hydrocarbons and solvent. The performance of PVD depends on various factors, such as solvent composition, membrane material, membrane structure, membrane morphology, membrane surface properties, feed composition, operating temperature, and pressure.

Adsorptive Pervaporative Desulfurization

Adsorptive Pervaporative Desulfurization (APD) is a combination of adsorption and pervaporation techniques used for oil desulfurization. The mechanisms involved in APD include:

Adsorption: The oil is passed through an adsorbent material, such as hydrophobic membrane [29], which selectively adsorbs sulfur-containing compounds. The adsorbent or membrane act as a molecular sieve, capturing the sulfur compounds from the oil stream. Metal organic fillers inside the membrane play

important role in adsorbing organic sulfur. The interaction between metal ions and polymers and the interaction between sulfur and metals share some similarities, particularly in terms of coordination chemistry and bonding [30–33]. In both cases, the interaction involves the coordination of atoms or ions with specific binding sites on the polymer or metal surface. Metal ions can coordinate with functional groups on the polymer, forming coordination complexes, sulfur of while can interact with metal surfaces through coordination bonding. The following are possible mechanisms for the adsorption of aromatic sulfur compounds onto adsorbents [34–39]:

1. π-Complexation:

– This mechanism includes the transfer of electrons from the π-orbitals of the sulfur compounds, like thiophene, in the fuel to the metal atom's vacant s-orbitals (orbitals with available electron density).

– Alternatively, electrons can be given from the metal atom's d-orbitals to the antibonding π-orbitals of aromatic sulfur compounds.

– π-Bond creation or electron donation from the metal atom's d-orbitals results in chemical bonding between the sulfur and the metal.

2. Acid-Base Interaction:

– In this process, metal sites on the adsorbent, such as iron, chromium, aluminum, copper, zinc, cobalt, and so on, operate as Lewis acidic sites.

– Lewis acidic sites in hydrocarbon structures interact with sulfur atoms via Lewis acid-base interactions.

– Lewis acid-base interactions are chemical interactions in which electron-rich Lewis bases (in this example, sulfur atoms) interact with electron-deficient Lewis acids (metal sites), resulting in chemical bond formation.

3. Direct Sulfur-Metal Interaction:

– The direct creation of a σ-bond between the sulfur in the fuel and the metal atoms in the adsorbent is involved in this mechanism.

– The bond is created by the donation of lone pair electrons from the hydrocarbon structure's sulfur atom to a metal atom.

– As a result, the sulfur forms a strong chemical bond with the metal surface.

These mechanisms demonstrate the various ways in which aromatic sulfur compounds can be adsorbed. One or more of them may be engaged in the adsorption process, depending on the individual metal and the chemical characteristics of the sulfur compounds. These mechanisms are critical in understanding how and why specific adsorption processes occur.

However, despite its increased sulfur content, application to heavy oil is impractical due to limited accessibility of large molecules such as dibenzothiophene and its derivatives in small pores and steric hindrance, which lowers adsorption efficacy.

Pervaporation: Pervaporation is a membrane-based process where a semi-permeable membrane selectively allows certain molecules (in this case, hydrocarbons) to pass through while blocking others (sulfur compounds and water).

Selective Permeation: The pervaporation membrane has a high affinity for hydrocarbons, allowing them to permeate through the membrane and exit as the purified oil product. At the same time, the sulfur compounds, which have a lower affinity for the membrane, are retained and concentrated on the feed side of the membrane. During the selective permeation process, the pervaporation membrane aids in the removal of sulfur-containing compounds from oil. This membrane exhibits a high affinity for hydrocarbons, allowing them to permeate through the membrane and exit as purified oil. The mechanisms of desulfurization involve interactions between the sulfur compounds and the active sites of the membrane material, such as hydrogen bonding and acid-base complexation. These interactions enable the preferential removal of sulfur compounds, such as thiophene, from the oil phase [37, 38].

Regeneration: Periodically, the adsorbent material becomes saturated with sulfur compounds. To maintain the desulfurization efficiency, the adsorbent is regenerated by heating or using other methods to remove the sulfur compounds and restore its adsorption capacity.

Through these mechanisms, APD can achieve efficient desulfurization, producing low-sulfur content oil with reduced environmental impact and meeting stringent fuel quality standards. APD is an attractive option for specific applications where other desulfurization methods may not be feasible or cost-effective.

Selecting Membrane Materials for pervaporative desulfurization

Pervaporative desulfurization (PVD) is a membrane-based separation process (Fig 2.) that has shown promise in the removal of sulfur compounds from crude oil and other industrial waste streams. Membrane materials play a crucial role in the performance of PVD, and the selection of appropriate materials depends on various factors, such as the chemical compatibility with the feed stream, the selectivity towards sulfur compounds, the mechanical strength, and the cost-effectiveness [39–41].
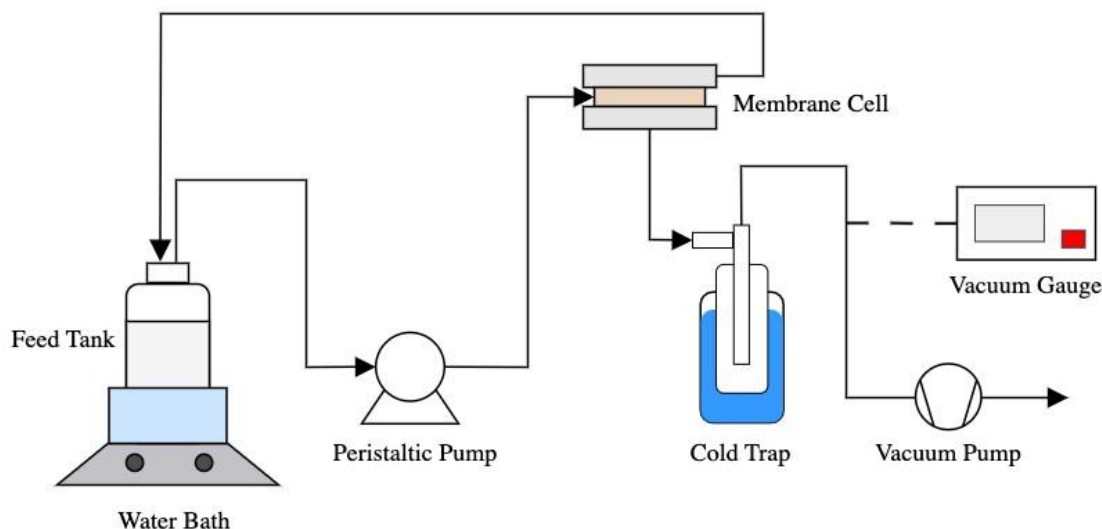
Figure 2. The schematic illustration of pervaporation process

Polymeric membranes, such as polydimethylsiloxane (PDMS) [42–44], polyvinylidene fluoride (PVDF) [45, 46], and cellulose acetate (CA) [47, 48], are the most commonly used membrane materials for PVD. PDMS is a highly permeable and flexible material that has shown excellent selectivity towards sulfur compounds due to its high affinity towards polar molecules. PVDF is a hydrophobic and mechanically robust material that has shown good selectivity towards sulfur compounds. CA is a hydrophilic and biocompatible material that has shown high selectivity towards small sulfur compounds.

Composite membranes, which are composed of two or more polymers or inorganic materials, have also been developed for PVD. Composite membranes have the advantage of combining the properties of different materials to achieve higher selectivity and permeability towards sulfur compounds. For example, Cao et al. (2011) designed PDMS/silica composite membranes that have shown higher selectivity towards sulfur compounds than pure PDMS membranes due to the presence of silica nanoparticles, which enhance the surface affinity towards sulfur compounds [41].

Inorganic membranes, such as ceramic and metal membranes, have also been investigated for PVD. Inorganic membranes have the advantage of high thermal and chemical stability, which makes them suitable for harsh environments. Ceramic membranes, such as alumina and zeolite membranes, have shown promising results in the removal of sulfur compounds from model oil and real crude oil [49, 50]. Metal membranes, such as palladium and silver membranes, have shown high selectivity towards hydrogen sulfide due to their ability to catalytically oxidize sulfur compounds to form sulfates [51, 52].

The choice of membrane material depends on the specific application and the available resources. Polymeric membranes are generally more cost-effective and easier to fabricate than inorganic membranes, but they may suffer from low mechanical strength and chemical compatibility issues. Inorganic membranes are more expensive and difficult to fabricate, but they may offer higher selectivity and stability in harsh environments.

Process Optimization of Pervaporative Desulfurization

In terms of materials, various types of membranes have been investigated for pervaporative desulfurization. For example, a study explored the use of a polyethylene glycol (PEG) membrane and found that it exhibited excellent desulfurization properties [53]. Another study incorporated a unique two-dimensional structure material, graphene egg yolk-shell nanostructure (GYSNs), into a polyurethane matrix to fabricate mixed

matrix membranes (MMMs) for pervaporative desulfurization [24]. Additionally, the incorporation of SiO$_2$ nanoparticles in polyvinyl butyral (PVB) membranes improved the performance of pervaporation for gasoline desulfurization [22]. Additionally, the incorporation of metal-organic frameworks (MOFs) such as CuBTC (copper benzene-1,3,5-tricarboxylate) into polyethylene glycol (PEG) membranes has been shown to improve desulfurization performance [54]. The use of novel thin film nanocomposite membranes based on chitosan succinate modified with Fe-BTC (iron benzene-1,3,5-tricarboxylate) has also been explored for enhanced pervaporation desulfurization. Furthermore, the incorporation of inorganic particles, such as silver oxide (Ag$_2$O), into polydimethylsiloxane (PDMS) membranes has been investigated to enhance the desulfurization properties. The interaction between the filler and thiophenes in the mixed matrix membrane improves the sulfur removal efficiency of the pervaporative desulfurization process [43].

Farsi et al. optimized PDMS, PEG, PES, and PAN composite membranes by changing cross-linking concentration, time, temperature, and concentration of TEOS. The composite membrane of PEG + PDMS had the highest overall flux (0.7732 L/h) and lowest sulfur backflow (1780 ppm). The utilization of tetraethyl orthosilicate (TEOS) resulted in a decline in the overall flux, accompanied by a reduction in the quantity of sulfur present in the recycled flow. The increase in the concentration of tetraethyl orthosilicate (TEOS) from 8 to 22 wt% in composite membranes consisting of polydimethylsiloxane (PDMS) combined with polyacrylonitrile (PAN), polyethersulfone (PES), polyethylene glycol (PEG), and PDMS alone resulted in a decrease in flux from 0.5412 to 0.5217 L/h, 0.6215 to 0.6033 L/h, 0.7583 to 0.6211 L/h, and 0.6813 to 0.6314 L/h, respectively. In a similar way, the sulfur content in the backflow decreased from 2035 to 1982 parts per million (ppm), 1933 to 1921 ppm, 1825 to 1811 ppm, and 2011 to 1972 ppm, correspondingly [55].

Membrane Fabrication techniques for Pervaporative Desulfurization

Membrane fabrication is a critical step in the development of pervaporative desulfurization (PVD) systems, as the performance of the membranes greatly influences the efficiency and selectivity of the process. Several membrane fabrication techniques have been developed for PVD, including solution casting, electrospinning, phase inversion, and layer-by-layer assembly. Each technique has its advantages and disadvantages, and the choice of the appropriate technique depends on various factors, such as the desired membrane properties, the target application, and the available resources.

Solution casting is a common membrane fabrication technique that involves the casting of a polymer solution onto a substrate and the subsequent evaporation of the solvent to form a thin film (Fig. 3). This technique is simple, cost-effective, and versatile, and can produce membranes with different thicknesses and compositions. However, solution casting may suffer from poor reproducibility and limited scalability, and the resulting membranes may have low mechanical strength and poor permeability.

Phase inversion is a membrane fabrication technique that involves the precipitation of a polymer solution by immersion in a non-solvent bath. This technique can produce membranes with a range of morphologies, such as asymmetric and porous structures, and can be used to tailor the membrane properties by controlling the composition and conditions of the precipitation bath. Phase inversion has been widely used in PVD, as it can produce membranes with high selectivity and permeability towards sulfur compounds. However, phase inversion may suffer from limited reproducibility and the use of toxic solvents.
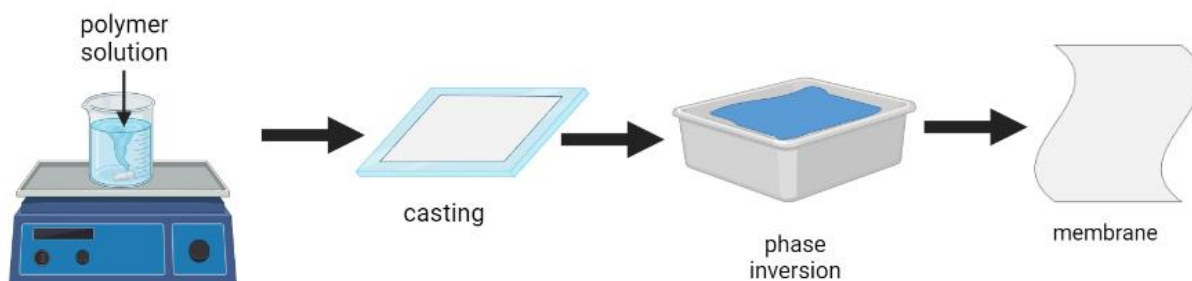
Figure 3. The schematic illustration of membrane fabrication by solution casting method

Layer-by-layer assembly is a membrane fabrication technique that involves the deposition of alternating layers of polyelectrolytes onto a substrate (Fig. 4). This technique can produce membranes with precise control over the thickness and composition of the layers, and can be used to tailor the membrane properties by selecting different polyelectrolytes. Used layer-by-layer assembly which has shown promising results in

PVD, as it can produce membranes with high selectivity and stability towards sulfur compounds. However, layer-by-layer assembly is a complex and time-consuming process that may require specialized equipment and expertise [53].
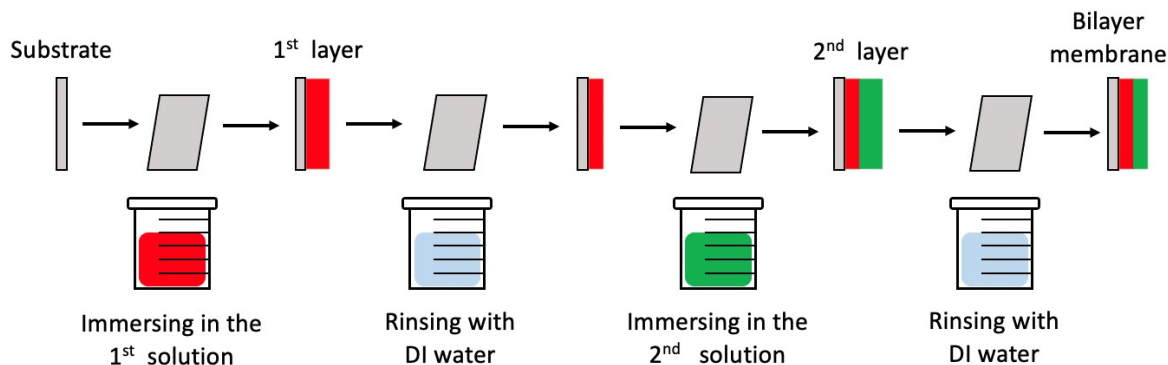
Figure 4. The schematic illustration of membrane casting by layer-by-layer technique

Storing sulfur-containing oils after desulfurization

Storing sulfur-containing oils requires careful consideration and proper handling to ensure safety, maintain oil quality, and comply with environmental regulations.

Storing sulfur-containing oils in superhydrophobic materials offers several benefits due to their water-repellent nature and unique surface properties. Superhydrophobic materials can effectively prevent water and moisture ingress into the stored oils, which is essential for preserving oil quality and preventing degradation [54]. Additionally, the use of superhydrophobic materials can minimize corrosion and oxidation of metal containers used for oil storage, as water contact with the container surfaces is reduced [55]. This leads to extended storage life and improved overall stability of the stored sulfur-containing oils.

Superhydrophobic coatings or linings applied to storage tanks, pipelines, and containers can also facilitate easier and cleaner oil transfer, preventing residual water from mixing with the oil during handling and transportation [56]. However, it is essential to consider the compatibility of the superhydrophobic materials with the specific sulfur-containing oils to ensure there are no adverse chemical interactions that may affect the oil's quality or the material's integrity [57]. Proper testing and selection of suitable superhydrophobic materials are crucial for successful and efficient storage of sulfur-containing oils [58].

Limitations of pervaporative desulfurization:

1. Membrane Stability: The stability of pervaporation membranes is crucial for long-term operation. Polymeric membranes, in particular, may suffer from limitations such as low stability under harsh operating conditions, including high temperatures and chemical exposure [23].

2. Fouling and Membrane Degradation: Fouling, deposition of contaminants on the membrane surface, and membrane degradation can occur during pervaporative desulfurization. Sulfur compounds or other impurities in the feed stream can lead to fouling, reducing the membrane performance over time [54].

3. Aggregation and Interface Defects: The incorporation of fillers or nanoparticles into membranes, such as metal-organic frameworks (MOFs), can enhance the separation performance. However, the aggregation of particles and interface defects can limit the efficiency and transport properties of the membranes [53].

4. Process Optimization: Achieving optimal operating conditions, including temperature, pressure, and feed composition, is crucial for maximizing the efficiency of pervaporative desulfurization. Process optimization requires a comprehensive understanding of the separation mechanism and transport phenomena [23].

5. Cost and Scalability: The cost of membrane materials, fabrication procedures, and overall process design can be a limitation for pervaporative desulfurization. Additionally, scaling up the process to industrial levels while maintaining efficiency and cost-effectiveness can be challenging [23].

6. Removal of Trace Sulfur: Pervaporative desulfurization may face limitations in achieving complete removal of trace sulfur compounds. Achieving ultra-low sulfur levels required for certain applications, such as in the production of high-purity chemicals or pharmaceuticals, may require additional purification steps [59, 60].

While pervaporative desulfurization offers advantages in sulfur removal, it also faces limitations and challenges. These include selectivity, membrane stability, fouling, specific sulfur compounds, aggregation and interface defects, process optimization, cost, scalability, and the removal of trace sulfur. Overcoming these limitations will require further research and development efforts to enhance the efficiency and applicability of pervaporative desulfurization in various industries.

Conclusions

In conclusion, this comprehensive review paper has provided a deep understanding of the principles, recent advances, and diverse applications of pervaporative desulfurization. By exploring the fundamental mechanisms, recent advancements in membrane materials and module design, and the integration of pervaporative desulfurization with other processes, the paper highlights the potential of this technology for efficient and selective sulfur removal from liquid hydrocarbon streams.

The review emphasizes the significance of novel polymeric membranes, nanocomposite membranes, and hybrid membranes in enhancing separation performance, selectivity, and durability. Additionally, surface modification techniques and tailoring membrane morphology have been identified as key factors in improving the overall efficiency of pervaporative desulfurization systems.

Finally, the review identifies future prospects and research directions, including the development of novel membrane materials, optimization of module design, process integration, scaling up for industrial implementation, and a focus on environmental and energy sustainability. These research directions will pave the way for the widespread adoption and commercialization of pervaporative desulfurization, addressing the challenges associated with sulfur removal and contributing to a cleaner and more sustainable energy landscape.

Overall, this review paper serves as a valuable resource for researchers, engineers, and stakeholders interested in the advancement and application of pervaporative desulfurization technology, facilitating further innovation and optimization in this field.

Acknowledgments

Declaration of competing interest

The authors declare that they have no known competing financial interests or personal relationships that could have appeared to influence the work reported in this paper.

References

1   Galloway, J. N., Dianwu, Z., Jiling, X., & Likens, G. E. (1987). Acid rain: China, United States, and a remote area. *Science, 236*(4808), 1559–1562. https://doi.org/10.1126/science.236.4808.1559

2   Hordijk, L. (1991). Use of the RAINS model in acid rain negotiations in Europe. *Environmental Science & Technology, 25*(4), 596-603. https://doi.org/10.1021/es00016a002

3   Hedin, L. O., & Likens, G. E. (1996). Atmospheric dust and acid rain. *Scientific American, 275*(6), 88–92. https://doi.org/10.1038/scientificamerican1296-88

4   Vahedpour, M., & Zolfaghari, F. (2011). Mechanistic study on the atmospheric formation of acid rain base on the sulfur dioxide. *Structural Chemistry, 22*(6), 1331–1338. https://doi.org/10.1007/s11224-011-9823-y

5   Campagna, D., Kathman, S. J., Pierson, R., Inserra, S. G., Phifer, B. L., Middleton, D. C., Zarus, G. M., & White, M. C. (2004). Ambient hydrogen sulfide, total reduced sulfur, and hospital visits for respiratory diseases in Northeast Nebraska, 1998–2000. *Journal of Exposure Science & Environmental Epidemiology, 14*(2), 180–187. https://doi.org/10.1038/sj.jea.7500313

6   Tang, F. R., & Loke, W. K. (2012). Sulfur mustard and respiratory diseases. *Critical Reviews in Toxicology, 42*(8), 688–702. https://doi.org/10.3109/10408444.2012.698405

7   Awano, S., Ansai, T., Takata, Y., Soh, I., Yoshida, A., Hamasaki, T., Kagiyama, S., Nakamichi, I., Sonoki, K., & Takehara, T. (2008). Relationship between volatile sulfur compounds in mouth air and systemic disease. *Journal of Breath Research, 2*(1), 017012. https://doi.org/10.1088/1752-7155/2/1/017012

8   Neal, R. A., & Halpert, J. (1982). Toxicology of thiono-sulfur compounds. *Annual Review of Pharmacology and Toxicology, 22*(1), 321–339. https://doi.org/10.1146/annurev.pa.22.040182.001541

9   Duayne Whitehurst, D., Isoda, T., & Mochida, I. (1998). Present state of the art and future challenges in the Hydrodesulfurization of Polyaromatic sulfur compounds. *Advances in Catalysis*, 345–471. https://doi.org/10.1016/s0360-0564(08)60631-8

10 Tanimu, A., & Alhooshani, K. (2019). Advanced Hydrodesulfurization catalysts: A review of design and synthesis. *Energy & Fuels, 33*(4), 2810–2838. https://doi.org/10.1021/acs.energyfuels.9b00354

11 Schuman, S. C., & Shalit, H. (1971). Hydrodesulfurization. *Catalysis Reviews, 4*(1), 245-318. https://doi.org/10.1080/01614947108075491

12 Saha, B., Vedachalam, S., & Dalai, A. K. (2021). Review on recent advances in adsorptive desulfurization. *Fuel Processing Technology, 214*, 106685. https://doi.org/10.1016/j.fuproc.2020.106685

13 Jiang, Z., Lü, H., Zhang, Y., & LI, C. (2011). Oxidative Desulfurization of fuel oils. *Chinese Journal of Catalysis, 32*(5), 707–715. https://doi.org/10.1016/s1872-2067(10)60246-x

14 Ismagilov, Z., Yashnik, S., Kerzhentsev, M., Parmon, V., Bourane, A., Al-Shahrani, F. M., Hajji, A. A., & Koseoglu, O. R. (2011). Oxidative Desulfurization of hydrocarbon fuels. *Catalysis Reviews, 53*(3), 199–255. https://doi.org/10.1080/01614940.2011.596426

15 Hossain, M., Park, H., & Choi, H. (2019). A comprehensive review on catalytic oxidative Desulfurization of liquid fuel oil. *Catalysts, 9*(3), 229. https://doi.org/10.3390/catal9030229

16 Otsuki, S., Nonaka, T., Takashima, N., Qian, W., Ishihara, A., Imai, T., & Kabe, T. (2000). Oxidative Desulfurization of light gas oil and vacuum gas oil by oxidation and solvent extraction. *Energy & Fuels, 14*(6), 1232–1239. https://doi.org/10.1021/ef000096i

17 Ghassa, M., Khorashe, F., Hajjar, Z., & Soltanali, S. (2023). Comparative study on adsorptive Desulfurization of Thiophenic compounds over terephthalic acid-based and Trimesic acid-based metal-organic frameworks. *Energy & Fuels, 37*(9), 6490–6502. https://doi.org/10.1021/acs.energyfuels.3c00091

18 Abdali, A., Mahmoudian, M., Eskandarabadi, S. M., Nozad, E., & Enayati, M. (2020). Elimination of dibenzothiophene from N-hexaNe by nano-composite membrane containing Cu-MOF in a pervaporation process. *Journal of the Iranian Chemical Society, 18*(5), 1015–1026. https://doi.org/10.1007/s13738-020-02087-7

19 Hou, Y., Xu, Y., Li, H., Li, Y., & Niu, Q. J. (2018). Polyvinyl Butyral/Modified SiO_2 Nanoparticle membrane for gasoline Desulfurization by Pervaporation. *Chemical Engineering & Technology, 42*(1), 65–72. https://doi.org/10.1002/ceat.201800327

20 Ong, Y. K., Shi, G. M., Le, N. L., Tang, Y. P., Zuo, J., Nunes, S. P., & Chung, T. (2016). Recent membrane development for pervaporation processes. *Progress in Polymer Science, 57*, 1–31. https://doi.org/10.1016/j.progpolymsci.2016.02.003

21 Peng, P., Lan, Y., Zhang, Q., & Luo, J. (2021). Application of graphene structure/polyurethane membrane in pervaporative desulfurization. *Journal of Applied Polymer Science, 139*(3), 51514. https://doi.org/10.1002/app.51514

22 Nie, Y., Li, S., Wu, C., Wang, C., He, D., & Mei, Y. (2018). Efficient removal of SO_2 from flue gas with phosphate rock slurry and investigation of reaction mechanism. *Industrial & Engineering Chemistry Research, 57*(44), 15138-15146. https://doi.org/10.1021/acs.iecr.8b03223

23 Sridhar, S., Smitha, B., & Shaik, A. (2005). Pervaporation-based separation of methanol/MTBE mixtures—A review. *Separation & Purification Reviews, 34*(1), 1–33. https://doi.org/10.1081/spm-200054949

24 Vane, L. M. (2013). Pervaporation and vapor permeation tutorial: Membrane processes for the selective separation of liquid and vapor mixtures. *Separation Science and Technology, 48(3)*, 429–437. https://doi.org/10.1080/01496395.2012.725792

25 Castro-Muñoz, R. (2019). Pervaporation-based membrane processes for the production of non-alcoholic beverages. *Journal of Food Science and Technology, 56(5)*, 2333-2344. https://doi.org/10.1007/s13197-019-03751-4

26 Gupta, K. M., Liu, J., & Jiang, J. (2019). A molecular simulation protocol for membrane pervaporation. *Journal of Membrane Science, 572*, 676–682. https://doi.org/10.1016/j.memsci.2018.11.052

27 Wang, L., Wang, Y., Wu, L., & Wei, G. (2020). Fabrication, properties, performances, and separation application of polymeric Pervaporation membranes: A review. *Polymers, 12*(7), 1466. https://doi.org/10.3390/polym12071466

28 Kancherla, R., Nazia, S., Kalyani, S., & Sridhar, S. (2021). Modeling and simulation for design and analysis of membrane-based separation processes. *Computers & Chemical Engineering, 148*, 107258. https://doi.org/10.1016/j.compchemeng.2021.107258

29 Nueraji, M., Toktarbay, Z., Ardakkyzy, A., Sridhar, D., Algadi, H., Xu, B. B., Althakafy, J. T., Alanazi, A. K., Abo-Dief, H. M., Adilov, S., & Guo, Z. (2023). Mechanically-robust electrospun nanocomposite fiber membranes for oil and water separation. *Environmental Research, 220*, 115212. https://doi.org/10.1016/j.envres.2023.115212

30 Li, Y., Jiang, W., Tan, P., Liu, X., Zhang, D., & Sun, L. (2015). What matters to the adsorptive Desulfurization performance of metal-organic frameworks? *The Journal of Physical Chemistry C, 119*(38), 21969–21977. https://doi.org/10.1021/acs.jpcc.5b07546

31 Ma, J., Ying, Y., Yang, Q., Ban, Y., Huang, H., Guo, X., Xiao, Y., Liu, D., Li, Y., Yang, W., & Zhong, C. (2015). Mixed-matrix membranes containing functionalized porous metal–organic polyhedrons for the effective separation of CO_2–CH_4 mixture. *Chemical Communications, 51*(20), 4249–4251. https://doi.org/10.1039/c5cc00384a

32 Wu, T., Jing, M., Yang, L., Zou, G., Hou, H., Zhang, Y., Zhang, Y., Cao, X., & Ji, X. (2019). Controllable chain-length for covalent sulfur-carbon materials enabling stable and high-capacity sodium storage. *Advanced Energy Materials, 9*(9), 1803478. https://doi.org/10.1002/aenm.201803478

33 Abdiyev, K. Z., Maric, M., Orynbayev, B. Y., Toktarbay, Z., Zhursumbaeva, M. B., & Seitkaliyeva, N. Z. (2022). Flocculating properties of 2-acrylamido-2-methyl-1-propane sulfonic acid-Co-allylamine polyampholytic copolymers. *Polymer Bulletin, 79*(12), 10741–10756. https://doi.org/10.1007/s00289-021-03994-2

34 Lee, K.X., & Valla, J.A. (2019). Adsorptive desulfurization of liquid hydrocarbons using zeolite-based sorbents: a comprehensive review, *React. Chem. Eng., 4*, 1357–1386. https://doi.org/10.1039/C9RE00036D

35 Azizian, S., Bashiri, H., & Volkov, A.G. (2009). Derivation of Azizian–Volkov (AV)-isotherm based on statistical thermo-dynamics, *Colloids Surf. A: Physicochem. Eng. Asp., 335*, 28–32. https://doi.org/10.1016/j.colsurfa.2008.10.030

36 Saha, B., Vedachalam, S., & Dalai, A.K. (2020). Review on recent advances in adsorptive desulfurization, *Fuel Process. Technol.*, 106685. https://doi.org/10.1016/j.fuproc.2020.106685

37 Gao, J., Meng, H., Lu, Y., Zhang, H., & Li, C. (2012). A carbonium pseudo Ionic liquid with excellent extractive desulfuriza-tion performance. *AIChE Journal, 59*(3), 948–958. https://doi.org/10.1002/aic.13869

38 Li, Z., Li, C., Chi, Y., Wang, A., Zhang, Z., Li, H., Liu, Q., & Welz-Biermann, U. (2012). Extraction process of Dibenzothi-ophene with new distillable amine-based Protic Ionic liquids. *Energy & Fuels, 26*(6), 3723–3727. https://doi.org/10.1021/ef3005064

39 Mitra, D. (2012). Desulfurization of gasoline by Pervaporation. *Separation & Purification Reviews, 41*(2), 97–125. https://doi.org/10.1080/15422119.2011.573044

40 Rychlewska, K., Konieczny, K., & Bodzek, M. (2015). Pervaporative desulfurization of gasoline — separation of thio-phene/n-heptane mixture. *Archives of Environmental Protection, 41*(2), 3–11. https://doi.org/10.1515/aep-2015-0013

41 Ogbonna, V. E., Popoola, P. I., Popoola, O. M., & Adeosun, S. O. (2021). A review on recent advances on improving polyi-mide matrix nanocomposites for mechanical, thermal, and tribological applications: Challenges and recommendations for future im-provement. *Journal of Thermoplastic Composite Materials, 36*(2), 836–865. https://doi.org/10.1177/08927057211007904

42 Chen, J., Li, J., Qi, R., Ye, H., & Chen, C. (2008). Pervaporation separation of thiophene–heptane mixtures with Polydime-thylsiloxane (PDMS) membrane for Desulfurization. *Applied Biochemistry and Biotechnology, 160*(2), 486-497. https://doi.org/10.1007/s12010-008-8368-z

43 Qi, R., Wang, Y., Chen, J., Li, J., & Zhu, S. (2007). Pervaporative desulfurization of model gasoline with Ag_2O-filled PDMS membranes. *Separation and Purification Technology, 57*(1), 170–175. https://doi.org/10.1016/j.seppur.2007.04.001

44 Cao, R., Zhang, X., Wu, H., Wang, J., Liu, X., & Jiang, Z. (2011). Enhanced pervaporative desulfurization by polydime-thylsiloxane membranes embedded with silver/silica core–shell microspheres. *Journal of Hazardous Materials, 187*(1-3), 324–332. https://doi.org/10.1016/j.jhazmat.2011.01.031

45 Yang, Z., Zhang, W., Li, J., & Chen, J. (2012). Preparation and characterization of PEG/PVDF composite membranes and ef-fects of solvents on its pervaporation performance in heptane desulfurization. *Desalination and Water Treatment, 46*(1-3), 321–331. https://doi.org/10.1080/19443994.2012.677563

46 Liu, K., Fang, C., Li, Z., & Young, M. (2014). Separation of thiophene/N-heptane mixtures using PEBAX/PVDF-composited membranes via pervaporation. *Journal of Membrane Science, 451*, 24-31. https://doi.org/10.1016/j.memsci.2013.09.045

47 Zhang, Q. G., Fan, B. C., Liu, Q. L., Zhu, A. M., & Shi, F. F. (2011). A novel poly(dimethylsiloxane) / poly(oligosilsesquioxanes) composite membrane for pervaporation desulfurization. *Journal of Membrane Science, 366*(1-2), 335–341. https://doi.org/10.1016/j.memsci.2010.10.022

48 Amarante, R. C., & Donaldson, A. A. (2021). Pervaporation separation of ethanol and 2-ethylhexanol mixtures using cellu-lose acetate propionate and poly(1-vinylpyrrolidone-co-vinyl acetate) blend membranes. *Separation and Purification Technology, 258*, 117953. https://doi.org/10.1016/j.seppur.2020.117953

49 Li, B., Yu, S., Jiang, Z., Liu, W., Cao, R., & Wu, H. (2012). Efficient desulfurization by polymer–inorganic nanocomposite membranes fabricated in reverse microemulsion. *Journal of Hazardous Materials, 211–212*, 296–303. https://doi.org/10.1016/j.jhazmat.2011.10.047

50 Li, B., Xu, D., Jiang, Z., Zhang, X., Liu, W., & Dong, X. (2008). Pervaporation performance of PDMS-Ni^{2+} Y zeolite hybrid membranes in the desulfurization of gasoline. *Journal of Membrane Science, 322*(2), 293–301. https://doi.org/10.1016/j.memsci.2008.06.015

51 Liu, W., Li, B., Cao, R., Jiang, Z., Yu, S., Liu, G., & Wu, H. (2011). Enhanced pervaporation performance of poly(dimethyl siloxane) membrane by incorporating Titania microspheres with high silver ion loading. *Journal of Membrane Science, 378*(1-2), 382–392. https://doi.org/10.1016/j.memsci.2011.05.027

52 Samanta, M., Roychowdhury, S., & Mitra, D. (2021). Studies on sorption kinetics and sorption isotherm for pervaporative separation of benzene from model pyrolysis gasoline using insitu nano silver/polyvinyl alcohol membrane. *Journal of Environmental Science and Health, Part A, 56*(13), 1397–1408. https://doi.org/10.1080/10934529.2021.2002094

53 Sun, H., Magnuson, Z., He, W., Zhang, W., Vardhan, H., Han, X., He, G., & Ma, S. (2020). Peg@ZIF-8/PVDF Nanocompo-site membrane for efficient Pervaporation Desulfurization via a layer-by-layer technology. *ACS Applied Materials & Interfaces, 12*(18), 20664–20671. https://doi.org/10.1021/acsami.0c02513

54 Cai, C., Fan, X., Han, X., Li, J., & Vardhan, H. (2020). Improved Desulfurization performance of Polyethyleneglycol mem-brane by incorporating metal organic framework CuBTC. *Polymers, 12*(2), 414. https://doi.org/10.3390/polym12020414

55 Farsi, M., Honarvar, B., Heydarinasab, A., & Arjmand, M. (2018). Experimental survey of temperature, time and cross-linking agent effects on polydimethylsiloxane composite membranes performances in sulfur removal. *International Journal of Indus-trial Chemistry, 9*(2), 177–183. https://doi.org/10.1007/s40090-018-0148-1

56 Kurbanova, A., Myrzakhmetova, N., Akimbayeva, N., Kishibayev, K., Nurbekova, M., Kanagat, Y., Tursynova, A., Zhunussova, T., Seralin, A., Kudaibergenova, R., Toktarbay, Z., & Toktarbaiuly, O. (2022). Superhydrophobic SiO_2/Trimethylchlorosilane coating for self-cleaning application of construction materials. *Coatings, 12*(10), 1422. https://doi.org/10.3390/coatings12101422

57 Hamilton, L. A., & Woods, W. W. (1950). Reaction of iron with organic sulfur compounds. *Industrial & Engineering Chem-istry, 42*(3), 513–519. https://doi.org/10.1021/ie50483a031

58 Cheng, X., Ma, H., Chen, S., Yu, R., Chen, X., & Yao, Z. (1998). Corrosion of stainless steels in acid solutions with organic sulfur-containing compounds. *Corrosion Science, 41*(2), 321–333. https://doi.org/10.1016/s0010-938x(98)00125-5

59 Rizzo, C., Misia, G., Marullo, S., Billeci, F., & D'Anna, F. (2022). Bio-based chitosan and cellulose Ionic liquid gels: Polymeric soft materials for the desulfurization of fuel. *Green Chemistry, 24*(3), 1318–1334. https://doi.org/10.1039/d1gc02679h

60 Boshagh, F., Rahmani, M., Rostami, K., & Yousefifar, M. (2021). Key factors affecting the development of oxidative Desulfurization of liquid fuels: A critical review. *Energy & Fuels, 36*(1), 98–132. https://doi.org/10.1021/acs.energyfuels.1c03396

Information about authors*

Ospanova, Aigerim — PhD Student, Department of Chemical & Materials Engineering, School of Engineering & Digital Science, Nazarbayev University, Kabanbay Batyr 53, 010000, Astana, Kazakhstan; e-mail: a.ospanova@alumni.nu.edu.kz;

Ardakkyzy, Aida — Graduate Student, Department of Chemical & Materials Engineering, School of Engineering & Digital Science, Nazarbayev University, Kabanbay Batyr 53, 010000, Astana, Kazakhstan; e-mail: aida.ardakkyzy@nu.edu.kz;

Kurbanova, Aliya — PhD Student at Renewable Energy Laboratory, National Laboratory Astana (NLA), Nazarbayev University, Kabanbay Batyr 53, 010000, Astana, Kazakhstan; e-mail: aliya.kurbanova@nu.edu.kz; https://orcid.org/0000-0002-1261-4582

Kanagat, Yernar — PhD Student at Department of Chemistry, Faculty of Natural Sciecnes, L.N. Gumilyov Eurasian National University, Kazhymukan Street 5, 010008, Astana, Kazakhstan; e-mail: yernarq@gmail.com

Abutalip, Munziya — PhD, Renewable Energy Laboratory, National Laboratory Astana (NLA), Nazarbayev University, Kabanbay Batyr 53, 010000, Astana, Kazakhstan; e-mail: munziya.abutalip@nu.edu.kz; https://orcid.org/0000-0003-2200-8479

Toktarbay, Zhexenbek — PhD, Satbayev University, Satbayev St. 22a, Almaty 050013, Kazakhstan; e-mail: zhexenbek.toktarbay@gmail.com; https://orcid.org/0000-0003-4131-0905

Nuraje, Nurxat — Associate Professor, PhD, Department of Chemical & Materials Engineering, School of Engineering & Digital Science; Renewable Energy Laboratory, National Laboratory Astana (NLA), Nazarbayev University, Kabanbay Batyr 53, 010000, Astana, Kazakhstan; e-mail: nurxat.nuraje@nu.edu.kz; https://orcid.org/0000-0002-4335-8905

---

*The author's name is presented in the order: *Last Name, First and Middle Names*

Annas Nurlan* [iD], Sapar R. Konuspayev [iD], Tleutay S. Abildin [iD]

Al-Farabi Kazakh National University, Almaty, Kazakhstan
(*Corresponding author's e-mail: annas-kz@mail.ru)

The Effect of Rh/BAC Catalyst Preparation and Pretreatment Methods on Benzene Hydrogenation

The challenge of developing catalytic materials with improved performance relies on the support of metal particles on carbon surfaces. The results of benzene hydrogenation on Rh/BAC (birch activated carbon) prepared by different methods, including adsorption and impregnation, depending on the moisture capacity of the support, were presented. The volumes and diameters of the pores on the BAC surface were determined by BET method, SEM and chemical compositions were characterized. Benzene hydrogenation took place on various carbon-supported catalysts at a temperature of 60 °C and a hydrogen partial pressure of 40.0 MPa. Catalysts produced through the impregnation process were more effective than those produced via adsorption. Rhodium cations enter the micro pores and remain in their metallic form during the adsorption of chloride salt solutions. Hydrogen adsorption on them is facile, while access of benzene molecules is difficult. Prior reduction in the hydrogen flow is essential for full completion of the hydrogenation reaction on catalysts, as rhodium reduction and hydrogenation reaction occur simultaneously.

Keywords: hydrogenation, benzene, cyclohexane, rhodium, catalysts, support, activity, activated carbon.

Introduction

Hydrogenation of benzene to cyclohexane is an essential process for the petroleum industry and environmental protection. Although it has been around for more than 200 years, the hydrogenation of aromatic compounds is still important today. For example, incomplete combustion of benzene in petrol produces the carcinogenic compound benzopyrene in exhaust gases. Thus, according to European standards, the volume of benzene in gasoline should not exceed 1 %, and during reforming, 1/3 of the volume is released as aromatic compounds [1–4]. Catalysts are therefore needed to ensure the selective hydrogenation of benzene. Secondly, benzene is needed to store hydrogen: one benzene molecule holds three hydrogen molecules. Other chemical syntheses require new catalysts to store active energy for the hydrogenation of aromatic compounds [5].

There are commercially available activated carbon supports and carbon-supported rhodium catalysts to determine the effect of the pore structure and chemical nature of carbons on Rh/C catalysts. Firstly, meso- and macro pores are important for the mass transfer of the metal precursor within the support particle; the larger the pores, the better the distribution of rhodium throughout the support particle. Secondly, the chemical composition of the carbon surface determines the degree of interaction between rhodium and the carbon surface; pH affects particle attraction, and the oxygen-containing groups of the surface act as adsorption sites for rhodium [6].

Very high catalytic activity has been observed in benzene to cyclohexane conversions using Rh/TPPTS catalysed in water [TPPTS=P(C_6H_4-m-SO_3Na)$_3$] in organic two-phase systems. There has been extensive research into the effects of a number of operating parameters on benzene hydrogenation in two phases. Advantage of this reaction is that the highest catalytic activity was obtained when the Rh/TPPTS catalytic complexes in the water/benzene phase (low volume ratio of 0.4) were dissolved in water and benzene. By using phase separation, sulphur-resistant compounds were easily removed, and recycling experiments demonstrated that the catalytic activity remained high for five consecutive cycles.

The benzene hydrogenation reaction has been extensively studied using heterogeneous catalysts including metal oxides, zeolites and carbonaceous supports as well as different preparation methods [7–14]. It is very common to use porous materials as supports or even catalysts in the hydrogenation reaction. This range of materials makes the active phase more accessible and prevents the accumulation of metals due to their

porous structure. Because of their adjustable pores, these materials can be used in a variety of processes to form the desired products more selectively.

Due to the toxicity of benzene, much attention has been paid to the hydrogenation of benzene to cyclohexane. Nanoparticles of various metals, including platinum, ruthenium and rhodium, have been used in the benzene hydrogenation process. Since metal nanoparticles tend to aggregate into large particles, a variety of support materials such as carbon nanotubes, titanium dioxide, and silicon dioxide were used to stabilise the metal nanoparticles and improve their function. For example, in benzene hydrogenation, Rh/SiO_2, Ru/SiO_2, Ru/zeolite, Ru/SBA-15, and Pt(0) nanoparticles are highly active catalysts [8].

Despite the large number of published works, it is necessary to find an optimal combination of metal and support to obtain efficient benzene hydrogenation catalysts. Cerium is believed to enhance the nanoparticle activity and stability of metals due to strong metal-support interactions. The high catalytic activity of the cerium oxide-based catalyst is closely related to the exchange of Ce^{4+} and Ce^{3+} in cerium oxide during catalytic reactions. The valence and defect structure of CeO_2 can be spontaneously altered by doping with other ions. An example of this is the catalytic use of rhodium nanoparticles deposited on cerium oxide (Rh NPs/CeO_2) in the hydrogenation of benzene [15].

The result of hydrogenation in ethanol and the effect of hydrogen pressure were compared using a rhodium and gold catalyst calcined on an amorphous synthetic aluminosilicate (ASA, Siral-40) substrate with a high specific surface area for benzene and toluene. The catalyst was prepared by two different methods, specifically absorption by moisture capacity and the colloidal method [16]. The impregnation method was also used to prepare the catalyst in two different ways: sequentially impregnating first one metal salt, then the other, and simultaneously impregnating gold and rhodium salts. It was discovered that hydrogenation is most successful for selectively hydrogenating benzene in terms of moisture capacity in catalysts made by impregnation. Catalyst activation depends on the amount of rhodium required to activate benzene and toluene on the catalyst surface. The amount of rhodium on the surface is close to that theoretically possible as it remains on the surface of catalysts prepared by the colloidal method [17].

By analysing recent literature data and experimental studies, it was clearly established that rhodium is highly active in hydrogenation reactions. We supported rhodium on AAC (apricot kernel) and BAC supported subunits and converted benzene to cyclohexane by complete hydrogenation. Rhodium catalysts seeded on AAC supported and modified catalysts showed high selectivity in the hydrogenation of benzene. Hydrogenation of benzene and toluene in the presence of rhodium catalyst supported on rice husk activated carbon (RHAC) and apricot kernel activated carbon (AAC). Since AAC is strong, whereas RHAC is light and volatile and difficult to isolate from the reaction mass, it was shown that birch wood activated carbon could be an effective support. The Rh/RAC catalyst was found to be five times lower than Rh/AAC, which is equivalent to catalysts based on activated Siberian charcoal and rhodium planted on AAC [18].

As can be seen from this work, rhodium was the most active metal in the benzene hydrogenation reaction. In the present study, we present the results on the catalytic activity of Rh/BAC catalysts prepared by different methods in the benzene hydrogenation reaction. The prepared catalysts were characterised by the BET method and scanning electron microscopy (SEM). The effects of catalyst types on benzene hydrogenation and catalytic performance were discussed.

Experimental

Materials
$RhCl_3 \cdot 3H_2O$ was purchased from Sigma-Aldrich (Germany). BAC (activated carbon from birch wood, Sorbis Group, Russia) was used as support. Ethanol was used as a solvent in the hydrogenation of benzene.

Hydrogenation method
Hydrogenation of benzene was carried out in a high-pressure kinetic system capable of maintaining a constant temperature and pressure of hydrogen. The autoclave part of the unit is equipped with an ultra thermostatic layer and turbulent stirrer. The amount of hydrogen that is absorbed from the burette is controlled as part of the research experiment, which is conducted by simultaneously adding the necessary amount of catalysts and reagents to the autoclave and heating it to the necessary pressure and temperature. Calculation of the reaction rate is thoroughly described in detail in the following literature [19–21].

Preparation of the catalyst
The catalysts were prepared by the methods of moisture absorption and adsorption. In the moisture absorption method, the required amount of a sample of the BAC studied was heated in a muffle furnace at a

temperature of 400 ºC for 4 hours. On the second day, the mass was measured and the moisture content was determined. To determine the moisture content, water was dripped from a burette up to a certain volume and stirred until a paste was formed. We determined that one volume of support was equal to the moisture content of water. A sample of the required quantity of $RhCl_3·3H_2O$ salt was taken from the glass bottle, dissolved in water with the required amount of moisture content, dried with careful mixing and left for the second day. After repeated stirring in the drying oven at 120 °C, we left it overnight and the next day for 4 hours in a furnace. It was then reduced with hydrogen at a temperature of 350–400 °C. The desired mass was measured and used for the hydrogenation reaction. Adsorption method: $RhCl_3·3H_2O$ salt required for the support was dissolved in a large volume of water, a support was added to it and kept for 30 minutes, heated with a stirrer up to 60–80 °C. When rhodium ions were adsorbed on the surface of the support, the solution became colourless and transparent. At this point, we assume that all the rhodium ions have been adsorbed. The catalyst was filtered by the vacuum filtration on the Buchner funnel, then it was heated in a drying oven at about 120 °C for 4-6 hours and it was left for the next day.

Characterisation of the catalyst

The following physical methods were used to characterise the catalyst: The specific surface area in the Akuasorb device was determined by the BET method by adsorption of nitrogen molecules.

Chemical composition was determined using scanning electron microscopy (JSM-6460LV (JEOL, SEM).

Results and Discussion

Table 1 summarises the Rh/BAC catalyst, meso, micro pore volumes and pore diameters. The rhodium cations mentioned above are still metallic and enter the pores during adsorption, based on their volume diameters. Therefore, these parameters can be considered as evidence that the catalysts prepared by the adsorption method are not active in the hydrogenation of benzene.

T a b l e 1

Texture characteristics of a BAC-based rhodium catalyst

Catalyst	V_{pore}, cm^3//g	S_{BET}, m^2/g	$D_{pore.}$ nm
Rh/BAC	0.298	934.0	0.6–0.8
Reduced Rh/BAC	0.319	988.0	0.6–0.9

The SEM image of Rh/BAC catalysts is shown in Figure 1. The figure shows different types of birch activated carbon granules taken at different scales. However, the rhodium granules are not visible. At the same time, pores are not visible in the images.
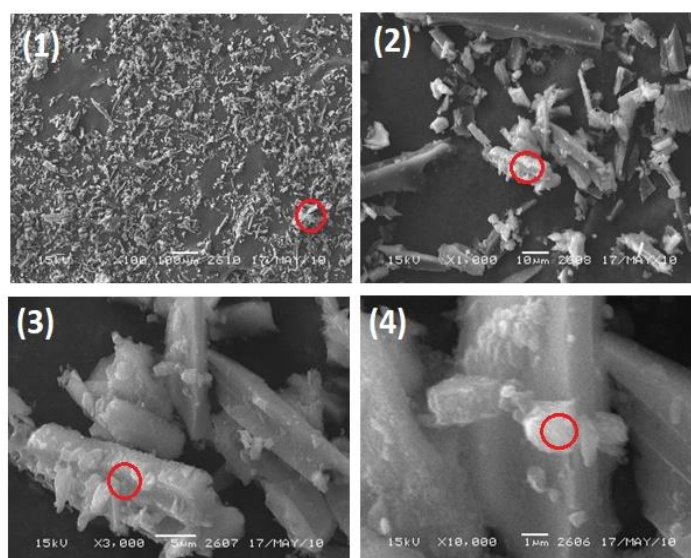
Figure 1. Scanning electron microscope (SEM) images of 1 % Rh/BAC catalysts:
1 — ×100; 2 — ×1000; 3 — ×3000; 4 — ×10000

Chemical composition of catalyst 1 % Rh/BAC

Elemental composition, (%)						
No.	Rh	Cl	O	K	Ca	S	Mg
1	-	0.71	4.67	0.12	0.1	-	-
2	-	0.91	5.47	0.13	0.12	0.12	-
3	0.2	0.5	5.74	0.17	0.21	0.13	0.08
4	0.41	0.74	6.74	0.14	0.27	0.32	0.13
5	-	0.75	3.97	0.43	0.08	0.1	0.14
6	-	0.18	5.09	0.05	0.11	0.1	-
7	3.48	4.19	2.17	0.9	1.56	0.82	-
8	-	0.21	2.38	0.0	0.09	0.07	-
9	-	-	3.46	-	-	-	0.02
10	0.1	0.32	4.66	0.11	0.23	0.1	0.07

Table 2 presents the chemical compositions. Rhodium was detected at points 3, 4, 7, and 10 out of ten used for its determination. At point 10, rhodium was discovered to be 0.1 %, and at points 3 and 4, it was 0.2 %. At point 7, it was identified as 0.41 %. Rhodium was not detected in other points, which suggests that its volume is lower than before, and the metallic rhodium atoms are not on the surface of the carbon. The aggregate comprises mixed carbon microgranules, resulting in an uneven distribution of rhodium volume throughout.

The table indicates that rhodium chloride salt and its associated chlorine anions are present in conjunction with the rhodium. Additionally, elements such as potassium, magnesium, calcium, sulfur, and oxygen were found on the Birch activated carbon (BAC) surface, which is believed to have originated from it. During the hydrogenation of benzene, analogous kinetic curves were observed on catalysts with a moisture capacity and an adsorption method, as depicted in Figures 2 and 3. The reaction rate for catalysts produced using the moisture capacity method is less than 10 mL/min, compared to only 1.8 mL/min for catalysts obtained by the adsorption method. The moisture capacity method is known for producing catalysts with a high rate of reaction.
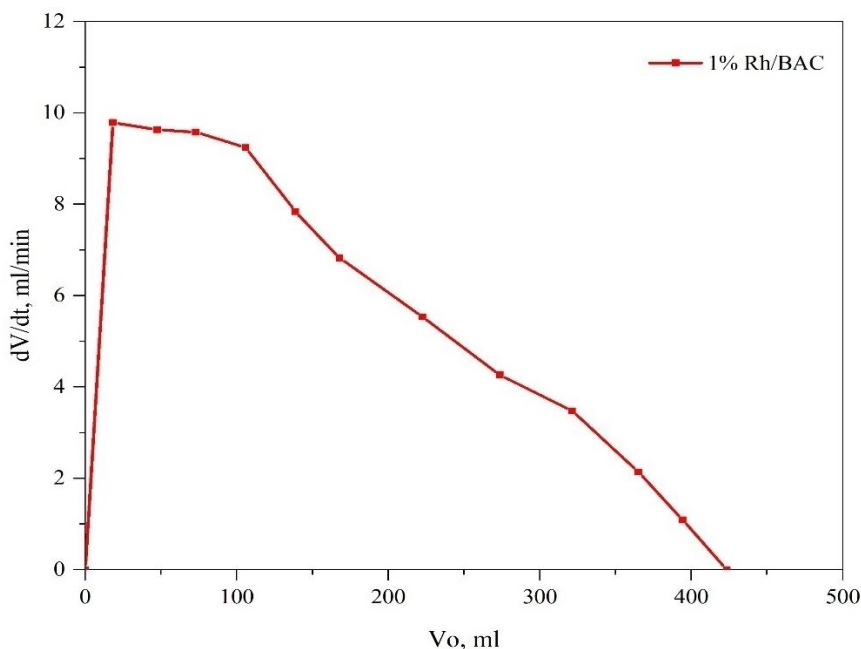
Figure 2. Kinetic curve for benzene hydrogenation using 1 % Rh/BAC catalyst.
Reaction conditions: 0.1 g of catalyst (moisture capacity), 60mL of ethanol, 1 mL of benzene, at 60 °C, 40 MPa
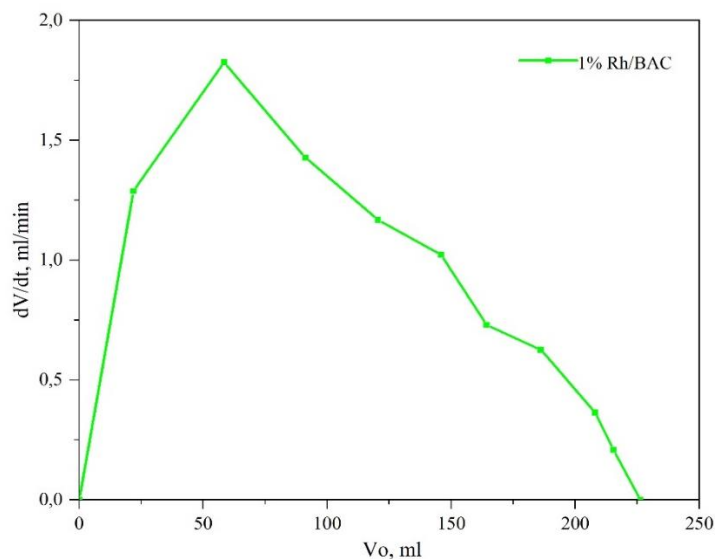
Figure 3. Kinetic curve for benzene hydrogenation using 1 % Rh/BAC catalyst. Reaction conditions: 0.1g of catalyst (adsorption), 60 mL of ethanol, 1 mL of benzene, at 60 °C and 40 MPa pressure

We believe that this trait is linked to the process of adsorption. Rhodium cations adsorb salt deep within the pores, thereby increasing its solubility. Even after hydrogen with reduction, the catalyst does not entirely vanish within the pore, leading to surface adsorption of hydrogen molecules. This makes it difficult for the benzene molecule to be adsorbed and enter the pores, resulting in a low hydrogenation rate.

Figure 4 illustrates the kinetic curve of benzene hydrogenation on catalysts that were prepared using the moisture capacity method with 1 % Rh/BAC. Nevertheless, certain alterations were observed during the pre-treatment. After annealing the first catalyst (1) without reduction, the second catalyst (2) was used in the hydrogen flow. Despite the high initial rate on the first catalyst, the reaction was stopped for not more than half of the counted amount of absorbed hydrogen. On the second catalyst, with a low initial rate, the reaction proceeded until all hydrogen was completely absorbed.
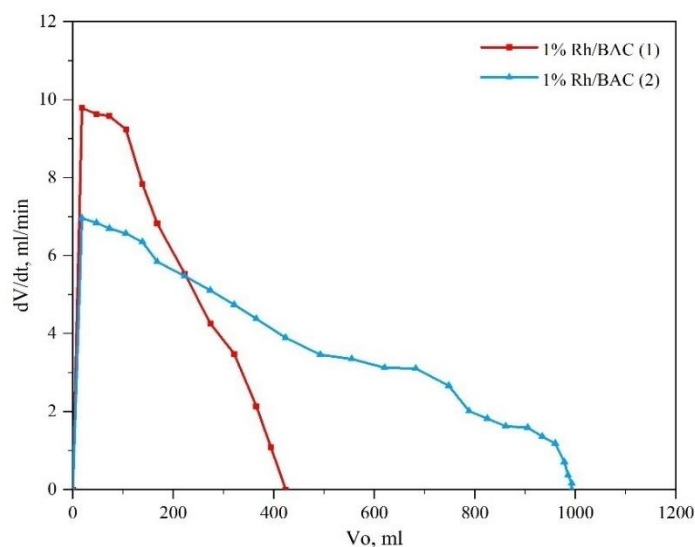
Figure 4. Kinetic curve of benzene hydrogenation. Experiment conditions: 0.1g, 1 % Rh/BAC (moisture capacity), 60 mL of ethanol, 1 mL of benzene, at 60°C, 40 MPa. *1* — not reduced; *2* — reduced by hydrogen

This phenomenon can be explained as follows: when the instantaneous hydrogenation catalyst is used without reduction in a hydrogen atmosphere, rhodium transitions from the cationic type to the metallic form occur through autocatalysis. Concurrently, the metallic surface that is formed undergoes hydrogenation. Consequently, the atoms in metallic rhodium take the shape of clusters. Additionally, due to the abundance

of metal atoms in rhodium, its initial rate is higher. The reaction achieves completion as the metals begin to cluster more slowly.
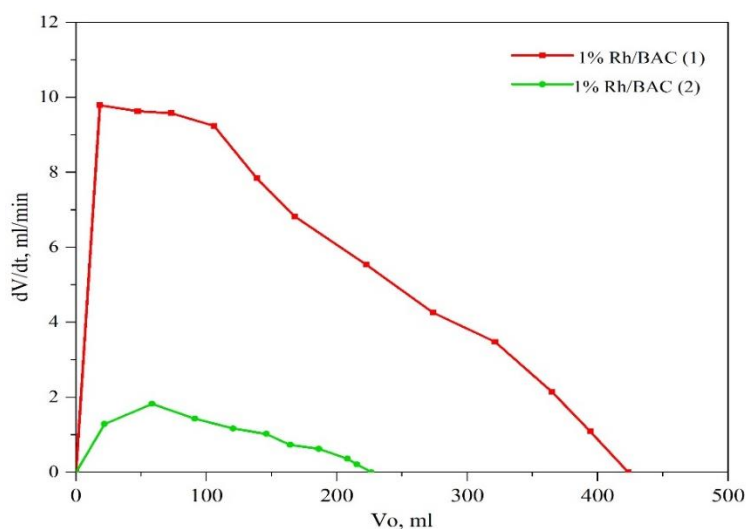
Figure 5. Kinetic curve of benzene hydrogenation with 1 % Rh/BAC.
Experiment conditions: 0.1g of catalyst (moisture capacity), 60 mL of ethanol, 1 mL of benzene, at 60 °C, 40 MPa.
1 — moisture capacity; *2* — adsorption.

Figure 5 illustrates the hydrogenation kinetic curves of catalysts for benzene production using different methods. On the first curve (green), the volume of hydrogen calculated is completely washed out on the catalyst, obtained by using the moisture capacity method with 1 % Rh/BAC. On the second catalyst (red curve), the reaction commences gradually at a rate of 1.8 mL/min and terminates entirely after eliminating 230 mL of hydrogen from the catalyst. As stated above, rhodium cations from the rhodium salt penetrate and remain as metals in the micropores. It is hypothesized that the reaction does not occur because the benzene molecule cannot reach this site.

Conclusions

Rhodium catalysts, supported on carbon materials, were created using adsorption and wet impregnation methods in this study. Liquid-phase benzene hydrogenation was conducted in a batch reactor. The physico-chemical characteristics of the rhodium catalysts on carbon materials were characterised using SEM and N_2 adsorption-desorption analysis. The catalysts' benzene hydrogenation activity is dependent on the method of creation. The catalyst obtained through adsorption is considerably inferior to that produced via the moisture capacity method. The catalyst itself, which has moisture capacity, is easily pre-treated. The reaction is completed by the reduced catalyst, but not by the unreduced catalyst.

References

1   Rautanen, P. (2002). Liquid phase hydrogenation of aromatic compounds on nickel catalyst. Helsinki University of Technology.

2   Kohan, M. (Ed.) (1995) Nylon plastics handbook. Hanser Publishers; Distributed in the USA and in Canada by Hanser/Gardner Publications, Munich etc., Cincinnati

3   Foppa L, Dupont J (2015) Benzene partial hydrogenation: advances and perspectives. *Chem Soc Rev 44*(7): 1886–1897. https://doi.org/10.1039/c4cs00324a

4   American Conference of Governmental Industrial Hygienists (2000) Documentation of TLV for gasoline. In Chemical Substance TLVs and BEIs–2000. https://www.acgih.org Accessed 02 Jul 2018.

5   Metaxas, K.C., & Papayannakos, N.G. (2008). Studying the internal mass transfer phenomena inside a Ni/Al₂O₃ catalyst for benzene hydrogenation. *Chemical Engineering Journal*, *140*(1-3), 352–357. https://doi.org/10.1016/j.cej.2007.10.010

6   Halttunen, M.E., Niemelä, M.K., Krause, A.O.I., Vaara, T., & Vuori, A.I. (2001). Rh/C catalysts for methanol hydrocarbonylation: I. Catalyst characterisation. *Applied Catalysis A: General*, *205*(1–2), 37–49. https://doi.org/10.1016/S0926-860X(00)00554-8

7 Vangelis, C., Bouriazos, A., Sotiriou, S., Samorski, M., Gutsche, B., & Papadogianakis, G. (2010). Catalytic conversions in green aqueous media: Highly efficient biphasic hydrogenation of benzene to cyclohexane catalyzed by Rh/TPPTS complexes. *Journal of Catalysis*, *274*(1), 21–28. https://doi.org/10.1016/j.jcat.2010.06.004

8 Akbayrak, S. (2018). Rhodium (0) nanoparticles supported on ceria as catalysts in hydrogenation of neat benzene at room temperature. *Journal of colloid and interface science*, *530*, 459–464. https://doi.org/10.1016/j.jcis.2018.07.011

9 Goncalves, A.H., Soares, J.C.S., de Araujo, L.R.R., Zotin, F.M., Mendes, F.M., & Gaspar, A.B. (2020). Surface investigation by X-ray photoelectron spectroscopy of Ru-Zn catalysts for the partial hydrogenation of benzene. *Molecular Catalysis*, *483*, 110710. https://doi.org/10.1016/j.mcat.2019.110710

10 Peyrovi, M.H., Parsafard, N., & Mohammadian, Z. (2018). Benzene selective hydrogenation over supported Ni (nano-) particles catalysts: Catalytic and kinetics studies. *Chinese Journal of Chemical Engineering*, *26*(3), 521–528. https://doi.org/10.1016/j.cjche.2017.05.022

11 Peyrovi, M.H., Parsafard, N., & Hajiabadi, M.A. (2017). Ni-W Catalysts Supported on HZSM-5/HMS for the Hydrogenation Reaction of Aromatic Compounds: Effect of Ni/W Ratio on Activity, Stability, and Kinetics. *International Journal of Chemical Kinetics*, *49*(4), 283-292. https://doi.org/10.1002/kin.21074

12 Zhan, Y., Zhou, C., Jin, F., Chen, C., & Jiang, L. (2020). Ru/TiO$_2$ catalyst for selective hydrogenation of benzene: Effect of surface hydroxyl groups and spillover hydrogen. *Applied Surface Science*, *525*, 146627. https://doi.org/10.1016/j.apsusc.2020.146627

13 Liu, H., Fang, R., Li, Z., & Li, Y. (2015). Solventless hydrogenation of benzene to cyclohexane over a heterogeneous Ru–Pt bimetallic catalyst. *Chemical Engineering Science*, *122*, 350-359. https://doi.org/10.1016/j.ces.2014.09.050

14 Chen, Z., Sun, H., Peng, Z., Gao, J., Li, B., Liu, Z., & Liu, S. (2019). Selective hydrogenation of benzene: progress of understanding for the Ru-based catalytic system design. *Industrial & Engineering Chemistry Research*, *58*(31), 13794–13803. https://doi.org/10.1021/acs.iecr.9b01475

15 Goris, B., Turner, S., Bals, S., & Van Tendeloo, G. (2014). Three-dimensional valency mapping in ceria nanocrystals. *Acs Nano*, *8*(10), 10878–10884. https://doi.org/10.1021/nn5047053

16 Konuspaev, S., & Nurlan, A. (2021). Influence of the Au-Rh /ASA catalyst preparation method on the benzene hydrogenation reaction. *Bulletin of the L.N. Gumilyov Eurasian National University. Chemistry. Geography. Ecology Series, 136*(3), 35–44. https://doi.org/10.32523/2616-6771-2021-136-3-35-44

17 Konuspayev, S., Shaimardan, M., Annas, N., Abildin, T.S., & Suleimenov, Y.Y. (2021). Hydrogenation of benzene and toluene over supported rhodium and rhodium-gold catalysts. In *MATEC Web of Conferences*, (Vol. 340, p. 01026). EDP Sciences. https://doi.org/10.1051/matecconf/202134001026

18 Konuspaev, S.R., Shaimardan, M., & Nurlan, A. (2020). Development of new carbon supports for rhodium in the creation of benzene hydrogenation catalysts. *Bulletin of the L.N. Gumilyov Eurasian National University. Chemistry. Geography. Ecology Series,* (1), 35–41. https://doi.org/10.32523/2616-6771-2020-130-1-35-41

19 Toshtay, K., & Auezov, A.B. (2020). Hydrogenation of vegetable oils over a palladium catalyst supported on activated Diatomite. *Catalysis in Industry*, *12*, 7–15. https://doi.org/10.1134/S2070050420010109

20 Toshtay, K., Auyezov, A., Aubakirov, Y. Amrousse, R., Azat, S., Sailaukhanuly, Y., & Nakan U. (2023). Palladium–Nickel Supported and Palladated Activated Diatomite as an Efficient Catalyst for Poly-α-olefins Hydrogenation. *Catalysis Surveys from Asia*, 27, 296–305 https://doi.org/10.1007/s10563-023-09394-y

21 Toshtay, K., Auyezov, A.B., Bizhanov, Z.A., Yeraliyeva, A.T., Toktasinov, S.K., Kudaibergen, B., & Nurakyshev, A. (2015). Effect of catalyst preparation on the selective hydrogenation of vegetable oil over low percentage Pd/diatomite catalysts. *Eurasian Chemico-Technological Journal*, *17*(1), 33–39. https://doi.org/10.18321/ectj192

Information about authors*

Nurlan, Annas (*corresponding author*) — Ph.D. student of the Department of physical chemistry, catalysis and petrochemistry, Al-Farabi Kazakh National University, 71 Al-Farabi ave., Almaty, Kazakhstan; e-mail: annas-kz@mail.ru; https://orcid.org/0009-0005-0294-7198

Konuspaev, Sapar Retaevich — Professor of the Department of physical chemistry, catalysis and petrochemistry, Al-Farabi Kazakh National University, 71 Al-Farabi ave., Almaty, Kazakhstan. E-mail: srkonuspayev@mail.ru; https://orcid.org/0000-0002-7962-6107

Abildin, Tleutay Sarsenbaevich — Associate Professor of physical chemistry, catalysis and petrochemistry, Al-Farabi Kazakh National University, 71 Al-Farabi ave., Almaty, Kazakhstan. E-mail: abildin54@mail.ru; https://orcid.org/0000-0002-2710-7233

_____

*The author's name is presented in the order: *Last Name, First and Middle Names*

Irada G. Melikova*[ID], Arif J. Efendi[ID], Natavan F. Aykan[ID], Elmir M. Babayev[ID], Guseyn M. Faradjev[ID], Ceyran T. Rustamova[ID]

Institute of Catalysis and Inorganic Chemistry named after acad. M .Nagiyev of Ministry of Science and Education of Republic of Azerbaijan, Baku, Azerbaijan
(*Corresponding author′s e-mail: iradam@rambler.ru)

Catalysts and Kinetic Regularities of Oxidation Processes of Chlorotoluenes

The article is devoted to the selection, synthesis and study of the activities of the vanadium oxide-based catalytic systems supported on SiO_2 and Al_2O_3 carriers in the oxidation process of chlorotoluenes. It was shown that V-P-O/SiO_2+Mo, V-Mo-O/SiO_2+V, V-P-O/Al_2O_3+Sb, V-Mo-O/Al_2O_3+Mo catalytic systems exhibit high activity and selectivity in the processes of selective oxidation of mono- and dichlorotoluenes in the gas phase. The oxidation processes of chlorotoluenes were studied in open-type reactors with stationary and fluidized catalyst beds. It was established that the conversion of chlorotoluenes in a reactor with a stationary bed is higher than in a fluidized bed reactor, but selectivity in stationary bed it is slightly lower. The optimal conditions ensuring high conversion (80–95 %) and selectivity of the obtained chloromaleic anhydrides (40–45 %) were determined in a wide range of changes of technological parameters T=673–773 K, τ=0.1–1.0 s, molar ratios XT:O_2=1:1–1:25. It is established that the activities of the catalytic systems were different depending on the method of preparation. Thus, it was noticed that among the catalysts obtained by the methods of precipitation, mechano-chemical impregnation and co-precipitation-impregnation, the latter has shown satisfactory results.

Keywords: aromatic hydrocarbons, chlorotoluene, dichlorotoluenes, catalyst, kinetic regularities, catalytic systems, activity, selectivity.

Introduction

These days, when there is a rapid development in the petrochemical industry, it is very important to investigate the wide application areas of hydrocarbons and their chlorinated analogs. Among the heterogeneous catalytic oxidation processes of aromatic hydrocarbons in the gas phase, the most widespread reactions of benzene and toluene to maleic anhydrides [1–5] should be mentioned. For a long time, the conversion processes of a number of compounds with aromatic ring on various oxide catalysts have been already thoroughly studied and applied on an industrial scale. In accordance with this, the study of oxidation reactions of halogen-containing, especially chlorine-containing chlorotoluenes is of both theoretical and practical importance. The theoretical determination of the influence of chlorine atoms of chlorine-containing toluene and benzenes on the oxidation reactions, the interaction of chlorine with the surface of the catalyst, the effect of the chlorine–oxygen medium on the catalysis process, and developing the general catalysis theory of the processes, the kinetic regularities and mechanism of the oxidation reactions of chlorinated toluenes are of great interest.

A number of scientists [6–9] carried out the oxidation processes of chlororganic industrial waste to CO, CO_2, HCl in a fluidized bed reactor in the presence of catalysts of Mo, Co, Cr, Ni metals added as promoters to the Pd/Al_2O_3 system. Some scientists achieved the oxidation process of 2,4-dichlorobenzoic acid, which is widely used as an intermediate in the pharmaceutical industry of 2,4-dichlorotoluene in the presence of cobalt stearate catalyst. At the same time, a special chromatographic method was developed to study the process in detail. By this method, it is possible to analyze the reaction product after the process without performing any analytical cleaning procedure [10].

Oxygenated derivatives of toluene are used as valuable intermediate products in the manufacture of polymers, rubber, resins and dyes [11, 12]. Conversion of toluene and its derivatives to corresponding aldehydes is one of the most useful processes. These traditional conversion reactions with low conversion and selectivity carried out in the presence of dissolved heavy metal salts of acetic acid via a homogeneous process were shown in [13, 14].

In addition, such processes are economically inconvenient, and heavy metal-containing reaction products released during the process are considered to be dangerous for the environment due to the difficulty of separation of soluble catalysts [15–18].

The main goal of this work is the synthesis and selection of active and selective catalytic systems for the oxidation of chlorotoluenes to chlorine and chloromaleic anhydrides, as well as the neutralization of waste substances released into the environment.

Some of these catalysts consist of only individual oxides, for example, V_2O_5, MoO_3, Sb_2O_5, P_2O_5, CuO and the others compose of mechanical mixtures. The most common method of synthesis is application of soluble salts of these metals, which are easily decomposed during heating, namely, nitrates, ammonium compounds, chlorine-containing and acetate compounds. Therefore, synthesis of such catalytic systems were carried out based on the known methods using ammonium and nitrate salts of V, Mo, P, Sb [15, 16].

In general, the transformation of chlorobenzene and chlorotoluene into widely used compounds by catalytic oxidation should also be considered as a solution of the environmental problem.

Experimental

Initially, a number of catalytic systems were synthesized in order to apply them to the catalytic oxidation reactions of chlorotoluenes. These catalytic systems mainly consist of vanadium, phosphorus, molybdenum, stibium oxides deposited on Al_2O_3 and SiO_2 carriers. In some samples, these oxides are also added as promoters. Catalyst samples in our research were synthesized according to the following technique: The catalytic systems are mainly obtained from ammonium vanadate (NH_4VO_3), ammonium molybdate ($(NH_4)_6Mo_7O_2 \cdot 4H_2O$), sodium phosphate ($Na_2HPO_4 \cdot H_2O$) and orthophosphate salts, occasionally from vanadium nitrate, stibium nitrates, stibium chloride or Sb_2O_5 by their dissolving in oxalic or HCl acid solutions. Depending on the synthesis method, the obtained solution can be deposited on Al_2O_3 or SiO_2 after its slight evaporation. After that, the obtained catalyst is heated in an air at a temperature of 453–533 K for 1 hour, then at 553–653 K for the next 2 hours, and then up to 773 K for 1 hour.

Thus, the synthesized catalyst samples were brought to working condition and their oxidation reactions were studied in both stationary and fluidized bed of open flow reactors.

Chlorotoluenes with a purity of ≥ 99.0 % and manufactured by Sigma Aldrich Company were used for the study of the heterogeneous catalytic oxidation process of chlorotoluenes in the gas phase.

The synthesized catalyst samples were studied by physicochemical analysis methods.

Prepared catalysts were characterized by X-ray phase diffraction, FT-IR, N_2 adsorption-desorption method, thermal analysis, elemental analysis and scanning electron microscope.

Phase formation processes, quantitative phase analysis, the properties of the phases were investigated based on the crystal structure of the synthesized catalytic systems and determined by X-ray D2 phase-X-ray diffraction analysis equipment manufactured by Bruker (Germany).

Information about the surface area (S_{bet}, m^2/g) and the pore area (total volume $V\Sigma$, cm^3/g, diameter d, Å) of the catalytic system were obtained from the adsorption-desorption isotherms at the liquid nitrogen (–196 °C) temperature (Gas adsorption analyzer for surface area and pore size). During the measurements, the samples were first degassed to 0.1Pa. From Brunauer Emmett Teller (B.E.T.) theory, surface area was calculated by its resemblance to the profile cross-section of 0.164 nm^2 corresponding to nitrogen.

Thermogravimetric analysis were carried out on a NETZSCH STA 449F3 (Germany) device programmed to 10 °C/min graduation in the temperature range of 25–900 °C. In this case, the weight of the investigated nanopowder sample was 0.6 g.

Results and Discussion

The results of the X-ray phase analysis of some studied systems are shown in Figure 1.

Figure 1a shows the result of the X-ray phase analysis of the V–P–O system with the ratio of the main components V:P=1:2 in the catalyst sample.

Figure 1b presents the X-ray phase diagram of the same catalyst sample on the Al_2O_3 substrate.

As is seen from figures, the $VO(PO_4)_2$ and $VOPO_4$ phases are mainly observed on the phase diagram. However, it was also determined that the phase formation process of V–P–O/Al_2O_3 catalyst arises from vanadium pentoxide (28.3 %), aluminum phosphate (19.2 %), AlPO (3 %), aluminum oxide (11.1 %), aluminum hexacyclophosphate (19.2 %) phases. The amorphous phase is the main part of the catalyst, mostly due to the use of Al_2O_3 as a carrier. At the same time, phases such as vanadium oxide and divanadium pentoxide dominate in the composition of the samples, which are responsible for the activity of the catalyst.
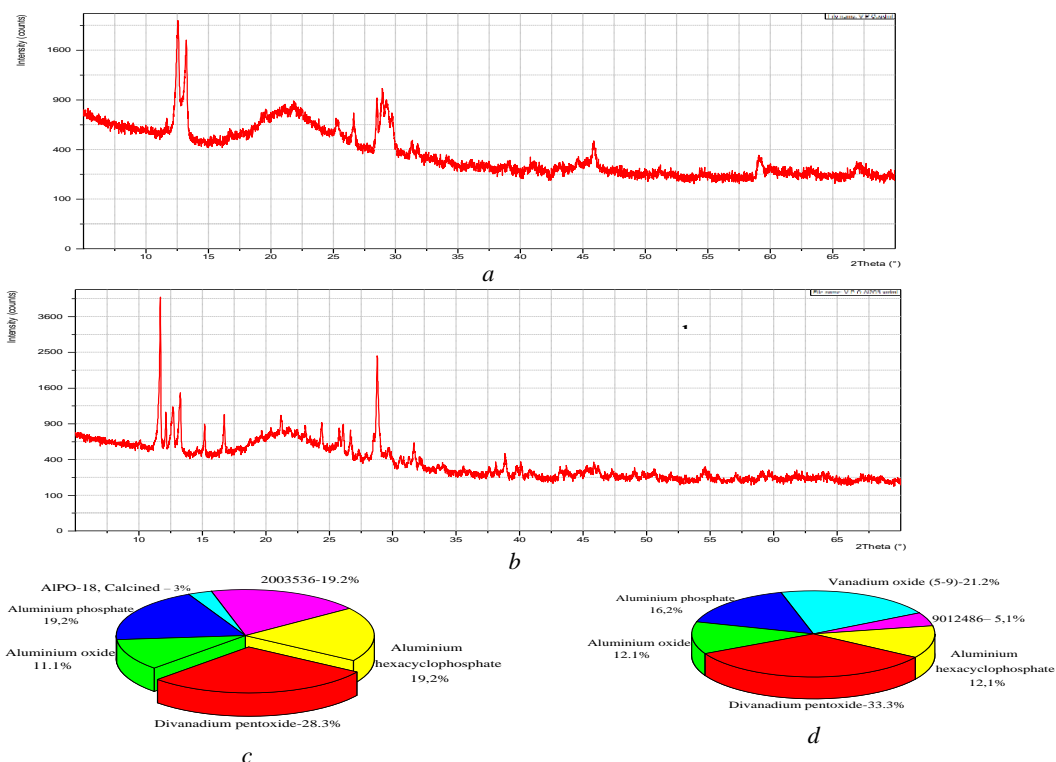
Figure 1. X-ray patterns of the *a*) V-P-O system and *b*) V-P-O/Al$_2$O$_3$catalyst;
c, d) Phase distribution in the catalysts

It should be noted that the phase composition of the catalyst samples varies depending on the proportions of the active components that make them up. It has been determined that the catalytic systems consist of mixed phases and these phases are distributed as shown in Table 1.

T a b l e 1

The formed phases in the V–P–Mo–O catalytic system

Mole ratio			Activation temperature, °C	Phases
V	Mo	P		
3	1	1	500	V$_2$MoO$_8$, VO(PO$_4$)$_2$, V$_2$O$_5$, P$_2$O$_5$, MoO$_3$
3	1	1	600	V$_2$MoO$_8$, V$_9$Mo$_6$O$_{40}$, VO(PO$_4$)$_2$, V$_2$O$_5$, P$_2$O$_5$
2	1	1	600	V$_2$MoO$_8$, V$_9$Mo$_6$O$_{40}$, VO(PO$_4$)$_2$, V$_2$O$_5$, P$_2$O$_5$
2	2	1	500	V$_2$MoO$_8$, V$_9$Mo$_6$O$_{40}$, PVMoPO$_4$, V$_2$O$_5$, P$_2$O$_5$
1	1	1	500	V$_2$MoO$_8$, V$_9$Mo$_6$O$_{40}$, VOPO$_4$, V$_2$O$_5$, P$_2$O$_5$, MoO$_3$
1	2	2	600	V$_2$MoO$_8$, V$_9$Mo$_6$O$_{40}$, V$_2$O$_5$, P$_2$O$_5$, MoO$_3$
1	1	2	600	V$_2$MoO$_8$, V$_9$Mo$_6$O$_{40}$, V$_2$O$_5$, P$_2$O$_5$, MoO$_3$
1	3	1	600	V$_2$MoO$_8$, V$_9$Mo$_6$O$_{40}$, H$_4$PVMo$_{11}$O$_{40}$, V$_2$O$_5$, P$_2$O$_5$

Thus, the formation of V$_2$MoO$_8$, VOPO$_4$, V$_9$Mo$_6$O$_{40}$ phases is mainly observed in the V:Mo:P=1:1:1 ratios in some mixing V–Mo–P–O catalyst samples. In these values of ratios (V:Mo:P=1:1:2, 1:2:2) VOPO$_4$ is not obtained, whereas other phases remain unchangeable. It should be noted that in this case V$_2$O$_5$, P$_2$O$_5$, MoO$_3$ phases are constantly observed. VO(PO$_4$)$_2$ phase formation together with V$_2$MoO$_8$, V$_9$Mo$_6$O$_{40}$ phases in V:Mo:P=1:1:2, 3:1:1 ratios, and PVMoPO$_4$ phase formation in V:Mo:P=2:2:1 ratio were observed. In the final case, it is necessary to note that the formation of V$_2$O$_5$, P$_2$O$_5$, MoO$_3$ phases were in sight, either. The activation temperature of the catalyst samples also affects the formation of these phases. When the activation temperature is 500–600 °C, that is, 50–150 °C higher than the reaction temperature, the formation of these phases is finished. At the same time, complete formation of phases is achieved during the oxidation process of chlorotoluenes. The change of initial components of catalyst samples also affects their degree of crystallization.

According to the surface characteristics of the VPO catalyst sample unsupported, supported and utilized in oxidation reaction, although the total surface area and radius of the pores rose from 12.025 m²/g to 18.362 m²/g and from 344 Å to 379 Å, respectively; the total volume of the pores in the supported VPO catalyst sample decreases. Considering the characteristic data of the surface after reaction, the earlier mentioned opinion — phase formation processes is over during oxidation process — has been confirmed. The increase of total surface area (23.355 m²/g) and pore radius (379 Å) after the oxidation reaction can also be explained by the adsorption of unconverted chlorotoluenes on the surface, which can be confirmed by thermal analysis and post-processing IR spectra of the catalyst.

The surface characteristics data of the V–P–O sample have been achieved via special programming based on the BET equation and adsorption-desorption equations (Fig. 2).
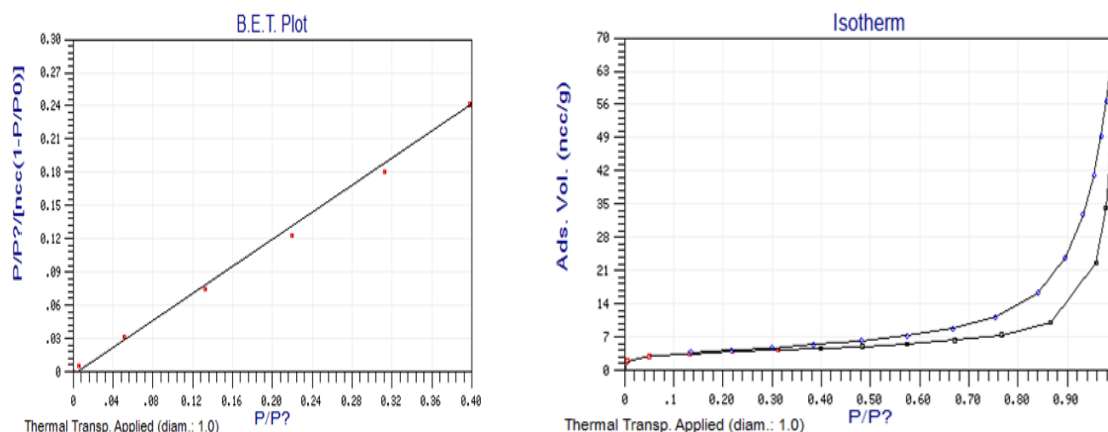
Figure 2. BET plot and adsorption isotherm of the VPO catalytic system

The corresponding surface data of the newly synthesized VPO catalysts, catalysts deposited on the support and catalysts applied in the oxidation process changes according to the following regularities are given in the Table 2.

T a b l e   2

Surface data of the newly synthesized VPO, supported catalyst before and after oxidation

Catalyst simples	State of simples	Area of the surface, m²/g	Radius, Å	Total volume, mL/g
V–P–O	Newly synthesized	12.025	344	0.710
V–P–O/SiO₂	Newly synthesized	18.362	379	0.072
V–P–O/SiO₂	After reaction	23.355	418	0.126

Thermogravimetric analysis revealed endothermic, exothermic effects and mass loss characteristics of catalytic systems. An endothermic effect corresponding to 140 °C is observed on the DTA curve of the investigated VPO/SiO₂ catalyst mixture before and after reaction (Fig. 3). Since the catalysts were analysed in their pure state, it can be assumed that the substances adsorbed on their surface are atmospheric water vapour and other low molecular weight compounds.

Strong and low-concentrated electron acceptor centers are formedin the unheated state of this sample, whereas strong and high-concentrated electron acceptor centers are formed after heating the sample and this is observed in the form of endothermic effects corresponding to the temperatures of 150, 480 and 550 °C on the DTG curve. When the catalyst is heated up to 400 °C, its activity decreases significantly, that is, very little physical adsorption and strong electron acceptor centers were detected after heating. In addition, in TA of the catalyst sample, a mass loss based on the destruction of the system is observed at a temperature above 700 °C, which is 200 °C higher than the reaction temperature and allows us to say that the catalysts are stable during the process and that no decomposition of their structure has occurred.
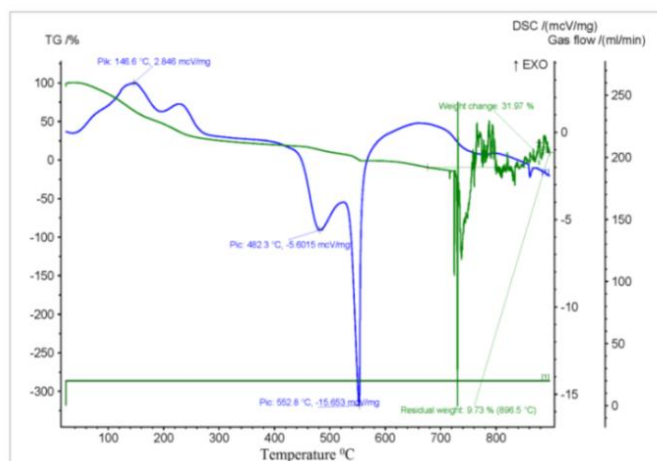
Figure 3. Thermogram obtained from the thermal analysis of the VPO/SiO₂ catalyst

Elemental analysis of the synthesized catalytic systems was also carried out. According to the obtained results, the compatibility between the theoretical calculations and the obtained practical data was tested, and also the correlation between parameters of the synthesized systems and theoretical calculations was determined (Table 3).

Table 3

Distribution of elements in the VPO system supported on SiO₂ (V:P=1:2)

Element	Weight, %	Atom, %	Compound, %	Formula
Na	0.43	0.39	0.58	Na_2O
Si	28.62	21.26	61.23	SiO_2
P	9.59	6.46	21.97	P_2O_5
Ca	0.21	0.11	0.30	CaO
V	8.92	3.66	15.93	V_2O_5
O	52.23	68.12		
Total	100.00			

From the values of the distribution percentages of the components in the newly synthesized VPO/SiO₂ sample that the ratio of the components is V:P=1:2 (Table 3 and Fig. 4 *a*), the distribution of the elements included in the synthesized catalyst and the composition of which was calculated theoretically was confirmed experimentally. Thus, the distribution of vanadium, phosphorus and silicon in the VPO/SiO₂ sample is 3.66 %, 6.46 % and 21.26 %, respectively. In addition, similar experiments were carried out for other catalytic systems, and the distribution characteristics of the components in the catalyst samples were studied.

From the results of the elemental analysis, it is observed that the catalyst contains a small amount of sodium and calcium oxides; the probability of their effect on the course of the oxidation process is negligible.

The results obtained with a scanning electron microscope (Fig. 4 *b*) allow us to say that the surface of the catalyst is uneffected, complete, and rough. 10–12 nm particles were also observed in the images of the surface topology.

The catalyst samples were first heated at 373 K for 1 hour, then at 473 K for 2 hours, and then at 673 K in order to activate the obtained catalytic systems. At this stage, first, water and then the relevant gases are separated from the catalyst. The phase formation process in the catalyst sample heated up to 773 K is almost completed. The active phase formation of the catalysts ends after the influence of both O₂ and chlorotoluenes during the oxidation reaction. Thus, after thermal activation of the catalyst sample, these catalysts indicate lower activity after the first 4 hours in comparison to their activity after the next 2 hours in the oxidation of chlorotoluenes. It should be noted that the phases in the obtained catalysts are different depending on the ratio of the components taken for preparing the catalyst. The phase constitution of these catalyst samples was recorded, and the distribution of the phases present in the catalyst sample was clarified.

a   *b*
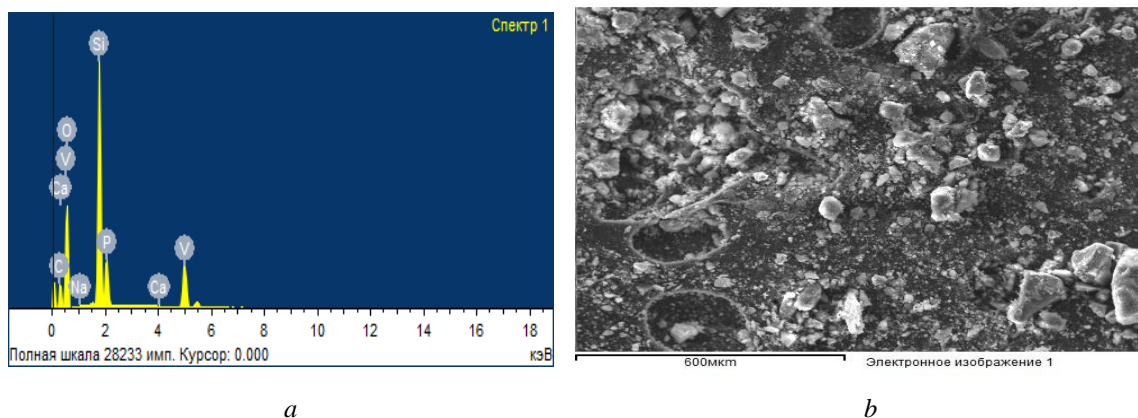
Figure 4. Distribution spectrum of the elements that make up the VPO catalyst (*a*),
Scanning electron microscope image of the VPO/SiO₂ catalytic system

Samples of synthesized active catalysts are as follows: 1. V–P–O/C, 2. V–P–O/TiO₂, 3. V–P–O/Al₂O₃, 4. V–P–O/SiO₂, 5. V–Mo–O/SiO₂, 6. V–Mo–O/Al₂O₃, 7. V–Sb–O/SiO₂, 8. V–Sb–O/Al₂O₃, 9. V–P–O/SiO₂+Mg, 10. V–Mo–O/Al₂O₃+Mg, 11. V–P–O/SiO₂+Zn, 12. V–Mo–O/SiO₂+Zn, 13. V–P–O/SiO₂+Sb, 14. V–P–O/SiO₂+Mo, 15. V–Mo–O/SiO₂+V, 16. V–Sb–O/Al₂O₃+V.

Monochlorotoluenes–2-chlorotoluene (2-*m*-ChT), 3-chlorotoluene (3-*m*-ChT), 4-chlorotoluene and dichlorotoluenes-2,4-dichlorotoluene (2,4-*d*-ChT), 2,3-dichlorotoluene (2,3-*d*-ChT), 2,5-dichlorotoluene (2,5-*d*-ChT), 3,4-dichlorotoluene (3,4-*d*-ChT) are mainly involved in the oxidation reaction. Initially, the temperature range, which is an essential factor of activity of catalytic syntheses in chlorotoluene oxidation process, is determined to find out the kinetic regularities of the process. The oxidation process of chlorotoluenes was carried out in open flow reactors with both stationary and fluidized layer of catalysts using the above-mentioned technique.

Oxidation of chlorotoluenes was carried out in the temperature range of 653–773K. The obtained results are shown in Figure 5.

1. V-P-O/C
2. V-P-O/TiO₂
3. V-P-O/Al₂O₃
4. V-P-O/SiO₂
13. V-P-O/SiO₂+Sb
14. V-P-O/SiO₂+Mo
15. V-Mo-O/SiO₂+V
16. V-Sb-O/Al₂O₃ +V
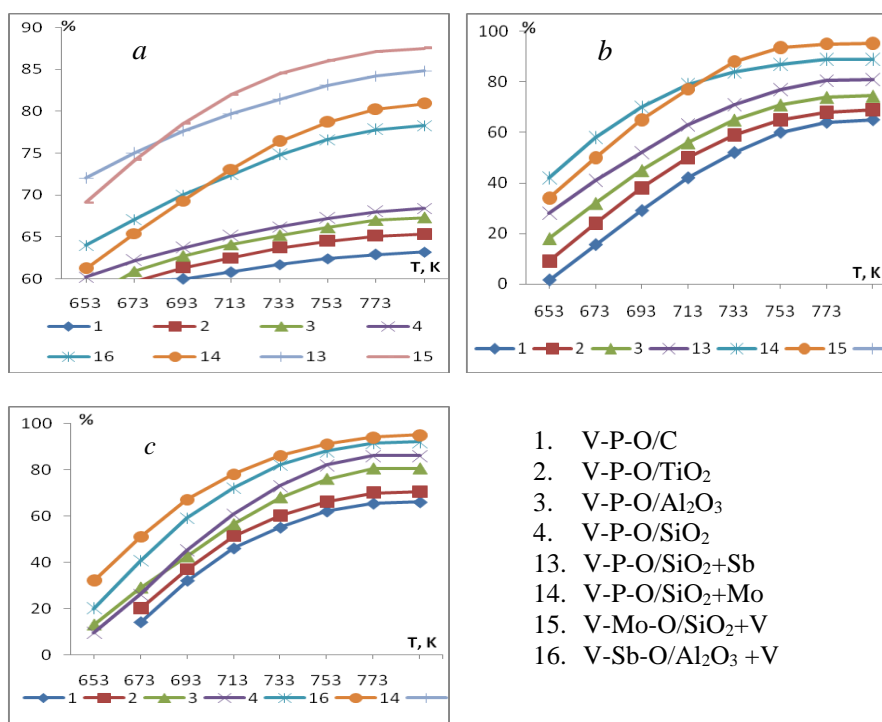
Figure 5. The effect of temperature on the catalytic activity
in the oxidation reactions of *a*) 2-ChT, *b*) 3-ChT, *c*) 4-ChT

As is seen from the results, although the increase in temperature from 653 K to 713 K causes a significant raise in the activities of catalysts in the oxidation of monochlorotoluenes, this varies within the conversion range of 50–70 %. The activities of a number of catalyst samples V–P–O/C, V-P-O/TiO$_2$ are very low (40–50 %), while although the activities of some catalysts V–P–O/Al$_2$O$_3$, V–M–O/SiO$_2$, V–Mo–O/Al$_2$O$_3$ goes up slightly at relatively high temperature values (733–773 K), it does not exceed the 80–90 % limit. However, catalyst samples modified with some elements, such as Zn, V and Mo showed relatively high catalytic activity.

Although the modification of V–P–O/SiO$_2$, V–Mo–O/Al$_2$O$_3$ catalysts with Zn and Mg slightly increased the activity of the catalysts, additional modification of these catalysts with Mo, V and Sb gave better results. Thus, catalyst samples additionally modified with V and Mo(V–P–O/SiO$_2$+Mo, V–Mo–O/SiO$_2$+V, V–Sb–O/Al$_2$O$_3$+V) represented high activity even at low temperatures (673–713 K), the conversion of monochlorotoluenes was over 80 %, and these activities reached 90–95 % at the further temperature rise up to 733–773 K. The most optimal temperature was determined as 733–773 K.

The influence of the synthesis method of catalysts on their activity in the oxidation reaction of chlorotoluenes was also studied. The obtained results are given in the Table 3. As is seen from the table, the synthesis methods of catalysts do not affect the oxidation reaction of chlorotoluenes, so the conversion is 80–90 %, the yield of the main product — m-ChMA varies between 10–15 %, which can be considered insignificant.

The individual selective oxidation of mono- and dichlorotoluenes and the distribution of oxidation products were studied in presence of the catalytic systems that are active in the total oxidation process. Here, the oxidation of chlorotoluenes were studied at the optimal temperatures, contact times and optimal ratios of ChT:O$_2$ previously determined according to the results of the prior studies. The results of the selective oxidation of 4-ChT are given in Table 4.

The activities of the catalysts were determined by carrying out the oxidation process of chlorotoluenes in both stationary and fluidized open-flow reactors. Initially, the activities of a number of catalysts were found in the oxidation process of 4-chlorotoluene and 2,4-dichlorotoluene. The results are given in Table 4.

T a b l e 4

Activities of the catalysts in the oxidation process of 4-m-ChT in the fluidized reactor

Selected components and oxides	Supporters	Reaction temperature, °C	Contact time, sec.	ChT:O$_2$ molar ratio	Conversion of the ChT, %	Yield of the products, %			
						ChBA	MA	m-ChMA	CO$_2$
V$_2$O$_5$	–	440	0.7	1:15	56	4	28	14	21
MoO$_3$	–	450	0.7	1:10	50	–	16	12	22
Sb$_2$O$_3$	–	420	0.6	1:10	84	–	10	6	18
P$_2$O$_5$	–	400	0.6	1:15	40	–	10	5	20
V$_2$O$_5$	SiO$_2$	440	0.7	1:15	60	5	18	15	22
MoO$_3$	SiO$_2$	450	0.7	1:10	55	–	15	14	23
P$_2$O$_5$	SiO$_2$	420	0.6	1:15	44	–	12	10	20
Sb$_2$O$_3$	SiO$_2$	420	0.6	1:10	38	–	8	4	18
V$_2$O$_5$	Al$_2$O$_3$	450	0.7	1:15	64	4	20	16	23
MoO$_3$	Al$_2$O$_3$	460	0.6	1:18	58	–	17	15	24
P$_2$O$_5$	Al$_2$O$_3$	420	0.7	1:10	47	–	14	12	20
Sb$_2$O$_3$	Al$_2$O$_3$	420	0.7	1:10	42	–	10	6	24
V$_2$O$_5$-P$_2$O$_5$	SiO$_2$	430	0.7	1:10	70	10	16	30	23
V$_2$O$_5$-P$_2$O$_5$	Al$_2$O$_3$	420	0.6	1:10	72	6	14	24	24
V$_2$O$_5$-MoO$_3$	SiO$_2$	430	0.6	1:15	70	5	15	25	22
V$_2$O$_5$-MoO$_3$	Al$_2$O$_3$	420	0.7	1:10	68	7	12	24	24
V$_2$O$_5$-Sb$_2$O$_3$	SiO$_2$	430	0.7	1:18	67	4	10	24	26
V$_2$O$_5$-Sb$_2$O$_3$	Al$_2$O$_3$	420	0.7	1:10	65	3	10	20	20
MoO$_3$- Sb$_2$O$_3$	SiO$_2$	430	0.6	1:10	63	–	8	18	26

The obtained results show that the conversion of 4-m-ChT varies between 40–84 % at 420–450 °C, 0.6–0.7 sec., and XT:O$_2$=1:15 molar ratio in the oxidation process carrying out in the presence of individual metal oxides without any supporter. However, chlorobenzaldehyde is obtained only up to 4 % in the pres-

ence of V_2O_5, while this is not observed in the presence of other oxides. At the same time, yields of MA and m-ChMA in the presence of V_2O_5 are 28 % and 14 %, respectively. But the value of this parameter decreases from MoO_3 to P_2O_5, namely from 16 % to 10 %, respectively. Even with this, it should be noted that the amount of CO_2, which is a product of deep oxidation, remains unchanged (20–22 %) in all cases. Studies conducted after depositing these oxides on the respective carriers Al_2O_3 and SiO_2 show that no major changes are observed. After deposition of V_2O_5 and P_2O_5 on SiO_2 supporter in a ratio of 1:2, both the yield of benzaldehydes and the yield of m-ChMA (30 %) increase in comparison with the previous ones. At this time, the yield of CO_2 is slightly reduced (23–24 %).

The effect of some technological parameters on the rate of the catalytic oxidation reactions of chlorotoluenes was studied with in wide temperature variation range (653–773 K), molar ratios of initial components 1:5–1:25 (chlorotoluene:oxygen), ratio of the active components of the catalyst 1:1–1:6, contact time of the reaction, concentrations of initial compounds and products of the reaction. It should be noted that among catalytic systems synthesized and utilized in the oxidation processes, V–P–O/SiO_2+Mo and V–Mo–O/SiO_2+V provide better results, so the experiments were basically carried out in the presence of these catalysts. First, the effect of contact time on the catalytic oxidation reactions of 4-chlorotoluene and 2,4-dichlorotoluene was studied, which resulted in conversion up to 84 % and total selectivity of about 65 %. The obtained results are given in Figure 6.
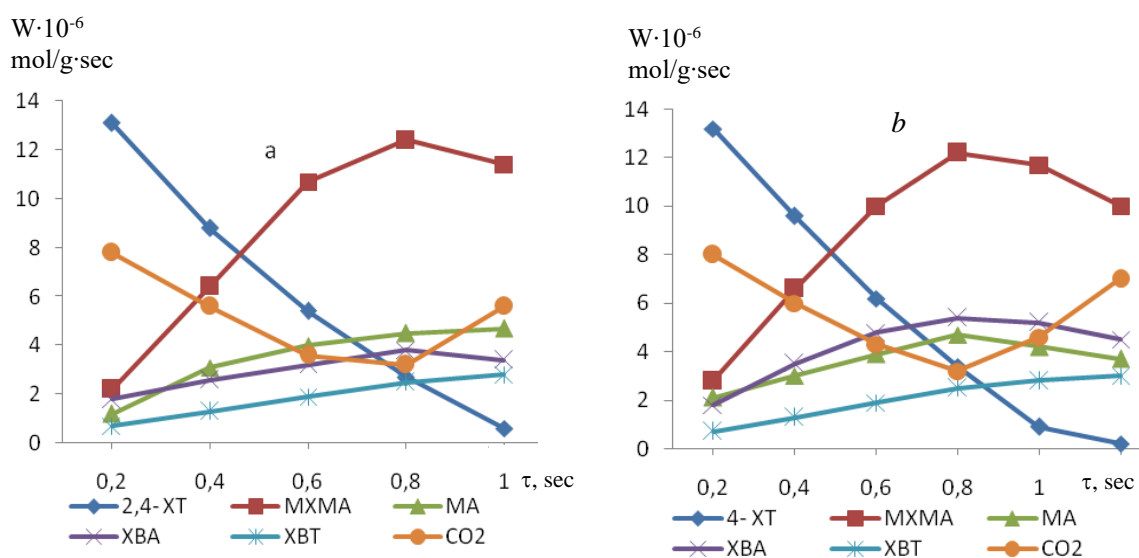
Figure 6. The effect of the contact time on the rate of the oxidation process
of 4-ChT (*b*) and 2,4-ChT (*a*), T = 723 K, ChT:O_2=1:20

As can be seen in Figure 6, the consumption rate of both mono- and dichlorotoluene goes up with the contact time rise within 0.2–1.0 sec. When the contact time rises from 0.2 to 0.8 sec., the formation rate of benzaldehydes, maleic and chloromaleic anhydrides, which are oxidation products of both mono-and dichlorotoluene, increases and tends to decrease with the further raise. In addition to that, although the rate of the formation reaction of carbon dioxide (CO_2), a product of deep oxidation and the one obtained via parallel reaction during oxidation reactions decreases at first, however it grows rapidly after 0.8 seconds. After the contact time value of 0.8 seconds, the formation rates of maleic and chloromaleic anhydrides, as well as chlorobenzaldehyde, which are reaction products, decrease, this allows us to say that maleic and chlormaleic anhydrides undergo partial oxidation, chlorobenzaldehyde converts into chlorobenzoic acid (ChBA) through consecutive reaction and decomposes in the direction of deep oxidation. This is also confirmed by the increase in formation rates of CO_2 and ChBA.

These results indicate that the formation of the main products and by-products occurs on the surface of the catalyst by a parallel-consecutive reaction mechanism. This can be confirmed experimentally by establishing the dependence curve of the selectivities of the reaction products on the conversion of chlorotoluenes during the oxidation of chlorotoluenes at different contact times.

The dependence presented in Figure 7 confirms that targeted reaction products are obtained indeed from the competing oxidation reaction of chlorotoluenes, and then, CO_2 is obtained through the mechanism of the consecutive oxidation reaction of the anhydrides.
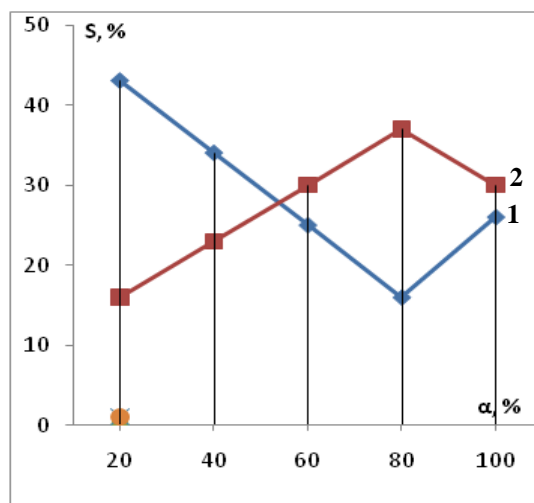
Figure 7. Dependence of selectivity (S) on conversion (α) in the oxidation reaction
of 2,4-dichlorotoluene (2,4-*d*-ChT). *1* — m-ChMA, *2* — CO_2

All necessary calculations were performed using the software package "Optim Me" [19, 20].

Conclusions

The effect of the active components and modifiers (additives), promoters of the catalysts on their activities and selectivities were determined in the oxidation of chlorotoluenes and it was shown that the process goes mainly in the direction of obtaining *m*-ChMA and *d*-ChMA, if the ratio of the components included in the composition of catalyst is V:P=1:2, V:Mo=1:2. When the content of vanadium in the catalysts changes from 1:2 to 1:5 and higher, the yield of chlorobenzenedehyde in the oxidation process goes extensively. The addition of Sb to the catalyst leads to the growth of its service life and stability. In the study of the kinetic regularities of the oxidation of chlorotoluenes it was determined that the process occurs through the parallel-consecutive reaction mechanism in the presence of V–P–O/SiO$_2$ and V–Mo–O/Al$_2$O$_3$ catalysts in a wide range of technological parameters.

References

1   Melikova, I.G., Efendiev, A.J., & Yunisova, F.A. (2001). Reaktsionnaia sposobnost khloruglevodorodov v reaktsiiakh kataliticheskogo okisleniia [Reactivity of chlorohydrocarbons in catalytic oxidation reactions]. *Azerbaidzhanskii khimicheskii zhurnal — Azerbaijan Chemistry Journal, 2,* 13–18 [in Russian]

2   Priyamvada, Sharma, Riya Sailani Anita, Meena, Chandra, & Lata Khandelwal. (2020). Oxidation of crotyl alcohol by N-chloro-4-methylbenzene sulphonamide in acidic medium and in alkaline media in the presence of Os(VIII) catalyst — a kinetic pathway. *Turkish Journal of Chemistr*y, *44*(4), 950–970. https://doi.org/10.3906/kim-2003-67

3   Shakhtaktinsky, T.N., Efendi, A.J., Salehli, N.F., Malikova, I.H., Manafov, M.R., et al. (2004). Issledovanie reaktsii okisleniia o-dikhlorbenzola na oksidnykh katalizatorakh [Study of oxidation reactions of o-Dichlorobenzene on oxide catalysts]. *Azerbaidzhanskii khimicheskii zhurnal — Azerbaijan Chemistry Journal, 3*, 13–17 [in Russian].

4   Federov, A.A., Asyuin, L.D., & Chekryshkin, Yu.S. (2003). Vzaimodeistvie khlorbenzola s poverkhnostiu oksidnykh vanadii-aliuminievykh katalizatorov [Interaction of chlorobenzene with the surface of oxide vanadium-aluminum catalysts]. *XVII Mendeleevskii sezd po obshchei i prikladnoi khimii (21-26 sentiabria 2003) — XVII Mendeleev Congress on General and Applied Chemistry* (pp. 476–481). Abstracts. Kazan [in Russian].

5   Aliyev, A.M., Shabanova, Z.A., Najaf-Guliyev, U.M., & Melikova, I.G. (2015). Selection of Active Modified Zeolite Catalyst and Kinetics of the Reaction of Selective Oxidative Dehydrogenation of Cyclohexane to Cyclohexadiene-1,3. *Modern Research in Catalysis, 04*(04), 87–96. https://doi.org/10.4236/mrc.2015.44011

6   Zhang, J., Qiu, L., He, J., et al. (2007). Occurrence and congeners specific of polychlorinated biphenyls in agricultural soils from Southern Jiangsu. China. *Journal of Environmental Science, 19*(3), 338–342. https://doi.org/10.1016/s1001-0742(07)60055-2

7 Zhang, T., Deng, Y.-Q., Zhou, W.-F., Au, C.-T., & Yin, S.-F. (2014). Selective oxidation of p-chlorotoluene to p-chloro-benzaldehyde with molecular oxygen over zirconium-doped manganese oxide materials. *Chemical Engineering Journal, 240*, 509–515. https://doi.org/10.1016/j.cej.2013.10.094

8 Yang, S., & Wang, J. (2013). Catalytic oxidation of o-chlorotoluene to o-chlorobenzaldehyde by vanadium doped anatase mesoporous TiO_2. *Advanced Materials Research*, *781-784*, 182–185. https://doi.org/10.4028/www.scientific.net/AMR.781-784.182

9 Andreeva, G., Grigor'eva, A., & Trusov, R. (1992). GZHKH-analiz produktov okisleniya 2,4-dikhlortoluola [GLC analysis of 2,4-dichlorotoluene oxidation products]. *Khimiko-Farmatsevticheskii Zhurnal — Chemical-Pharmaceutical Journal, 26*(2), 84–86 [in Russian].

10 Deng, Q., Zhang, T., Au, C., & Yin, Sh. (2013). Liquid-phase catalytic oxidation of p-chlorotoluene to p-chlorobenzaldehyde over manganese oxide octahedral molecular sieves. *Applied Catalysis, 467*, 117–123. https://doi.org/10.1016/j.apcata.2013.07.015

11 Acharyya, S.S., Ghosh, S., Tiwari, R., Sarkar, B., Singha, R.K., Pendem, C., Sasaki, T., & Bal, R. (2014). Preparation of the $CuCr_2O_4$ spinel nanoparticles catalyst for selective oxidation of toluene to benzaldehyde. *Green Chem., 16*(5), 2500–2508. https://doi.org/10.1039/c3gc42369g

12 Kalevaru, N., Lücke, B., & Martin, A. (2009). Synthesis of 2,6-dichlorobenzonitrile from 2,6-dichlorotoluene by gas phase ammoxidation over VPO catalysts. *Catalysis Today*, *142*(3–4), 158–164. https://doi.org/10.1016/j.cattod.2008.09.009

13 Anastas, P., & Warner, J. (1998). *Green Chemistry: Theory and Practice*. New York: Oxford University Press, 30–36.

14 Antunes, A., Ribeiro, M., Silva, J., et al. (2013). Catalytic oxidation of toluene over CuNaHY zeolites: Coke formation and removal. *Applied Catalysis B, 3*, 149–164. https://doi.org/10.1016/S0926-3373(01)00174-6

15 Efendi, A., Babayev, E., Malikova, I., İsmayilova, B., & Aykan, N. (2016). Gas phase heterogeneous catalytic oxidation of chlorohydrocarbons. *Azerbaijan Chemistry Journal*, 3, 193–205.

16 Melikova, I.H. (2022). Oxidation of chlorotoluene, toluene and chlorobenzene in the presence of Ag/MnO_2 catalyst. *Azerbaijan Oil Industry, 10*, 47–52. https://doi.org/10.37474/0365-8554/%202022-10-47-52

17 Ge, H., Chen, G., Yuan, Q., et al. (2007). Gas phase partial oxidation of toluene over modified V_2O_5/TiO_2 catalysts in a micro reactor. *Chemical Engineering Journal, 127*(1-3), 39–46. https://doi.org/10.1016/j.cej.2006.09.024

18 Ma, B., Zhang, Z, Song, W., Xue, X., Yu, Y., et al. (2013). Solvent-free selective oxidation of C-H bonds of toluene and sub-stituted toluene to aldehydes by vanadium-substituted polyoxometalate catalyst. *Journal of Molecular Catalysis A-Chemical, 368*, 152–158. https://doi.org/10.1016/J.MOLCATA.2012.11.022

19 Manafov, M.R. (2015). Development of a Software Application for Solving of Problems of Chemical Kinetics and its Im-plementation in a C#. *Int. J. Eng. Appl. Sci, 2*(10), 33–37.

20 Manafov, M.R. (2016). Software application for solving some typical problems of chemical technology. *Azerbaijan Chemical Journal, 4*, 89–94.

Information about authors*

Melikova, Irada Gasan (*corresponding author*) — Candidate of technical sciences, Leading Research-er, Institute of Catalysis and Inorganic Chemistry named after acad. M. Nagiyev of Ministry of Science and Education of Republic of Azerbaijan, H. Javid Ave. 113, Baku St. Az-1143, Azerbaijan; e-mail: ira-dam@rambler.ru; https://orcid.org/0000-0002-7906-1556

Efendi, Arif Javanshir — Doctor of Chemistry, Professor, Institute of Catalysis and Inorganic Chem-istry named after acad. M. Nagiyev of Ministry of Science and Education of Republic of Azerbaijan, H. Javid Ave. 113, Baku St. Az-1143, Azerbaijan; e-mail: efendi-arif@mail.ru; https://orcid.org/0000-0002-5529-980X

Aykan, Natavan Fakhraddin — Candidate of chemical sciences, Senior Researcher, Institute of Ca-talysis and Inorganic Chemistry named after acad. M. Nagiyev of Ministry of Science and Education of Re-public of Azerbaijan, H. Javid Ave. 113, Baku St. Az-1143, Azerbaijan; e-mail: ntvn-78@hotmail.com, https://orcid.org/0000-0003-2245-7047

Babayev, Elmir Maqsad — Candidate of chemical sciences, Senior Researcher, Institute of Catalysis and Inorganic Chemistry named after acad. M. Nagiyev of Ministry of Science and Education of Republic of Azerbaijan, H. Javid Ave. 113, Baku St. Az-1143, Azerbaijan; e-mail: e.babayev@science.az; https://orcid.org/0000-0001-9507-3111

Faradjev, Guseyn Mamed — Candidate of chemical sciences, Senior Researcher, Institute of Cataly-sis and Inorganic Chemistry named after acad. M. Nagiyev of Ministry of Science and Education of Republic of Azerbaijan, H. Javid Ave. 113, Baku St. Az-1143, Azerbaijan; e-mail: chem@science.az; https://orcid.org/0000-0003-0816-7414

Rustamova, Ceyran Teymur — Candidate of chemical sciences, Senior Researcher, Institute of Catalysis and Inorganic Chemistry named after acad. M. Nagiyev of Ministry of Science and Education of Republic of Azerbaijan, H. Javid Ave. 113, Baku St. Az-1143, Azerbaijan; e-mail: chem@science.az; https://orcid.org/0000-0003-2300-8120

_____

*The author's name is presented in the order: *Last Name, First and Middle Names*

Index of articles published in
"Eurasian Journal of Chemistry"
in 2023

PHYSICAL AND ANALYTICAL CHEMISTRY

PREFACE

QUANTUM CHEMISTRY AND QUANTUM NANOTECHNOLOGIES OF MATERIALS